Universitat d'Alacant
Universidad de Alicante

Copper-based catalysts for the Preferential CO Oxidation in H2-rich streams (CO-PROX reaction)

Arantxa Davó Quiñonero

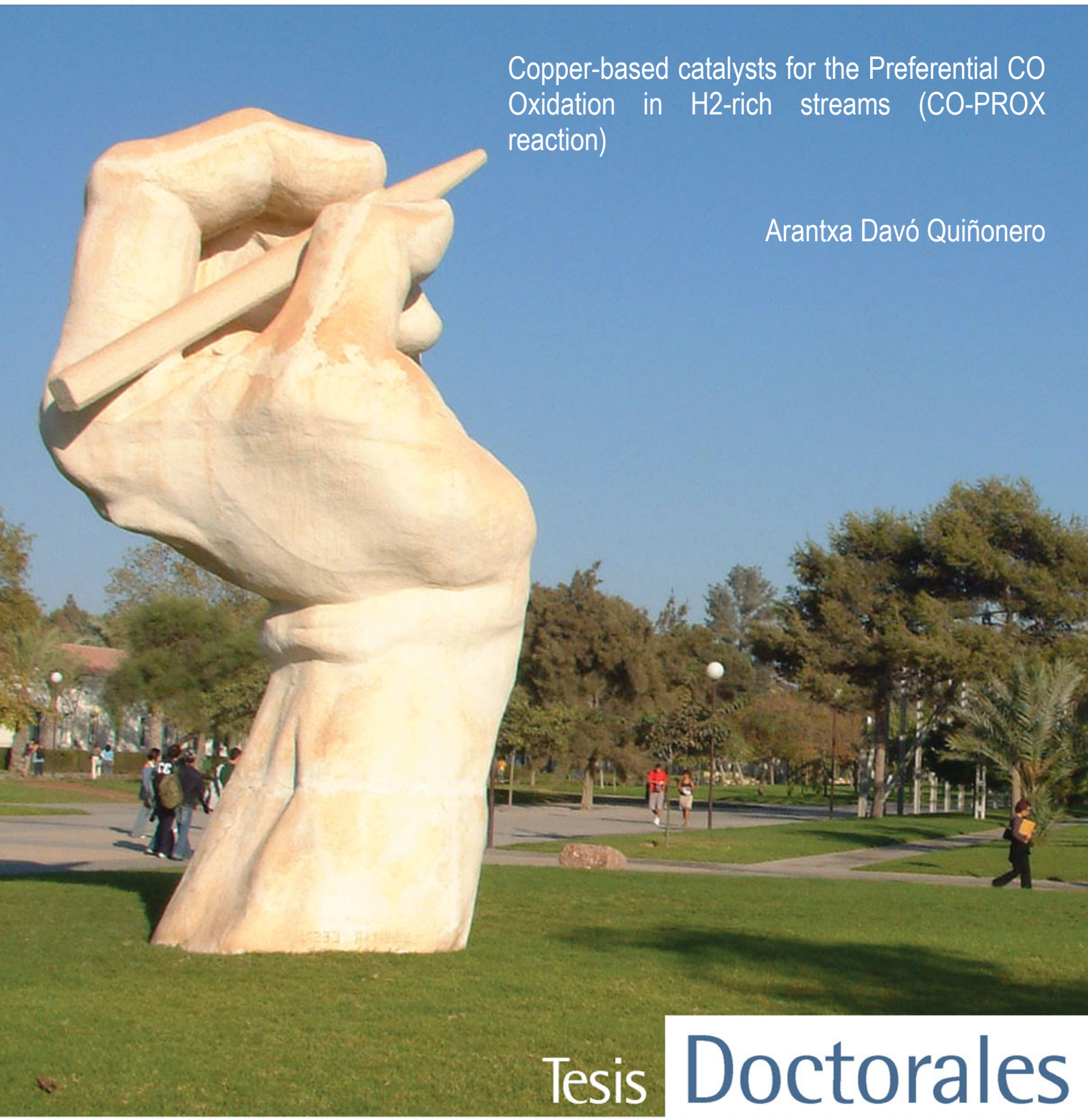

Tesis Doctorales

www.eltallerdigital.com

UNIVERSIDAD de ALICANTE

Universitat d'Alacant
Universidad de Alicante

Departamento de Química Inorgánica
Instituto Universitario de Materiales de Alicante (IUMA)
Grupo de Materiales Carbonosos y Medio Ambiente (MCMA)

Copper-based catalysts for the Preferential Oxidation of CO in H_2-rich streams (CO-PROX reaction)

Memoria presentada para aspirar al grado de DOCTORA EN CIENCIA DE MATERIALES POR LA UNIVERSIDAD DE ALICANTE con MENCIÓN DE DOCTORA INTERNACIONAL

Arantxa Davó Quiñonero

Directores del trabajo:

Dolores Lozano Castelló
Catedrática de Universidad
Área de Química Inorgánica

Agustín Bueno López
Catedrático de Universidad
Área de Química Inorgánica

Alicante, Julio 2019

Universitat d'Alacant
Universidad de Alicante

Agradecimientos

A mis directores de Tesis, Agus y Lola, que son el motor principal de este trabajo. Gracias por contagiarme de vuestra pasión e impulsarme a llegar más lejos de lo que nunca imaginé. Gracias por todo, porque me habéis hecho sentir mil veces afortunada.

A mis compañeros y amigos del doctorado, que han sido de lo bueno, lo mejor de estos años. Gracias por haber compartido conmigo esta bonita etapa.
En especial, a Esther y al petit comité, menciones más que merecidas.

Agradecer a mi grupo de investigación, MCMA y al Departamento de Química Inorgánica, por todos los recursos facilitados y la ayuda brindada.
A Germán, por su inestimable contribución a esta Tesis.

To Prof. Andrzej Kotarba and his group from the Jagiellonian University. Kraków is always in my memories.

To Prof. Max García and his group from the Trinity College Dublin. See you very soon, my friends.

To the Langan family, who made me fall in love with Ireland.

A todas las buenas personas de las que he tenido la suerte de rodearme: los que siempre han estado, los que llegaron después, y los que ya no están. Por todo el apoyo y por cada lección, gracias.

A mi familia, mi pilar fundamental, porque este trabajo es también vuestro.

Universitat d'Alacant
Universidad de Alicante

Universitat d'Alacant
Universidad de Alicante

"No te rindas, que la vida es eso,
continuar el viaje,
perseguir tus sueños,
destrabar el tiempo,
apartar los escombros
y destapar el cielo"

– Mario Benedetti

Universitat d'Alacant
Universidad de Alicante

A mi familia

Universitat d'Alacant
Universidad de Alicante

Índex of contents

Summary of contents and Thesis structure 13

CHAPTER 1. Introduction..... 19

1.1 General introduction 20

1.1.1 Environmental concerns: an overview 20

1.1.2 Future prospects and mitigation actions 20

1.1.3 Hydrogen as energy vector 22

1.1.4 Hydrogen Fuel Cells..... 23

1.1.4.1 Basic principles..... 23

1.1.4.2 Fuel Cell types 24

1.2 Proton Exchange Membrane (PEM) fuel cells 27

1.2.1 PEM fuel cell operation 27

1.2.2 Challenges and fundamental research over PEM fuel cells. 27

1.2.3 Pt-based electrodes susceptibility 29

1.3 Fuel processing for fuel cell applications..... 31

1.3.1 Current hydrogen market status..... 33

1.3.2 Electrolytic water splitting..... 33

1.3.3 Steam Reforming and Water-Gas Shift reaction pathway ... 34

1.3.3.1 Sulfur removal..... 35

1.3.3.3. Water-Gas Shift 37

1.3.4. The exhaustive CO clean-up in H_2-rich streams..... 37

1.3.4.1. Physical methods..... 38

1.3.4.2. Catalytic methods 39

1.3.5. The Preferential Oxidation of CO (CO-PROX)..... 39

1.4. State-of-the-art of the catalytic Preferential CO Oxidation (CO-PROX) reaction..... 40

1.4.1. General background..... 40

1.4.2. Active catalysts for CO-PROX reaction 43

1.5. The copper oxide – cerium oxide systems 45

1.5.1. General features 45

1.5.2. The CO-PROX reaction mechanism over CuO/CeO_2 catalysts 46

1.5.3. Rational design of CuO/CeO_2 systems..... 49

Universitat d'Alacant
Universidad de Alicante

1.5.4. Criticality of cerium oxides and catalytic opportunities for manganese oxides 52

1.6. Main objectives of the Project Thesis 54

1.7. Conclusions 56

References 57

CHAPTER 2. Methods and techniques description.....81

2.1 Methodology and research approach 82

2.2 Experimental methods 82

2.2.1 Catalyst synthesis 82

2.2.1.1 Preparation of CeO_2 support..... 83

2.2.1.2 Preparation of Cryptomelane ($K_xMn_8O_{16}$)..... 83

2.2.1.3 Preparation of CuO-supported catalysts 84

2.2.2 Catalyst characterization techniques..... 84

2.2.3 CO-PROX activity tests..... 98

2.2.4 Advanced chracterization techniques relevant in mechanistic studies 99

2.3 Computational approach..... 102

2.3.1 Density Functional Theory (DFT) 102

2.3.2 Computational details..... **¡Error! Marcador no definido.**

References 103

CHAPTER 3. Into the Preferential Oxidation of CO reaction mechanism over CuO/CeO_2 catalyst 107

3.1 Introduction 108

3.2 Experimental details..... 109

3.2.1 Catalysts preparation and characterization 109

3.2.2 CO-PROX activity tests and mechanistic studies 109

3.2.3 CO-PROX *operando* NAP-XPS and *operando* XANES 109

3.2.4 Computational activities 110

3.3 Results and discussion..... 110

3.3.1 Catalyst characterization..... 110

3.3.2 $^{36}O_2$ pulse isotopic experiments..... 116

3.3.3 *In-situ* Raman experiments 119

3.3.4 CO-PROX *operando* NAP-XPS experiments..... 121

3.3.5 Density Functional Theory (DFT) Calculations 128

Universitat d'Alacant
Universidad de Alicante

3.4 Conclusions 131
References 131

CHAPTER 4. Role of hydroxyl groups in CO-PROX reaction over CuO/CeO_2 catalysts 135

4.1 Introduction 136
4.2 Experimental section 136
4.2.1 Catalysts preparation 136
4.2.2 Catalysts characterization 137
4.2.3 CO-PROX activity tests 137
4.2.4 *Operando* DRIFTS-MS experiments. 137
4.3 Results 137
4.3.1 Textural and crystalline catalysts characterization 137
4.3.2 Catalysts characterization by H_2-TPR. 141
4.3.3 Catalytic tests in a fixed-bed reactor 143
4.3.4 *Operando* DRIFTS-MS experiments. 144
4.3.4.1 Role of the catalyst hydroxyls groups 145
4.3.4.2 Products poisoning versus Cu^+-CO carbonyl 148
4.3.4.3 Comparing CO-PROX with other catalytic reactions 150
4.4 Conclusions 151
References 151

CHAPTER 5. CuO/Cryptomelane catalyst for preferential oxidation of CO in the presence of H_2 155

5.1 Introduction 156
5.2 Experimental details 157
5.2.1 Catalyst synthesis 157
5.2.2 CO-PROX catalytic activity tests 157
5.2.3. Catalysts characterization 158
5.3. Results and discussion 158
5.3.1. CO-PROX catalytic tests 158
5.3.2. Long-term catalytic tests 160
5.3.3. XPS characterization 162
5.3.4. H_2-TPR characterization 164
5.3.5. Characterization by XRD and N_2 adsorption-desorption 167

Universitat d'Alacant
Universidad de Alicante

5.4. Conclusions 169
References 170

CHAPTER 6. Effect of CO_2 and H_2O in the catalytic performance of CuO/Cryptomelane for the preferential oxidation of CO 175

6.1 Introduction 176
6.2 Experimental details 176
6.3 Results and discussion 177
6.3.1 CO-PROX reaction catalytic tests 177
6.3.2 Temperature Programmed Desorption (TPD) experiments 180
6.3.3 Characterization of fresh and used catalysts 182
6.4 Conclusions 187
References 188

CHAPTER 7. Into the Preferential Oxidation of CO reaction mechanism over CuO/Cryptomelane catalyst 193

7.1 Introduction 194
7.2 Experimental details 195
7.2.1 Catalysts preparation 195
7.2.2 CO-PROX activity tests 195
7.2.3 Catalysts characterization 195
7.2.4 *In-situ* Work Function measurements 196
7.2.5 Density Functional Theory (DFT) Calculations 196
7.3 Results and discussion 197
7.3.1 Catalyst characterization 197
7.3.2. CO-PROX catalytic activity tests 199
7.3.3. CuO – Cryptomelane redox interaction study 201
7.3.4. Role of K in CuO – CR interaction 206
7.3.5. Study of CO/H_2 interaction with Cu/CR catalysts 208
7.4 General discussion 215
7.5 Conclusions 217
References 218

CHAPTER 8. Comparative analysis between CuO/CeO_2 and CuO/Cryptomelane: real opportunities in CO-PROX application 223

8.1 Introduction 224
8.2 Experimental Section 225
8.3 Results 225
8.3.1 CO-PROX activity tests 225
8.3.1.1 Effect of CO_2, H_2O and CO_2+H_2O 225
8.3.1.2 Catalysts stability in CO-PROX reaction conditions 227
8.3.2 Temperature Programmed Desorption (TPD) experiments 229
8.3.3 Physicochemical characterization of fresh and spent samples 231
8.3.3.1 X-Ray diffraction (XRD) 231
8.3.3.2 Temperature Programmed Reduction with H_2 (H_2-TPR) . 234
8.3.3 Isotopic $^{36}O_2$ pulse experiments 235
8.4 Conclusions 241
References 243

CHAPTER 9. 3D-printing technology for the fabrication of improved asymmetrical honeycomb monolith catalyst 245

9.1 Introduction 246
9.2 Experimental Section 247
9.2.1. Catalysts preparation 247
9.2.2 Catalysts characterization 248
9.2.3 Catalytic tests 248
9.3 Results and Discussion 249
9.2.3 Catalysts characterization .250**¡Error! Marcador no definido.**
9.3.2 CO oxidation in oxygen excess 252
9.3.3 CO oxidation in CO-PROX conditions 255
9.4 Conclusions 256
References 256

CHAPTER 10. General conclusions 259

Resumen en castellano 265

Curriculum Vitae 281

Universitat d'Alacant
Universidad de Alicante

Universitat d'Alacant
Universidad de Alicante

Summary of contents and Thesis structure

Universitat d'Alacant
Universidad de Alicante

This Thesis is divided into 10 Chapters, and main description of each is presented in the following lines:

Chapter 1 provides an extensive contextualization into the current opportunities for hydrogen utilization as energy vector, which is eventually dependent on an efficient CO clean-up processing step. In this regard, catalytic Preferential Oxidation of CO (CO-PROX) reaction, topic of this Project Thesis, is the most promising approach with excellent opportunities in mobile H_2-dependent devices. This Chapter describes in detail the state-of-the art of CO-PROX catalysts employed so far, among which, copper-based catalysts possess a great potential. At the end of Chapter 1, main objectives addressed in this Project Thesis are presented.

Chapter 2 describes the methodology and research approach developed in this Project Thesis, comprising experimental techniques complemented with punctual computational calculations based on Density Functional Theory (DFT). The fundamental principles of each technique, instrumentation, experimental set-ups and specific operation conditions are presented in this Chapter, which will be referred henceforward in all along the Thesis extension.

Chapter 3 reviews main significative advances achieved so far into the CO-PROX reaction mechanism study over CuO/CeO_2 catalysts, tested and fully characterized through a battery of techniques: N_2 physisorption at -196ºC, X-Ray Diffraction (XRD), Temperature Programmed Reduction (TPR) and Raman spectroscopy, proving inherent synergistic Cu-Ce effects, which turn beneficial into the ongoing Mars-van Krevelen mechanism as demonstrated by pulse O_2-isotopic exchange and *in-situ* Raman spectroscopy. Additionally, cutting-edge experimental techniques for the detailed molecular mechanism elucidation are presented herein. Namely, CO-PROX *operando* Near-Ambient Pressure X-ray Photoelectron spectroscopy (NAP-XPS), and X-ray Absorption Near-Edge Structure (XANES) experiments, reveal altogether clear evidences of CeO_2 very surface reduction, assigned to the role of CeO_2 in oxygen assistance to Cu_xO in Cu – Ce interfacial points, when highly reduced Cu_xO particles are inefficiently undertaking direct O_2 uptake at advanced CO-PROX reaction degrees. Finally, complementary DFT calculations confirm that lattice oxygen restitution by O_2 gas phase should be at first directly favored in Cu_xO when partially oxidized, but then via CeO_2 when Cu_xO particles are reduced at surface by the effect of the reaction course. Since reoxidation issues in CO-PROX reaction have been rarely addressed, this Chapter presents relevant insights for the state-of-the-art in the CuO/CeO_2 catalysts study.

Chapter 4 presents a thorough Diffuse Reflectance Infra-red Fourier Transformed (DRIFT) spectroscopic study on CO-PROX reaction with model

$CuO/Ce_{0.8}X_{0.2}O_{\delta}$ catalysts (with X =Ce, Zr, La, Pr, or Nd). These have been fully characterized exhibiting different chemical features that correlate with catalytic activity. The CO oxidation rate over CuO/CeO_2 catalysts correlates with the formation of the Cu^{+}−CO carbonyl above a critical temperature (90 °C for the experimental conditions in this study) because copper−carbonyl formation is the rate-limiting step. Above this temperature, CO oxidation capacity depends on the redox properties of the catalyst. However, decomposition of adsorbed intermediates is the slowest step below this threshold temperature. The hydroxyl groups on the catalyst surface play a key role in determining the nature of the carbon-based intermediates formed upon CO chemisorption and oxidation. Hydroxyls favor the formation of bicarbonates with respect to carbonates, and catalysts forming more bicarbonates produce faster CO oxidation rates than those which favour carbonates.

These results have been published in: Role of hydroxyl groups in the preferential oxidation of CO over copper oxide-cerium oxide catalysts. A. Davó-Quiñonero, M. Navlani-García, D. Lozano-Castelló, A. Bueno-López, J. Anderson. *ACS Catalysis*, **6(3)** (2016) 1723-1731.

In **Chapter 5**, Non-RE metal-based, Cryptomelane and CuO/Cryptomelane catalysts have been tested in CO-PROX reaction, paying special attention to deactivation and regeneration issues. Cryptomelane was stable during CO-PROX reactions in ramp experiments until 200ºC and in a long-term isothermal experiment, exhibiting after use no changes neither in crystallinity nor H_2 reducibility. On the contrary, CuO/Cryptomelane, though being much more active, deactivated in consecutive CO-PROX reaction cycles performed until 200ºC, but the catalytic activity was partially restored reoxidising the catalyst at 200ºC or 400ºC, the latter temperature being more effective. After four cycles of reaction, stable behavior was achieved, and then CuO/Cryptomelane demonstrated higher catalytic activity than that of Cryptomelane, even after its deactivation along cycles. Such deactivation has been attributed to potential causes: cryptomelane structure collapse into the cyrstallization of new phases (hausmannite (Mn_3O_4) and/or hopcalite ($CuMn_2O_4$)); segregation of potassium and decrease of the copper cations reducibility, whereas possible changes in the porous texture of CuO/Cryptomelane was ruled out.

These results have been published in: CuO/Cryptomelane catalyst for preferential oxidation of CO in the presence of H_2: deactivation and regeneration. A. Davó-Quiñonero, M. Navlani-García, D. Lozano-Castelló, A. Bueno-López. *Catalysis Science & Technology*, **6(14)** (2016) 5684-5691.

The catalytic activity of CuO/Cryptomelane in CO-PROX reaction has been studied in the absence and presence of H_2O and CO_2 in **Chapter 6**, paying special attention to the catalyst stability and to changes on its

physical-chemical properties. For fresh CuO/cryptomelane catalyst, the presence of CO_2 and/or H_2O in the CO-PROX feed partially inhibits CO oxidation due to chemisorption of H_2O and CO_2 on the catalyst. H_2O chemisorption on CuO/Cryptomelane is stronger than CO_2 chemisorption, and simultaneous CO_2 and H_2O adsorption has a synergistic effect that enhances co-adsorption and significantly hinders CO oxidation. On the contrary, the presence of CO_2 + H_2O in the CO-PROX reaction mixture has a positive effect in the CuO/Cryptomelane stability upon several consecutive reaction cycles in the 25-200ºC range. XRD showed that chemisorbed CO_2 + H_2O species partially prevent the catalyst deactivation due to cryptomelane reduction to hausmannite (Mn_3O_4) under the strongly reductive environment of the CO-PROX reaction, and H_2-TPR and Raman spectroscopy characterization support that the cryptomelane structure is less damaged under CO-PROX conditions in the presence of CO_2 and H_2O than in the absence of these species. Therefore, interestingly under CO_2 + H_2O environment (realistic CO-PROX conditions) CuO/Cryptomelane catalyst performs an improved catalytic activity once stable behavior is reached.

These results have been published in: Unexpected stability of CuO/Cryptomelane under Preferential Oxidation of CO reaction conditions in the presence of CO_2 and H_2O. A. Davó-Quiñonero, D. Lozano-Castelló, A. Bueno-López. *Applied Catalysis B: Environmental* **217** (2017) 459-465.

In **Chapter 7**, CuO/Cryptomelane catalyst was subjected to a mechanistic study over CO-PROX reaction by means of indirect techniques by the preparation, advanced characterization and testing of catalysts with different Cu nominal contents. Their CO-PROX catalytic activity has been tested in CO-PROX reaction and evaluated according to Cu dispersion and synergistic interaction between copper and manganese-rich phases. This work entails the use of conventional characterization techniques such as XRD, Raman, XPS and Auger spectroscopies, as well as complementary basic DFT simulation. Additionally, it is reported for the first time, *in-situ* Work Function measurements over CO and O_2 interaction in CuO/Cryptomelane catalysts. Results reveal a strong influence in the electronic properties of CuO/Cryptomelane depending on CuO-cryptomelane interaction at the interface contact points, which stabilize Cu^{+} states upon Cu^{+2}/Cu^{+} and Mn^{3+}/Mn^{4+} redox interplay. The optimal performance is achieved by the efficient participation of two active species: (1) interfacial Cu^{+}–Mn pairs, as the active sites for CO oxidation; and (2) CuO bulky particles for the efficient O_2 refilling. Thus, these results bring the conclusion the that clear analogies exist within the ongoing CO-PROX mechanism involving copper species in CuO/Cryptomelane and the well-reported CuO/CeO_2 catalysts.

Chapter 8 compiles main remarks referring to CuO/CeO_2 and CuO/Cryptomelane catalysts utilization in the Preferential CO Oxidation reaction and the most relevant outcomes achieved along the development of

this Project Thesis are presented altogether for their direct comparison. With fresh sample on the reactor, CuO/Cryptomelane shows better performance than CuO/CeO_2 on a first catalytic run, but latter CuO/Cryptomelane deactivation on successive reaction cycles flips their relative activities. Nevertheless, in CO_2+H_2O environment, the enhanced stability of CuO/Cryptomelane allows to reach a much more active state after the succession of catalytic runs, which sets closer the CuO/CeO_2 and CuO/Cryptomelane performances, up to the point that the latter shows big competitive potential.

Chapter 9 presents the study on the scalability of powdered copper-based active phases in medium-sized monolithic catalysts with unconventional designs prepared by means of 3D-printing technology. An improved honeycomb-like monolith with asymmetrical channels, where the channels section decrease along the monolith, was fabricated using a template prepared by 3D printing. A reference honeycomb monolith was also prepared in the same way but with conventional straight channels. Cu/Ceria active phase was loaded on these supports, and Scanning Electron Microscopy (SEM), Raman spectroscopy and XRD showed that the supported active phase is similar on both monoliths. The supported catalysts were tested for CO oxidation in excess oxygen and for preferential CO oxidation in H_2-rich mixtures (CO-PROX), and the catalyst with the improved support achieved higher conversions in both reactions. The supported catalyst with asymmetrical channels has two benefits with regard to the counterpart catalyst with conventional symmetrical channels: improves the reaction rate with regard to the conventional one because fits better to the equation rate, and favors the turbulent regime of gases with regard to the laminar flow that prevails in symmetrical channels.

These results have been published in: Improved asymmetrical honeycomb monolith catalyst prepared using a 3D printed template. A. Davó-Quiñonero, D. Sorolla-Soriano, E. Bailón-García, D. Lozano-Castelló, A. Bueno-López. *Journal of Hazardous Materials* **368** (2019) 638–643.

Finally, **Chapter 10** summarizes the most relevant conclusions obtained in this thesis.

Since this thesis applies for the International Doctorate Mention, it has been written in English and a summary in Spanish is included at the end of the Thesis to fulfil the requirements of this mention.

Universitat d'Alacant
Universidad de Alicante

CHAPTER 1

Introduction

Chapter 1 provides an extensive contextualization into the current opportunities for hydrogen utilization as energy vector, which is eventually dependent on an efficient CO clean-up processing step. In this regard, catalytic CO-PROX reaction, topic of this Project Thesis, is the most promising approach with excellent opportunities in mobile H_2-dependent devices. This Chapter describes in detail the state-of-the art of CO-PROX catalysts employed so far, among which, copper-based catalysts possess a great potential. At the end of Chapter 1, main objectives addressed in this Project Thesis are presented.

Universitat d'Alacant
Universidad de Alicante

1.1 General introduction

1.1.1 Environmental concerns: an overview

The human activity track record in the industrial and economic development starting in the 20th century has resulted in a worrying environmental situation that is patent nowadays with irrefutable evidences. Namely, global warming [1] and ocean acidification [2] caused by anthropogenic emissions of greenhouse gases (GHG), mainly CO_2 [3]; air-polluted cities by industrial processes and vehicle motion with harmful effects in public health [4–6]; or the serious deforestation and persistent destruction of ecosystems by the uncontrolled utilization of natural resources [7].

In turn, the society is in general expressing a major sensitivity for the dramatic environmental consequences of the inaction and there is a rising consciousness to resolve and mitigate in the short-term the severe impacts of the non-sustainable development conducted so far. The 21st century is a critical moment in which we are meant to face two highly interdependent energy-related challenges: the sustainable economic growth and global climate change, targets in which catalysis science and technology may play a key role.

1.1.2 Future prospects and mitigation actions

According to near-future forecast, the global energy demand is predicted to grow in an unstoppable trend, along with the world economic development, which exhibits increasing growth rate year after year [8,9]. Thus, new power sources with sustainable carbon-neutral balance are an urgent imperative to avoid further energy-related CO_2 emissions according to current energy policies scenario.

Universidad de Alicante

In this regard, the Sustainable Development Goals (SDGs) adopted by world leaders in the United Nations' *2030 Agenda for Sustainable Development* [8] promoted, among other targets, the establishment of environmental protection compromises in a cooperative international framework. Whereas complementarily, the Nationally Determined Contributions (NCDs) made for the *Paris Agreement* in 2015 [11] meant a landmark agreement aiming to bring all nations into a common on cause on behalf of temperature rise mitigation.

Nevertheless, despite efforts, 2018 recorded a historic of 33.1 Gt global GHG by energy-related CO_2 emissions, up 1.7% after 2015-2017 flat term [12]. Furthermore, according to future projections, these CO_2 emissions are alarmingly expected to continue increasing by 2030 and thereafter (Figure 1.1) [13].

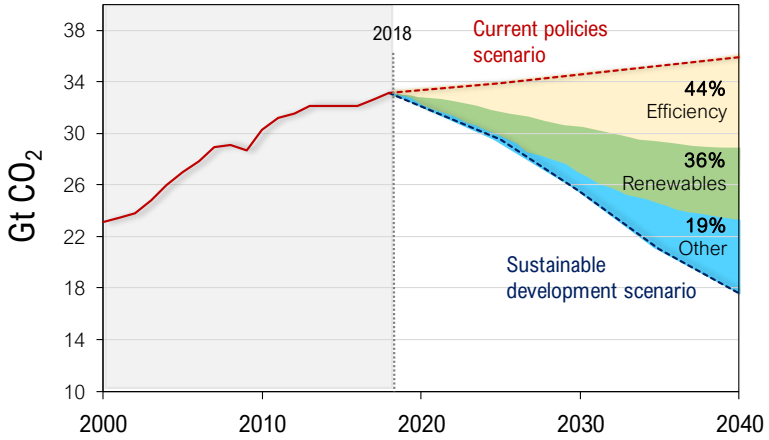

Figure 1.1. Global energy-related CO_2 emissions, gigatones (Gt). Dashed lines describe forecasted trends in separate scenarios and colored areas the inferred relative contribution among different CO_2 mitigation strategies. Source: International Energy Agency, 2018 [12].

The reasons for the encountered recent setback against climate change was the large increase in primary energy demands accounted in 2018, which grew by nearly twice the average increment rate registered since 2010 [14]. Among global energy consumers, the strengthen emerging block from the non-OECD nations: Brazil, China, India and the Russian Federation, as well as the United States, experienced the largest growth [8] with mainly coal-powered economies, which had dramatical impact since coal is the largest single CO_2 emitter [12].

Hence, in order to meet long-term climate and other sustainability goals, it is imperative to accelerate in low-carbon and renewable energy development to increase their share in the global primary energy mix, which is expected to reach 12.4% by 2023. Among renewables, bioenergy currently holds 50% of total energy produced, followed by hydropower (31%), wind (9%), solar photovoltaic (PV) (4%), solar thermal (4%) and geothermal (2%) [15]. Furthermore, stronger energy efficiency policies are crucial, since these would allow to reduce energy consumption yet the increasing energy demands.

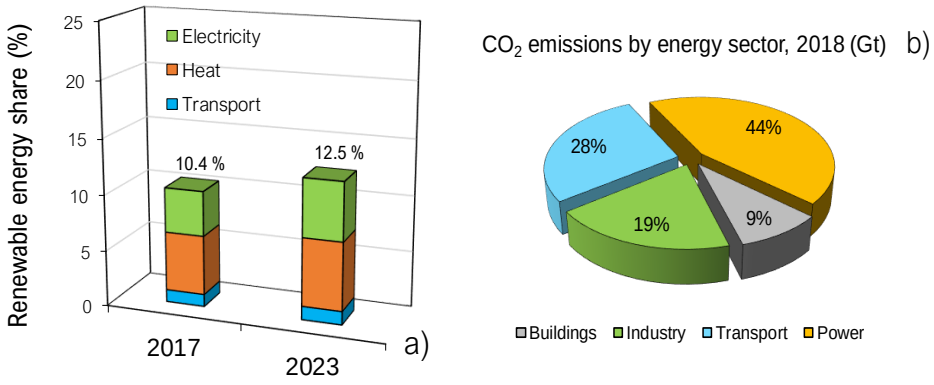

Figure 1.2. a) Share of modern renewable energy by sector in total final worldwide energy consumption, 2017-2023 [15]. **b)** Global energy-related global CO_2 emissions (Gt) by sector, 2018 [12].

Under current policies scenario, it is predicted that renewables will gain big importance in electricity sector, but their development is too slow and according to current pace, the share of renewables in the total energy share consumption will roughly reach 18% by 2040, much below a sustainable scenario benchmark [15]. In particular, renewable energy displays a very low base in transport sector, which is worrying indicator since large fraction of energy-related CO_2 emissions comes from aviation and transportation on road or rail modes (Figure 1.2), sectors considered hard-to-decarbonize.

1.1.3 Hydrogen as energy vector

In this scenario, big attention is attracted by the potential hydrogen (H_2) deployment, thoroughly considered a key element with promising features to be used in the broad energy sector. Namely, hydrogen is a carbon-free fuel, with the highest energy content per unit mass (143.0 MJ/kg) [16,17] that releases no environmentally harmful compounds when burned neither contributes to CO_2 emissions, theoretically [18], in contrast with the fossil fuels.

However, the consolidation of a practicable and extended hydrogen market in the mid-term scenario exhibits certain challenges still pending to be resolved. Chiefly, despite being widely distributed as a component of water and other compounds, only traces of free hydrogen are present in the lower part of earth's atmosphere [19], so H_2 has to be produced by means of energy-consuming processes. In consequence, notice that H_2 is designated as an *energy carrier*, or energy vector, not as *energy source*, so that, the overall hydrogen economy sustainability is subjected to the energy cycle involved in production, too [20].

Likewise, storage and transport are additional vast drawbacks when it comes to hydrogen utilization, given the physicochemical properties of

gaseous H_2, like its lightness and high difusion, volumetric energy density (the lowest, at 0.0108 MJ/L), and hazardous combination with air [20]. In this regard, a battery of well-reported options, such as high-pressure systems; cryogenic liquid hydrogen tanks; the formation of chemical hydrides; or adsorption in highly porous materials, show broad different gravimetric and volumetric hydrogen, but experimental systems capable to meet targets have not been found yet [16,17,21–23].

Conversely, despite the pending challenges involved, H_2-based technologies have already opened up entirely new approaches to integrate hydrogen in the energy system [24,25]. As a chemical fuel, H_2 is a versatile *energy carrier* that can be traded and stored in ways that electricity cannot, enabling to tackle sectors with minimum disruption, as long-distance transport in hydrogen-powered vehicles and also power plants [15].

Namely, produced hydrogen can be stored over long periods and transformed to electricity when required (*power-to-power*) [26–28]; mixed into the natural gas network or converted to synthetic methane (*power-to-gas*) [29–31]; or directly introduced in hydrogen fuel cells (*power-to-fuel*) [32,33], electrochemical devices with vast potential in wide range of applications [34,35].

In particular, fuel cells (FCs) hold a very promising niche in transportation sector as implemented in Fuel Cell Electric Vehicles (FCEV). To date, FCEVs can provide the mobility service of today's conventional cars at potentially very low-carbon emissions [25,36]. As a positive indicator, the global FCEV car stock reached 8000 units in 2017 [37,38], though presenting very high manufacturation costs. However, it is encouragingly predicted that the cost of FCEVs will decrease up to 50% by 2030, being then closer competitor to conventional combustion vehicles [25], allowing a gradual decarbonization in road transportation sector.

Provided the large potential and promising outlook of FCs, these remain hot research topic since the last years, and main insights into fuel cell technology are presented in the following Section.

1.1.4 Hydrogen Fuel Cells

1.1.4.1 Basic principles

In fundamental terms, fuel cells (FCs) are electrochemical devices able to convert chemical energy into electrical energy by means of a direct and efficient process spurred by an applied potential difference. By and large, the basic operation of a fuel cell requires a combustible substance, such as H_2, and an oxidant, or comburent, as O_2, which are supplied separately to the electrode compartments, anode and cathode, respectively, where electrochemical processes are physically taking place. In order to accelerate

reactions up to a relevant rate, a suitable catalyst must be deployed in both electrodes, specially, in low-temperature operation fuel cells, provided the very slow intrinsic kinetics.

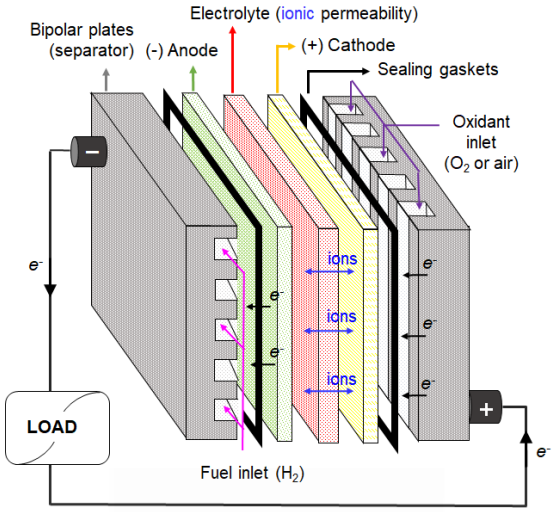

Figure 1.3. General scheme of a hydrogen fuel cell simple configuration.

As Figure 1.3 depicts, the electrodes are connected by an ionic-conducting solid or liquid electrolyte media, which is selectively permeable to specific ions; while electrically connected by current collectors to an external circuit that allows to produce electrical energy upon the generated current. Since fuel cells operation requires from a continuous supply of reactants, characteristic feature of the so-called *tertiary cells* [39], FCs may tentatively remind to a certain extent, to combustion machines, though much higher efficiencies can be achieved since FCs skip the intrinsic limitation of Carnot cycle [40,41].

Generally, multiple cells are connected together in stacked assemblies, so separator elements, the bipolar plates, are included in the design. These not only keep the electrical interconnection between the different cells, but also, their grooved design promotes the efficient gas inlet and products outlet paths. Moreover, edge sealing gaskets prevent from leaks, enabling the safe handling of gas and liquid components and an adequate fuel cell configuration should allow proper heat management to ensure safety and enhance durability [53,54].

1.1.4.2 Fuel Cell types

Table 1.1. shows the main fuel cell categories and their diverse characteristics, which evidence the large versatility over FC technology. As common aspects, fuel cells present very positive features in terms of high efficiency, simplicity, silent operation and lack of noxious emissions. However, the prohibitive high expenses involved in fuel cell technology, and

their limited durability are currently very strong barriers on their extended implementation [42–44].

For most of the fuel cell types, the preferred fuel is hydrogen, though hydrocarbons and alcohols can be used, too. Regarding the gas inlet feeding requirements, whereas the choice of oxidant for the cathode is either air or oxygen, the selection of an appropriate fuel is not so straightforward, and notice that for some fuel cell types, it is emphasized that *pure* H_2 is the demanded anode feeding [54]. The degree of required purity is determined by the compatibility of the electrodes and electrolyte with certain impurities present in H_2 streams, which is highly dependent on the operation temperature. So that, in general terms, purity demand becomes more stringent with the lower temperature.

Likewise, as a very positive feature in the high-temperature fuel cell types, Molten-Carbonate Fuel Cells (MCFCs) and Solid Oxide Fuel Cells (SOFCs), hydrocarbons standalone can be directly fed to the cell, to be either electrochemically oxidized or *in-situ* converted to hydrogen by internal reforming and latter electrooxidation [32]. In turn, current natural gas pipelines and the available distribution infrastructure is as well valid for the high-temperature fuel cells feeding, enabling their operation where required, bypassing hydrogen production, transportation and storage issues [33]. Today, MCFCs and SOFCs are highly utilized in combined heat and power systems, provided their high-grade waste heat.

However, hydrogen-fuelled *Polymer Electrolyte Fuel Cells* (PEFCs), are preferred for automotive applications, since they present immediate start-up and offer much higher power densities than any other FC type.

In PEFC, the electrolyte is a solid polymer, which is an ionic-conducting membrane permeable to H^+ (proton) or OH^- (hydroxide) ions. In turn, two different sub-categories are found: *Proton Exchange Membrane* (PEM); and *Anionic Exchange Membrane* (AEM) fuel cells; respectively [48]. In general terms, proton exchange membranes exhibit higher conductivity and reliability [49,50]. Besides, working with acid media turns into better catalytic performances, so the required catalyst loading is significatively lower in PEM, with regards to AEM devices [51,52]. As a result, because of practical interest, most of the commercial fuel cells and related research have focused mainly on PEM fuel cell configuration, which is revised in the next Section 1.2.

Table 1.1. Fuel cell types and main characteristics [34,39,41,45–48].

Fuel cell type	**Electrode feeding**; catalyst	Electrolyte; **Mobile ion**	**Operation range (ºC)**; Power range (W) *Start-up*	**Field of application**
PEFC: Polymer electrolyte fuel cell *(1)* **PEM:** Proton Exchange Membrane *(2)* **AEM:** Anionic Exchange Membrane	*Anode (-):* **Pure H_2**; Pt/C catalyst *Cathode (+):* **O_2/air**; Pt/C and alternatives	Ionic-conducting polymer membrane *(1)* In PEMFC: **H^+** (proton) *(2)* In AEMFC: **OH^-**(hydroxide)	**30-90 ºC;** 1-100 kW *Immediate*	Road vehicles, stationary electricity generation, heat and electricity co-generation, submarines, space travel Most commercialized
AFC: Alkaline fuel cell	*(-)*: **Pure H_2**; Pt/C *(+)*: **O_2**; Pt/C	Aq KOH; **OH^-** (hydroxide)	**30-90 ºC;** 1-10 kW; *Immediate*	Space travel, road vehicles, submarines
DMFC: Direct-methanol fuel cell	*(-)*: **Methanol, methanol-water**; Pt/C *(+)*: **O_2/air**; Pt/C	Proton-conducting polymer membrane; **H^+**	**50-90 ºC;** 1-100 kW *Immediate*	Portable, mobile electronic devices
PAFC: Phosphoric-acid fuel cell	*(-)*: **Pure H_2**; Pt/C *(+)*: **O_2/air**; Pt/C	Concentrated phosphoric acid; **H^+**	**~200 ºC;** 10 kW- 1 MW *30 min from 'hot standby'*	Stationary electricity generation, heat and electricity co-generation
MCFC: Molten-carbonate fuel cell	*(-)*: **H_2 or natural gas**; porous Ni *(+)*: **O_2/air** ; porous NiO	Molten carbonate (Li_2CO_3, K_2CO_3); **CO_3^{2-}** (carbonate)	**~600 ºC;** 100 kW-100 MW *Several hours after cold start*	Stationary electricity generation, heat and electricity co-generation Hydrocarbon fuels reformed in situ
SOFC: Solid-oxide fuel cell	*(-)*: **Gasoline or natural gas**; porous cermet of Ni or Co and yttria-zirconia *(+)*: **O_2/air**; strontia-doped lanthanum-manganite perovskite	Ion-conducting ceramic (yttrium-stabilised zirconia); **O^{2-}** (oxide)	**~900 ºC;** 1 kW-100 MW *Several hours after cold start*	Stationary electricity generation, heat and electricity co-generation Hydrocarbon fuels reformed in situ

Universitat d'Alacant
Universidad de Alicante

1.2 Proton Exchange Membrane (PEM) fuel cells

1.2.1 PEM fuel cell operation

Briefly, PEM fuel cells operation is well-known and can be summarized as follows [34,41]: *(1)* In the anodic side, inlet H_2 gas flows towards the catalytic layers where it is oxidized in the Hydrogen Oxidation Reaction (HOR) (Equation 1.1). *(2)* In the cathode, the oxidant inlet (O_2 or air) is electro-reduced to H_2O by means of the Oxygen Reduction Reaction (ORR), which is ideally simplified as (Equation 1.2).

Anode (HOR):	$2\ H_2 \rightarrow 4\ H^+ + 4\ e^-$	Eq. 1.1
Cathode (ORR):	$O_2 + 4\ e^- + 4\ H^+ \rightarrow 2\ H_2O$	Eq. 1.2
Global process:	$2\ H_2 + O_2 \rightarrow 2\ H_2O$	E^0= 1.229V

Notice that according to the global process, H_2O is released as the lone overall exhaust product. Likewise, a proper outlet product release strategy is critical, in order to guarantee the fuel cell durability. Namely, an adequate H_2O management is necessary to keep suitable humidity levels and maintain invariable the properties of the membrane and electrodes [45, 53]. Meanwhile in the anode, the H_2 excess, should be reconduced in outlet lines and recirculated back towards the anode to gain fuel efficiency.

1.2.2 Challenges and fundamental research over PEM fuel cells

For the sake of extended implementation and commercialization, there are three main criteria that fuel cell technology must fulfill: cost, performance and durability, the targeted pillars on which fuel cell research is based [35,54,55]. Particularly, the rational optimization of the catalysts comprises all of them, since they directly influence the performance, limit durability and involve major costs derived from fuel cells [25,56]. In this regard, fundamental research has enabled remarkable advances, such as the design of high-performance membrane-electrode assemblies (MEAs) [39,54,57].

Figure 1.4 depicts a cross-section of a PEM fuel cell, exhibiting a typical MEA configuration [58,59].

Universidad de Alicante

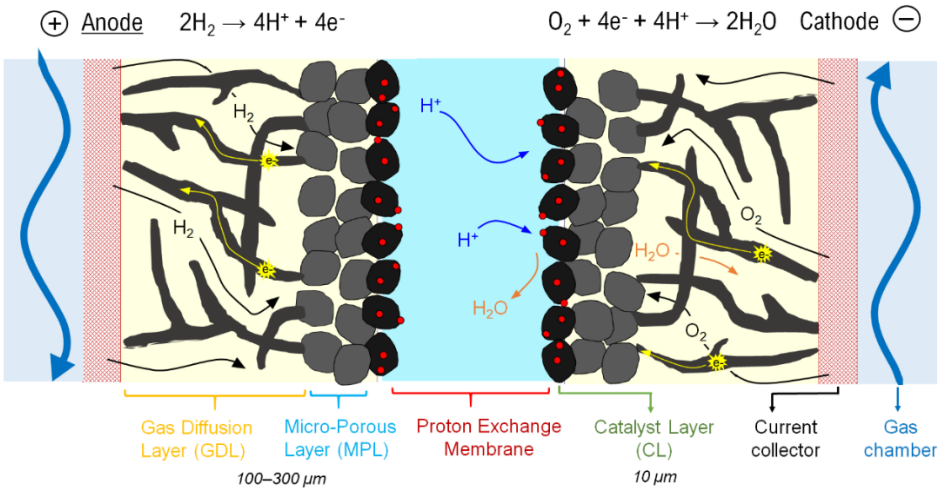

Figure 1.4. PEM fuel cell electrode assembly and electrochemical processes involved.

Thus, PEM fuel cell electrodes are commonly constituted by three main elements. Namely, **(1)** the Gas Diffusion Layer (GDL), carbon fiber paper (Toray); together with **(2)** the Micro-Porous Layer (MPL), usually fabricated by intermixing a hydrophobic polytetrafluoroethylene with carbon black; provide the adequate multi-physics media and enable coupled mobility of electrons and gas diffusion, while facilitating water transport [60]. And last, **(3)** the Catalytic Layer (CL), where electrochemical processes anodic (HOR) and cathodic (ORR) take place. The most common CL configuration, and well-established reference catalyst, comprises very small Pt nanoparticles (2-5 nm) finely dispersed in carbon-black powder, *i.e.,* Vulcan-XC72® (Cabot) [57].

Since the electrochemical processes are confined to occur in the triple-phase boundaries (TPB), that is, the interface region between the protonic membrane and the Pt/C particles [61], most attempts to improve the catalytic activity are focused on the maximization of exposed area of the Pt/C catalyst to enable efficient contact with the electrolyte. For instance, the advanced preparation of high-surface catalytic thin films, so-called extended surface area catalysts [54,62], as well as novel Pt deposition procedures [63], are well-reported approaches that have allowed powerful enhancements in catalytic activity, while reducing by large Pt content.

Nevertheless, despite the thorough optimization over the years, the costs of PEM cell devices remain still prohibitive because of Pt utilization. Furthermore, the severe scarcity of Earth's Pt resources turns unfeasible the widespread implementation of PEM fuel cell devices with current demanded loading. Noticeably, the Pt content in PEM electrocatalysts has dramatically decreased, from 28 $mg \cdot cm^{-2}$ in the first commercial devices, to ~0.4 $mg \cdot cm^{-2}$, yet increasing overall activity in current systems [57,64].

Thus, although present in both electrodes, the cathode side contains nearly the 90% of total Pt content in the cell [65], since the sluggish kinetics and mechanistically complex ORR process require far more Pt to deliver high currents, when compared to HOR. In fact, Pt-catalyzed HOR is extremely facile and exhibits kinetics 10^5 to 10^7 times faster than ORR [66], the reason why current platinum share in the PEM fuel cell is usually ~0.4 $mg \cdot cm^{-2}$ in the cathode and ~0.05 $mg \cdot cm^{-2}$ in the anode. Conversely, to result economically feasible, it has been targeted that total Pt content (anode + cathode) should not overcome the maximum 0.125 $mg \cdot cm^{-2}$ loading in PEM fuel cells, [56], which is a vast research challenge [67].

In this scenario, great majority of studies focus on ORR rather than HOR, since ORR optimization is much more necessary and results determinant to achieve improvements in the overall fuel cell performance. Among the different strategies conducted so far, the most studied is Pt alloying, which dilutes Pt content with the presence of secondary metals that modify electronic properties of Pt, too [48,54,68–70]. Additionally, multiple non Pt-based alternative catalysts have been developed, such as Pd and its alloys [71], Rh, Ir [72]; non-noble metal catalysts such as metal-organic complexes [73], enzymes [74], oxides [75] or functionalized N-doped carbon materials [76,77]. Nevertheless, the use of non-Pt alternative active materials has presented important drawbacks as limited durability and poorer performance when compared to Pt/Vulcan reference catalyst, and even though some total Pt-free configurations have arised [78–80], Pt and Pt-based alloys are still the catalyst choice by excellence for PEM fuel cells.

1.2.3 Pt-based electrodes susceptibility

Apart from the logistic issues related to Pt deployment, another relevant drawback facing the PEM fuel cell commercialization is the electrode susceptibility to potential impurities in H_2 streams, such as carbon monoxide (CO), or sulfur compounds (H_2S, or COS).

For Pt-based catalysts, specially in acid media, CO leads to an activity loss and damages seriously the durability of the fuel cell, even when present in very low trace levels. This effect is attributed to the strong CO-Pt binding, which blocks preferentially and irreversibly Pt electrocatalyst active sites at the low-temperature operation of PEM fuel cell [81,82]. Specifically, adsorbed CO prevents the dissociative electro-sorption of molecular hydrogen in Pt sites, which is the rate-limiting step in HOR [83,84]. On the other hand, although CO-containing fuel is only fed to the anode side, physically separated from the cathode, it has been reported that CO could occasionally cross through the membrane reaching cathodic electrode and causing detrimental effect in ORR performance, too [85,86].

Recent standard requirements over H_2 streams composition for PEM FC applications with Pt/C catalysts set the maximum CO concentration at the very strict 0.2 ppm values (ISO 14687-2, SAE J2719) [87]. Nevertheless, conducted efforts into the design of CO-resistant catalysts have expanded the acceptable tolerance levels up to 10-100 ppm CO in certain configurations, yet depending on the fuel cell specifications [88–91].

Tentatively, a first approach to mitigate CO contamination could be to rise the temperature of operation, from conventional ~80ºC to 100-200ºC, since it is well-known that CO tolerance increases with temperature [92]. However, increasing the temperature decreases significatively the membrane lifetime and hampers to keep its suitable humidity. Hence, currently there is considerable interest on the development of high temperature performance membranes, but these have not demonstrated sufficient stability yet [93].

Provided that increasing the temperature seems to be impracticable for the moment, current attempts to suppress electrode CO contamination are centred on the preparation of bimetallic Pt-based anodic catalysts, such as Pt-Ru [88,89,94], Pt-Sn [95,96], Pt-Fe [90,97,98] or Pt-Mo [91,99]. The mitigation of the CO problem by Pt-alloying is ascribed to mainly two different effects, such as: the promotion of CO electrooxidation by OH species formed in the second metal sites, so-called *bifunctional effect*; or the modification of Pt electronic properties for the Pt-CO bond weakening, also known as *ligand effect*. Among the binary combinations, Pt-Ru/C catalysts have been most studied because of their well-known enhanced CO-resistance, as well as high performance [81,88,100]. In fact, further optimization of morphological aspects [88], or ternary combinations [101], core-shell architectures [102] or the incorporation of different metal oxides [103,104] have presented acceptable results towards gaining CO-tolerance, though stability of such configurations over long-time operation is still unclear [100].

Complementarily, several approaches have been proposed to palliate the CO contamination effects on PEM fuel cells, which mainly rely on the conversion of the poisoning CO, to the harmless CO_2, by means of different set-ups. For instance, *air bleeding*, consists in the introduction of low contents (2-5%) of O_2 (from air) into the H_2 stream, so the Pt-catalyst itself activates CO oxidation reaction (Equation 1.3), process that removes sorbed CO, and, therefore, suppresses CO-poisoning [105–107]. Conversely, the addition of O_2, a comburent, beside the combustible, H_2 in the presence of a catalyst, facilitates also the undesired direct H_2 oxidation reaction (Equation 1.4)

$$CO + ½\ O_2 \leftrightarrow CO_2 \qquad \Delta H^0 = -283\ kJ/mol \qquad \text{Eq. 1.3}$$

$$H_2 + ½\ O_2 \leftrightarrow H_2O \qquad \Delta H^0 = -242\ kJ/mol \qquad \text{Eq. 1.4}$$

Nevertheless, apart from the efficiency loss by the fuel consumption, the main drawback over air bleeding technique is the local temperature increase within the MEA because of the very exothermic CO oxidation and H_2 oxidation reactions occurring in the anode layer, causing Pt sintering and consequent activity loss. In this regard, a possible modification of air bleeding procedure is the incorporation of an additional Pt-catalyst layer between the MPL and the Pt or Pt-Ru catalyst layer (CL), configuration named *bilayer anodes* [108]. In turn, the CO and H_2 oxidation reactions would take place in the intermediate layer, while temperature would remain controlled in the CL for stable HOR operation. Nonetheless, despite good operation, the complex bilayer anodic assembly presents additional costs to the fuel cell manufacturing, which is, precisely, not wanted. Yet, in-situ regeneration of CO-poisoned electrodes has also been reported by means electrical pulsed CO oxidation techniques [109–111], but, there is still much lack of understanding of the complicated potential oscillations in the PEM system, and despite good results, the set-up presents uncertain safety issues which hinders extended implementation.

In conclusion, despite conducted efforts, CO poisoning over well-consolidated Pt and Pt-alloyed electrocatalysts is still an unresolved challenge. Besides, considering other additional contaminants present as impurities in H_2 streams, such as H_2S or SO_2, which cause severe damage in the Pt-based catalyst, even more detrimental and more difficult to mitigate than with CO [82,112], the durability of PEM cell utilization becomes critical.

As a consequence, it is an urgent requirement to set a particular research focus into the efficient and exhaustive H_2 purification, to clean-up CO and sulfur species from stream to the *ppmv* tolerance levels, in order to ensure the prospective PEM fuel cells utilization.

Universidad de Alicante

1.3 Fuel processing for fuel cell applications

Provided that purity requirements over inlet hydrogen in PEM fuel cell is very stringent, several methodologies have arisen to produce clean H_2 streams aiming to tackle this particular application. Thus, the target utilization of PEM fuel cell, whether in large or small-scale, either portable or stationary application, will determine the most suitable strategy among the existing battery for pure hydrogen production technology.

In the case of automotive PEM fuel cells, these are generally fueled with gaseous hydrogen stored in high pressure tanks (35 to 70 MPa), seeking large hydrogen capacity within acceptable volume constraints in order to meet the sufficient vehicle autonomy. Such high pressure containers require of expensive composite materials that significatively increase overall costs [113] besides depend on extremely expensive refueling stations and a proper distribution network supplied by large-scale high-purity hydrogen production

plants [25], which in overall should accomplish demanding critical features [114].

Conversely, as an alternative fueling mode, the *on-board* fuel reforming concept rose to be implemented in low-temperature PEM fuel cells, in analogue approach to the *in-situ* hydrocarbon reforming process carried out in the high-temperature MCFCs and SOFCs [115,116]. Thus, *on-board* reforming would allow direct hydrocarbon supply to the automotive system, comprised mainly, by a fuel reforming reactor, for the hydrocarbon conversion to H_2; and the coupled PEM fuel cell, among other elements as schematized in Figure 1.5.

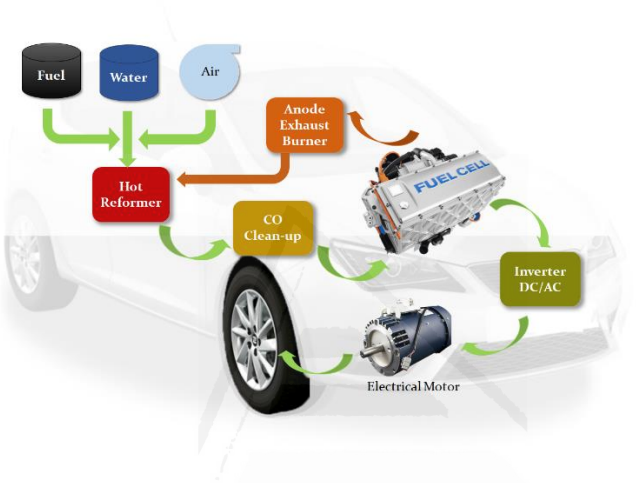

Figure 1.5. *On-board* fuel reforming operational scheme.

Universitat d'Alacant
Universidad de Alicante

The exploitation of *on-board* reforming concept was initiated in the 1970s [115,117,118] which came long way and relevant outcomes where achieved, as one of the first FCEVs prototype. However, a seismic shift occurred when in 2004, the US Department of Energy in 2004, determined to stop further research funding in the field at expenses of hydrogen storage technology investments [116,119], decision that brought ground to a halt *on-board* reforming achievements, comprising hydrogen production and purification at portable scale by means of an advanced catalysis science development.

Nevertheless, although the DOE support would had been a key driver, on-board research has been taking place in a second plane during last decade, and currently hold relevant niche in the recently developed *exhaust gas reforming* concept, for the sake of the partial hydrogen introduction in fuel mixture over conventional engines [120,121].

In agreement with this contextualization in PEM fuel cells application, next sub-sections review most relevant hydrogen production and purification pathways.

1.3.1 Current hydrogen market status

To date, hydrogen production accounts for *ca.* 7.7 exajoules (EJ) every year, mainly targeted to ammonia production and oil refining industries [122] in a growing global H_2 market forecasted to rise up to 10 EJ/year by 2050. Regrettably, most of hydrogen production relies on fossil fuels: coal, oil and natural gas, which paradoxically results in significative CO_2 emissions associated to H_2 utilization.

Figure 1.6. schematizes principal H_2 generation pathways with current available technologies, yet in different stages of development, large and small-scale. In terms of efficiency and volume of production, steam reforming of natural gas is by large, the preferred and most extended, accounting for nearly 48% of produced H_2. Next, oil reforming and coal gasification contribute with the 30% and 18%, respectively, whereas merely the balance of total H_2 is produced by water electrolysis [25].

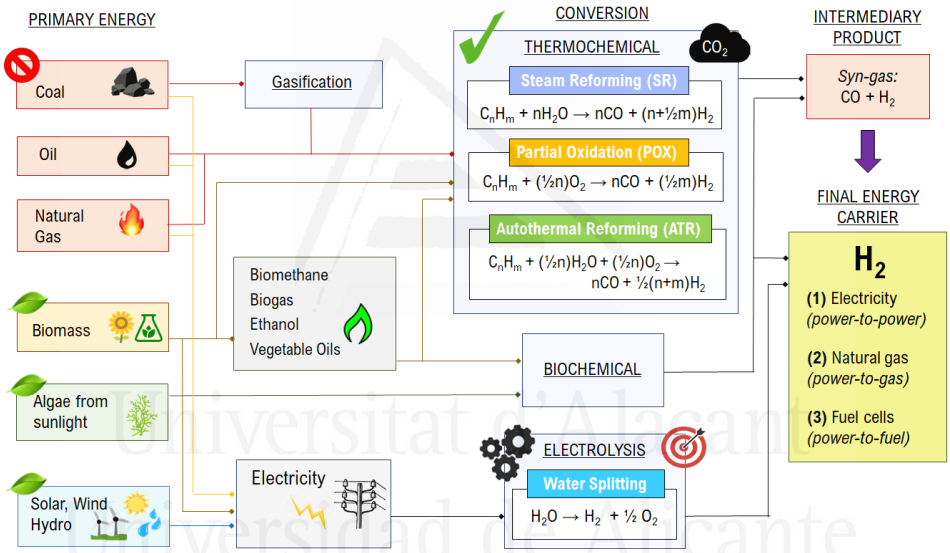

Figure 1.6. Principal H_2 generation routes by primary sources, and energy-related uses.

That is to say, only a mere 4% fraction of overall large-scale produced H_2 is not fossil fuel dependent, at least, not directly. So short-term research goals in the field are determined to optimize water electrolysis and increase its share in hydrogen production market.

1.3.2 Electrolytic water splitting

By and large, electrolysis is the process of splitting water (Equation 1.6) into its elemental compounds, H_2 and O_2, by using electrical current applied between two electrodes in electrochemical devices, electrolyzers or electrolytic cells (EC) [123–125].

$$H_2O\ (l) \rightarrow H_2\ (g) + ½\ O_2\ (g) \qquad \text{Eq. 1.6}$$

As a result, *pure* H_2 and O_2, a useful by-product, are created in a very efficient process with virtually, zero carbon emissions involved. However, water electrolysis is obviously conditioned by the expenses of the required electricity and by the environmental impact related to its production. In this regard, taking into account current electricity production scenario, investments in water electrolysis technology are just not globally accountable in terms of cost, beside it results in large amount of indirect CO_2 emissions [126].

Technically, only renewable electricity production may drive to zero-emission electrolytic H_2, which is the premise in current worldwide *power-to-x* plants [30], aimed to use renewable electricity surplus in off-peak times to produce electrolytic hydrogen. Stored as chemical energy, it can be delivered afterwards when demanded in the fluctuating renewable electricity generation. However, much efforts are pending in this regard as, to date, though implemented mature electrolytic technology, few pilot plants have demonstrated sufficient long-period operation and cost-efficiency.

1.3.3 Steam Reforming and Water-Gas Shift reaction pathway

Hence, in the transition to the sustainable H_2 economy alongside the gradual progress on water electrolysis technology deployment, the current H_2 market is mainly sustained by Natural Gas Steam Reforming (NGSR), an economically affordable process most often produced in large dedicated plants managed by industrial gas companies [25]. Although composed of a mixture of light hydrocarbons, natural gas is mostly methane (CH_4), so an approximate description of NGSR is provided by Equation 1.7.

$$CH_4 + H_2O \leftrightarrow CO + 3\ H_2 \qquad \Delta H^0 = +206\ kJ/mol \qquad \text{Eq. 1.7}$$

Noticeable, hydrogen generation via steam reforming comprises a significative CO co-production, leading to a H_2-rich mixture with a variable 10-12% vol. CO, depending on the operation temperature and the inlet feed [127,128]. The outcome reducing mixture, so-called *synthesis gas* or shortly, *syn-gas,* is standalone a good fuel and a relevant intermediate in chemical industry such as in ammonia, or methanol production, and feedstock in Fischer-Tropsch process, among multiple uses [129,130]. Nevertheless, the variable syn-gas mixture is not suitable for stoichiometric applications and if pure hydrogen is demanded, the outlet reforming stream has to be treated in a subsequent refinement process, namely the Water-Gas Shift (WGS) reaction (Equation 1.8).

$$CO + H_2O \leftrightarrow CO_2 + H_2 \qquad \Delta H^0 = -41.2\ kJ/mol \qquad \text{Eq. 1.8}$$

Consequently, the outlet stream is enriched in H_2 while CO content lowered to the variable 0.5-2% [127,128,131], yet insufficiently clean to be directly fed in the PEM fuel cell, according to the well-known stringent ppmv

Universitat d'Alacant
Universidad de Alicante

CO-tolerance of Pt-based anodes. So latter purification processes are required to achieve targeted CO removal. Among different strategies to conduct CO clean-up, the catalytic methods allow much better miniaturization of the process since they do not need specific heavy components for their set up. In particular, as described in detail in the following sections, the Preferential CO Oxidation (CO-PROX) reaction has been claimed as the most promising approach [127,132], besides it brings the possibility to undertake the so-called *process intensification* concept, aiming to unify WGS and CO-PROX reactions in a single advanced catalytic reactor, which may reduce costs and overall system volume requirements [133].

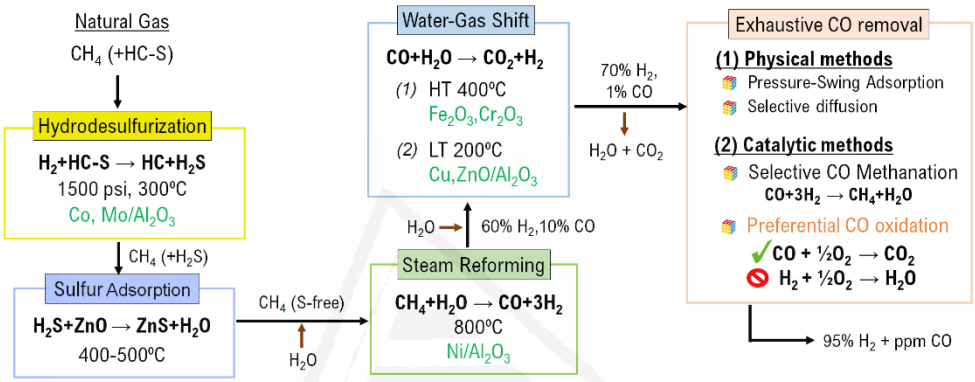

Figure 1.7. Conventional unit operations for generating hydrogen from natural gas.

Thus, in the overall H_2 production by coupled NGSR and WGS processes, engineering design is meant to overcome thermodynamic limitations and favor the corresponding forward reactions to the products side [134,135]. Furthermore, in order to accelerate reaction kinetics up to a relevant rate, catalysts with specific formulations are employed on each operational unit. Figure 1.7 schematizes principal chemical processes in a conventional H_2 production plant, and in the following sub-sections the main characteristics of the catalytic processes are described in detail.

1.3.3.1 Sulfur removal

Provided that natural gas may come from different geological sources according to local availability, the reforming fuel feedstock presents variable composition, such as sulfur compounds from different nature (R-S). Since sulfur is a strong poisonining agent that permanently deactivates the subsequent Ni-based reforming catalyst, the exhaustive sulfur removal is a critical first step to guarantee overall reforming process and PEM fuel cell operation [136–138].

Typically, sulfur removal from natural gas takes place in two steps:

(1) Catalytic hydrodesulfurization, that is, the retention of the sulfur-containing hydrocarbon (R-S) into solid catalysts and adsorbents (Co,

Mo/Alumina) at elevated temperatures (300–400 ºC) and pressures (30–40 bar). When an equilibrium sulfur composition is achieved (catalyst sulfide formation), the excess sulfur is released as H_2S [139], so the overall process can be described as in Equation 1.9:

$$R\text{-}S + H_2 \rightarrow H_2S + HR \qquad \text{Eq. 1.9}$$

(2) Sulfur adsorption, which comprises the H_2S retention on particulate high-surface ZnO bed, occuring at 400ºC, process that is actually controlled by the reaction defined as Equation 1.10, that forms inert insoluble zinc sulfide [140]:

$$H_2S + ZnO \rightarrow ZnS + H_2O \qquad \text{Eq. 1.10}$$

The spent ZnO sorbent is non-hazardous for waste disposal, and by these coupled processes, sulfur levels can be successfully decreased up to 0.02 *ppmv* in the fuel stream [127].

1.3.3.2. Steam Reforming reaction

After desulfurization, S-free fuel enters the steam reforming reactor. Since methane steam reforming reaction (Equation 1.7) is strongly endothermic, high temperatures are required to favor thermodynamics, so typically the reactor should operate above 700ºC [134,135]. However, different strategies allow to lower operation temperature up to nearly 500ºC [141]. For instance, the *in-situ* removal of either or both H_2 and CO_2 shifts equilibria towards product side, which can be performed by means of H_2-selective membranes [142] and/or CO_2 solid sorbents [143], integrated in the conveniently designed reactor operating at high pressures (3-25 bar) [144]. On the other hand, modern steam-reforming units consist of a primary reformer with an adiabatic pre-reformer upstream, which reduces the load of the primary reformer, and minimizes the risk of sulfur poisoning [145].

Among active materials to accelerate methane steam reforming, two main categories are generally discerned: (1) catalysts based on precious metals, such as Pt or Rh; and (2) based on non-precious metals, as Ni, or Co [146,147]. By large, the most employed catalysts in industry are based on the less expensive nickel formulations, chiefly, Ni dispersed in the refractory support alumina (Al_2O_3). However, at high temperatures nickel-based catalysts may promote coke formation, leading to carbon deposition on the catalytic surface with corresponding active site blocking, specially when feeding low steam to carbon ratios into the reactor [148,149]. In this regard, structural and electronic promoters such as Mg, K or other alkaline components are added to the support to prevent from massive coke deposition [127,128,150,151].

In general, steam reforming is a mature industrial process with low initial investment costs, long life time and efficiencies reaching the 85%, for which it is well-stablished and covers most of hydrogen production [152,153]. Furthermore, despite environmental impact because of fossil fuels utilization, low carbon emissions via steam reforming industrial process is feasible if appropriate CCS strategies are implemented to the highly-concentrated CO_2 output streams, which are optimum targets for CCS technology [25]. In fact, almost 80% of CO_2 emissions can be reduced by coupling CCS, so reformate hydrogen could be tentatively considered a low-carbon fuel if CCS mitigation measures are installed. This remark is quite encouraging, since it is possible to provide certain sustainability to current hydrogen production market while enabling the interdependent fuel cell implementation and development.

1.3.3.3 Water-Gas Shift

The effluent reformate gases are introduced into the WGS reactor and which typically operates at two catalytic stages, in order to achieve higher CO conversion. Firstly, in the high-temperature (HT) shift, operating near equilibrium in the 320-450ºC range, lowers initial CO content to ~4%. Secondly, the low-temperature (LT) shift, performed at 180-240ºC allows to decrease CO content up to targeted 0.5-2% CO vol. in the WGS output [139,154,155]. Because of thermodynamic limitations, WGS process cannot decrease farther CO content in the H_2 stream to meet PEM Pt-based electrodes requirement, but the choice of a proper catalyst for both HT and LT bed is critical for the well performance of the WGS unit.

In conventional design, catalysts for HT and LT processes employ well-known standard formulations. For the HT, it comprises the mixture: Fe_2O_3 (80-90%) and Cr_2O_3 (8-10%), balanced with promoters (Al_2O_3, alkali, MgO, ZnO, CuO); while for the LT, the catalyst is $Cu/ZnO/Al_2O_3$, where Cu^0 is the active site and the others textural promoters of Cu dispersion [156,157]. In both cases, the catalysts should undergo controlled reducing pre-treatments in order to activate the catalytic sites, and it is well-known that this pre-treatment largely affects overall performance [158].

Alternative catalysts have been tested and exhibited comparable activities with regards to the standard ones. Namely, Pt based catalysts have been claimed to be good for HT process, whereas Au-based catalysts have shown promising activities in the LT operation. Worth to mention, is the key role of CeO_2 supports, which have arisen and consolidated with leading outlook in WGS catalysts [155,159–161].

1.3.4 The exhaustive CO clean-up in H_2-rich streams

The residual CO concentration left upon WGS in H_2-rich streams must be processed in clean-up post-treatments. These are categorized in two

main groups: (1) physical, and (2) catalytic methods, as described in the following.

1.3.4.1 Physical methods

Physical methods compile different hydrogen separation techniques, namely: Pressure Swing Adsorption (PSA), cryogenic distillation and membrane separation [162]. Among them, the multi-step PSA process is the most employed in the large-scale industrial hydrogen production in refineries [163]. Following this methodology, the impure H_2 stream is passed through physic adsorbers (zeolite, alumina, or activated carbon), that capture main impurities: H_2O, CO_2, CO, CH_4 and N_2 which are efficiently removed from the gas stream and essentially pure H_2 is left, at expenses of not full recovery values [164]. Basically, the PSA units are based on the capacity of these adsorbents to retain more impurities at high pressures than at lower ones, so the overall process is roughly consisting in five steps: (1) adsorption; (2) concurrent depressurization; (3) countercurrent depressurization; (4) purgue; and (5) countercurrent pressurization, although actual industrial version of this process is divided in 11 cyclic steps [163,164]. Therefore, provided the complex experimental set-up required, consisting in poly-bed systems with multiple parallel columns and heavy compressor instrumentation, it is not feasible to adapt PSA procedures in downsize H_2 processor units.

Regarding cryogenic distillation, the separation is undertaken in a low-temperature and high energy demanding process, which is based on the different boiling temperatures of the feed components, since H_2 has a high relative volatility [165]. However, the system itself is not efficient for CO and CO_2 isolation, so an additional wash column is required. Compared to PSA, higher H_2 recovery is achieved, but the purity of the produced H_2 is moderate [162].

Finally, membrane separation techniques make use of selective permeable barriers from different nature: inorganic (metallic or ceramic), organic (polymeric or biological) and hybrid composites [166] to separate H_2 from impurities in a process forced by diverse phenomena: molecular sieving, Knudsen diffusion, solution-diffusion and surface-diffusion. In general terms, membrane separation presents several advantages when compared to mature PSA and cryogenic procedures, namely: easy and cost-effective operation, low investment costs and low energy consumption. Among different materials, the inorganic type have attracted wider attention, and in particular, Pd membranes are by far the most studied [167,168]. But since Pd is an expensive material, alternative ceramic or polymeric membranes are more convenient for practical reasons. Currently, technical feasibility has already been demonstrated, so the potential role of membranes as part of fuel processing systems depends on the cost issues instead, still challenge pending to address [127,169,170].

Universitat d'Alacant
Universidad de Alicante

1.3.4.2 Catalytic methods

Catalytic methods include mainly two processes: (1) Selective CO Methanation (CO-SMET); and (2) Preferential CO Oxidation (CO-PROX), and these have potential real opportunities in low-size fuel processing units, in contrast with the physical approaches. In fact, the DOE support on *on-board* fuel processing had been key driver for these technologies and relevant achievements were provided [139].

The selective CO methanation, ruled by equilibrium from Equation 1.11, involves partial hydrogen consumption to undertake CO hydrogenation to methane, product which does not affect to the fuel cell operation [139,171,172]. Thus, considering that CO content is very low in the initial feeding, the proportional hydrogen consumption derived from CO-SMET is not a relevant issue, while the no-need of additional inlet gas supply is a very positive aspect from CO-SMET process.

$$CO + 3\ H_2 \leftrightarrow H_2O + CH_4 \qquad \Delta H^0 = -206\ kJ/mol \qquad \text{Eq. 1.11}$$

CO-SMET catalysts are commonly based on Ru or Ni active metals [173,174] supported on different metal oxides, such as TiO_2 or ZrO_2 [175], which are able to achieve the removal CO targets up to the tolerance level from Pt-electrode when the performance is optimal. However, main drawback of CO-SMET is the competitive CO_2 methanation reaction, which may occur in the same catalytic environment, driving to a large H_2 consumption provided the significative CO_2 content.

In practice, the alternative PReferential OXidation of CO (CO-PROX), topic of the present Project Thesis is the preferred catalytic methodology, despite being a more exothermic process, hence operation more difficult to control, since it does not lead to hydrogen consumption [127,132,176,177]. Next section reviews CO-PROX process in detail.

1.3.5 The Preferential Oxidation of CO (CO-PROX)

Back to a broad contextualization, the CO-PROX reactor would be situated downstream LT WGS and directly connected to the PEM fuel cell, so the ideal operating temperature is governed by the two frontier processes, that is, in the range from 80 to 250ºC. As a *selective* oxidation of carbon monoxide, it is required a continuous air/O_2 supply to the reactor within extensive control upon the operating temperature, pressure and residence since several undesired side reactions can additionally take place in the reaction mixture.

Principally, the CO oxidation reaction (Equation 1.3) competes with H_2 oxidation reaction (Equation 1.4), which provokes an efficiency loss provided the fuel consumption.

CO oxidation reaction:

$CO + ½\ O_2 \leftrightarrow CO_2$ $\Delta H^0 = -283$ kJ/mol Eq. 1.3

H_2 oxidation reaction:

$H_2 + ½\ O_2 \leftrightarrow H_2O$ $\Delta H^0 = -242$ kJ/mol Eq. 1.4

Furthermore, other side or consecutive reactions may occur from a thermodynamic point of view, such as:

CO methanation reaction:

$CO + 3\ H_2 \leftrightarrow H_2O + CH_4$ $\Delta H^0 = -206$ kJ/mol Eq. 1.11

CO_2 methanation reaction:

$CO_2 + 4\ H_2 \leftrightarrow 2\ H_2O + CH_4$ $\Delta H^0 = -165$ kJ/mol Eq. 1.12

Reverse Water-Gas Shift reaction (RWGS):

$CO_2 + H_2 \leftrightarrow H_2O + CO$ $\Delta H^0 = +41$ kJ/mol Eq. 1.13

Particularly, CO and CO_2 methanation reactions described in Equations 1.11 and 1.12, respectively, consume hydrogen and would contribute to the non-controlled emissions. Besides, as exothermic reactions, these could give rise to a thermal run away in the CO-PROX reactor. On the other hand, RWGS (Equation 1.13) is the most undesired side-process since it ruins the achieved clean-up.

Accordingly, since catalytic CO-PROX reaction is manifold, a high selectivity is the critical requirement to stablish suitable catalysts for this process [178]. Additionally, the catalyst must be active within the operating CO-PROX temperature window and keep stable performance along lifetime and in long time-on-stream utilization. Besides, it should be compatible with CO_2 and H_2O and display acceptable performance in these conditions, since these inhibitors would be present in real CO-PROX reaction environment.

Based on these considerations, the catalysis science over the Preferential CO Oxidation reaction has addressed the study and optimization of classical oxidation catalysts, such as Pt, Ru or Rh, which has been extended to other non-noble active metals with promising results. Next section revises the state-of-the art of CO-PROX active catalysts presented so far.

1.4 State-of-the-art of the catalytic Preferential CO Oxidation (CO-PROX) reaction

1.4.1 General background

The concept of Preferential CO Oxidation (CO-PROX) dates back to the 1920s, when it was recognized the practicability of a catalytic combustion process for the selective removal of carbon monoxide from hydrogen,

targeted to purify H_2 streams for the Haber-Bosch process in the ammonia synthesis [179,180]. Thus, one of the first applied studies was presented by Lamb, Scalione and Edgar, who revealed the potential application of hopcalite catalyst to oxidize 0.5% of carbon monoxide in hydrogen by adding air in a slight excess of oxygen over that required for complete oxidation of CO [181,182]. Hopcalite, a well-known CO removal substance developed during World War I by the US Army as part of respiratory protection equipments [183], consisting in a mixture of amorphous manganese (~60%) and copper (~40%) oxides and small quantities of iron, cobalt or silver oxides [184–186], used to show good CO oxidation performance in dry air, although the presence of moisture seemed to be strongly deactivating.

Nevertheless, despite destabilizing hopcalite structure, the presence of H_2O in the inlet stream had two secondary positive benefits in the catalytic activity relying on (1) the improved heat dissipation upon the exothermic process occurring, and (2) the thermodynamically hindered H_2 oxidation, which widened hopcalite CO selective operation. Thus, it was preluded the possibility to tune the catalytic performance and separate both oxidation processes, in agreement with the general rule that reducible oxides, such as hopcalite, are reduced at lower temperatures by carbon monoxide than by hydrogen [187].

In fundamental terms, reducible oxides are characterized by their relative facility to exchange oxygen, provided by their moderate energy difference between the lowest empty states in the conduction band with respect to the valence band [188]. Thus, reducible oxides are typically semiconductor d-metal oxides, such as TiO_2, Fe_2O_3, NiO, MnO_2, CuO or CeO_2, able to form non-stoichiometric oxides arisen from the variable oxidation state from M^{n+} to $M^{(n-1)+}$ upon their facile lattice oxygen abstraction [189,190]. In turn, elements from the broad family of reducible oxides present chemical reactivity particularities, which bring relevant impact in their utilization in industrial catalytic processes, specially, those based on oxidation reactions.

Namely, when reducible oxides act as active catalysts, they easily follow the well-reported Mars-van Krevelen (MVK) mechanism [191], where surface oxygen ions from the catalyst are directly involved in the reaction. In result, lattice oxygen is gradually being depleted along with the oxidation reaction course, at expenses of creating anionic oxygen vacancies in the crystal and the partial reduction of the metal oxide. Figure 1.8 depicts key steps in MVK mechanism for a reducible metal oxide catalyst ongoing a general oxidation reaction [192], besides Langmuir-Hinshelwood (LH) mechanism [193] is annexed for comparative reasons.

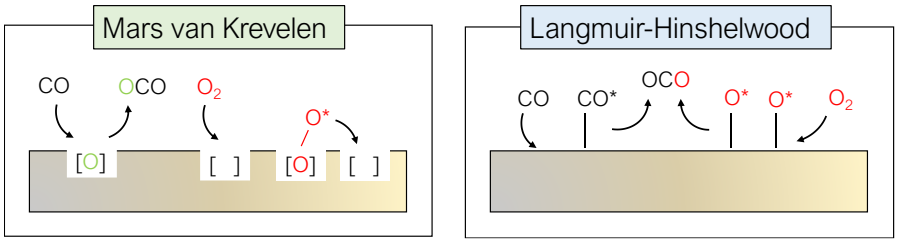

Figure 1.8. Schematization of MVK and LH mechanism key steps for CO oxidation reaction.

As figure 1.8 shows, the anionic vacancies in the lattice should be replenished by an auxiliary oxygen source, such as molecular O_2 gas supply in the reactant mixture, ideally equilibrating lattice oxygen abstraction by its balanced restitution. In turn, in contrast with oxidation catalysis where reaction occurs in dissociatively adsorbed O-* species from O_2 gas phase, in MVK mechanism there may not be a correlation between the reactant oxidation and O_2 dissociation sites. Evidences of MVK mechanism have been extensively presented along decades of well-reported literature by means of different experimental settings, such as MS-monitored pulsed-isotopic experiments for the molecular labeling and traceability of species.

Hence, the positive catalytic features over reducible oxides rely on the fact that the “active” sites are virtually extended to most of the exposed surface, rather than punctual spots where activated adsorbed molecules should locally meet on surface to react. In agreement with this, the improvement in the relative reduction facility (so-called reducibility), would lead to the creation of more active and more reactive sites for the catalytic oxidation, but also a facile and efficient re-oxidation guarantees continuity of the reaction by the regeneration of technically unlimited active sites.

Regarding this, main parameters that determine reducibility in metal oxides is the nature and strength of M – O bonds, the relative energies of the resulting reducible cations, besides characteristic surface topology and surface reconstruction issues upon lattice relaxation, which are in global, determining factors into the overall reactivity in MVK mechanism.

In result, there is a vast research field focused on the improvement of redox properties in solids in order to achieve an optimum catalytic performance, and hopcalite catalyst (amorphous $CuMn_2O_4$) was one of the first examples that, by chance, accomplished with these considerations even before being aware of them. In timeline, a general CO oxidation mechanism upon hopcalite catalyst based on its reduction and latter O lattice uptake was described for the first time by Rogers et al. in 1921 [194], being afterwards confirmed by other authors [195,196] and modelized with kinetic equations in 1970 by Brittan and co-workers [197]. However, despite decades of spread utilization, the reasons for the promoted activity of hopcalite catalyst into CO oxidation remained unclear.

In this regard, Schwab and Kanungo [198] hypothesized in 1977 the solid-state charge transfer in the redox system: $Cu^{2+} + Mn^{3+} \leftrightarrow Cu^{+} + Mn^{4+}$ as the driving force for the "anomalous promotion" of the catalytic activity of manganese oxide when mixed with copper oxide. Later, in 1986, Cocke and Veprek [199,200] demonstrated for the first time direct experimental evidences for the existence of that Cu – Mn redox interplay and its critical effect into the encountered hopcalite catalytic activity. Most interestingly, tough, the authors remarked the possibility to open-up a general concept of solid-state redox systems and extend it to other systems with potential uses in catalysis, which currently holds large part catalysis research field.

Thus, although hopcalite was being widely used, its limited stability and low activity in ambient conditions of temperature and humidity, triggered to set the focus on different catalytic alternatives towards CO oxidation with a reproducible and durable performance. Likewise, deep fundamental studies brought truly important research outcomes from heterogeneous catalysis science, using CO oxidation as test reaction over different catalyst configurations [201–205], such as the well-reported Pt/Al_2O_3 or Au/TiO_2, which showed excellent activity.

However, along with the PEM fuel cell technology revolution, a suitable CO oxidation catalyst was required to operate in presence of large H_2 excess, which actually means a challenge, and the necessity to develop cost-effective and large-scale produced materials for extended application. Thus, as section 1.5.2 reviews, catalytic approaches into the CO-PROX reaction compile mainly three types of catalysts, and they are result of thorough development efforts conducted along decades of research.

1.4.2 Active catalysts for CO-PROX reaction

The most commonly employed active catalysts in the Preferential Oxidation of CO reaction are categorized into three main families, distributed as follows:

Noble metal-based catalysts [206–209], constituted by a variable 0.5-5% w/w content of dispersed noble metal nanoparticles, Pt [210,211], Pd [212], Rh [213], Ir [214], Ru [215,216] into different metal oxide supports, such as Al_2O_3, SiO_2, zeolites, CeO_2 and CeO_2-derived materials. Furthermore, after the long track record of CO-PROX basis research into this type of materials, several efficient strategies to improve noble metal-based catalysts performance have arisen. Namely, (i) the bimetallic combinations [217], in terms of metal alloying [218] or core-shell architectures [219,220]; (ii) the promotion with reducible metal oxides, mainly iron oxide in Pt-Fe systems [221,222], and Pt-Sn [223]; or (iii) alkali doping [224,225], have been widely reported and thoroughly studied.

In turn, there is vast research literature into the potential application in CO-PROX reaction over noble metal catalysts, which show fairly satisfactory results. By and large, most of these reproduce high CO oxidation activity with acceptable CO selectivity within the 60-150ºC framework, as well as good CO_2 and H_2O compatibility. In contrast, their high expenses are strong limiting agents to their spread implementation. In result, despite large optimization and encouraging rational design achievements, noble metal-derived research outcomes are virtually focused on fundamental research rather than a realistic commercial outputs.

Nano-gold catalysts [226–231], traditionally involving highly dispersed Au nanoparticles into reducible metal oxide supports from variate nature ranging from TiO_2 [232,233], Fe_2O_3 [234,235], Al_2O_3 [236], ZrO_2 [237], CeO_2 and CeO_2-doped materials [238–240]. From the well-reported literature, size control over gold nanoparticles is crucial, as well as the choice of the support results determining for the catalytic performance by means of the tunable $Au^{\delta+}$ – MO_x interfacial redox exchange.

After the pioneer work from Haruta *et al.* [229] the catalysis by nano-sized gold gained much attention. For this purpose, gold-based catalysts are particularly interesting provided the low capacity of Au to chemisorb and dissociate hydrogen [241], which turns into excellent CO selectivity in CO-PROX reaction application. However in practice, although working in lower temperature window than noble metals, Au-based exhibit in general incomplete CO conversion, a notorious limited reproducibility on their performance, a rapid decline in CO selectivity and suffer from severe detrimental effects by CO_2 presence [230]. Hence, because of these drawbacks, despite much research efforts so far, the wide instauration of Au-catalyzed CO-PROX systems is not practicable yet, to the best of my knowledge.

Mixed non-noble metal oxides [177,242–245], mainly compiling transition metal oxides, such as Co_3O_4 [246,247] or CuO [243,248,249], in combination with other major compounds forming binary mixtures in multiple configurations. In this family of CO-PROX catalysts, MVK mechanism takes place in the labile lattice oxygen from the MO_x active phases, which is promoted upon a facile redox cycle in the intimate interfacial interaction with the other component, mostly used CeO_2 [250]. Thus, it is not trivial to overall discern active sites in this type of catalysts provided the complex nature of the occurring interfacial redox interactions. Interestingly, in contrast with noble metal and gold-based catalysts, the nominal distribution of “active site” with regard to the “support” is absolutely tunable, from the typical low 0.5-10% range in MO_x/CeO_2 conventional catalysts, in increasing percent up to above 50% in the so-called inverse CeO_2/MO_x catalysts [251].

In the case of cobalt oxides, these exhibit optimum performance in terms of CO conversion and CO selectivity, although at high temperatures

CO methanation reaction (Eq. 1.11) becomes dominant process at expenses of CO-PROX [252]. Furthermore, provided their higher expenses with regard to copper oxides, the latter have attracted far more attention, specially, when constituting the binary system: copper oxide – cerium oxide [177,253,254].

Copper oxide – cerium oxide catalysts present excellent activity and selectivity to CO oxidation in the low temperature range of CO-PROX reaction conditions, besides a moderate price, advantage over noble metal-based catalysts; and large stability, in contrast to gold-supported materials. Thus, in addition to its acceptable CO_2 and H_2O compatibility, these systems have proven to be perfectly suitable for long time operation in real conditions of CO-PROX reaction [255,256].

Hence, provided the great importance relying on their large extended use and encouraging catalytic outcomes as practicable high-performance CO-PROX catalysts, CuO/CeO_2 systems are reviewed in detail in next Section.

1.5 The copper oxide – cerium oxide systems

1.5.1 General features

The family of CuO/CeO_2 systems constitutes one of the greatest block of catalysts ever studied, with nearly 1000 research papers centred on their catalytic performance in a broad range of targeted applications. Namely, volatile organic compounds (VOCs) oxidation [257], water-gas shift (WGS) reaction [258,259], low temperature CO oxidation [260], preferential CO oxidation (CO-PROX) reaction [261], CO_2 hydrogenation [262], soot oxidation [263], selective catalytic reduction (SCR) of NO_x [264] or even N_2O decomposition [265].

Universitat d'Alacant
Universidad de Alicante

As thoroughly reported all over literature, CuO/CeO_2 systems possess unique properties and superior performance provided by synergistic Cu – Ce interactions arising from labile exchange between $Cu^{2+} + Ce^{3+} \leftrightarrow Cu^{+} + Ce^{4+}$ redox interplay [266–268]. It should be noticed that copper-based catayst are prone to participate in such redox exchanges when in contact with suitable complementary metal oxide, as demonstrated in the classic hopcalite catalyst occurring between Cu – Mn. In the case of copper oxide – cerium oxide systems, the redox features of bare CeO_2 play an essential role, with the co-existence of Ce^{4+}/Ce^{3+} species and its capacity to behave as "oxygen buffer" under reducing or oxidizig conditions [269].

In this respect, CuO/CeO_2 composites exhibit enhanced reducibility when compared to single counterparts since, interfacial sites are highly reactive provided the facile oxygen activation which drives to a consequent generation of defects, such as oxygen vacancies [250,270]. Therefore, a

large battery of reported strategies has been devoted to promote interfacial Cu – Ce contact aiming to trigger the redox properties and eventually improve CuO/CeO_2 catalysts performance. Namely, the study upon particle size effect by different procedures [271,272], the formation of conventional or inverse catalysts [251,259], mixed $Cu_{2X}Ce_{1-X}O_2$ oxides [255,256] or the doping effect of CeO_2 with different elements [263,273–275], has been addressed in a large list of research papers making use of multiple *ex-situ* and *in-situ* characterization techniques as well as complementary theoretical studies. Next sections review main advances in the state-of-the art for copper oxide – cerium oxide catalysts for the particular application into the Preferential CO Oxidation (CO-PROX) reaction.

1.5.2 The CO-PROX reaction mechanism over CuO/CeO_2 catalysts

According to general consensus established by renowned studies [276–278], Cu^+ species are the active CO oxidation sites in CuO/CeO_2 catalysts, whose formation and stabilization would be promoted via $Cu^{2+} + Ce^{3+} \leftrightarrow Cu^+ + Ce^{4+}$ redox equilibrium in the labile Cu – Ce interface [279,280]. To date, part of the biggest achievements on the description of accurate CO-PROX reaction mechanism over CuO/CeO_2 catalysts must be acknowledged to the exhaustive work from Prof. Martínez-Arias and co-workers, who consolidated the identification of the postulated active sites by means of conclusive advanced spectroscopic results [281,282], and presented a complete comprehensive description of the whole process. Briefly, it is summarized as follows according to MVK involving redox cycle in copper and cerium species:

Universitat d'Alacant
Universidad de Alicante

1. *CO chemisorption in Cu^{n+} centers:*

$CO_{(g)} + O – Cu^+ \rightarrow CO^* – O – Cu^+$ Step 1

2. *CO_2 desorption and Cu^{n+} reduction*:

$CO^* – O – Cu^+ \rightarrow CO_{2(g)} + [x] – Cu^0$ Step 2

3. *Lattice O restitutution and Cu^{n+} re-oxidation (two pathways):*

3a. Direct mechanism:

$O_{2(g)} + 2\{ [x] – Cu^0 \} \rightarrow 2\{ O – Cu^+ \}$ Step 3a

3b. Synergistic mechanism (via CeO_2 in Cu – Ce contact):

$Ce^{4+} – O + [x] – Cu^0 \rightarrow Ce^{3+} – [x] + O – Cu^+$ Step 3b.1

$O_{2(g)} + 2\{ Ce^{3+} – [x] \} \rightarrow 2\{ Ce^{4+} – O \}$ Step 3b.2

Note: [x] stands for surface O vacancy in either Cu_2O or CeO_2 lattice; while "Cu^{n+} centers" may also refer to Cu^{2+} besides Cu^{+}, although only the latter has been schematized.

Steps 1-3 compile basic redox cycles involved in CO oxidation mechanism over CuO/CeO_2 catalysts. Prior to the overall interpretation, it is convenient to bear in mind that CuO/CeO_2 catalysts show inherently an average oxidized state, with major Cu^{2+} and Ce^{4+} components, that is, unless exceptions, their initial natural state in the moment when CO-PROX gas reactant mixture is supplied.

In first instance, carbon monoxide molecules get adsorbed in Cu^{n+} sites, either Cu^{2+} or Cu^{+}, where CO_2 is formed and released upon O lattice abstraction and consequent Cu^{n+} local reduction [283,284]. In this regard, experimental results on probe molecular adsorption point out that CO chemisorbs much stronger on Cu^{+} sites than on Cu^{2+} [285], which is attributed to the balance within electronic donation and back-donation phenomena between CO – Cu^{n+} entities. Thus, it is expected that CO would prefer to bind Cu^{+} species, whose abundance increases along with reaction course by means of the gradual O vacancy formation via MVK mechanism.

According to well-reported analyses, when CO interacts with the CuO/CeO_2 catalytic surface, Cu^{+}–CO carbonyl species are formed, which are detected by means of DRIFT spectroscopy as an intense and sharp signal at ~2100 cm^{-1}, immediately after CO-PROX gas mixture is fed to the analysis chamber [284]. The early identification of the Cu^{+}– CO band reveals the occurrence of a low temperature CO reduction process, proving the high reducibility of the CuO/CeO_2 catalyst as promoted by the Cu – Ce synergistic interaction. Furthermore, the position of such band is highly sensitive to the coordination and electronic density of copper [286], and its evolution with temperature relates with CO oxidation rate [276,278].

Finally, the lattice oxygen abstraction occurring by means of reaction course needs to be restored by molecular O_2 from gas phase (step 3). This process may take place either directly in Cu_xO, or via Ce –O –Cu labile entities, which constitute the direct or synergistic mechanism for the lattice O recovery [250,270]. In this regard, the prevalence or concurrence between both O-restoration pathways is still a matter of debate, although it is believed to be strongly dependent, among other factors, on crystal-plane exposure between CuO and CeO_2 contacting phases [287,288].

Up to this point, detailed issues are descriptive for pure CO oxidation process with CuO/CeO_2 catalysts. However, in the Preferential CO Oxidation (CO-PROX) reaction there is a large H_2 excess in the ($CO + O_2 + H_2$) reactant mixture, which is expected to get involved in the competitive process corresponding to its oxidation (Eq. 1.4). Luckily, as stated before as general rule for reducible oxides, CO is better reducing agent than H_2. In consequence, CO oxidation should take place at lower temperatures than H_2

oxidation, which provides a CO selective temperature window corresponding to the difference between the on-sets for CO and H_2 oxidation reactions. Thus, light-off curves in CO-PROX activity tests (CO + O_2 + H_2) with high-performance catalysts may show three distinguishable regions, though dependent on test conditions:

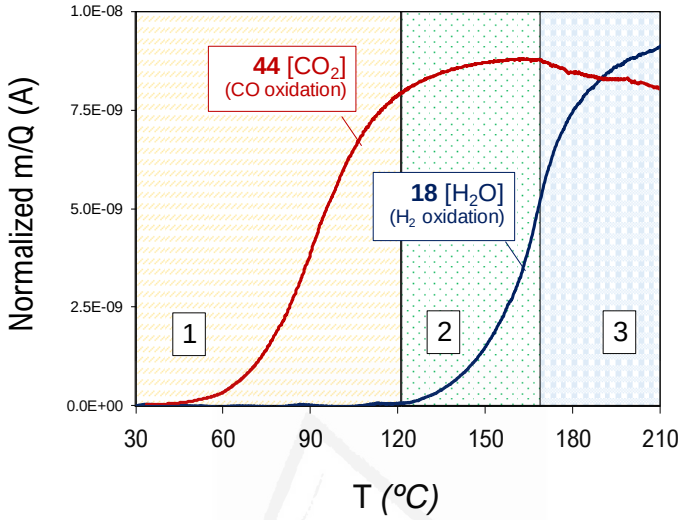

Figure 1.9. MS monitored product signals for 44 (CO_2) and 18 (H_2O) from CO-PROX activity test conducted in high-performance catalysts. Three different reaction regimes are discerned.

In the region (1) at lowest temperatures, CO oxidation reaction is the only process taking place, so it is called the *CO selective regime*. Rising the temperature above certain critical point comprises overcoming H_2 oxidation reaction *on-set*, so that it starts taking place in concurrence with CO oxidation reaction during regime (2), so-called the *non-CO selective regime*. In this stage, both processes compete for O_2, so depending on the inlet O_2 stoichiometric excess, CO conversion should be more or less affected [210,289]. Finally, a farther rising of temperatures reaches regime (3), with an observable average gain of H_2 oxidation reaction in detriment to CO oxidation, provided the higher activation energy for the former process [177]. Depending on experimental conditions, there may not be difference between regimes (2) and (3), in the cases when the start of H_2 oxidation reaction directly leads to a CO conversion fall.

Interestingly, although there is still debate regarding the competitive nature of CO and H_2 oxidation reactions, clear evidences of the key role of copper oxidation state in this regard have been presented [268,276,278,290,291]. For instance, Martínez-Arias and co-workers published truly relevant papers studying CuO/CeO_2 systems by means of CO-PROX *operando* XAS and advanced complementary techniques, which concluded that, though physically sharing copper as catalytic location, CO and H_2 oxidation are activated in different sites. Namely, CO oxidation is

favored in stable and active surface Cu^{I} species balanced in a CuO bulky environment, whereas H_2 oxidation is claimed to occur massively when metal Cu entities are formed in partially reduced Cu_xO particles resulting by the effect of temperature in the reducing CO-PROX atmosphere [278].

Yet, it has been reported the presence of a high excess of H_2 not only determines the optimum temperature for CO-PROX reactor operation, established in terms of CO conversion / CO selectivity compromise, but also may condition surface chemistry during the ongoing processes [292–294]. As a result, CO-PROX reaction is rather complex, and multiple approaches aiming to tune CuO/CeO_2 catalytic performance have been reported so far, as shortly reviewed in next Section 1.5.3.

1.5.3 Rational design of CuO/CeO_2 systems

As shortly described in previous section, research track record on catalytic CO-PROX reaction over copper oxide – cerium oxide systems has enabled to disentangle the specific features implicated in CO-PROX catalytic performance from the abstract Cu – Ce interaction concept. Namely, a labile cyclability upon Cu^{2+}/Cu^{+} and Ce^{4+}/Ce^{3+} redox pairs exchange, for the sake of a facile formation of surface oxygen vacancies, and stabilization of the active Cu^{+} states. In turn, the optimization into the preparation of CuO/CeO_2 systems with improved performance comprises the enhancement in the efficient contact between CuO and CeO_2 phases, and different approaches have been explored so far.

In this regard, computational studies supported on Density Functional Theory (DFT) basis have demonstrated electronic perturbations when Cu ad-atoms are deposited on CeO_2 crystal surfaces [295–298]. Results indicate that Cu loading on CeO_2 facilitates oxygen vacancy formation, besides it was found that interaction degree is strongly dependent on CeO_2 exposed facet. Likewise, in CeO_2(111), the most stable and abundant facet in polycristalline ceria, Cu is prone to be stabilized as Cu^{+} [299], whereas in CeO_2(110), Cu ad-atom remains as oxidized Cu^{2+}, instead [300]. However, it is hard to assume such pure considerations, though well-shaped, real CuO_x/CeO_2 catalysts, which exhibit dissimilar results and declare the intersection between the low-index (110)/(100) terminations as the most reactive positions for CO oxidation [301–303]. Thus, experimental studies devoted to achieve fine control over CeO_2 nano-shape and morphology [304,305], have enabled the preparation of well-reported CeO_2 nano-cubes (110), nano-rods (110)+(100), among which, the later intrinsically show the highest relative

Universitat d'Alacant
Universidad de Alicante

abundance of defects and oxygen vacancies in good correlation with their observed improved catalytic performance.

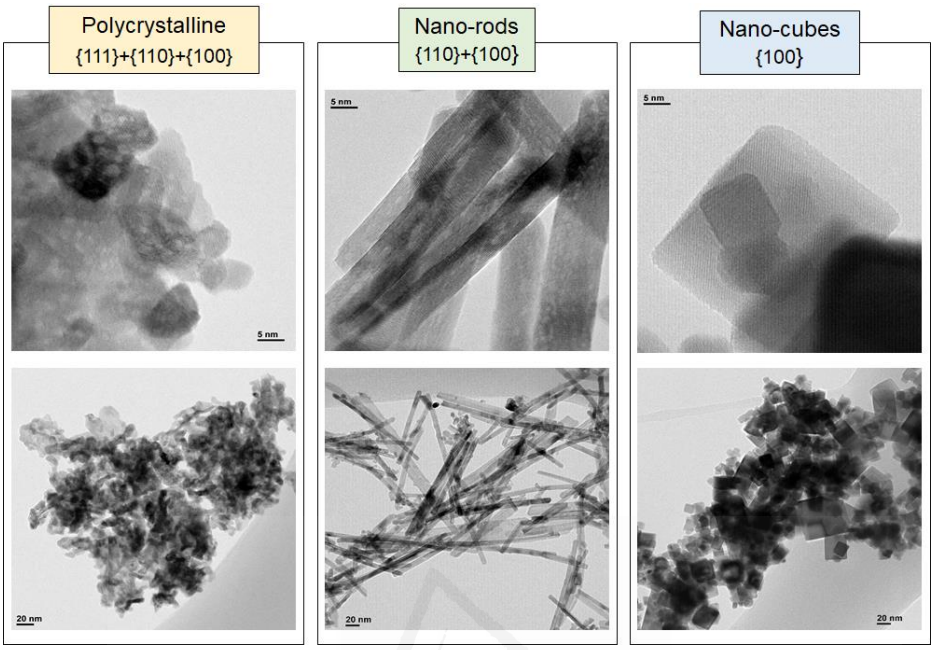

Figure 1.10. TEM images of CeO_2 displaying different nano-shapes.

As alternative approach aimed to improve CeO_2 unique properties, the effect of the lattice insertion of different elements in CeO_2 has been well-reported, too, which showed very positive outcomes in the extensive investigations in the Three-Way Catalysts (TWC) field [263,274]. By and large, it is widely known that doping CeO_2 with suitable foreign cations has several benefits on its bare catalytic features, such as improving the thermal stability and surface reducibility, oxygen storage capacity and oxygen mobility [306]. However, when at practical application for CO-PROX reaction, the effect of CeO_2 doping in variable cation loading of Zr, Pr, La, Sm, or Tb among others, frequently results detrimental for the overall catalytic performance in most of the studies reported [275,307,308]. In this regard, the postulated arguments to understand this particular behavior rely on the low-temperature intrinsic nature of CO-PROX reaction, being targeted below the 250ºC threshold. Hence, although improved properties by CeO_2 doping, such as the sintering prevention or the increase in oxygen storage capacity, may result beneficial in applications at higher temperatures, these do not lead to a relevant effect in the CO-PROX thermal window operation. On the contrary, the presence of foreign cations, instead of being positive, is proven to limit the synergistic effect from copper oxide – cerium oxide interactions, hindering the formation of interfacial Cu – O – Ce reactive sites [292], which is a key feature in CO-PROX catalysis.

Conversely, the preparation of inverse CeO_2/CuO catalysts, where copper oxide is main component from the binary system has resulted in positive catalytic features with regards to the conventional CuO/CeO_2

configuration, and mixed $Cu_xCe_{1-x}O_2$ reference oxides [251,259]. According to theoretical and experimental findings, the disperse CeO_2 particles in inverse catalysts present much larger Ce^{3+} population, thus more oxygen vacancy defects and a greater active oxygen mobility [259]. Likewise, the big-size CuO particles in inverse catalysts show more limited reducibility and bulky redox features. Hence, despite easily reaching surface Cu_2O states upon the interfacial contact points with CeO_2 nanoparticles, these Cu^+ species are not gradually reduced to growing Cu^0 local entities as in the conventional design. Instead, the deeper extension from the CuO bulky environment prevents farther reduction as it is much more affected by kinetic limitations, and Cu^+ states are eventually stabilized [251]. This resulted in a highly positive widening of the CO selective regime in CO-PROX reaction conditions as expected according to the postulated mechanism within the role of Cu^0, so that H_2 oxidation reaction *on-set* was efficiently delayed up to higher temperatures.

Finally, other synthetic approaches worth to mention have been presented, too, as the preparation of CeO_2-based materials with improved textural properties. For instance, meso-structured CeO_2 [309–311] or the so-called three-dimensionally ordered macroporous (3DOM) CeO_2 [312], prepared via colloidal crystal templating on PMMA or PS packed spheres [313,314]. Interestingly, this polymer-templated procedure allows not only to achieve the efficient gas path with largely interconnected wide pores, but also has been related to the creation of a higher population of surface oxygen defects in CeO_2 [315,316]. Thus, CeO_2-based 3DOM samples show a more reactive surface than analogue references, which leads to an improved catalytic performance. However, the synergistic copper oxide – cerium oxide interaction in 3DOM materials has been found to be poor because of the limited Cu – Ce contact in the wide open 3DOM structure, so it is a challenge still pending to address for the improved use of this promising materials.

In this scenario, provided the inherent outstanding performance of conventional CuO/CeO_2 materials, for instance, prepared by the very simple metal nitrate calcination and impregnation, major part of the complex synthetic attempts to improve CuO/CeO_2 catalytic properties result either detrimental or negligible in most cases. Nevertheless, outcomes from the multitude of potential approaches to tune critical CuO/CeO_2 features, eventually mean valuable fundamental knowledge towards an improved CO-PROX application. So, in conclusion, despite the advanced rational design conducted up to date, conventional CuO/CeO_2 catalyst would be preferred in the hypothetical wide implementation of PEM fuel cell technology, because of simplicity and excellent behavior.

Universidad de Alicante

1.5.4 Criticality of cerium oxides and catalytic opportunities for manganese oxides

As detailed in the previous section, CuO/CeO_2 catalysts have demonstrated excellent performance, being appropriate materials to hold multiple catalytic applications without the expensive costs of noble metals. Nevertheless, cerium oxides are not cheap either, whose price in 2018 was globally set near 5500 USD/metric ton [317], in contrast with the easily affordable alumina (Al_2O_3) or titania (TiO_2) supports, averaged in 470 and 140 USD/metric ton units, respectively [318,319].

Regarding cerium oxide market, as in the case for Rare Earth (RE) metal-derived resources, China accounts for about the 90% of global production [320,321], holding an unquestionable supremacy in the global manufacturing and exportation of these high-added value materials, which eventually brings powerful geopolitical interests. Provided that RE mining and production involve very high costs, and dramatic environmental impact via strongly polluting practices, [322,323], no other economies are much interested or do not have the economic facilities to invest in RE metal manufacturing, so China will continue retaining in the future the absolute leadership, controlling the RE metals market price.

In consequence, there is a rising concern regarding RE metals use, which are nowadays present in nearly every electronic device and their demand is dramatically rising [324]. In the particular case of Ce element, it is the most abundant RE metal on Earth's crust, and though current demand its weak, the US Department of Energy considered as *near-critical* the Ce supply risk in the short and medium term [325], highlighting the importance to find alternative material substitutions for the sake of a less critically dependent market.

Universidad de Alicante

With current industrial application niche in UV filters, polishing powders, ceramics, phosphors, glasses, pigments, and three-way automotive exhaust emission control catalysts [320], the implementation of ceria-based catalytic technologies in CO-PROX reaction is only partially practicable since near-future strategies are meant to restrict RE use whenever efficient substitutes are available [326]. As a result, potential reliable catalytic alternatives to cerium oxide materials are a strategically pursued, as for the Preferential CO oxidation reaction, among which, manganese oxides have been claimed as promising candidates.

First, in contrast with RE metal resources, mineral manganese oxides are abundant, non-toxic, and environmentally-friendly, besides highly versatile as naturally found in several polymorphs with multiple manganese oxidation states [327].

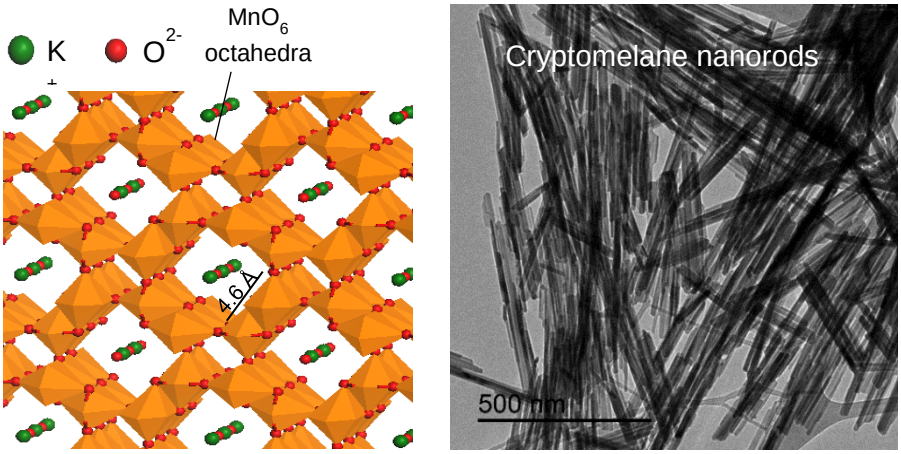

Figure 1.10. (a) Cryptomelane (KMn_8O_{16}) tridimensional simulation with 2 x 2 MnO_6 octahedra arrangement and intratunnel K species. **(b)** TEM images of cryptomelane nanorods.

From the broad family of manganese oxides, a promising material for catalytic applications is cryptomelane (Figure 1.10), a potassium-manganese mixed oxide derived from α-hollandite MnO_2 consisting in a tunneled structure formed by double chains of corner-sharing MnO_6 octahedra basic units [328,329]. The channel size left in between the 2 x 2 octahedra arrangement is 0.46 x 0.46 nm, and K ionic species and water molecules are hosted inside, compensating charge imbalance by the co-existence of various Mn oxidation states, and providing structural stability, respectively [330,331]. Furthermore, the structure and composition of mineral cryptomelane oxide can be achieved easily by laboratory procedures leading to a synthetic material commonly named as Octahedral Molecular Sieve 2 x 2 (OMS-2) [328,329].

The excellent catalytic aptitude of OMS-2 materials has been extensively reported over a wide range of applications, namely catalysts for volatile organic compounds (VOCs) oxidation [332,333], oxidation of CO [334], catalytic water splitting [335]; as well as in electrochemical supercapacitors [336]; or as electrode in batteries [337]. The unique versatility over cryptomelane-based materials relies on the high porosity, acidity, hydrophobicity, electronic and ionic conductivities, and easy removal of lattice oxygen and recovery [338–340], features provided by the facile redox cycling among Mn^{2+}, Mn^{3+}, and Mn^{4+} states, leading to an average manganese valence of *ca.* 3.8 [341,342].

In addition, it is well-known that cryptomelane redox properties can be tuned by means of the introduction of different framework dopants such as Fe [343,344], Ce [345–347], Ni [348–350], Co[347,349,351–354], Ag [355,356], V [357–359] or Cu[360–365], whose effect is dependent on, first, dopant location and distribution, and second, the target Mn species being

substituted in each case, determined by similarities in cation size, charge, and polarizability. From above, the best catalytic improvements have been achieved with Cu^{2+} doping, in a curiously interesting analogy with the first hopcalite catalysts. Cu-doping beneficial effect is generally attributed to several factors: (1) the higher electronegativity of Cu, which weakens in a large extent the Mn–O bond in Mn–O–Cu bridges, resulting in the mobility and reactivity of the active oxygen species; (2) the versatile insertion of Cu-rich phase substituting Mn^{2+}, fitting into CuO_6 octahedra, or tunnel K^+ cations, which increases Mn average oxidation state and provokes crystal structure distortion and the promotion of defects [343,360,366–368]. As a result, Cu-modified cryptomelane materials are more catalytically active systems, tough less thermally stable than bare cryptomelane, which is a challenging limitation for their durable utilization in a hypothetic implemented use.

Furthermore, it may be tentatively ascribed certain analogy of Cu-doped cryptomelane with the well-reported CuO/CeO_2 catalysts, where special interfacial redox properties by means of synergistic effects result in an excellent performance [278,369]. So that, the promising cryptomelane-type manganese oxides are meant to hold a key role in the substitution of catalytic CuO/CeO_2 systems in certain applications, including CO-PROX reaction. Therefore, a critical analysis of the feasibility of Cu-doped cryptomelane analysis in terms of activity and stability is determinant to ensure its adequate implementation and the potentially efficient substution of cerium oxides, which has not been presented so far, to the best of my knowledge.

1.6 Main objectives of the Project Thesis

Taking in thorough consideration the general contextualization exposed in previous Sections along Chapter 1, this Project Thesis arises with focus on the exploration into green active catalysts for the Preferential Oxidation of CO (CO-PROX) reaction, which is critical step in the exhaustive H_2 purification processing with current available production technologies.

With the aim to avoid expensive noble metals utilization and the non-stable performance characteristic of nano-gold catalysts, this Project Thesis addresses the study over copper-based catalysts as a target cost-effective potential option to undertake CO-PROX reaction. As a first approach, conventional CuO/CeO_2 systems have been studied in order to establish a background knowledge upon a high-performance well-reported catalyst. Then, outcomes from fundamental research with CuO/CeO_2 catalyst are to be taken as reference standards in view of the consideration of their possible substitution by alternative abundant and eco-friendly copper oxide – manganese oxide catalysts, namely CuO/Cryptomelane formulations.

Therefore, the main objectives set in this Project Thesis can be synthesized in the following five broad points:

1. *The fundamental study over CuO/CeO_2 systems for the assessment of key mechanistic features and the specific physico-chemical properties that turn into their outstanding performance as CO-PROX catalysts.*

According to this Project Thesis structure and organization, Objective n. 1 is addressed in Chapters 3 and 4, comprising CO-PROX mechanistic studies over pure and doped CuO/CeO_2 catalysts, respectively.

2. *The preparation, characterization and activity testing of alternative CO-PROX catalysts supported on non-RE metal oxides, being CuO/Cryptomelane the particular system under critical evaluation.*

In this regard, Objective n. 2 is mainly aborded along Chapters 5 and 6, with the systematic study of CuO/Cryptomelane stability and regenerative issues in CO-PROX operation conditions, including real performance simulation.

3. *The proposal of a reliable mechanistic study over CO-PROX reaction with the alternative CuO/Cryptomelane catalyst, in analogy with the well-reported on CuO/CeO_2 systems.*

With the aim to tackle Objective n. 3, Chapter 7 comprehends the use of sophisticated non-conventional methods on the study of CO-PROX mechanistic issues in CuO/Cryptomelane catalysts, provided the intrinsic limitations of conventionally extended techniques at their application on this particular material.

4. *The critical comparison between CuO/CeO_2 and CuO/Cryptomelane catalysts in CO-PROX application, in terms of activity and stability in diverse reaction conditions, including the presence of CO_2 and H_2O inhibitors.*

Regarding Objective n. 4, Chapter 8 compiles relevant data from CuO/CeO_2 and CuO/Cryptomelane catalysts for their direct inter-related evaluation.

5. *The scalability of powdered copper-based active phases in medium-sized monolithic catalysts with improved performance prepared by means of 3D-printing technology.*

In the last instance, Objective n. 5 comprises a technological leap moving from the small-scale powdered catalysts to monolith-supported testing, which is furthermore conducted under a non-conventional approach by 3D-printing, as presented in Chapter 9.

Universitat d'Alacant
Universidad de Alicante

1.7 Conclusions

(1) The non-sustainable current energy-related policies are predicted to match inevitably global worldwide development with an increasing rate in GHG emissions unless deep restructuration of energy system is seriously undertaken from now.

(2) Hydrogen deployment as energy vector, although challenging, involves multiple advantages in the decarbonization of the energy system, for instance in fuel cell technology, and mainly, PEM fuel cells.

(3) The fueling requirements for PEM fuel cells comprise H_2 with very high purity degree, as the particularly low (10-100 ppm) CO content, a strong poisons for the necessary Pt-based electrode.

(4) Among the explored CO clean-up processes, the Preferential CO Oxidation (CO-PROX) catalytic reaction is the most feasible and holds promising outlook, specially in portable PEM fuel cell applications with *on-board* fuel processing.

(5) Catalysis research over CO-PROX reaction has resulted in a deep knowledge and the preparation of multiple active phases from diverse nature, namely: noble metal, nano-gold and metal oxides, being the latter the most convenient according to a performance – cost balance.

(6) Copper oxides dispersed in reducible oxides have demonstrated a large potential to conduct catalytic CO-PROX reaction with outstanding results, specially when mixed with cerium oxides and related systems.

(7) The wide range of configurations tested over copper oxide – cerium oxide systems in CO-PROX reaction has allowed to conduct a fine tuning of the process, while optimizing the catalytic performance by means of an enhanced synergistic Cu – Ce effect towards the promotion of the active Cu^{I} states.

(8) The geopolitical criticality linked to RE extraction and manufacturing, that affects cerium oxides, is encouraging the pursue of other analogue alternatives to act as an efficient support for the copper active phases.

(9) Manganese oxides are principal candidates in the substitution of cerium oxides provided their high oxygen mobility, oxidation state variability, and proven excellent copper compatibility as in the classic hopcalite catalyst.

(10) Cryptomelane is a mineral potassium-manganese mixed oxide with excellent catalytic features, although its long time operation and stability have not been studied to critically evaluate its wide implementation as CO-PROX catalyst.

Universitat d'Alacant
Universidad de Alicante

References

[1] Intergovernmental Panel on Climate Change, Climate Change 2013 – The Physical Science Basis: Working Group I Contribution to the Fifth Assessment Report of the Intergovernmental Panel on Climate Change, Cambridge University Press, Cambridge, 2014.

[2] S.C. Doney, V.J. Fabry, R.A. Feely, J.A. Kleypas, Ocean Acidification: The Other CO_2 Problem, Ann. Rev. Mar. Sci. 1 (2009) 169–192.

[3] Intergovernmental Panel on Climate Change, ed., Anthropogenic and Natural Radiative Forcing, in: Clim. Chang. 2013 – Phys. Sci. Basis Work. Gr. I Contrib. to Fifth Assess. Rep. Intergov. Panel Clim. Chang., Cambridge University Press, Cambridge, 2014: pp. 659–740.

[4] G. Hoek, R.M. Krishnan, R. Beelen, A. Peters, B. Ostro, B. Brunekreef, J.D. Kaufman, Long-term air pollution exposure and cardio- respiratory mortality: a review, Environ. Heal. 12 (2013) 43-59.

[5] J. Lelieveld, J.S. Evans, M. Fnais, D. Giannadaki, A. Pozzer, The contribution of outdoor air pollution sources to premature mortality on a global scale, Nature. 525 (2015) 367–371.

[6] O. Raaschou-Nielsen, Z.J. Andersen, R. Beelen, E. Samoli, M. Stafoggia, G. Weinmayr, B. Hoffmann, P. Fischer, M.J. Nieuwenhuijsen, B. Brunekreef, W.W. Xun, K. Katsouyanni, K. Dimakopoulou, J. Sommar, B. Forsberg, L. Modig, A. Oudin, B. Oftedal, P.E. Schwarze, P. Nafstad, U. De Faire, N.L. Pedersen, C.-G. Östenson, L. Fratiglioni, J. Penell, M. Korek, G. Pershagen, K.T. Eriksen, M. Sørensen, A. Tjønneland, T. Ellermann, M. Eeftens, P.H. Peeters, K. Meliefste, M. Wang, B. Bueno-de-Mesquita, T.J. Key, K. de Hoogh, H. Concin, G. Nagel, A. Vilier, S. Grioni, V. Krogh, M.-Y. Tsai, F. Ricceri, C. Sacerdote, C. Galassi, E. Migliore, A. Ranzi, G. Cesaroni, C. Badaloni, F. Forastiere, I. Tamayo, P. Amiano, M. Dorronsoro, A. Trichopoulou, C. Bamia, P. Vineis, G. Hoek, Air pollution and lung cancer incidence in 17 European cohorts: prospective analyses from the European Study of Cohorts for Air Pollution Effects (ESCAPE), Lancet Oncol. 14 (2013) 813–822.

[7] M.C. Hansen, P. V Potapov, R. Moore, M. Hancher, S.A. Turubanova, A. Tyukavina, D. Thau, S. V Stehman, S.J. Goetz, T.R. Loveland, A. Kommareddy, A. Egorov, L. Chini, C.O. Justice, J.R.G. Townshend, High-Resolution Global Maps of 21st-Century Forest Cover Change, Science (80-.). 342 (2013) 850-853.

[8] U.S. Energy Information Administration, International Energy Outlook 2018 (IEO2018), 2018. https://www.eia.gov/.

[9] International Enerrgy Agenci, World Energy Outlook (2018), 2018. https://www.iea.org/weo/.

[10] Transforming our World: The 2030 Agenda for Sustainable Development. United Nations (2015), 2015. Agenda for Sustainable Development web.pdf.

[11] UNFCC, Paris Agreement. United Nations Framework Convention on Climate Change, 2015, n.d.

[12] I.E. Agency, Global Energy & CO_2 Status Report, 2018. https://www.iea.org/geco/.

[13] L.A.M. B. Metz, O.R. Davidson, P.R. Bosch, R. Dave, IPCC (2007). Climate Change 2007: Mitigation, Cambridge University Press, Cambridge, United Kingdom and New York, NY, USA., n.d.

[14] Annual Energy Outlook 2019 with projections to 2050, 2018. https://www.eia.gov/outlooks/aeo/.

[15] IEA, Market Report Series: Renewables 2018. Analysis and Forecasts to 2023, 2018. https://webstore.iea.org/market-report-series-renewables-2018.

[16] D.K. Ross, Hydrogen storage: The major technological barrier to the development of hydrogen fuel cell cars, Vacuum. 80 (2006) 1084–1089.

[17] D.J. Durbin, C. Malardier-Jugroot, Review of hydrogen storage techniques for on board vehicle applications, Int. J. Hydrogen Energy. 38 (2013) 14595–14617.

[18] L.M. Gandía, G. Arzamendi, P.M. Diéguez, Chapter 1 - Renewable Hydrogen Energy: An Overview, in: L.M. Gandía, G. Arzamendi, P.M.B.T.-R.H.T. Diéguez (Eds.), Elsevier, Amsterdam, 2013: pp. 1–17.

[19] W.B. Jensen, Holleman-Wiberg's Inorganic Chemistry (edited by Wiberg, Nils), J. Chem. Educ. 79 (2002) 944.

[20] N. Armaroli, V. Balzani, The Hydrogen Issue, ChemSusChem. 4 (2011) 21–36.

[21] S.W. Jorgensen, Hydrogen storage tanks for vehicles: Recent progress and current status, Curr. Opin. Solid State Mater. Sci. 15 (2011) 39–43.

[22] D. Mori, K. Hirose, Recent challenges of hydrogen storage technologies for fuel cell vehicles, Int. J. Hydrogen Energy. 34 (2009) 4569–4574.

[23] L. Schlapbach, Hydrogen-fuelled vehicles, Nature. 460 (2009) 809-811.

[24] M. Balat, Potential importance of hydrogen as a future solution to environmental and transportation problems, Int. J. Hydrogen Energy. 33 (2008) 4013–4029.

[25] International Energy Agency, Technology Roadmap Hydrogen and Fuel Cells (2015).

[26] A. Sternberg, A. Bardow, Power-to-What? – Environmental assessment of energy storage systems, Energy Environ. Sci. 8 (2015) 389–400.

[27] D. Kroniger, R. Madlener, Hydrogen storage for wind parks: A real options evaluation for an optimal investment in more flexibility, Appl. Energy. 136 (2014) 931–946.

[28] R. Loisel, L. Baranger, N. Chemouri, S. Spinu, S. Pardo, Economic evaluation of hybrid off-shore wind power and hydrogen storage system, Int. J. Hydrogen Energy. 40 (2015) 6727–6739.

[29] M. Götz, J. Lefebvre, F. Mörs, A. McDaniel Koch, F. Graf, S. Bajohr, R. Reimert, T. Kolb, Renewable Power-to-Gas: A technological and economic review, Renew. Energy. 85 (2016) 1371–1390.

[30] G. Gahleitner, Hydrogen from renewable electricity: An international review of power-to-gas pilot plants for stationary applications, Int. J. Hydrogen Energy. 38 (2013) 2039–2061.

[31] K. Ghaib, F.-Z. Ben-Fares, Power-to-Methane: A state-of-the-art review, Renew. Sustain. Energy Rev. 81 (2018) 433–446.

[32] N.Q. Minh, Solid oxide fuel cell technology—features and applications, Solid State Ionics. 174 (2004) 271–277.

[33] P.P. Edwards, V.L. Kuznetsov, W.I.F. David, N.P. Brandon, Hydrogen and fuel cells: Towards a sustainable energy future, Energy Policy. 36 (2008) 4356–4362.

Universitat d'Alacant
Universidad de Alicante

[34] J. Larminie, A. Dicks, Fuel Cell Systems Explained, Chapter 1:Introduction, John Wiley & Sons Ltd,. (2003) 1-24.

[35] P. Zegers, Fuel cell commercialization: The key to a hydrogen economy, J. Power Sources. 154 (2006) 497–502.

[36] B.D. McNicol, D.A.J. Rand, K.R. Williams, Fuel cells for road transportation purposes — yes or no?, J. Power Sources. 100 (2001) 47–59.

[37] World Energy Outlook (2018), 2018. https://www.iea.org/weo/.

[38] IEA, Global Trends and Outlook for Hydrogen (2017), 2017.

[39] F. Marscheider-Weidemann, E. Schirrmeister, A. Roser, Key role of fuel cells, in: M. Wietschel, M. Ball (Eds.), Hydrog. Econ. Oppor. Challenges, Cambridge University Press, Cambridge, 2009: pp. 348–384.

[40] A.K.N. Bockris, John O'M., Reddy, Conversion and Storage of Electrochemical Energy, in: Mod. Electrochem. 2B. Electrodics Chem. Eng. Biol. Environ. Sci., 2000: pp. 1789–1901.

[41] M. Winter, R.J. Brodd, What Are Batteries, Fuel Cells, and Supercapacitors?, Chem. Rev. 104 (2004) 4245–4270.

[42] I. Bar-On, R. Kirchain, R. Roth, Technical cost analysis for PEM fuel cells, J. Power Sources. 109 (2002) 71–75.

[43] J. Wang, H. Wang, Y. Fan, Techno-Economic Challenges of Fuel Cell Commercialization, Engineering. 4 (2018) 352–360.

[44] J. Wang, Barriers of scaling-up fuel cells: Cost, durability and reliability, Energy. 80 (2015) 509–521.

[45] Y. Wang, K.S. Chen, J. Mishler, S.C. Cho, X.C. Adroher, A review of polymer electrolyte membrane fuel cells: Technology, applications, and needs on fundamental research, Appl. Energy. 88 (2011) 981-1007.

[46] A.F. Burke, Batteries and ultracapacitors for electric, hybrid, and fuel cell vehicles, Proc. IEEE. 95 (2007) 806-820.

[47] A.J. Appleby, From Sir William Grove to today: fuel cells and the future, J. Power Sources. 29 (1990) 3–11.

[48] M. Watanabe, D.A. Tryk, Fuel Cells: An Overview with Emphasis on Polymer Electrolyte Fuel Cells BT - Electrochemical Science for a Sustainable Society: A Tribute to John O'M Bockris, in: K. Uosaki (Ed.), Springer International Publishing, Cham, 2017: pp. 51–94.

[49] J.R. Varcoe, P. Atanassov, D.R. Dekel, A.M. Herring, M.A. Hickner, P.A. Kohl, A.R. Kucernak, W.E. Mustain, K. Nijmeijer, K. Scott, T. Xu, L. Zhuang, Anion-exchange membranes in electrochemical energy systems, Energy Environ. Sci. 7 (2014) 3135–3191.

[50] M. Roca-Ayats, S. Pérez-Rodríguez, G. García, E. Pastor, Recent Advances on Electrocatalysts for PEM and AEM Fuel Cells BT - Advanced Electrocatalysts for Low-Temperature Fuel Cells, in: F.J. Rodríguez-Varela, T.W. Napporn (Eds.), Springer International Publishing, Cham, 2018: pp. 51–89.

[51] J. Maruyama, M. Inaba, K. Katakura, Z. Ogumi, Z. Takehara, Influence of Nafion® film on the kinetics of anodic hydrogen oxidation, J. Electroanal. Chem. 447 (1998) 201–209.

[52] W. Sheng, H.A. Gasteiger, Y. Shao-Horn, Hydrogen Oxidation and Evolution Reaction Kinetics on Platinum: Acid vs Alkaline Electrolytes, J. Electrochem. Soc.157 (2010) B1529–B1536.

[53] N. Rajalakshmi, T.T. Jayanth, R. Thangamuthu, G. Sasikumar, P. Sridhar, K.S. Dhathathreyan, Water transport characteristics of polymer electrolyte membrane fuel cell, Int. J. Hydrogen Energy. 29 (2004) 1009–1014.

[54] M.K. Debe, Electrocatalyst approaches and challenges for automotive fuel cells, Nature. 486 (2012) 43-51.

[55] B.C.H. Steele, A. Heinzel, Materials for fuel-cell technologies, Nature. 414 (2001) 345–352.

[56] US Department of Energy (DOE), US DRIVE Fuel Cell Technical Team Technology Roadmap, 2017 (Report).

[57] J. Larminie, A. Dicks, Fuel Cell Systems Explained, Chapter 4: Proton Exchange Membrane Fuel Cells, John Wiley & Sons Ltd,. (2003) 67-119.

[58] B. N.P, B. D.J, Engineering porous materials for fuel cell applications, Philos. Trans. R. Soc. A Math. Phys. Eng. Sci. 364 (2006) 147–159.

[59] S. Litster, G. McLean, PEM fuel cell electrodes, J. Power Sources. 130 (2004) 61–76.

[60] J. Zhou, S. Shukla, A. Putz, M. Secanell, Analysis of the role of the microporous layer in improving polymer electrolyte fuel cell performance, Electrochim. Acta. 268 (2018) 366–382.

[61] R. O'Hayre, F.B. Prinz, The Air/Platinum/Nafion Triple-Phase Boundary: Characteristics, Scaling, and Implications for Fuel Cells, J. Electrochem. Soc. . 151 (2004) A756–A762.

[62] M.S. Wilson, S. Gottesfeld, Thin-film catalyst layers for polymer electrolyte fuel cell electrodes, J. Appl. Electrochem. 22 (1992) 1–7.

[63] Z. Wei, K. Su, S. Sui, A. He, S. Du, High performance polymer electrolyte membrane fuel cells (PEMFCs) with gradient Pt nanowire cathodes prepared by decal transfer method, Int. J. Hydrogen Energy. 40 (2015) 3068–3074.

[64] X. Wang, F.W. Richey, K.H. Wujcik, Y.A. Elabd, Ultra-low platinum loadings in polymer electrolyte membrane fuel cell electrodes fabricated via simultaneous electrospinning/electrospraying method, J. Power Sources. 264 (2014) 42–48.

[65] H.A. Gasteiger, J.E. Panels, S.G. Yan, Dependence of PEM fuel cell performance on catalyst loading, J. Power Sources. 127 (2004) 162–171.

[66] A. Parthasarathy, C.R. Martin, S. Srinivasan, Investigations of the O_2 Reduction Reaction at the Platinum/Nafion® Interface Using a Solid-State Electrochemical Cell, J. Electrochem. Soc. 138 (1991) 916–921.

[67] I.E.L. Stephens, A.S. Bondarenko, U. Grønbjerg, J. Rossmeisl, I. Chorkendorff, Understanding the electrocatalysis of oxygen reduction on platinum and its alloys, Energy Environ. Sci. 5 (2012) 6744–6762.

[68] H. Liu, D. Xia, J. Zhang, Platinum-based Alloy Catalysts for PEM Fuel Cells BT - PEM Fuel Cell Electrocatalysts and Catalyst Layers: Fundamentals and Applications, in: J. Zhang (Ed.), Springer London, London, 2008: pp. 631–654.

[69] T. Toda, H. Igarashi, H. Uchida, M. Watanabe, Enhancement of the Electroreduction of Oxygen on Pt Alloys with Fe, Ni, and Co, J. Electrochem. Soc. . 146 (1999) 3750–3756.

[70] Y. Bing, H. Liu, L. Zhang, D. Ghosh, J. Zhang, Nanostructured Pt-alloy electrocatalysts for PEM fuel cell oxygen reduction reaction, Chem. Soc. Rev. 39 (2010) 2184–2202.

Universidad de Alicante

[71] E. Antolini, Palladium in fuel cell catalysis, Energy Environ. Sci. 2 (2009) 915–931.

[72] J. Uribe-Godínez, V. García-Montalvo, O. Jiménez-Sandoval, Development of Ir-based and Rh-based catalyst electrodes for PEM fuel cell applications, Int. J. Hydrogen Energy. 38 (2013) 7680–7683.

[73] M.S. Thorum, J. Yadav, A.A. Gewirth, Oxygen Reduction Activity of a Copper Complex of 3,5-Diamino-1,2,4-triazole Supported on Carbon Black, Angew. Chemie Int. Ed. 48 (2009) 165–167.

[74] F.A. Armstrong, J. Hirst, Reversibility and efficiency in electrocatalytic energy conversion and lessons from enzymes, Proc. Natl. Acad. Sci. 108 (2011) 14049-14054.

[75] Y. Gorlin, T.F. Jaramillo, A Bifunctional Nonprecious Metal Catalyst for Oxygen Reduction and Water Oxidation, J. Am. Chem. Soc. 132 (2010) 13612–13614.

[76] G. Wu, K.L. More, C.M. Johnston, P. Zelenay, High-Performance Electrocatalysts for Oxygen Reduction Derived from Polyaniline, Iron, and Cobalt, Science 332 (2011) 443-447.

[77] J. Quílez-Bermejo, E. Morallón, D. Cazorla-Amorós, Oxygen-reduction catalysis of N-doped carbons prepared via heat treatment of polyaniline at over 1100°C, Chem. Commun. 54 (2018) 4441–4444.

[78] P. Chandran, A. Ghosh, S. Ramaprabhu, High-performance Platinum-free oxygen reduction reaction and hydrogen oxidation reaction catalyst in polymer electrolyte membrane fuel cell, Sci. Rep. 8 (2018) 3591-3602.

[79] F. Jaouen, D. Jones, N. Coutard, V. Artero, P. Strasser, A. Kucernak, Toward Platinum Group Metal-Free Catalysts for Hydrogen/Air Proton-Exchange Membrane Fuel Cells, 62 (2018) 231–255.

[80] J.K. Dombrovskis, A.E.C. Palmqvist, Recent Progress in Synthesis, Characterization and Evaluation of Non-Precious Metal Catalysts for the Oxygen Reduction Reaction, Fuel Cells. 16 (2016) 4–22.

[81] M.P. Ralph, T. R., Hogarth, Catalysis for Low Temperature Fuel Cells. Part II: Anode Challenges, Platin. Met. Rev. 46 (2002) 117–135.

[82] H. Li, C. Song, J. Zhang, J. Zhang, Catalyst Contamination in PEM Fuel Cells BT - PEM Fuel Cell Electrocatalysts and Catalyst Layers: Fundamentals and Applications, in: J. Zhang (Ed.), Springer London, London, 2008: pp. 331–354.

[83] T. V. Reshetenko, K. Bethune, M.A. Rubio, R. Rocheleau, Study of low concentration CO poisoning of Pt anode in a proton exchange membrane fuel cell using spatial electrochemical impedance spectroscopy, J. Power Sources. 269 (2014) 344–362.

[84] S.J. Lee, S. Mukerjee, E.A. Ticianelli, J. McBreen, Electrocatalysis of CO tolerance in hydrogen oxidation reaction in PEM fuel cells, Electrochim. Acta. 44 (1999) 3283–3293.

[85] Z. Qi, C. He, A. Kaufman, Effect of CO in the anode fuel on the performance of PEM fuel cell cathode, J. Power Sources. 111 (2002) 239–247.

[86] Z. Qi, C. He, A. Kaufman, Poisoning of Proton Exchange Membrane Fuel Cell Cathode by CO in the Anode Fuel, Electrochem. Solid-State Lett. 4 (2001) A204–A205.

[87] US Office of Energy Efficiency & Renewable Energy, Hydrogen Fuel Quality Specifications for Polymer Electrolyte Fuel Cells in Road Vehicles, 2016.

Universitat d'Alacant
Universidad de Alicante

[88] S.M.M. Ehteshami, S.H. Chan, A review of electrocatalysts with enhanced CO tolerance and stability for polymer electrolyte membarane fuel cells, Electrochim. Acta. 93 (2013) 334–345.

[89] C.-Y. Chen, K.-P. Huang, Performance and transient behavior of the kW-grade PEMFC stack with the PtRu catalyst under CO-contained diluted hydrogen, Int. J. Hydrogen Energy. 42 (2017) 22250–22258.

[90] L.G.S. Pereira, V.A. Paganin, E.A. Ticianelli, Investigation of the CO tolerance mechanism at several Pt-based bimetallic anode electrocatalysts in a PEM fuel cell, Electrochim. Acta. 54 (2009) 1992–1998.

[91] S. Mukerjee, R.C. Urian, S.J. Lee, E.A. Ticianelli, J. McBreen, Electrocatalysis of CO Tolerance by Carbon-Supported PtMo Electrocatalysts in PEMFCs, J. Electrochem. Soc. 151 (2004) A1094–A1103.

[92] T.E. Springer, T. Rockward, T.A. Zawodzinski, S. Gottesfeld, Model for Polymer Electrolyte Fuel Cell Operation on Reformate Feed: Effects of CO, H_2 Dilution, and High Fuel Utilization , J. Electrochem. Soc. 148 (2001) A11–A23.

[93] J.A. Mader, B.C. Benicewicz, Sulfonated Polybenzimidazoles for High Temperature PEM Fuel Cells, Macromolecules. 43 (2010) 6706–6715.

[94] T. Sato, K. Okaya, K. Kunimatsu, H. Yano, M. Watanabe, H. Uchida, Effect of Particle Size and Composition on CO-Tolerance at Pt–Ru/C Catalysts Analyzed by In Situ Attenuated Total Reflection FTIR Spectroscopy, ACS Catal. 2 (2012) 450–455.

[95] G.A. Camara, E.A. Ticianelli, S. Mukerjee, S.J. Lee, J. McBreen, The CO Poisoning Mechanism of the Hydrogen Oxidation Reaction in Proton Exchange Membrane Fuel Cells, J. Electrochem. Soc. 149 (2002) A748–A753.

[96] E. Antolini, E.R. Gonzalez, The electro-oxidation of carbon monoxide, hydrogen/carbon monoxide and methanol in acid medium on Pt-Sn catalysts for low-temperature fuel cells: A comparative review of the effect of Pt-Sn structural characteristics, Electrochim. Acta. 56 (2010) 1–14.

[97] S.M.M. Ehteshami, Q. Jia, A. Halder, S.H. Chan, S. Mukerjee, The role of electronic properties of Pt and Pt alloys for enhanced reformate electro-oxidation in polymer electrolyte membrane fuel cells, Electrochim. Acta. 107 (2013) 155–163.

[98] Z. Liu, G.S. Jackson, B.W. Eichhorn, Tuning the CO-tolerance of Pt-Fe bimetallic nanoparticle electrocatalysts through architectural control, Energy Environ. Sci. 4 (2011) 1900–1903.

[99] A. Pozio, L. Giorgi, E. Antolini, E. Passalacqua, Electroxidation of H_2 on Pt/C Pt–Ru/C and Pt–Mo/C anodes for polymer electrolyte fuel cell, Electrochim. Acta. 46 (2000) 555–561.

[100] E. Antolini, The problem of Ru dissolution from Pt–Ru catalysts during fuel cell operation: analysis and solutions, J. Solid State Electrochem. 15 (2011) 455–472.

[101] E. Antolini, Platinum-based ternary catalysts for low temperature fuel cells: Part II. Electrochemical properties, Appl. Catal. B Environ. 74 (2007) 337–350.

[102] L. Zhang, J. Kim, H.M. Chen, F. Nan, K. Dudeck, R.-S. Liu, G.A. Botton, J. Zhang, A novel CO-tolerant PtRu core–shell structured electrocatalyst with Ru rich in core and Pt rich in shell for hydrogen oxidation reaction and its implication in proton exchange membrane fuel cell, J. Power Sources. 196 (2011) 9117–9123.

Universidad de Alicante

[103] C. He, H.R. Kunz, J.M. Fenton, Electro-oxidation of Hydrogen with Carbon Monoxide on Pt/Ru-Based Ternary Catalysts, J. Electrochem. Soc. 150 (2003) A1017–A1024.

[104] X. Cui, L. Guo, F. Cui, Q. He, J. Shi, Electrocatalytic Activity and CO Tolerance Properties of Mesostructured Pt/WO3 Composite as an Anode Catalyst for PEMFCs, J. Phys. Chem. C. 113 (2009) 4134–4138.

[105] S. Gottesfeld, J. Pafford, A New Approach to the Problem of Carbon Monoxide Poisoning in Fuel Cells Operating at Low Temperatures, J. Electrochem. Soc. 135 (1988) 2651–2652.

[106] W. Wang, The effect of internal air bleed on CO poisoning in a proton exchange membrane fuel cell, J. Power Sources. 191 (2009) 400–406.

[107] L.-Y. Sung, B.-J. Hwang, K.-L. Hsueh, W.-N. Su, C.-C. Yang, Comprehensive study of an air bleeding technique on the performance of a proton-exchange membrane fuel cell subjected to CO poisoning, J. Power Sources. 242 (2013) 264–272.

[108] G.J.M. Janssen, M.P. de Heer, D.C. Papageorgopoulos, Bilayer Anodes for Improved Reformate Tolerance of PEM Fuel Cells, Fuel Cells. 4 (2004) 169–174.

[109] L.P.L. Carrette, K.A. Friedrich, M. Huber, U. Stimming, Improvement of CO tolerance of proton exchange membrane (PEM) fuel cells by a pulsing technique, Phys. Chem. Chem. Phys. 3 (2001) 320–324.

[110] W.A. Adams, J. Blair, K.R. Bullock, C.L. Gardner, Enhancement of the performance and reliability of CO poisoned PEM fuel cells, J. Power Sources. 145 (2005) 55–61.

[111] H. Lu, L. Rihko-Struckmann, K. Sundmacher, Spontaneous oscillations of cell voltage, power density, and anode exit CO concentration in a PEM fuel cell, Phys. Chem. Chem. Phys. 13 (2011) 18179–18185.

[112] V.A. Sethuraman, J.W. Weidner, Analysis of sulfur poisoning on a PEM fuel cell electrode, Electrochim. Acta. 55 (2010) 5683–5694.

[113] T.Q. Hua, R.K. Ahluwalia, J.-K. Peng, M. Kromer, S. Lasher, K. McKenney, K. Law, J. Sinha, Technical assessment of compressed hydrogen storage tank systems for automotive applications, Int. J. Hydrogen Energy. 36 (2011) 3037–3049.

[114] M. V Lototskyy, M.W. Davids, I. Tolj, Y. V Klochko, B.S. Sekhar, S. Chidziva, F. Smith, D. Swanepoel, B.G. Pollet, Metal hydride systems for hydrogen storage and supply for stationary and automotive low temperature PEM fuel cell power modules, Int. J. Hydrogen Energy. 40 (2015) 11491–11497.

[115] N. Edwards, S.R. Ellis, J.C. Frost, S.E. Golunski, A.N.J. Van Keulen, N.G. Lindewald, J.G. Reinkingh, On-board hydrogen generation for transport applications: The HotSpot™ methanol processor, J. Power Sources. 71 (1998) 123–128.

[116] S. Golunski, What is the point of on-board fuel reforming?, Energy Environ. Sci. 3 (2010) 1918–1923.

[117] S. Golunski, HotSpot™ fuel processor: Advancing the case for fuel cell powered cars, Platin. Met. Rev. 42 (1998) 2–7.

[118] I. Carpenter, N. Edwards, S. Ellis, J. Frost, S. Golunski, N. van Keulen, M. Petch, J. Pignon, J. Reinkingh, On-board Hydrogen Generation for PEM Fuel Cells in Automotive Applications, in: Int. Congr. Expo., SAE International, 1999.

[119] US Department of Energy, On-board fuel processing GO/NO-GO decision.

Universitat d'Alacant
Universidad de Alicante

DOE Decision Team Committee Report, 2004.

[120] A. Tsolakis, A. Megaritis, M.L. Wyszynski, Application of Exhaust Gas Fuel Reforming in Compression Ignition Engines Fueled by Diesel and Biodiesel Fuel Mixtures, Energy & Fuels. 17 (2003) 1464–1473.

[121] H. Eichlseder, T. Wallner, R. Freymann, J. Ringler, The Potential of Hydrogen Internal Combustion Engines in a Future Mobility Scenario, in: Futur. Transp. Technol. Conf. Expo., SAE International, 2003.

[122] H. Council, Hydrogen scaling up. A sustainable pathway for the global energy transition, 2017.

[123] M. David, C. Ocampo-Martínez, R. Sánchez-Peña, Advances in alkaline water electrolyzers: A review, J. Energy Storage. 23 (2019) 392–403.

[124] M. Carmo, D.L. Fritz, J. Mergel, D. Stolten, A comprehensive review on PEM water electrolysis, Int. J. Hydrogen Energy. 38 (2013) 4901–4934.

[125] J.D. Holladay, J. Hu, D.L. King, Y. Wang, An overview of hydrogen production technologies, Catal. Today. 139 (2009) 244–260.

[126] B. Parkinson, P. Balcombe, J.F. Speirs, A.D. Hawkes, K. Hellgardt, Levelized cost of CO_2 mitigation from hydrogen production routes, Energy Environ. Sci. 12 (2019) 19–40.

[127] R. Farrauto, S. Hwang, L. Shore, W. Ruettinger, J. Lampert, T. Giroux, Y. Liu, O. Ilinich, Generating Hydrogen for the PEM Fuel Cell, Annu. Rev. Mater. Res. 33 (2003) 1–27.

[128] J.N. Armor, The multiple roles for catalysis in the production of H_2, Appl. Catal. A Gen. 176 (1999) 159–176.

[129] F.Y. Hagos, A.R.A. Aziz, S.A. Sulaiman, Trends of Syngas as a Fuel in Internal Combustion Engines, Adv. Mech. Eng. 6 (2014) 401587-401597.

[130] G.A. Richards, K.H. Casleton, N.T. Weiland, Synthesis Gas Combustion: Fundamentals and Applications, Chapter 7: Syngas Utilization, CRC Press (2010) 197–222.

[131] J.N. Armor, Catalysis and opportunities for the production of H_2, ACS Div. Fuel Chem. Prepr. 45 (2000) 165–167.

[132] A.F. Ghenciu, R eview of fuel processing catalysts for hydrogen production in PEM fuel cell systems, Curr. Opin. Solid State Mater. Sci. 6 (2002) 389–399.

[133] T.R. Reina, E. Papadopoulou, S. Palma, S. Ivanova, M.A. Centeno, T. Ioannides, J.A. Odriozola, Could an efficient WGS catalyst be useful in the CO-PrOx reaction?, Appl. Catal. B Environ. 150–151 (2014) 554–563.

[134] A. Boyano, A.M. Blanco-Marigorta, T. Morosuk, G. Tsatsaronis, Exergoenvironmental analysis of a steam methane reforming process for hydrogen production, Energy. 36 (2011) 2202–2214.

[135] G. Ji, J.G. Yao, P.T. Clough, J.C.D. da Costa, E.J. Anthony, P.S. Fennell, W. Wang, M. Zhao, Enhanced hydrogen production from thermochemical processes, Energy Environ. Sci. 11 (2018) 2647–2672.

[136] V.A. Sethuraman, J.W. Weidner, Analysis of Sulfur Poisoning on a PEM Fuel Cell Electrode, 55(20) (2011) 5683-5694.

[137] S. Hernández, L. Solarino, G. Orsello, N. Russo, D. Fino, G. Saracco, V. Specchia, Desulfurization processes for fuel cells systems, Int. J. Hydrogen Energy. 33 (2008) 3209–3214.

[138] C. Ratnasamy, J.P. Wagner, S. Spivey, E. Weston, Removal of sulfur

compounds from natural gas for fuel cell applications using a sequential bed system, Catal. Today. 198 (2012) 233–238.

[139] R.A. Dagle, A. Karim, G. Li, Y. Su, D.L. King, Chapter 12 - Syngas Conditioning, in: D. Shekhawat, J.J. Spivey, D.A.B.T.-F.C.T. for F.P. Berry (Eds.), Elsevier, Amsterdam, 2011: pp. 361–408.

[140] M.A. Sayyadnejad, H.R. Ghaffarian, M. Saeidi, Removal of hydrogen sulfide by zinc oxide nanoparticles in drilling fluid, Int. J. Environ. Sci. Technol. 5 (2008) 565–569.

[141] Y. Matsumura, T. Nakamori, Steam reforming of methane over nickel catalysts at low reaction temperature, Appl. Catal. A Gen. 258 (2004) 107–114.

[142] G. Barbieri, A. Brunetti, T. Granato, P. Bernardo, E. Drioli, Engineering Evaluations of a Catalytic Membrane Reactor for the Water Gas Shift Reaction, Ind. Eng. Chem. Res. 44 (2005) 7676–7683.

[143] M. Shokrollahi Yancheshmeh, H.R. Radfarnia, M.C. Iliuta, High temperature CO_2 sorbents and their application for hydrogen production by sorption enhanced steam reforming process, Chem. Eng. J. 283 (2016) 420–444.

[144] L. Barelli, G. Bidini, F. Gallorini, S. Servili, Hydrogen production through sorption-enhanced steam methane reforming and membrane technology: A review, Energy. 33 (2008) 554–570.

[145] T.S. Christensen, Adiabatic prereforming of hydrocarbons — an important step in syngas production, Appl. Catal. A Gen. 138 (1996) 285–309.

[146] S.D. Angeli, G. Monteleone, A. Giaconia, A.A. Lemonidou, State-of-the-art catalysts for CH_4 steam reforming at low temperature, Int. J. Hydrogen Energy. 39 (2014) 1979–1997.

[147] S.D. Angeli, L. Turchetti, G. Monteleone, A.A. Lemonidou, Catalyst development for steam reforming of methane and model biogas at low temperature, Appl. Catal. B Environ. 181 (2016) 34–46.

[148] J.R. Rostrup-Nielsen, Coking on nickel catalysts for steam reforming of hydrocarbons, J. Catal. 33 (1974) 184–201.

[149] J. Sehested, J.A.P. Gelten, I.N. Remediakis, H. Bengaard, J.K. Nørskov, Sintering of nickel steam-reforming catalysts: effects of temperature and steam and hydrogen pressures, J. Catal. 223 (2004) 432–443.

[150] K. Tomishige, D. Li, M. Tamura, Y. Nakagawa, Nickel–iron alloy catalysts for reforming of hydrocarbons: preparation, structure, and catalytic properties, Catal. Sci. Technol. 7 (2017) 3952–3979.

[151] J. Wei, E. Iglesia, Mechanism and Site Requirements for Activation and Chemical Conversion of Methane on Supported Pt Clusters and Turnover Rate Comparisons among Noble Metals, J. Phys. Chem. B. 108 (2004) 4094–4103.

[152] E. Cetinkaya, I. Dincer, G.F. Naterer, Life cycle assessment of various hydrogen production methods, Int. J. Hydrogen Energy. 37 (2012) 2071–2080.

[153] I. Dincer, C. Acar, Review and evaluation of hydrogen production methods for better sustainability, Int. J. Hydrogen Energy. 40 (2015) 11094–11111.

[154] R.M. Navarro, M.A. Peña, J.L.G. Fierro, Hydrogen Production Reactions from Carbon Feedstocks: Fossil Fuels and Biomass, Chem. Rev. 107 (2007) 3952–3991.

[155] D.B. Pal, R. Chand, S.N. Upadhyay, P.K. Mishra, Performance of water gas

shift reaction catalysts: A review, Renew. Sustain. Energy Rev. 93 (2018) 549–565.

[156] P.G. Smirniotis, G.K. Reddy, Water Gas Shift Reaction: Research Developments and Applications, Elsevier Ltd., 2015.

[157] C. Ratnasamy, J.P. Wagner, Water Gas Shift Catalysis, Catal. Rev. 51 (2009) 325–440.

[158] D.G. Rethwisch, J. Phillips, Y. Chen, T.F. Hayden, J.A. Dumesic, Water-gas shift over magnetite particles supported on graphite: Effects of treatments in CO/CO_2 and H_2/H_2O gas mixtures, J. Catal. 91 (1985) 167–180.

[159] S. Hilaire, X. Wang, T. Luo, R.J. Gorte, J. Wagner, A comparative study of water-gas-shift reaction over ceria-supported metallic catalysts, Appl. Catal. A Gen. 258 (2004) 271–276.

[160] R.J. Gorte, S. Zhao, Studies of the water-gas-shift reaction with ceria-supported precious metals, Catal. Today. 104 (2005) 18–24.

[161] A. Trovarelli, Catalysis by Ceria and Related Materials, Catal. Sci. Ser. Volume 2 (2002) 528.

[162] S. Adhikari, S. Fernando, Hydrogen Membrane Separation Techniques, Ind. Eng. Chem. Res. 45 (2006) 875–881.

[163] S. Sircar, T.C. Golden, Purification of Hydrogen by Pressure Swing Adsorption, Sep. Sci. Technol. 35 (2000) 667–687.

[164] S. Sircar, T.C. Golden, Hydrogen and Syngas Production and Purification Technologies, Chapter 10: Pressure Swing Adsorption Technology for Hydrogen Production, Wiley Ltd., (2009) 414-450.

[165] A.B. Hinchliffe, K.E. Porter, A Comparison of Membrane Separation and Distillation, Chem. Eng. Res. Des. 78 (2000) 255–268.

[166] G.Q. Lu, J.C. Diniz da Costa, M. Duke, S. Giessler, R. Socolow, R.H. Williams, T. Kreutz, Inorganic membranes for hydrogen production and purification: A critical review and perspective, J. Colloid Interface Sci. 314 (2007) 589–603.

[167] Y.-M. Lin, G.-L. Lee, M.-H. Rei, An integrated purification and production of hydrogen with a palladium membrane-catalytic reactor, Catal. Today. 44 (1998) 343–349.

[168] S. Yun, S. Ted Oyama, Correlations in palladium membranes for hydrogen separation: A review, J. Memb. Sci. 375 (2011) 28–45.

[169] R.W. Baker, Future Directions of Membrane Gas Separation Technology, Ind. Eng. Chem. Res. 41 (2002) 1393–1411.

[170] N.W. Ockwig, T.M. Nenoff, Membranes for Hydrogen Separation, Chem. Rev. 107 (2007) 4078–4110.

[171] C. Galletti, S. Specchia, G. Saracco, V. Specchia, CO Methanation as Alternative Refinement Process for CO Abatement in H_2-Rich Gas for PEM Applications, Int. J. Chem. React. Eng. 5 (2007) 1-11.

[172] G. Ercolino, M. a. Ashraf, V. Specchia, S. Specchia, Performance evaluation and comparison of fuel processors integrated with PEM fuel cell based on steam or autothermal reforming and on CO preferential oxidation or selective methanation, Appl. Energy. 143 (2015) 138–153.

[173] R.A.D. Betta, A.G. Piken, M. Shelef, Heterogeneous methanation: Initial rate of CO hydrogenation on supported ruthenium and nickel, J. Catal. 35 (1974) 54–60.

Universitat d'Alacant
Universidad de Alicante

[174] R.A. Dagle, Y. Wang, G.-G. Xia, J.J. Strohm, J. Holladay, D.R. Palo, Selective CO methanation catalysts for fuel processing applications, Appl. Catal. A Gen. 326 (2007) 213–218.

[175] S. Takenaka, T. Shimizu, K. Otsuka, Complete removal of carbon monoxide in hydrogen-rich gas stream through methanation over supported metal catalysts, Int. J. Hydrogen Energy. 29 (2004) 1065–1073.

[176] T. V. Choudhary, D.W. Goodman, CO-free fuel processing for fuel cell applications, Catal. Today. 77 (2002) 65–78.

[177] E.D. Park, D. Lee, H.C. Lee, Recent progress in selective CO removal in a H_2-rich stream, Catal. Today. 139 (2009) 280–290.

[178] K.A. Starz, E. Auer, F. Baumann, T. Lehmann, S. Wieland, R. Zuber, Advanced Catalyst Systems for Mobile PEMFC Applications - The Challenge of Carbon Monoxide, in: SAE 2000 World Congr., SAE International, 2000.

[179] W.E. Kuentzel, The preferential catalytic oxidation of carbon monoxide in the presence of hydrogen. I. The activity of two water gas conversion catalysts, of copper oxide, of manganese dioxide and of a mixture of these oxides, J. Am. Chem. Soc. 52 (1930) 437–444.

[180] W.E. Kuentzel, The preferential catalytic oxidation of carbon monoxide in the presence of hydrogen. II. The activity of 2-component hopcalites, J. Am. Chem. Soc. 52 (1930) 445–455.

[181] A.B. Lamb, C.C. Scalione, G. Edgar, The preferential catalytic combustion of carbon monoxide in hydrogen, J. Am. Chem. Soc. 44 (1922) 738–757.

[182] A.B. Lamb, W.E. Vail, The effect of water and of carbon dioxide on the catalytic oxidation of carbon monoxide and hydrogen by oxygen, J. Am. Chem. Soc. 47 (1925) 123–142.

[183] Lamb, Arthur B, Bray, William C, Frazer, J.C.W, The removal of carbon monoxide from air, J. Ind. Eng. Chem. 12 (1920) 213–221.

[184] J.A. Almquist, W.C. Bray, The catalytic oxidation of carbon monoxide. i. efficiency of the catalysts, manganese dioxide, cupric oxide and mixtures of these oxides, J. Am. Chem. Soc. 45 (1923) 2305–2322.

[185] D.R. Merrill, C.C. Scalione, The catalytic oxidation of carbon monoxide at ordinary temperatures, J. Am. Chem. Soc. 43 (1921) 1982–2002.

[186] E.C. Pitzer, J.C.W. Frazer, The Physical Chemistry of Hopcalite Catalysts., J. Phys. Chem. 45 (1941) 761–776.

[187] H.H.B.T.-S. in S.S. and C. Kung, ed., Chapter 6 Reduction of Oxides, in: Transit. Met. Oxides, Elsevier, 1989: pp. 91–109.

[188] A. Ruiz Puigdollers, P. Schlexer, S. Tosoni, G. Pacchioni, Increasing Oxide Reducibility: The Role of Metal/Oxide Interfaces in the Formation of Oxygen Vacancies, ACS Catal. 7 (2017) 6493–6513.

[189] G. Pacchioni, Numerical Simulations of Defective Structures: The Nature of Oxygen Vacancy in Non-reducible (MgO, SiO_2, ZrO_2) and Reducible (TiO_2, NiO, WO_3) Oxides BT - Defects at Oxide Surfaces, in: J. Jupille, G. Thornton (Eds.), Springer International Publishing, Cham, 2015: pp. 1–28.

[190] R.A. van Santen, I. Tranca, E.J.M. Hensen, Theory of surface chemistry and reactivity of reducible oxides, Catal. Today. 244 (2015) 63–84.

[191] P. Mars, D.W. van Krevelen, Oxidations carried out by means of vanadium oxide catalysts, Chem. Eng. Sci. 3 (1954) 41–59.

[192] C. Doornkamp, V. Ponec, The universal character of the Mars and Van Krevelen mechanism, J. Mol. Catal. A Chem. 162 (2000) 19–32.

[193] G. Somorjai, The surface science of heterogeneous catalysis, Surf. Sci. 299–300 (1994) 849–866.

[194] T.H. Rogers, C.S. Piggot, W.H. Bahlke, J.M. Jennings, The catalytic oxidation of carbon monoxide.1, J. Am. Chem. Soc. 43 (1921) 1973-1982.

[195] A.F. Benton, The adsorption of gases by oxide catalysts, J. Am. Chem. Soc. 45 (1923) 887–899.

[196] A.F. Benton, Adsorption and catalysis in carbon monoxide oxidation, J. Am. Chem. Soc. 45 (1923) 900–907.

[197] M.I. Brittan, H. Bliss, C.A. Walker, Kinetics of the Hopcalite-catalyzed oxidation of carbon monoxide, AIChE J. 16 (1970) 305–314.

[198] G.M. Schwab, S.B. Kanungo, Die katalytische Verstärkung im Hopcalit , Zeitschrift Für Phys. Chemie . 107(1) (1977) 109-120.

[199] S. Vepřek, D.L. Cocke, S. Kehl, H.R. Oswald, Mechanism of the deactivation of Hopcalite catalysts studied by XPS, ISS, and other techniques, J. Catal. 100 (1986) 250–263.

[200] D.L. Cocke, S. Vepřek, First direct evidence of a solid state charge transfer redox system $Cu^{+2} + Mn^{3+} \leftrightharpoons Cu^{1+} + Mn^{4+}$ in copper manganese oxide, Solid State Commun. 57 (1986) 745–748.

[201] C.R. Henry, Surface studies of supported model catalysts, Surf. Sci. Rep. 31 (1998) 231–325.

[202] B.K. Min, C.M. Friend, Heterogeneous Gold-Based Catalysis for Green Chemistry: Low-Temperature CO Oxidation and Propene Oxidation, Chem. Rev. 107 (2007) 2709–2724.

[203] F. Zaera, Nanostructured materials for applications in heterogeneous catalysis, Chem. Soc. Rev. 42 (2013) 2746–2762.

[204] T. Engel, G. Ertl, Elementary Steps in the Catalytic Oxidation of Carbon Monoxide on Platinum Metals, in: D.D. Eley, H. Pines, P.B.B.T.-A. in C. Weez (Eds.), Academic Press, 1979: pp. 1–78.

[205] R.G.B.T.-C.C.K. Compton, ed., Chapter 6 Studies of Kinetic Models for Oxidation Reactions over Metals (Exemplified by CO Oxidation), in: Kinet. Model. Catal. React., Elsevier, 1991: pp. 311–360.

[206] M. Kipnis, E. Volnina, New approaches to preferential CO oxidation over noble metals, Appl. Catal. B Environ. 98 (2010) 193–203.

[207] K. Liu, A. Wang, T. Zhang, Recent Advances in Preferential Oxidation of CO Reaction over Platinum Group Metal Catalysts, ACS Catal. 2 (2012) 1165–1178.

[208] S.H. Oh, R.M. Sinkevitch, Carbon Monoxide Removal from Hydrogen-Rich Fuel Cell Feedstreams by Selective Catalytic Oxidation, J. Catal. 142 (1993) 254–262.

[209] F. Mariño, C. Descorme, D. Duprez, Noble metal catalysts for the preferential oxidation of carbon monoxide in the presence of hydrogen (PROX), Appl. Catal. B Environ. 54 (2004) 59–66.

[210] M.J. Kahlich, H. Gasteiger, R.J. Behm, Kinetics of the Selective CO Oxidation in H_2-Rich Gas on Pt/Al_2O_3, J. Catal. 171 (1997) 93–105.

[211] Y. Gao, W. Wang, S. Chang, W. Huang, Morphology Effect of CeO_2 Support in the Preparation, Metal–Support Interaction, and Catalytic Performance of Pt/CeO_2 Catalysts, ChemCatChem. 5 (2013) 3610–3620.

[212] I. Miguel-García, Á. Berenguer-Murcia, D. Cazorla-Amorós, Preferential

Universitat d'Alacant
Universidad de Alicante

oxidation of CO catalyzed by supported polymer-protected palladium-based nanoparticles, Appl. Catal. B Environ. 98 (2010) 161–170.

[213] C. Galletti, S. Specchia, G. Saracco, V. Specchia, Catalytic Performance of Rhodium-Based Catalysts for CO Preferential Oxidation in H_2-Rich Gases, Ind. Eng. Chem. Res. 47 (2008) 5304–5312.

[214] Y. Huang, A. Wang, X. Wang, T. Zhang, Preferential oxidation of CO under excess H_2 conditions over iridium catalysts, Int. J. Hydrogen Energy. 32 (2007) 3880–3886.

[215] Y.-F. Han, M.J. Kahlich, M. Kinne, R.J. Behm, Kinetic study of selective CO oxidation in H_2-rich gas on a Ru/γ-Al_2O_3 catalyst, Phys. Chem. Chem. Phys. 4 (2002) 389–397.

[216] S. Chin, O. Alexeev, M. Amiridis, Preferential oxidation of CO under excess H_2 conditions over Ru catalysts, Appl. Catal. A Gen. 286 (2005) 157–166.

[217] S. Alayoglu, B. Eichhorn, Rh−Pt Bimetallic Catalysts: Synthesis, Characterization, and Catalysis of Core−Shell, Alloy, and Monometallic Nanoparticles, J. Am. Chem. Soc. 130 (2008) 17479–17486.

[218] H. Zhang, M. Jin, H. Liu, J. Wang, M.J. Kim, D. Yang, Z. Xie, J. Liu, Y. Xia, Facile Synthesis of Pd–Pt Alloy Nanocages and Their Enhanced Performance for Preferential Oxidation of CO in Excess Hydrogen, ACS Nano. 5 (2011) 8212–8222.

[219] S. Alayoglu, A.U. Nilekar, M. Mavrikakis, B. Eichhorn, Ru–Pt core–shell nanoparticles for preferential oxidation of carbon monoxide in hydrogen, Nat. Mater. 7 (2008) 333-338.

[220] A.U. Nilekar, S. Alayoglu, B. Eichhorn, M. Mavrikakis, Preferential CO Oxidation in Hydrogen: Reactivity of Core−Shell Nanoparticles, J. Am. Chem. Soc. 132 (2010) 7418–7428.

[221] M. Watanabe, H. Uchida, K. Ohkubo, H. Igarashi, Hydrogen purification for fuel cells: selective oxidation of carbon monoxide on Pt–Fe/zeolite catalysts, Appl. Catal. B Environ. 46 (2003) 595–600.

[222] P. Chin, X. Sun, G.W. Roberts, J.J. Spivey, Preferential oxidation of carbon monoxide with iron-promoted platinum catalysts supported on metal foams, Appl. Catal. A Gen. 302 (2006) 22–31.

[223] M.M. Schubert, M.J. Kahlich, G. Feldmeyer, M. Hüttner, S. Hackenberg, H. a. Gasteiger, R.J. Behm, Bimetallic PtSn catalyst for selective CO oxidation in H_2-rich gases at low temperatures, Phys. Chem. Chem. Phys. 3 (2001) 1123–1131.

[224] C. Pedrero, T. Waku, E. Iglesia, Oxidation of CO in H_2–CO mixtures catalyzed by platinum: alkali effects on rates and selectivity, J. Catal. 233 (2005) 242–255.

[225] H. Tanaka, M. Kuriyama, Y. Ishida, S. Ito, K. Tomishige, K. Kunimori, Preferential CO oxidation in hydrogen-rich stream over Pt catalysts modified with alkali metals: Part I. Catalytic performance, Appl. Catal. A Gen. 343 (2008) 117–124.

[226] M. Kipnis, Gold in CO oxidation and PROX: The role of reaction exothermicity and nanometer-scale particle size, Appl. Catal. B Environ. 152–153 (2014) 38-45.

[227] R.J.H. Grisel, B.E. Nieuwenhuys, Selective Oxidation of CO, over Supported Au Catalysts, J. Catal. 199 (2001) 48–59.

[228] S. Ivanova, V. Pitchon, C. Petit, V. Caps, Support Effects in the Gold-Catalyzed Preferential Oxidation of CO, ChemCatChem. 2 (2010) 556–563.

Universitat d'Alacant
Universidad de Alicante

[229] M. Haruta, Size- and support-dependency in the catalysis of gold, Catal. Today. 36 (1997) 153–166.

[230] P. Lakshmanan, J.E. Park, E.D. Park, Recent Advances in Preferential Oxidation of CO in H_2 Over Gold Catalysts, Catal. Surv. from Asia. 18 (2014) 75-88.

[231] M. Kipnis, E. Volnina, H_2 oxidation and preferential CO oxidation over Au: New approaches, Appl. Catal. B Environ. 103 (2011) 39–47.

[232] B. Schumacher, Y. Denkwitz, V. Plzak, M. Kinne, R.J. Behm, Kinetics, mechanism, and the influence of H_2 on the CO oxidation reaction on a Au/TiO_2 catalyst, J. Catal. 224 (2004) 449–462.

[233] Y. Denkwitz, B. Schumacher, G. Kučerová, R.J. Behm, Activity, stability, and deactivation behavior of supported Au/TiO_2 catalysts in the CO oxidation and preferential CO oxidation reaction at elevated temperatures, J. Catal. 267 (2009) 78–88.

[234] T. Shodiya, O. Schmidt, W. Peng, N. Hotz, Novel nano-scale $Au/\alpha\text{-}Fe_2O_3$ catalyst for the preferential oxidation of CO in biofuel reformate gas, J. Catal. 300 (2013) 63–69.

[235] M.J. Kahlich, H.A. Gasteiger, R.J. Behm, Kinetics of the Selective Low-Temperature Oxidation of CO in H_2-Rich Gas over $Au/\alpha\text{-}Fe_2O_3$, J. Catal. 182 (1999) 430–440.

[236] E. Quinet, F. Morfin, F. Diehl, P. Avenier, V. Caps, J.-L. Rousset, Hydrogen effect on the preferential oxidation of carbon monoxide over alumina-supported gold nanoparticles, Appl. Catal. B Environ. 80 (2008) 195–201.

[237] M. Lomello-Tafin, A.A. Chaou, F. Morfin, V. Caps, J.-L. Rousset, Preferential oxidation of CO in H_2 over highly loaded Au/ZrO_2 catalysts obtained by direct oxidation of bulk alloy, Chem. Commun. 3 (2005) 388–390.

[238] O.H. Laguna, F. Romero Sarria, M.A. Centeno, J.A. Odriozola, Gold supported on metal-doped ceria catalysts (M=Zr, Zn and Fe) for the preferential oxidation of CO (PROX), J. Catal. 276 (2010) 360–370.

[239] G. Avgouropoulos, M. Manzoli, F. Boccuzzi, T. Tabakova, J. Papavasiliou, T. Ioannides, V. Idakiev, Catalytic performance and characterization of Au/doped-ceria catalysts for the preferential CO oxidation reaction, J. Catal. 256 (2008) 237–247.

[240] L. Ilieva, G. Pantaleo, I. Ivanov, R. Zanella, A.M. Venezia, D. Andreeva, A comparative study of differently prepared rare earths-modified ceria-supported gold catalysts for preferential oxidation of CO, Int. J. Hydrogen Energy. 34 (2009) 6505–6515.

[241] G.C. Bond, C. Louis, D.T. Thompson, Catalysis by Gold, Published by Imperial College Press and distributed by World Scientific Publishing CO., 2006.

[242] D. Li, X. Liu, Q. Zhang, Y. Wang, H. Wan, Cobalt and Copper Composite Oxides as Efficient Catalysts for Preferential Oxidation of CO in H_2-Rich Stream, Catal. Letters. 127 (2009) 377–385.

[243] G. Avgouropoulos, T. Ioannides, H.K. Matralis, J. Batista, S. Hocevar, $CuO–CeO_2$ mixed oxide catalysts for the selective oxidation of carbon monoxide in excess hydrogen, Catal. Letters. 73 (2001) 33–40.

[244] G. Avgouropoulos, T. Ioannides, C. Papadopoulou, J. Batista, S. Hocevar, H.K. Matralis, A comparative study of $Pt/\gamma\text{-}Al_2O_3$, $Au/\alpha\text{-}Fe_2O_3$ and $CuO\text{-}CeO_2$ catalysts for the selective oxidation of carbon monoxide in excess hydrogen, Catal. Today. 75 (2002) 157-167.

Universitat d'Alacant
Universidad de Alicante

[245] Y.I. Hasegawa, R.U. Maki, M. Sano, T. Miyake, Preferential oxidation of CO on copper-containing manganese oxides, Appl. Catal. A Gen. 371 (2009) 67–72.

[246] Z. Zhao, M.M. Yung, U.S. Ozkan, Effect of support on the preferential oxidation of CO over cobalt catalysts, Catal. Commun. 9 (2008) 1465–1471.

[247] X. Xie, Y. Li, Z.-Q. Liu, M. Haruta, W. Shen, Low-temperature oxidation of CO catalysed by Co_3O_4 nanorods, Nature. 458 (2009) 746.

[248] Y. Liu, Q. Fu, M.F. Stephanopoulos, Preferential oxidation of CO in H_2 over CuO-CeO_2 catalysts, Catal. Today. 93–95 (2004) 241–246.

[249] I. López, T. Valdés-Solís, G. Marbán, An attempt to rank copper-based catalysts used in the CO-PROX reaction, Int. J. Hydrogen Energy. 33 (2008) 197–205.

[250] J.S. Elias, K.A. Stoerzinger, W.T. Hong, M. Risch, L. Giordano, A.N. Mansour, Y. Shao-Horn, In Situ Spectroscopy and Mechanistic Insights into CO Oxidation on Transition-Metal-Substituted Ceria Nanoparticles, ACS Catal. 7 (2017) 6843–6857.

[251] A. Hornés, A.B. Hungría, P. Bera, A. López Cámara, M. Fernández-García, A. Martínez-Arias, L. Barrio, M. Estrella, G. Zhou, J.J. Fonseca, J.C. Hanson, J.A. Rodriguez, Inverse CeO_2/CuO catalyst as an alternative to classical direct configurations for preferential oxidation of CO in hydrogen-rich stream., J. Am. Chem. Soc. 132 (2010) 34–35.

[252] E.-Y. Ko, E.D. Park, K.W. Seo, H.C. Lee, D. Lee, S. Kim, A comparative study of catalysts for the preferential CO oxidation in excess hydrogen, Catal. Today. 116 (2006) 377–383.

[253] N. Bion, F. Epron, M. Moreno, F. Mariño, D. Duprez, Preferential oxidation of carbon monoxide in the presence of hydrogen (PROX) over noble metals and transition metal oxides: Advantages and drawbacks, Top. Catal. 51 (2008) 76–88.

[254] J. Beckers, G. Rothenberg, Sustainable selective oxidations using ceria-based materials, Green Chem. 12 (2010) 939-948.

[255] D. Gamarra, A. Hornés, Z. Koppány, Z. Schay, G. Munuera, J. Soria, A. Martínez-Arias, Catalytic processes during preferential oxidation of CO in H_2-rich streams over catalysts based on copper–ceria, J. Power Sources. 169 (2007) 110–116.

[256] D. Gamarra, G. Munuera, A.B. Hungria, M. Fernandez-Garcia, J.C. Conesa, P.A. Midgley, X.Q. Wang, J.C. Hanson, J.A. Rodriguez, A. Martinez-Arias, Structure-Activity Relationship in Nanostructured Copper-Ceria-Based Preferential CO Oxidation Catalysts, J. Phys. Chem. C. 111 (2007) 11026–11038.

[257] D. Delimaris, T. Ioannides, VOC oxidation over CuO–CeO_2 catalysts prepared by a combustion method, Appl. Catal. B Environ. 89 (2009) 295–302.

[258] X. Qi, M. Flytzani-Stephanopoulos, Activity and Stability of Cu−CeO_2 Catalysts in High-Temperature Water−Gas Shift for Fuel-Cell Applications, Ind. Eng. Chem. Res. 43 (2004) 3055–3062.

[259] J.A. Rodriguez, J. Graciani, J. Evans, J.B. Park, F. Yang, D. Stacchiola, S.D. Senanayake, S. Ma, M. Pérez, P. Liu, J.F. Sanz, J. Hrbek, Water-Gas Shift Reaction on a Highly Active Inverse CeO_x/Cu(111) Catalyst: Unique Role of Ceria Nanoparticles, Angew. Chemie Int. Ed. 48 (2009) 8047–8050.

[260] X. Tang, B. Zhang, Y. Li, Y. Xu, Q. Xin, W. Shen, Carbon monoxide oxidation over CuO/CeO_2 catalysts, Catal. Today. 93–95 (2004) 191–198.

[261] A. Gómez-Cortés, Y. Márquez, J. Arenas-Alatorre, G. Díaz, Selective CO oxidation in excess of H_2 over high-surface area CuO/CeO_2 catalysts, Catal. Today. 133–135 (2008) 743–749.

[262] G. Bonura, F. Arena, G. Mezzatesta, C. Cannilla, L. Spadaro, F. Frusteri, Role of the ceria promoter and carrier on the functionality of Cu-based catalysts in the CO_2-to-methanol hydrogenation reaction, Catal. Today. 171 (2011) 251–256.

[263] A. Bueno-López, Diesel soot combustion ceria catalysts, Appl. Catal. B Environ. 146 (2014) 1–11.

[264] L. Chen, Z. Si, X. Wu, D. Weng, DRIFT Study of $CuO–CeO_2–TiO_2$ Mixed Oxides for NO_x Reduction with NH_3 at Low Temperatures, ACS Appl. Mater. Interfaces. 6 (2014) 8134–8145.

[265] M. Lykaki, E. Papista, S.A.C. Carabineiro, P.B. Tavares, M. Konsolakis, Optimization of N_2O decomposition activity of $CuO–CeO_2$ mixed oxides by means of synthesis procedure and alkali (Cs) promotion, Catal. Sci. Technol. 8 (2018) 2312–2322.

[266] A. Martínez-Arias, M. Fernández-García, J. Soria, J.C. Conesa, Spectroscopic study of a Cu/CeO_2 catalyst subjected to redox treatments in carbon monoxide and oxygen, J. Catal. 182 (1999) 367–377.

[267] E. Aneggi, M. Boaro, C. de Leitenburg, G. Dolcetti, A. Trovarelli, Insights into the redox properties of ceria-based oxides and their implications in catalysis, J. Alloys Compd. 408–412 (2006) 1096–1102.

[268] A. Martínez-Arias, D. Gamarra, M. Fernández-García, A. Hornés, C. Belver, Spectroscopic Study on the Nature of Active Entities in Copper–Ceria CO-PROX Catalysts, Top. Catal. 52 (2009) 1425–1432.

[269] A. Trovarelli, Catalytic Properties of Ceria and CeO_2-Containing Materials, Catal. Rev. 38 (1996) 439–520.

[270] W.-W. Wang, W.-Z. Yu, P.-P. Du, H. Xu, Z. Jin, R. Si, C. Ma, S. Shi, C.-J. Jia, C.-H. Yan, Crystal Plane Effect of Ceria on Supported Copper Oxide Cluster Catalyst for CO Oxidation: Importance of Metal–Support Interaction, ACS Catal. 7 (2017) 1313–1329.

[271] G. Avgouropoulos, T. Ioannides, H. Matralis, Influence of the preparation method on the performance of $CuO–CeO_2$ catalysts for the selective oxidation of CO, Appl. Catal. B Environ. 56 (2005) 87–93.

[272] D. Gamarra, G. Munuera, A.B. Hungría, M. Ferna, A Martínez-Arias, Structure - Activity Relationship in Nanostructured Copper - Ceria-Based Preferential CO Oxidation Catalysts, J. Phys. Chem. C. 111 (2007) 11026–11038.

[273] A. Trovarelli, M. Boaro, E. Rocchini, C. de Leitenburg, G. Dolcetti, Some recent developments in the characterization of ceria-based catalysts, J. Alloys Compd. 323–324 (2001) 584–591.

[274] A. Trovarelli, Catalytic Properties of Ceria and CeO_2-Containing Materials, Catal. Rev. 38 (1996) 439–520.

[275] J.A. Cecilia, A. Arango-Díaz, V. Rico-Pérez, A. Bueno-López, E. Rodríguez-Castellón, The influence of promoters (Zr, La, Tb, Pr) on the catalytic performance of $CuO-CeO_2$ systems for the preferential oxidation of CO in the presence of CO_2 and H_2O, Catal. Today. 253 (2015) 115–125.

Universitat d'Alacant
Universidad de Alicante

[276] C.S. Polster, H. Nair, C.D. Baertsch, Study of active sites and mechanism responsible for highly selective CO oxidation in H_2 rich atmospheres on a mixed Cu and Ce oxide catalyst, J. Catal. 266 (2009) 308–319.

[277] G. Sedmak, S. Hočevar, J. Levec, Kinetics of selective CO oxidation in excess of H_2 over the nanostructured $Cu0.1Ce_{0.9}O_{2-y}$ catalyst, J. Catal. 213 (2003) 135–150.

[278] A. Martínez-Arias, D. Gamarra, A. Hungría, M. Fernández-García, G. Munuera, A. Hornés, P. Bera, J. Conesa, A. Cámara, Characterization of Active Sites/Entities and Redox/Catalytic Correlations in Copper-Ceria-Based Catalysts for Preferential Oxidation of CO in H_2-Rich Streams, Catalysts. 3 (2013) 378–400.

[279] T. Caputo, L. Lisi, R. Pirone, G. Russo, On the role of redox properties of CuO/CeO_2 catalysts in the preferential oxidation of CO in H_2-rich gases, Appl. Catal. A Gen. 348 (2008) 42–53.

[280] H. Zou, X. Dong, W. Lin, Selective CO oxidation in hydrogen-rich gas over CuO/CeO_2 catalysts, Appl. Surf. Sci. 253 (2006) 2893–2898.

[281] M. Monte, G. Munuera, D. Costa, J.C. Conesa, A. Martínez-Arias, Near-ambient XPS characterization of interfacial copper species in ceria-supported copper catalysts., Phys. Chem. Chem. Phys. 17 (2015) 29995–30004.

[282] D. Gamarra, A.L. Cámara, M. Monte, S.B. Rasmussen, L.E. Chinchilla, A.B. Hungría, G. Munuera, N. Gyorffy, Z. Schay, V.C. Corberán, J.C. Conesa, A. Martínez-Arias, Preferential oxidation of CO in excess H_2 over CuO/CeO_2 catalysts: Characterization and performance as a function of the exposed face present in the CeO_2 support, Appl. Catal. B Environ. 130–131 (2013) 224–238.

[283] X. Guo, R. Zhou, Identification of the nano/micro structure of CeO_2(rod) and the essential role of interfacial copper-ceria interaction in CuCe(rod) for selective oxidation of CO in H_2-rich streams, J. Power Sources. 361 (2017) 39–53.

[284] D. Gamarra, C. Belver, M. Fernández-García, A. Martínez-Arias, Selective CO Oxidation in Excess H_2 over Copper−Ceria Catalysts: Identification of Active Entities/Species, J. Am. Chem. Soc. 129 (2007) 12064–12065.

[285] Y. Fu, Y. Tian, P. Lin, A low-temperature IR spectroscopic study of selective adsorption of NO and CO on $CuO/\gamma\text{-}Al_2O_3$, J. Catal. 132 (1991) 85–91.

[286] R. Kydd, D. Ferri, P. Hug, J. Scott, W.Y. Teoh, R. Amal, Temperature-induced evolution of reaction sites and mechanisms during preferential oxidation of CO, J. Catal. 277 (2011) 64–71.

[287] M. Monte, D. Gamarra, a. López Cámara, S.B. Rasmussen, N. Gyorffy, Z. Schay, a. Martínez-Arias, J.C. Conesa, Preferential oxidation of CO in excess H_2 over CuO/CeO_2 catalysts: Performance as a function of the copper coverage and exposed face present in the CeO_2 support, Catal. Today. 229 (2014) 104–113.

[288] S. Yao, K. Mudiyanselage, W. Xu, A.C. Johnston-Peck, J.C. Hanson, T. Wu, D. Stacchiola, J.A. Rodriguez, H. Zhao, K.A. Beyer, K.W. Chapman, P.J. Chupas, A. Martínez-Arias, R. Si, T.B. Bolin, W. Liu, S.D. Senanayake, Unraveling the Dynamic Nature of a CuO/CeO_2 Catalyst for CO Oxidation in Operando: A Combined Study of XANES (Fluorescence) and DRIFTS, ACS Catal. 4 (2014) 1650–1661.

[289] F. Mariño, C. Descorme, D. Duprez, Supported base metal catalysts for the preferential oxidation of carbon monoxide in the presence of excess hydrogen (PROX), Appl. Catal. B Environ. 58 (2005) 175–183.

[290] A. Martínez-Arias, A. B. Hungría, G. Munuera, D. Gamarra, Preferential oxidation of CO in rich H_2 over CuO/CeO_2: Details of selectivity and deactivation under the reactant stream, Appl. Catal. B Environ. 65 (2006) 207–216.

[291] L. Yang, S. Zhou, T. Ding, M. Meng, Superior catalytic performance of non-stoichiometric solid solution $Ce_{1-x}Cu_xO_{2-\delta}$ supported copper catalysts used for CO preferential oxidation, Fuel Process. Technol. 124 (2014) 155–164.

[292] A. Davó-Quiñonero, M. Navlani-García, D. Lozano-Castelló, A. Bueno-López, J.A. Anderson, Role of Hydroxyl Groups in the Preferential Oxidation of CO over Copper Oxide-Cerium Oxide Catalysts, ACS Catal. 6 (2016) 1723-1731.

[293] A. Di Benedetto, G. Landi, L. Lisi, CO reactive adsorption at low temperature over CuO/CeO_2 structured catalytic monolith, Int. J. Hydrogen Energy. 42 (2017) 12262–12275.

[294] J. Zheng, W. Sheng, Z. Zhuang, B. Xu, Y. Yan, Universal dependence of hydrogen oxidation and evolution reaction activity of platinum-group metals on pH and hydrogen binding energy, Sci. Adv. 2 (2016) 1501602-1501610.

[295] M. Nolan, Charge transfer and formation of reduced Ce^{3+} upon adsorption of metal atoms at the ceria (110) surface, J. Chem. Phys. 136 (2012) 134703-134712.

[296] L. Szabová, M.F. Camellone, M. Huang, V. Matolín, S. Fabris, Thermodynamic, electronic and structural properties of Cu/CeO_2 surfaces and interfaces from first-principles DFT+U calculations, J. Chem. Phys. 133 (2010) 234705-234716.

[297] Y. Tang, H. Zhang, L. Cui, C. Ouyang, S. Shi, W. Tang, H. Li, L. Chen, Electronic states of metal (Cu, Ag, Au) atom on CeO_2(111) surface: The role of local structural distortion, J. Power Sources. 197 (2012) 28–37.

[298] M. Nolan, Enhanced oxygen vacancy formation in ceria (111) and (110) surfaces doped with divalent cations, J. Mater. Chem. 21 (2011) 9160–9168.

[299] Z. Yang, B. He, Z. Lu, K. Hermansson, Physisorbed, Chemisorbed, and Oxidized CO on Highly Active $Cu{-}CeO_2$(111), J. Phys. Chem. C. 114 (2010) 4486–4494.

[300] L. Cui, Y. Tang, H. Zhang, L.G. Hector, C. Ouyang, S. Shi, H. Li, L. Chen, First-principles investigation of transition metal atom M (M = Cu, Ag, Au) adsorption on CeO_2(110), Phys. Chem. Chem. Phys. 14 (2012) 1923–1933.

[301] Y. Xie, J. Wu, G. Jing, H. Zhang, S. Zeng, X. Tian, X. Zou, J. Wen, H. Su, C.-J. Zhong, P. Cui, Structural origin of high catalytic activity for preferential CO oxidation over CuO/CeO_2 nanocatalysts with different shapes, Appl. Catal. B Environ. 239 (2018) 665–676.

[302] K. Zhou, X. Wang, X. Sun, Q. Peng, Y. Li, Enhanced catalytic activity of ceria nanorods from well-defined reactive crystal planes, J. Catal. 229 (2005) 206–212.

[303] M. Lykaki, E. Pachatouridou, S.A.C. Carabineiro, E. Iliopoulou, C. Andriopoulou, N. Kallithrakas-Kontos, S. Boghosian, M. Konsolakis, Ceria nanoparticles shape effects on the structural defects and surface chemistry: Implications in CO oxidation by Cu/CeO_2 catalysts, Appl. Catal. B Environ. 230 (2018) 18–28.

[304] N. Ta, J. Liu, W. Shen, Tuning the shape of ceria nanomaterials for catalytic applications, Chinese J. Catal. 34 (2013) 838–850.

Universitat d'Alacant
Universidad de Alicante

[305] E. Aneggi, D. Wiater, C. de Leitenburg, J. Llorca, A. Trovarelli, Shape-Dependent Activity of Ceria in Soot Combustion, ACS Catal. 4 (2014) 172–181.

[306] E. Aneggi, C. de Leitenburg, A. Trovarelli, On the role of lattice/surface oxygen in ceria–zirconia catalysts for diesel soot combustion, Catal. Today. 181 (2012) 108–115.

[307] A. Martínez-Arias, A.B. Hungría, M. Fernández-García, J.C. Conesa, G. Munuera, Preferential oxidation of CO in a H_2-rich stream over CuO/CeO_2 and $CuO/(Ce,M)O_x$ (M=Zr, Tb) catalysts, J. Power Sources. 151 (2005) 32–42.

[308] Q. Liang, X. Wu, D. Weng, Z. Lu, Selective oxidation of soot over Cu doped ceria/ceria–zirconia catalysts, Catal. Commun. 9 (2008) 202–206.

[309] J. Roggenbuck, H. Schäfer, T. Tsoncheva, C. Minchev, J. Hanss, M. Tiemann, Mesoporous CeO_2: Synthesis by nanocasting, characterisation and catalytic properties, Microporous Mesoporous Mater. 101 (2007) 335–341.

[310] C. Ho, J.C. Yu, T. Kwong, A.C. Mak, S. Lai, Morphology-Controllable Synthesis of Mesoporous CeO_2 Nano- and Microstructures, Chem. Mater. 17 (2005) 4514–4522.

[311] W. Shen, X. Dong, Y. Zhu, H. Chen, J. Shi, Mesoporous CeO_2 and CuO-loaded mesoporous CeO_2: Synthesis, characterization, and CO catalytic oxidation property, Microporous Mesoporous Mater. 85 (2005) 157–162.

[312] Y. Zhang, H. Liang, X.Y. Gao, Y. Liu, Three-dimensionally ordered macro-porous $CuO–CeO_2$ used for preferential oxidation of carbon monoxide in hydrogen-rich gases, Catal. Commun. 10 (2009) 1432–1436.

[313] A. Stein, R.C. Schroden, Colloidal crystal templating of three-dimensionally ordered macroporous solids: materials for photonics and beyond, Curr. Opin. Solid State Mater. Sci. 5 (2001) 553–564.

[314] H. Yan, C.F. Blanford, B.T. Holland, W.H. Smyrl, A. Stein, General Synthesis of Periodic Macroporous Solids by Templated Salt Precipitation and Chemical Conversion, Chem. Mater. 12 (2000) 1134–1141.

[315] A. Davó-Quiñonero, J. González-Mira, I. Such-Basañez, J. Juan-Juan, D. Lozano-Castelló, A. Bueno-López, Improved CO oxidation activity of 3DOM Pr-doped ceria catalysts: Something other than an ordered macroporous structure, Catalysts. 7 (2017) 67-79.

[316] V. Alcalde-Santiago, A. Davó-Quiñonero, D. Lozano-Castelló, A. Bueno-López, On the soot combustion mechanism using 3DOM ceria catalysts, Appl. Catal. B Environ. 234 (2018) 187-197.

[317] Forecast of cerium oxide price globally 2009-2025, (n.d.). https://www.statista.com/statistics/450146/global-reo-cerium-oxide-price-forecast/.

[318] Alumina Price Outlook. Forus Economics., (2019). https://www.focus-economics.com/commodities/base-metals/alumina.

[319] Titanium dioxide prices, markets & analysis. ICIS Price Forecast Reports, 2019.

[320] G. Charalampides, K.I. Vatalis, B. Apostoplos, B. Ploutarch-Nikolas, Rare Earth Elements: Industrial Applications and Economic Dependency of Europe, Procedia Econ. Financ. 24 (2015) 126–135.

[321] I. Borges de Lima, Chapter 19 - Rare Earths Industry and Eco-management: A Critical Review of Recycling and Substitutes, in: I. Borges De Lima, W.B.T.-R.E.I. Leal Filho (Eds.), Elsevier, Boston, 2016: pp. 293–304.

[322] B. Zhou, Z. Li, C. Chen, Global Potential of Rare Earth Resources and Rare Earth Demand from Clean Technologies, Miner. 7(11) (2017) 203-217.

[323] S.A. Abdelnour, M.E. Abd El-Hack, A.F. Khafaga, A.E. Noreldin, M. Arif, M.T. Chaudhry, C. Losacco, A. Abdeen, M.M. Abdel-Daim, Impacts of rare earth elements on animal health and production: Highlights of cerium and lanthanum, Sci. Total Environ. 672 (2019) 1021–1032.

[324] S. Massari, M. Ruberti, Rare earth elements as critical raw materials: Focus on international markets and future strategies, Resour. Policy. 38 (2013) 36–43.

[325] S. Chu, US Department of Energy, Critical materials strategy report, 2011.

[326] N.T. Nassar, X. Du, T.E. Graedel, Criticality of the Rare Earth Elements, J. Ind. Ecol. 19 (2015) 1044–1054.

[327] J.E. Post, Manganese oxide minerals: Crystal structures and economic and environmental significance, Proc. Natl. Acad. Sci. 96 (1999) 3447-3454.

[328] N. Duan, S.L. Suib, C.-L. O'Young, Sol–gel synthesis of cryptomelane, an octahedral molecular sieve, J. Chem. Soc. Chem. Commun. (1995) 1367–1368.

[329] R.N. DeGuzman, Y.F. Shen, E.J. Neth, S.L. Suib, C.L. O'Young, S. Levine, J.M. Newsam, Synthesis and characterization of Octahedral Molecular Sieves (OMS-2) having the hollandite structure, Chem. Mater. 6 (1994) 815–821.

[330] S. Ching, J.L. Roark, N. Duan, S.L. Suib, Sol−Gel Route to the Tunneled Manganese Oxide Cryptomelane, Chem. Mater. 9 (1997) 750–754.

[331] C.H. Chen, S.L. Suib, Control of catalytic activity via porosity, chemical composition, and morphology of nanostructured porous manganese oxide materials, J. Chinese Chem. Soc. 59 (2012) 465–472.

[332] J. Luo, Q. Zhang, J. Garcia-Martinez, S.L. Suib, Adsorptive and acidic properties, reversible lattice oxygen evolution, and catalytic mechanism of cryptomelane-type manganese oxides as oxidation catalysts, J. Am. Chem. Soc. 130 (2008) 3198–3207.

[333] H.C. Genuino, S. Dharmarathna, E.C. Njagi, M.C. Mei, S.L. Suib, Gas-Phase Total Oxidation of Benzene, Toluene, Ethylbenzene, and Xylenes Using Shape-Selective Manganese Oxide and Copper Manganese Oxide Catalysts, J. Phys. Chem. C. 116 (2012) 12066–12078.

[334] S. Ching, D.A. Kriz, K.M. Luthy, E.C. Njagi, S.L. Suib, Self-assembly of manganese oxide nanoparticles and hollow spheres. Catalytic activity in carbon monoxide oxidation, Chem. Commun. 47 (2011) 8286–8288.

[335] A. Iyer, J. Del-Pilar, C.K. King'ondu, E. Kissel, H.F. Garces, H. Huang, A.M. El-Sawy, P.K. Dutta, S.L. Suib, Water Oxidation Catalysis using Amorphous Manganese Oxides, Octahedral Molecular Sieves (OMS-2), and Octahedral Layered (OL-1) Manganese Oxide Structures, J. Phys. Chem. C. 116 (2012) 6474–6483.

[336] N. Subramanian, B. Viswanathan, T.K. Varadarajan, A facile, morphology-controlled synthesis of potassium-containing manganese oxide nanostructures for electrochemical supercapacitor application, RSC Adv. 4 (2014) 33911–33922.

[337] A.S. Poyraz, J. Huang, L. Wu, D.C. Bock, Y. Zhu, A.C. Marschilok, K.J. Takeuchi, E.S. Takeuchi, Potassium-Based α-Manganese Dioxide Nanofiber Binder-Free Self-Supporting Electrodes: A Design Strategy for High Energy Density Batteries, Energy Technol. 4 (2016) 1358–1368.

[338] R.N. De Guzman, A. Awaluddin, Y.-F. Shen, Z.R. Tian, S.L. Suib, S. Ching, C.-L. O'Young, Electrical Resistivity Measurements on Manganese Oxides with Layer and Tunnel Structures: Birnessites, Todorokites, and Cryptomelanes, Chem. Mater. 7 (1995) 1286–1292.

[339] J. Luo, Q. Zhang, A. Huang, S.L. Suib, Total oxidation of volatile organic compounds with hydrophobic cryptomelane-type octahedral molecular sieves, Microporous Mesoporous Mater. 35–36 (2000) 209–217.

[340] Y. Ding, X. Shen, S. Sithambaram, S. Gomez, R. Kumar, V.M.B. Crisostomo, S.L. Suib, M. Aindow, Synthesis and Catalytic Activity of Cryptomelane-Type Manganese Dioxide Nanomaterials Produced by a Novel Solvent-Free Method, Chem. Mater. 17 (2005) 5382–5389.

[341] S.L. Suib, Porous Manganese Oxide Octahedral Molecular Sieves and Octahedral Layered Materials, Acc. Chem. Res. 41 (2008) 479–487.

[342] S.L. Suib, Structure, porosity, and redox in porous manganese oxide octahedral layer and molecular sieve materials, J. Mater. Chem. 18 (2008) 1623-1631.

[343] X. Shen, A.M. Morey, J. Liu, Y. Ding, J. Cai, J. Durand, Q. Wang, W. Wen, W.A. Hines, J.C. Hanson, J. Bai, A.I. Frenkel, W. Reiff, M. Aindow, S.L. Suib, Characterization of the Fe-Doped Mixed-Valent Tunnel Structure Manganese Oxide K-OMS-2, J. Phys. Chem. C. 115 (2011) 21610–21619.

[344] S. Sultana, Z. Ye, S.K.P. Veerapandian, A. Löfberg, N. De Geyter, R. Morent, J.-M. Giraudon, J.-F. Lamonier, Synthesis and catalytic performances of K-OMS-2, Fe/K-OMS-2 and Fe-K-OMS-2 in post plasma-catalysis for dilute TCE abatement, Catal. Today. 307 (2018) 20–28.

[345] M. Abecassis-Wolfovich, R. Jothiramalingam, M. V Landau, M. Herskowitz, B. Viswanathan, T.K. Varadarajan, Cerium incorporated ordered manganese oxide OMS-2 materials: Improved catalysts for wet oxidation of phenol compounds, Appl. Catal. B Environ. 59 (2005) 91–98.

[346] R. Jothiramalingam, B. Viswanathan, T.K. Varadarajan, Preparation, characterization and catalytic properties of cerium incorporated porous manganese oxide OMS-2 catalysts, Catal. Commun. 6 (2005) 41–45.

[347] Y. Li, Z. Fan, J. Shi, Z. Liu, J. Zhou, W. Shangguan, Modified manganese oxide octahedral molecular sieves M′-OMS-2 (M′=Co,Ce,Cu) as catalysts in post plasma-catalysis for acetaldehyde degradation, Catal. Today. 256 (2015) 178–185.

[348] P. Stelmachowski, A.H.A. Monteverde-Videla, T. Jakubek, A. Kotarba, S. Specchia, The Effect of Fe, Co, and Ni Structural Promotion of Cryptomelane (KMn_8O_{16}) on the Catalytic Activity in Oxygen Evolution Reaction, Electrocatalysis. 9 (2018) 762–769.

[349] W.Y. Hernández, M. A. Centeno, F. Romero-Sarria, S. Ivanova, M. Montes, J.A. Odriozola, Modified cryptomelane-type manganese dioxide nanomaterials for preferential oxidation of CO in the presence of hydrogen, Catal. Today. 157 (2010) 160–165.

[350] R. Kumar, N. Kushwaha, S. Pandey, R. Priya, J. Mittal, Superior NH_3 Sensor Using Ni Doped K-OMS-2 Nanofibers, IEEE Sens. J. 18 (2018) 956–961.

[351] J. Yang, H. Zhou, L. Wang, Y. Zhang, C. Chen, H. Hu, G. Li, Y. Zhang, Y. Ma, J. Zhang, Cobalt-Doped K-OMS-2 Nanofibers: A Novel and Efficient Water-Tolerant Catalyst for the Oxidation of Carbon Monoxide, ChemCatChem. 9 (2017) 1163–1167.

[352] L.R. Pahalagedara, S. Dharmarathna, C.K. King'ondu, M.N. Pahalagedara, Y.-T. Meng, C.-H. Kuo, S.L. Suib, Microwave-Assisted Hydrothermal Synthesis of α-MnO_2: Lattice Expansion via Rapid Temperature Ramping and Framework Substitution, J. Phys. Chem. C. 118 (2014) 20363–20373.

[353] G.G. Xia, Y.G. Yin, W.S. Willis, J.Y. Wang, S.L. Suib, Efficient stable catalysts for low temperature carbon monoxide oxidation, J. Catal. 185 (1999) 91–105.

[354] X. Chen, Y.-F. Shen, S.L. Suib, C.L. O'Young, Characterization of Manganese Oxide Octahedral Molecular Sieve (M−OMS-2) Materials with Different Metal Cation Dopants, Chem. Mater. 14 (2002) 940–948.

[355] H. Huang, Y. Meng, A. Labonte, A. Dobley, S.L. Suib, Large-Scale Synthesis of Silver Manganese Oxide Nanofibers and Their Oxygen Reduction Properties, J. Phys. Chem. C. 117 (2013) 25352–25359.

[356] M. Özacar, A.S. Poyraz, H.C. Genuino, C.-H. Kuo, Y. Meng, S.L. Suib, Influence of silver on the catalytic properties of the cryptomelane and Ag-hollandite types manganese oxides OMS-2 in the low-temperature CO oxidation, Appl. Catal. A Gen. 462–463 (2013) 64–74.

[357] M. Polverejan, J.C. Villegas, S.L. Suib, Higher Valency Ion Substitution into the Manganese Oxide Framework, J. Am. Chem. Soc. 126 (2004) 7774–7775.

[358] H.C. Genuino, Y. Meng, D.T. Horvath, C.H. Kuo, M.S. Seraji, A.M. Morey, R.L. Joesten, S.L. Suib, Enhancement of catalytic activities of octahedral molecular sieve manganese oxide for total and preferential co oxidation through vanadium ion framework substitution, ChemCatChem. 5 (2013) 2306–2317.

[359] X. Tang, J. Li, J. Hao, Significant enhancement of catalytic activities of manganese oxide octahedral molecular sieve by marginal amount of doping vanadium, Catal. Commun. 11 (2010) 871–875.

[360] W.Y. Hernández, M.A. Centeno, S. Ivanova, P. Eloy, E.M. Gaigneaux, J. a. Odriozola, Cu-modified cryptomelane oxide as active catalyst for CO oxidation reactions, Appl. Catal. B Environ. 123–124 (2012) 27–35.

[361] Y. Yang, J. Huang, S. Zhang, S. Wang, S. Deng, B. Wang, G. Yu, Catalytic removal of gaseous HCBz on Cu doped OMS: Effect of Cu location on catalytic performance, Appl. Catal. B Environ. 150–151 (2014) 167–178.

[362] A.L. Ramstad, Ø. Mikkelsen, Structural characterisation of copper-containing manganese oxide octahedral molecular sieve (Cu-OMS-2) materials by X-ray absorption spectroscopy and cyclic voltammetry, J. Mol. Struct. 697 (2004) 109–117.

[363] Y. Shen, Cu Containing Octahedral Molecular Sieves and Octahedral Layered Materials, J. Catal. 161 (1996) 115–122.

[364] E. Nicolas-Tolentino, Z.R. Tian, H. Zhou, G. Xia, S.L. Suib, Effects of Cu^{2+} ions on the structure and reactivity of todorokite- and cryptomelane-type manganese oxide octahedral molecular sieves, Chem. Mater. 11 (1999) 1733–1741.

[365] R. Kumar, J. Mittal, N. Kushwaha, B. V Rao, S. Pandey, C.-P. Liu, Room temperature carbon monoxide gas sensor using Cu doped OMS-2 nanofibers, Sensors Actuators B Chem. 266 (2018) 751–760.

[366] M. Sun, L. Yu, F. Ye, G. Diao, Q. Yu, Z. Hao, Y. Zheng, L. Yuan, Transition metal doped cryptomelane-type manganese oxide for low-temperature catalytic combustion of dimethyl ether, Chem. Eng. J. 220 (2013) 320–327.

[367] Y.G. Yin, W.Q. Xu, R. DeGuzman, S.L. Suib, C.L. O'Young, Studies of stability and reactivity of synthetic cryptomelane-like manganese oxide octahedral molecular sieves, Inorg. Chem. 33 (1994) 4384-4389.

[368] C.K. King'ondu, N. Opembe, C. Chen, K. Ngala, H. Huang, A. Iyer, H.F. Garcés, S.L. Suib, Manganese Oxide Octahedral Molecular Sieves (OMS-2) Multiple Framework Substitutions: A New Route to OMS-2 Particle Size and Morphology Control, Adv. Funct. Mater. 21 (2011) 312–323.

[369] M. Konsolakis, The role of Copper–Ceria interactions in catalysis science: Recent theoretical and experimental advances, Appl. Catal. B Environ. 198 (2016) 49–66.

Universitat d'Alacant
Universidad de Alicante

Universitat d'Alacant
Universidad de Alicante

CHAPTER 2

Methods and techniques description

Chapter 2 describes the methodology and research approach developed in this Project Thesis, comprising experimental techniques complemented with punctual computational calculations based on Density Functional Theory (DFT). The fundamental principles of each technique, instrumentation, experimental set-ups and specific operation conditions are presented in this Chapter, which will be referred henceforward in all along the Thesis extension.

Universitat d'Alacant
Universidad de Alicante

2.1 Methodology and research approach

This Project Thesis focused on the study of copper-based formulations for their potential application as active catalysts in the Preferential CO Oxidation (CO-PROX) reaction, has fundamentally followed an experimental research approach, although it is complemented with Density Functional Theory (DFT) calculations to either predict or interpret certain experimental data outcomes. As evidenced in the evolution along these last years in current research methodology, a dual theoretical – experimental approach is optimum to reach an in-depth understanding of the studied catalytic reaction.

Hence, aiming to address catalytic CO-PROX reaction with ground-breaking first principles approach, this Project Thesis comprises the utilization of a complete battery of conventional characterization techniques combined with cutting-edge experimental analyses and advanced computational methods for the detailed description of the catalytic systems. Provided the wide range of techniques operated in this Project Thesis, these are categorized and presented in detail in the following sections along this Chapter 2, namely experimental and computational approach.

2.2 Experimental methods

The experimental approach deals with the synthesis, characterization and activity testing of active copper-based catalysts in CO-PROX reaction. Thus, the experimental methodology described in the following details: (1) the specific synthetic procedures for the preparation of catalytically active inorganic formulations; (2) the physicochemical characterization techniques employed for the elucidation of particular properties from the prepared materials and their critical interpretation in view of the best catalytic performance; (3) the conductance of CO-PROX catalytic activity tests in order to assess their performance in different simulated operation conditions; (4) advanced studies upon the formulations with best performance for the fine description of the catalytic environment and mechanistic issues.

A brief explanation of main procedures, techniques, equipments and related experimental setup, as well as operation conditions is listed below.

2.2.1 Catalyst synthesis

The preparation of the catalytically active materials has been conducted using simple procedures with well-reported good outputs, comparable to more complex and expensive synthetic routes [1]. Roughly, two type of catalysts were prepared during this Project Thesis, namely copper oxide – cerium oxide systems (CuO/CeO_2), and copper oxide – manganese oxide catalysts (CuO/Cryptomelane). Both were targeted with

nominal 5% weight (wt.) of Cu (metal) loading, as a compromise loading taken from preliminary studies, and copper incorporation was carried out by means impregnation on each previously prepared support.

Although each Chapter already will describe specific experimental modifications when corresponding, in general terms a common procedure can be detailed as follows for each formulation:

2.2.1.1 Preparation of CeO_2 support

CeO_2 was obtained via thermal decomposition of cerium(III) nitrates treated in muffle furnace following the chemical process described in Equation 2.1, which occurs in the range between 220-280ºC [2–4]:

$$Ce(NO_3)_3\,(s) \rightarrow CeO_2\,(s) + \text{nitrogen oxides}\,(g) \qquad \text{Eq. 2.1}$$

The resultant metal oxide from this simple procedure, CeO_2 or so-called *ceria*, is expected to present polycrystalline structure, irregular particle size and an heterogeneous micro- and meso-porosity left upon the exhaust gases release [5]. The thermal treatment in air conditions was conducted according to a "flash" calcination procedure, method that emerged to improve compositional homogeneity in citrate gel route for the preparation of $Ce_xZr_{1-x}O_2$ mixed oxides [6]. Likewise, "flash" calcination involved the direct introduction of metal precursor $Ce(NO_3)_3{\cdot}6H_2O$ (Panreac) in a preheated muffle at 200ºC in static air, stabilization for 1 hour and later gradual temperature increase (10ºC/min) up to the calcination temperature (500ºC) [7,8].

According to previous research conducted in the group [8], the choice of these particular conditions does not affect much on the properties of the resultant CeO_2 with regards to a counterpart sample prepared through analogue conventional ramp calcination program (room temperature to 500ºC at 10ºC/min pace), but these were established as routine to standarize the synthesis protocol.

2.2.1.2 Preparation of Cryptomelane ($K_xMn_8O_{16}$)

Synthetic cryptomelane was prepared following an adaptation from the so-called *reflux* method, procedure described by DeGuzman et al. [9,10], ruled by the redox chemical process occurring between $KMnO_4$ and Mn^{2+} species to produce amorphous MnO_2 forms (Equation 2.2), which in very controlled conditions transform into cryptomelane ($K_xMn_8O_{16}$) nano-rods.

$$2\,MnO^{4-}(ac) + 3\,Mn^{2+}(ac) + 2\,H_2O(l) \rightarrow 5\,MnO_2(s) + 4\,H^+(ac) \qquad \text{Eq. 2.2}$$

Particularly, cryptomelane catalysts presented in this Project Thesis were prepared establishing the following protocol: 11 g of manganese(II) acetate (Aldrich) are dissolved in 40 g of water and the pH of the solution

gets fixed at 5 using glacial acetic acid. This acid solution is heated and maintained at the boiling temperature under reflux for 30 min. After that, a solution of 6.5 g of potassium permanganate (Aldrich) dissolved in 150 ml of water is added to the boiling mixture, where a brownish slurry is immediately formed, and it is kept under reflux with vigorous stirring for 24 hours. The resulting substance is filtered, washed with distilled water until neutral pH and dried at 120ºC overnight. Finally, the dark-colored solid is calcined at 450ºC for 2 hours to obtain cryptomelane.

2.2.1.3 Preparation of CuO-supported catalysts

Once supports were prepared, the grinded powders were impregnated with an aqueous solution of copper salt precursor, namely $Cu(NO_3)_2{\cdot}(5{\cdot}½)H_2O$ (Panreac), prepared by dissolving the corresponding amount to a target 5% nominal wt. Cu content in the accurate volume, according to *incipient wetness impregnation* methodology. Thus, the volume of the solution is restricted to by the volume of the matrix to be filled, so that the solution is entirely drawn into the pores by capillary forces and merely coating in a thin film solution the external particle surface, which enables the maximum control on the metal loading and leads to higher yields with regards to *excess,* or *wet, impregnation* [11]. Accordingly, the precisely determined volume of copper salt precursor solution was added dropwise to the powdered supports, and homogeneity was ensured by physical mixing during the careful impregnation process. Hence, depending on the support, the impregnated samples were treated different successive steps:

On the one hand, in CuO/CeO_2, the impregnated sample was directly introduced in a preheated muffle furnace and followed “flash” calcination procedure equivalent as the detailed in Section 2.2.1.1 for the preparation of bare CeO_2. Conversely, CuO/Cryptomelane catalyst was obtained after drying the impregnated solid at 110ºC overnight and calcined in conventional ramp program in a rate of 5ºC/min up to 400ºC for 5 hours.

2.2.2 Catalyst characterization techniques

In catalysis science, it is well-known that the physicochemical features of the catalytic materials, such as composition, porosity and crystalline structure, surface chemistry and redox properties correlate well their performance in reaction tests and determine their latter application. Thus, in order to understand the catalytic activity behavior and discern optimum features, a systematic characterization study on the potential active samples is crucial. With this aim, the prepared catalytic materials, fresh or spent samples when convenient, were characterized in detail by means of a battery of complementary techniques.

Next sub-sections present main characterization techniques used in this regard all along this Project Thesis, describing briefly their fundamentals, experimental settings and selected operation conditions.

2.2.2.1 Physisorption of gases

Heterogeneous catalysis is a phenomenon governed by a solid-gas interaction, where reactants in the gas phase are activated on the surface of powders or porous catalytic materials. Hence, since it is essentially meant to occur on the boundaries of the catalyst surface, the proper determination of accessible surface area and textural properties of potential active materials is a key issue in catalysis science, which is most generally conducted by means of gas physical adsorption techniques [12,13].

In general terms, physical adsorption comprises the accumulation of certain species from an interacting gas phase on the surface of solids, which is leveraged by uncompensated surface cohesion molecular forces. Since the capacity of gas retention is dependent on the solid porosity and accessible surface, the precise determination of pressure changes upon gas exposure at constant temperature, which brings adsorbed volume, enables the calculation of the surface area by means of the application of accurate mathematical models.

Today, most commonly used approach on texture characterization is N_2 adsorption at -196ºC, although other adsorbates in alternative conditions are well-reported as well as long as these are chemically inert on surface, present spherical shape when adsorbed and preferably possess a high saturation pressure at the operative temperature. In the case of N_2 adsorption, the mathematical determination of surface area is most often conducted by means of the application of equations derived from the Brunauer-Emmett-Teller (BET) theory [14], widely considered the standard method for this purpose over the last 50 years, though depending on critical approximations that may not be fully representative of each particular studied system.

The linear expression of BET equation is defined by Equation 2.3, being “p” the pressure; “p_0” the saturation pressure (1 bar in N_2, -196ºC conditions); “C” a parameter related to the adsorption heat; “n” the number of adsorbed moles per catalyst gram; and “n_m” is the so-called monolayer capacity expressed in moles/g, which is considered to be directly dependent on total surface area according to the fundamentals this theory (S_{BET}, expressed in m^2/g), as described in Equation 2.4.

$$\frac{\frac{p}{p_0}}{n \cdot \left(1 - \frac{p}{p_0}\right)} = \frac{1}{n_m \cdot C} + \frac{(C-1)}{n_m \cdot C} \cdot \frac{p}{p_0} \qquad \text{Eq. 2.3}$$

$$S_{BET} = n_m \cdot a_m \cdot N_A \cdot 10^{-21}$$ Eq. 2.4

In the latter, N_A stands for Avogadro's constant ($6.022 \cdot 10^{-23}$ molecules/mol), whereas "a_m" is the occupied area of a single adsorbed molecule (defined as 0,162 nm^2 for N_2 in -196ºC) [15]; and 10^{-21} is a unit conversion factor. Thus, by the appropriate graphical representation of Equation 2.3, "n_m" is mathematically calculated, enabling S_{BET} determination by Equation 2.4.

The textural characterization of the catalysts prepared for this Project Thesis, was conducted using a volumetric Quantachrome Autosorb-6B instrument, that determines adsorbed volume in an automatic multi-measurement process ruled by systematic vacuum and filling steps at different tunable adsorbate pressures ($0 < p/p_0 < 1$) supplied (Figure 2). Prior to analysis, the samples were processed to clean the targeted surface in a degassing unit for the removal of adsorbed ambient CO_2 and H_2O molecules by means of a heating treatment at 150ºC in vacuum for 6 hours.

Figure 2.1. Degasification (left) and adsorption (right, Quantachrome Autosorb-6B) instruments to record N_2 adsorption isotherms -196ºC.

The representation of adsorbed volume against partial pressure "p/p_0" on both adsorption and desorption branches, from increasing and decreasing adsorbate pressures recorded output data, respectively, comprises the so-called *adsorption isotherm*. N_2 adsorption isotherms may be categorized in 6 main types according to standard IUPAC classification depending on the overall shape, whereas hysteresis loop defines different sub-types, too [16]. Thus, the visual interpretation of adsorption isotherms provides valuable information on the assessment of textural properties of porous materials, revealing key insights on pore size distribution, surface area, and adsorbate-adsorbent affinity.

Regarding porosity characterization, three broad pore types are mainly considered in terms of average radii size, which eventually determine different adsorption mechanisms. Namely, these are mainly discerned on micro-pores (with radii below 2 nm); meso-pores (radii in the 2 – 50 nm range); or macro-pores (for pores with radii larger than 50 nm), among which, micro-pores exhibit the strongest adsorption potential so their determination is of special interest [16]. Hence, the Dubinin-Radushkevich equation (Equation 2.5), based on the fundamentals of Polanyi's equipotential surfaces model [12], enables the calculation of micro-pore volume on the adsorbent solid.

$$\log \mathrm{V} = \log \mathrm{V_0} - \mathrm{D} \cdot \log^2 \left(\frac{\mathrm{p}}{\mathrm{p_0}} \right) \qquad \text{Eq. 2.5}$$

Where, "V" is the adsorbed volume on liquid state at different particular relative pressures, "p/p_0"; "D" is a dimensionless parameter defined by adsorbent-adsortive affinity; and "V_0" stands for the micro-pore volume per gram of solid, target variable obtained via simple mathematical operation after the proper graphical representation.

In certain cases when considered interesting, CO_2 adsorption isotherms at 0ºC were performed as well in analogue Quantachrome Autosorb 6 instrument. The corresponding V_0 values, attributed to the so-called *ultra micro-pores* (with radii narrower than 0.7 nm) were determined in complement with V_0 from N_2 adsorption (that accounts for pore radii in the 0.7 – 2 nm range, because of intrinsic diffusion restrictions of N_2 molecules at -196ºC) [17]. Thus, N_2 complemented with CO_2 adsorption brings a more complete characterization on the micro-pore range, particularly useful in highly micro-porous materials.

Universidad de Alicante

2.2.2.2 X-Ray Diffraction (XRD)

The sample characterization by means of X-Ray Diffraction (XRD) provides information regarding the crystalline features of the prepared catalytic materials. The technique es based on the optical interference phenomenon known as *diffraction*, occurring when X-ray beams are reflected in preferential directions when they reach the surface of a solid with certain degree of ordering, roughly being approximated as a periodic array of atoms. The recorded directions from diffracted X-rays and their relative accumulation in a determined incident angle range comprises an X-ray diffractogram, which is characteristic from particular lattice geometries, type and form of atoms aggrupation in a crystal structure.

As a diffraction basic principle, X-ray need to accomplish the ***Bragg's law*** defined by Equation 2.6, so diffraction angles depend on the interatomic distances accordingly:

$$n \cdot \lambda = 2 \cdot d \cdot \text{sen}\ \theta \qquad \text{Eq. 2.6}$$

Being, “d” the characteristic interplanar atomic distance; “λ” the radiation wavelength; “n” an integer number, and “θ” the diffraction angle from scattered X-rays (rad).

Thus, XRD allows to identify crystalline structures by the comparison with standard diffractogram patterns, such as the provided by the Joint Committee on Powder Diffraction Standards (JCPDS) cards database, currently known as the International Centre for Diffraction Data® (ICDD). Furthermore, XRD also permits to discern lattice distortions from their corresponding standard crystal structures, mainly produced by the presence of defects. Hence, XRD results particularly interesting in the case of Cu-supported catalysts, as enables the assessment on Cu ions location, whether inserted or segregated, by considering the lattice distortion upon Cu loading with regards to bare supports.

For CuO/CeO_2, lattice distortion is easily guessed by changes on the lone characteristic lattice parameter, “a”, reported to be 0.5411 nm for bare fluorite-type cubic CeO_2 crystals [1]. For cubic crystal arrangements, interplanar spacing “d” is defined in terms of “a” as expressed in Equation 2.7, being (111) the plane typically used in calculation for CeO_2 since it turns into the most intense diffraction peak:

$$\frac{1}{d^2} = \frac{h^2 + k^2 + l^2}{a^2} \qquad \text{Eq. 2.7}$$

Conversely, cryptomelane, though presenting an irregularly distorted tetragonal crystal structure, can be approximated as $K_{1.33}Mn_8O_{16}$ in a tetragonal crystal structure that exhibits two characteristic lattice parameters, namely “a” and “c”, which are reported as 0.9866 nm and 0.2872 nm, respectively [18]. The general formula that describes interplanar spacing on tetragonal crystal structures is expressed by Equation 2.8. Thus, the more complex calculation of “a” and “b” requires of two interplanar “d” spaces, obtained from two different diffraction peaks, choosing for practical convenience, (211) and (310) in this Project Thesis.

$$\frac{1}{d^2} = \frac{h^2 + k^2}{a^2} + \frac{l^2}{c^2} \qquad \text{Eq. 2.8}$$

On the other hand, XRD can also provide the crystallite size (D) when calculated by means of the Scherrer’s equation (Equation 2.9) [19,20].

$$D = \frac{K \cdot \lambda}{\beta \cdot \cos\theta} \qquad \text{Eq. 2.9}$$

Universitat d'Alacant
Universidad de Alicante

Being, “K” is the Scherrer’s constant or shape factor; “λ” is the radiation wavelength; “θ” is the diffraction angle; and “β” the full-width at half maximum (FWHM) of a selected peak (rad), generally the most intense. Alternatively, more accurate crystallite size results can be achieved by means of Williamson-Hall’s method [20,21], which separates FWHM contribution from crystal size and strain (distortion in a non-uniform crystal by atom displacement), as expressed by Equation 2.10:

$$\beta = \beta_{size} + \beta_{strain} = \frac{0.9 \cdot \lambda}{D \cdot \cos\theta} + \frac{4 \cdot \Delta d \cdot \sin\theta}{d \cdot \cos\theta} \qquad \text{Eq. 2.10}$$

Where Δd is the difference of the d spacing corresponding to a typical peak, and D can be obtained by the graphical representation of β·cos θ plotted against 4·sin θ.

In this Project Thesis, X-ray diffractograms were recorded in a Bruker D8-Advance diffractometer (Figure 2.2) provided with Göebel mirror with an X-ray generator Kristalloflex K 760-80F, using Cu Kα radiation (λ= 1.540598 Å). Diffractograms were recorded at 2θ between 10º and 90º, with a step size of 0.05º and a time of 3s per step, and “K” factor was set as K = 0.94, as reported in literature for CeO_2 and cryptomelane-type materials.

Figure 2.2. X-ray diffractometer Bruker D-8 Advance.

2.2.2.3 Raman spectroscopy

The fundamentals of Raman spectroscopy are well-known and can be revised elsewhere [22]. By and large, it is based on the inelastic interaction of a monochromatic light beam of incident frequency (v_0), with a material with under an oscillating electric field, that produces new frequencies on the dispersed photons ($-v_k$ and $+v_k$). This set of v_k values, so-called Raman frequencies are characteristic of each structure, and the difference: $v_k - v_0$ is

referred to as Raman shift, which is generally represented in terms of wavenumber (cm^{-1}) in Raman spectra.

Hence, Raman spectroscopy is a technique aimed to study the crystalline structure of solid materials, being frequently used as good complement to the information obtained by means X-ray diffraction. In comparison, Raman spectroscopy presents higher sensitivity to lattice parameter changes or crystalline disruption upon the presence of defects, but the analyzed depth volume in the sample is much lower than XRD, which is total, as considered a “bulk” analysis.

In this Project Thesis, Raman spectroscopy has been used to study the structure of bare CeO_2 and cryptomelane supports, assess possible structural effects by CuO loading, and the catalyst stability study on the analysis of spent samples. To this aim, Raman spectra were recorded in a Jasco NRS-5100 dispersive Raman using laser source of He:Ne (632.8 nm) and a 4-stage Peltier cooled CCD detector. The Raman signal was collected using a 20x (0.45 NA) objective. The laser power, calibrated on the sample, was kept close to 1.8 mW. The Raman shift was calibrated using the 520.7 cm^{-1} line of crystalline silicon prior to the sample analysis.

Figure 2.3. LabRam (Jobin-Ivon) Raman dispersive spectrometer, with confocal microscope.

On the other hand, *in-situ* Raman spectroscopy experiments are presented in Chapter 3 comprising the spectra measurement in selected well-controlled temperature and atmosphere conditions. These analyses were recorded using a LabRam Jobin Ivon Horiba instrument (Figure 2.3) with He:Ne laser excitation source and a high temperature chamber with a stable flow and temperature control. Namely, 100 ml/min flow of He was fed to the chamber containing the catalyst and heated up to 250 ºC in a slow rate doing steps at certain temperatures, 50, 100, 150, 200 and 250ºC keeping sufficient time to achieve representative stationary stage. Then, Raman spectra were recorded at each temperature in (1) He; and in (2) CO-PROX reaction environment, after switching inlet gases to CO-PROX gas mixture: 2% CO, 2% cO_2, 30% H_2, while keeping a total flow of 100 ml/min. Comparing

in-situ He and CO-PROX Raman spectra at each recorded temperature allows to stablish a correlation with structural changes on reaction course, associated with the ongoing CO-PROX reaction mechanism, which is highly valuable information.

2.2.2.4 Temperature Programmed Reduction (TPR)

Temperature Programmed Reduction (TPR) is, in general terms, an experimental procedure that allows to determine the reducibility of the catalysts, and comprises the monitorization of a solid-gas reaction in a reducing atmosphere alongside rising temperature. The thermal response of the material in certain reducing gas environments (H_2 or CO mixtures, mainly) is registered in profiles plotted versus temperature, exhibiting characteristic peaks related to the kinetics of the transformation and the nature of the studied systems.

In the case of CuO-supported catalysts, TPR experiments are essential element among the battery of catalyst characterization techniques, since provide concluding evidences regarding the degree of synergistic interaction between CuO and the metal oxide support. As stated in Chapter 1, the positive synergistic effect upon Cu loading on the support, either CeO_2 or cryptomelane, should result in the promotion on the labile redox exchange between Cu – Ce, or Cu – Mn species, respectively, leading to an activation in the reduction susceptibility, also seen as an improved *reducibility* [23,24]. In turn, reduction events registered in TPR profiles should exhibit a proportional shift towards lower temperatures when compared to the corresponding constituting individual phases. Furthermore, provided that CO oxidation is expected to occur by means of a Mars-van Krevelen (MVK) mechanism, involving lattice oxygen, the relative facile reduction of the catalysts correlates well with the catalytic activity.

Universidad de Alicante

Figure 2.4. Micromeritics Pulse Chemisorb 2705 equipment.

In this Project Thesis, Temperature Programmed Reduction experiments were conducted with H_2 (H_2-TPR) in a Micromeritics Pulse Chemisorb 2705 instrument (Figure 2.4) establishing the following conditions: 40 ml/min of 5% H_2/Ar gas mixture flowing through a quartz fixed-bed reactor containing 40 mg of catalyst in a heating ramp of 10 ºC/min up to 950ºC. A cryogenic bath prepared by isopropanol/liquid nitrogen mixture traps H_2O from the outlet stream to protect the Thermal Conductivity Detector (TCD), that is used to determine H_2 consumption alongside temperature increase.

A CuO reference sample, provided by the instrument manufacturer, was used to quantify the amount of H_2 consumed in the experiments in order to check the extension of the reduction in the catalyst.

2.2.2.5 Temperature Programmed Desorption (TPD)

Temperature programmed desorption (TPD) experiments were performed to study the retention capacity of CO_2 and H_2O in catalyst, since these are, respectively, the products from CO oxidation and H_2 oxidation reactions, occurring in the CO-PROX reaction environment. In this regard, the higher amount of retained CO_2 and H_2O, and the greater stability of these surface intermediate species may be tentatively associated with a less efficient product desorption in CO-PROX reaction conditions. Therefore, the interaction with new reactant molecules would be hampered by the presence of blocking species in the active sites.

In general terms, TPD experiments consist in the analysis and quantification of released species by the effect of heating a sample in inert atmosphere. Being from particular interest, CO_2 and H_2O retention capacity were estimated in this Project Thesis by their total release upon the inert heating after an appropriate saturation step is conducted on the catalyst sample. Additionally, the effect of concomitant CO_2 and H_2O chemisorption was studied by means of CO_2 + H_2O co-addition in the saturation step.

Briefly, the specific performed protocol was: 80 mg of catalyst was placed in a tubular quartz reactor coupled to mass spectrometer (MS) Pfeiffer Vacuum OmniStar for the outlet gases analysis and TPD profile construction. Firstly, a cleaning surface pre-treatment was conducted at 400ºC for 30 min in a 100 ml/min flow of Ar. Then, a saturation step with the selected gases was carried out, which consisted of heating the catalyst at 150ºC and keeping that temperature for 1 hour under 100 ml/min of 10% CO_2/Ar (for CO_2-TPD), 5% H_2O/Ar (for H_2O-TPD) or 10% CO_2 + 5% H_2O/Ar (for CO_2+H_2O-TPD). After that, the gas mixture was switched to Ar, and once CO_2 and H_2O signals were stabilized, the reactor was heated from 150ºC up to 650ºC following a ramp of 10ºC/min in 100 ml/min of Ar.

2.2.2.6 X-Ray Photoelectron Spectroscopy (XPS)

X-Ray Photoelectron Spectroscopy (XPS), is a highly useful characterization technique in catalysis research since it provides information regarding chemical composition and electronic environments on a solid surface, analyzing up to few nanometers depth. In fundamental terms, it is based on the excitation and emission of most internal electrons from surface atoms by the interaction with a monochromatic X-ray beam. As established in the *photoelectric effect* basic principles, the energy of the released electrons must be the difference between incident X-ray energy and the energy which they were bonded to the atom, so-called *binding energy* (BE).

Figure 2.5. Fully automated X-ray Photoelectron spectrometer K-Alpha from Thermo-Scientific.

Universitat d'Alacant
Universidad de Alicante

In this Project Thesis, X-ray photoelectron spectroscopy (XPS) analysis was performed by using an automated K-Alpha spectrophotometer (Thermo-Scientific) equipped with a high-resolution monochromator yielding a focused X-ray spot with a diameter of 400 µm, at 3 mA x 12 kV. XPS spectra were collected using a AlK_{α} X-ray source (1486.6 eV), and the alpha hemispherical analyzer was operated in the constant energy mode and pass energy of 50 eV (Figure 2.5). Charge compensation was achieved with the system flood gun that provides low energy electrons and low energy argon ions from a single source. The pressure in the chamber analysis was kept at the UHV values of $5 \cdot 10^{-10}$ mbar, and binding energies were adjusted using the C 1s transition, appearing at 284.6 eV. Binding energy values measured are accurate to ±0.2 eV.

Thus, the detailed analysis on specific XPS transitions allow to discern different electronic contributions for a given element with characteristic BEs on distinct well-known energy ranges in the XPS spectrum. Namely, targeted regions under analysis in the whole battery of studied catalysts have been:

C1s (280-300 eV); O1s (525-540 eV); Cu2p (925-965 eV); Ce3d (870-925 eV); Mn2p (630-660 eV); and K2p (290-230 eV). Although the detailed analysis on each region is properly explained when corresponding XPS results are presented along next Chapters 3-10 from this Project Thesis, a brief introductory discussion on the complex Cu2p and Ce3d XPS region analysis and must be presented at this point for the sake of clarity in future data interpretation.

On the one hand, Figure 2.6 displays a representative example of the characteristic Ce3d XPS spectrum, including the assignment of the multiple contributions based on the standard nomenclature provided by Burroughs [25].

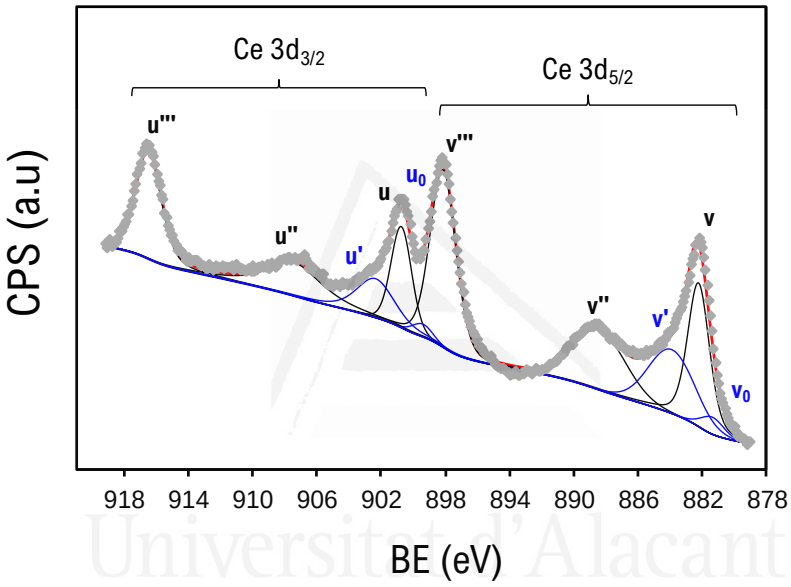

Figure 2.6. Characteristic Ce 3d XPS spectrum with assignation on the different contributions, displayed in **(blue)** for Ce_2O_3; **(black)** for CeO_2 species.

The XPS spectrum of the $3d_{5/2}$ Ce level is composed of three compounds for CeO_2 (v, v'' and v''') and two compounds for Ce_2O_3 (v_0 and v'). However, because of spin-orbit coupling ($3d_{5/2}$ + $3d_{3/2}$), the whole 3d level for Ce comprises ten structures under the same spectrum, corresponding to (v + u) terms, which unfortunately display small energy separation between them [26]. Thus, despite being truly complex to analyze, the quantification of CeO_2 and Ce_2O_3 relative proportion allows to estimate the fraction of reduced Ce^{3+} in the catalyst [27], as described by the formula in Equation 2.11:

$$Ce^{3+} = \frac{\text{area}\,(v_0 + v' + u_0 + u')}{\sum \text{area}\,(v + u)} \qquad \text{Eq. 2.11}$$

In this regard, although surface Ce species may be reduced by the intrinsic UHV operating conditions of XPS experiment, the establishment of

a correlation between reduced Ce^{3+} fraction in a series of CeO_2-based catalysts enables to infer the presence of oxygen defects at surface, which is highly valuable information in view of the understanding of its catalytic performance on CO-PROX reaction.

On the other hand, characteristic Cu2p XPS region exhibits much simpler spectrum, as shown in Figure 2.7.

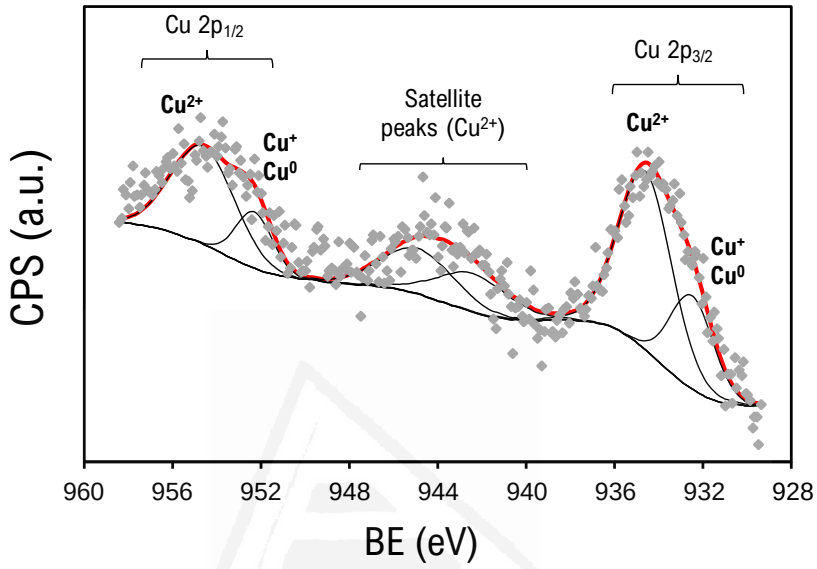

Figure 2.7. Example of Cu2p XPS spectrum with assignation on different species, Cu^0, Cu^+, and Cu^{2+}.

Figure 2.7, shows a representative example of Cu2p XPS spectrum, exhibiting the characteristic broad $Cu2p_{3/2}$ and $Cu2p_{1/2}$ peaks, and the characteristic Cu^{2+} shake-up satellite which is used by some authors to provide qualitative fashion establishing a linear relation main $2p_{3/2}$ peak [29,30]. The latter is composed by two contributions assigned to (1) Cu^+ and/or Cu^0, at lower BE; and (2) Cu^{2+}, at higher BE, in agreement with standard values reported for pure copper species, as presented in Table 2.1 [28,31].

Table 2.1. Standard values obtained for Cu species by XPS and Auger spectroscopy analysis [28].

Compound	Cu $2p_{3/2}$ peak maximum Eb (eV)	Cu LMM Auger peak maximum Ek (eV)	Modified Auger parameter (eV) (α')
Cu(0)	932.6	918.6	1851.5
Cu_2O	932.2	917.0	1849.2
CuO	933.8	917.6	1851.3

Notice that $Cu2p_{3/2}$ peak could be theoretically deconvoluted into three components, attributed to Cu^0, Cu^+ and Cu^{+2} contributions, but instead, a two-peak fitting is presented. The reason is the very little statistical peak position separation between Cu^0 and Cu^+ species, which does not allow their resolution with lone XPS characterization [28,32]. However, a widely used analytical approach is to roughly discern between *oxidized* (Cu^{2+}) and *reduced* (Cu^+ and Cu^0) copper species, using the precise representative constrains on BE, FWHM and peak-shape parameters.

Likewise, further resolution among the three copper species is possible if XPS characterization is complemented by Auger spectroscopic analysis of CuLMM line, where Cu^0 and Cu^+ display maximum separation, as Table 2.1 shows. However, the most extended and accurate criteria for total elucidation on copper species takes into account the calculation of the modified Auger parameter (α') to be compared with tabulated values, and/or its latter positioning in a Wagner plot representation when the reported dataset for similar compounds is available [33,34]. The modified Auger parameter (α') is defined by Equation 2.12:

$$\alpha' = E_B\ (Cu2p_{3/2}) + E_K\ (CuLMM) \qquad \text{Eq. 2.12}$$

Being, "E_B ($Cu2p_{3/2}$)" the BE from $Cu2p_{3/2}$ XPS peak, and "E_K (CuLMM)", the kinetic energy (KE) from Auger CuLMM line, calculated as indicated by Equation 2.13:

$$E_k\ (CuLMM) = AlK_\alpha - E_B\ (CuLMM) \qquad \text{Eq. 2.13}$$

Where "AlK_α" stands for the source X-ray energy (1486.6 eV); and "E_B (CuLMM) is the BE of Auger CuLMM line.

Universitat d'Alacant
Universidad de Alicante

2.2.2.7 Transmission Electron Microscopy (TEM)

The TEM microscope uses the transmission/scattering of the electrons produced upon the irradiation of a high energy electron beam on a thin sample (maximum thickness 100 nm), to form images, the diffraction of electrons to obtain information about the crystal structure and the emission of characteristic X-rays to determine the elemental composition of the sample. This technique allows to determine the morphology of the sample (size and position of the microcrystals or the particles) and also the crystallography (position of the crystal planes, study of defects, as well as chemical composition of the material).

TEM characterization was performed using a JEOL (JEM-2010) microscope, equipped with a detector (Oxford, model INCA Energy TEM 100) for microanalysis Energy-Dispersive X-ray Spectroscopy (EDS) (Figure 2.8). A few droplets of an ultrasonically dispersed suspension of the catalyst

in ethanol were placed in a copper grid with lacey carbon film and dried at ambient conditions.

Figure 2.8. JEOL (JEM-2010) microscope.

2.2.2.8 Scanning Electron Microscopy (SEM)

SEM provides morphological and topographical information of the solids surface. To obtain an image of the surface, it is scanned with a very thin electron beam with high energy that gives several types of signals as retro-dispersed electrons, secondary electrons, etc.

Catalysts were characterized by SEM in a Hitachi S-3000N microscope with a secondary electrons detector, a retro-dispersed electrons detector and X-ray detector (XFlash 3001, Bruker) for microanalysis (EDS) and chemical mapping (Figure 2.9).

Figure 2.9. SEM Hitachi S-3000N microscope.

2.2.3 CO-PROX activity tests

Catalytic Preferential CO Oxidation (CO-PROX) reaction activity tests were performed in an atmospheric pressure fixed-bed reaction system coupled to gas chromatography (GC), according to the experimental set-up displayed in Figure 2.10.

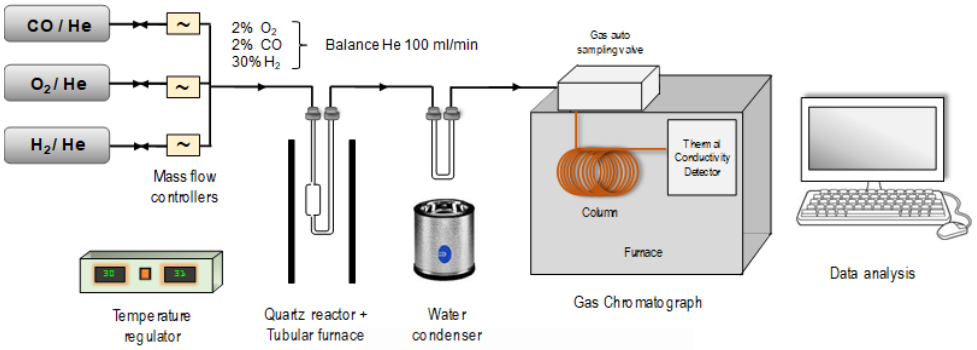

Figure 2.10. Experimental set-up for the CO-PROX catalytic activity tests.

In each experiment, a regular 100 ml/min flow of gas reactant mixture (2% CO, 2% O_2, 30% H_2), set by means of Mass Flow Controllers (Bronkhorst) was fed to a quartz reactor (16 mm inner diameter), where 150 mg of the powdered catalyst sample were placed (GHSV = ~30,000 h^{-1}). Catalytic tests were performed in a slow-pace heating ramp of 2ºC/min up to 250ºC, which comprises near-stationary conditions according to preliminary assays. Reaction progress, *i.e.* product evolution, was monitored by means of a GC HP model 6890 Plus Series equipped with two columns: (1) Porapak Q 80/100 for CO_2 and H_2O separation; and (2) Molecular Sieve 13X for O_2 and CO separation, coupled to a TCD detector for the outlet gases analysis and generation of light-off curves.

Thus, for the convenient comparison on the catalytic performance among the battery of prepared active samples, the catalytic parameters: *CO conversion* (X_{CO}); *O_2 conversion* (X_{O2}) and *CO selectivity*, or selectivity to CO_2 formation (Sel) were determined along the temperature profile being defined as in the following Equations 2.3-2.5:

$$X_{CO} = \frac{p_{CO_{\text{in}}} - p_{CO_{\text{out}}}}{p_{CO_{\text{in}}}} \qquad \text{Eq. 2.3}$$

$$X_{O2} = \frac{p_{O2_{\text{in}}} - p_{O2_{\text{out}}}}{p_{O2_{\text{in}}}} \qquad \text{Eq. 2.4}$$

$$Sel = \frac{1}{\lambda} \cdot \frac{p_{CO_{\text{in}}} - p_{CO_{\text{out}}}}{p_{O2_{\text{in}}} - p_{O2_{\text{out}}}} \qquad \text{Eq. 2.5}$$

Where, p_X stands for partial pressure of gas "x", either CO or O_2 in the inlet (in) or outlet (out) stream. On the other hand, λ corresponds to O_2 stoichiometric excess, which was set to λ=2 in routine experiments, comprising a double O_2 feeding with regard to the required for the total CO consumption. Extensive research on the effect of λ parameter demonstrated that it critically determines CO oxidation activity and residual H_2 oxidation [35,36], being in general optimum when takes values in between 1-2.

Reproducibility of CO-PROX activity tests was proven by performing repeated tests, which typically exhibit average error below 2%. Furthermore, when considered convenient, successive reaction runs were conducted to test catalyst stability upon cyclability, besides long time-on-stream experiments to discard or determine catalytic activity loss in a continuous operation regime at certain chosen temperatures.

Finally, the effect of (1) CO_2, (2) H_2O and (3) CO_2+H_2O in the catalytic activity was studied by means of the introduction of, either separated or together, 9% CO_2 and 5% H_2O in the reactant gas mixture feeding. In analogy with CO+O_2+H_2 experiments, the total flow was kept in all cases as 100 ml/min balanced with He and temperature rose following a 2ºC/min ramp up to 200ºC.

2.2.4 Advanced chracterization techniques relevant in mechanistic studies

2.2.4.1 Operando DRIFTS

The reaction mechanism was studied in a Fourier Transform Infrared Spectrometer Shimadzu (IR Tracer-100) with a Harrick reaction cell coupled to a EcoSys-P mass spectrometer. The reaction cell was designed to allow the reaction gas mixture (2% CO, 2% O_2 and 58% H_2 balanced with He; 50 ml/min) to pass through the catalyst bed (100 mg without any diluent) with the gas exit at the bottom.

The catalysts were first pre-treated at 400ºC for 15 min in a flow of air, and the reaction cell was cooled afterwards to room temperature while maintaining the air flow. A background spectrum was recorded for each catalyst at room temperature after this cleaning step, and then, air was replaced by the reaction gas mixture and the temperature was raised at 5ºC/min while infrared spectra were recorded at 10ºC intervals. Each spectrum was obtained as an average of 75 scans, measured from 4000 to 1000 cm^{-1} with a resolution of 2 cm^{-1}. The background spectrum of each

catalyst was subtracted from those obtained under reaction conditions, and therefore, the features observed can be attributed to surface species formed or depleted during the reaction rather than to the catalysts structure.

2.2.4.2 Operando XAS and NAP-XPS

Near-Ambient Pressure X-ray Photoelectron Spectroscopy (NAP-XPS) is a highly sophisticated technique that allows to elucidate the surface reactivity and structure in real environments. Compared to XPS traditional measurements, in UHV, NAP-XPS may reveal dramatic differences when working under realistic operation conditions in order to get information during the reactions or processes of interest. This cutting-edge technique has huge relevance and impact in heterogeneous catalysis science and is being used in top catalysis research since the last years.

The X-ray photoemission spectra in CO-PROX reaction conditions were recorded at the NAPP branch from the modulable beamline CIRCE using ALBA Synchrotron Light Source by means of a PHOIBOS NAP150 energy analyzer from SPECS [37]. For each analysis, two different photon energies were used, being: (1) 1082 and 1372 eV for Ce3d and Cu2p region; (2) 972 and 722 eV for O1s and C1s, providing a variability in the surface depth sensitivity, according to the corresponding estimations on mean free paths (MFP) in the solid structure of CeO_2-based materials.

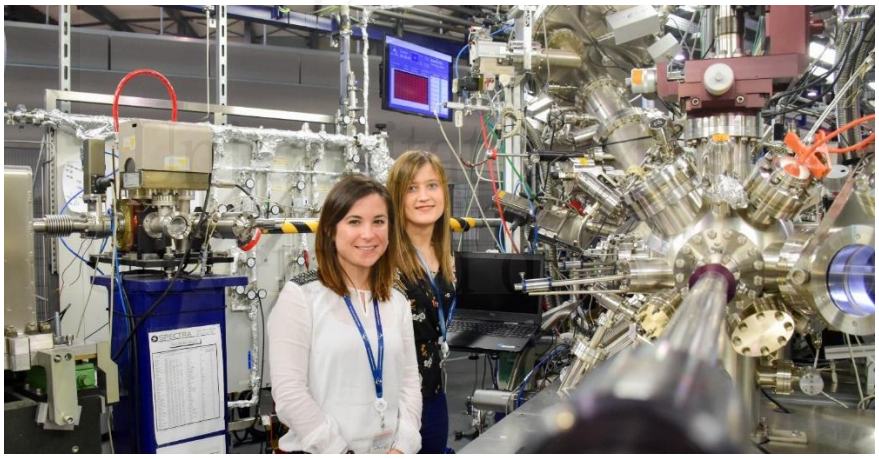

Figure 2.11. NAP-XPS CIRCE beamline in ALBA Synchrotron (March 2019).

The CuO/CeO_2 catalyst was pelletized with a gold mesh to prevent from surface charge and, providing at the same time, an Au4f reference for the peak position of XPS analysis. Catalytic activity of the gold mesh was experimentally ruled out. The CO-PROX reacting mixture: 1% CO, 1% O_2, 30% H_2, 30 mL/min balance N_2 was dosed into the analysis chamber by means of a leak valve and controlled with a Puregas UHV gas inlet system (SPECS). During the NAP-XPS experiments the pressure was kept constant at 1 mbar and the CO-PROX reaction course was monitored with a mass

spectrometer (MS) installed in the second stage of the differential pumping system of the analyzer. For each temperature, the spectra were recorded after MS signals stabilization once achieved stationary state.

Near Edge X-ray absorption (NEXAFS or XAS) measurements at the Cu L edge (930-950 eV) were performed in Total Electron Yield mode measuring sample current at each temperature after the series of NAP-XPS scans using the same experimental conditions.

2.2.4.3 $^{36}O_2$ pulse isotopic experiments

The capacity of a metal oxide catalyst to exchange oxygen under a fluctuating oxidizing-reducing atmosphere is tightly linked to its ability to produce labile surface oxygen species with enhanced reactivity on MVK-ruled chemical reactions, such as in the case of CO-PROX reaction. Thus, the molecular labeling of such exchangeable oxygen species and its traceability in ongoing chemical processes, may provide crucial information regarding the catalyst performance and reveal the different factors governing the mechanism of reaction.

Isotopic exchange experiments were carried out with $^{36}O_2$ by means of an injection valve with a loop (100 µl) and two high sensitivity pressure transducers. The experiments were carried out in a fixed-bed tubular quartz reactor with 80 mg of catalyst in a constant 20 ml/min of 1% CO, 30% H_2 balanced He feeding mixture. The exhaust gases were monitored with MS and the $^{36}O_2$ pulses (Isotec, 99%; 100 µl and 9 psi) were injected at 75, 100 and 150 ºC once achieved signals stabilization. Prior to this, several pulses of Ar (100 µl and 9 psi) were used as a test to confirm reproducibility of the method.

Universitat d'Alacant
Universidad de Alicante

Figure 2.12. (Left) Control module actuator of the two-position high precision injection valve. **(Right)** injection valve with loop.

2.3 Computational approach

2.3.1 Density Functional Theory (DFT)

Density functional theory (DFT) is one of the most commonly used computational tools to study and predict properties of isolated molecules, bulk solids or interfaces, such as crystal surfaces [38]. DFT principles are based on the Hohenberg-Kohn and Kohn-Sham Theorems, which consider electrons as uniformly distributed around the nuclei, comprising the so-called *electron density*, which is mathematically expressed as a *functional*, that is a function of other functions [39–41].

For periodic DFT calculations, such as crystal structures or crystal surfaces, a *plane wave* basis set, introduced by the treatment of the Bloch's Theorem, is very commonly used to solve Kohn-Sham equations, which require trial functions. Accordingly, plane waves describe electrons that travel through the real space along the repeatedly unit cell, with spacing equal to the lattice constant. However, it is much easier to represent the interaction of plane wave's periodicity with the reciprocal lattice instead, by the analysis of a set of k-points in the Brillouin zone space referred for a number of wavefunctions.

In this regard, there are several software packages able to use plane wave basis sets to calculate electronic properties of solids, such as the Vienna Ab-initio Simulation Package (VASP) [42]. Likewise, DFT computational calculations are performed by means of the set of specific input parameters carefully chosen that: (1) define the nature and particularities of the calculations and; (2) provide a representative description of the real studied systems. Therefore, a deep knowledge of the working catalytic environments is absolutely required to reproduce good theoretical results.

Universidad de Alicante

As stated in the overview and general introduction to the methodology undertaken along this PhD Thesis, though mostly comprised of experimental activities, computational studies regarding solid-gas interactions specific catalytic surface properties have been also conducted in order to gain complementary information. Next Section reviews main aspects of the computational approach followed in this research.

2.3.2 Computational details

Calculations have been conducted by means of periodic density functional theory (DFT) using the Perdew–Burke–Ernzenhof (PBE) exchange-correlation functional, as implemented in the Vienna Ab-Initio Simulation Package (VASP) code. The core electrons of Ce, Cu and O ions have been described using projector augmented wave potentials, while the valence states were represented by plane-waves with a kinetic cut-off energy

of 500 eV. In the particular case of Ce, a Hubbard U corrective term has been added to the DFT calculated energies (DFT+U) for the on-site correction of electrons in the orbital 4f, as described in literature.[6-8]

Copper oxide and cerium oxide catalysts have been modelled as surface slabs built from the corresponding bulk structures. The geometry of the CuO, Cu_2O and CeO_2 bulk crystal structures were optimized using a Γ-centred k-point grid of 5 x 5 x 5, and the equilibrium lattice parameter fitted to the Birch-Murnaghan equation of state.

From the optimised bulks, the most exposed surface facets have been prepared, namely CuO(111), Cu_2O(111) and CeO_2 (111) planes, by the adequate crystal cleavage. Surface slabs are set as thick enough to ensure there is minimal interaction between the top and the bottom, and a sufficiently large (*ca*. 15 Å) vacuum gap perpendicular to the surface is added to minimize the interaction between periodic slabs in the z-axis. Geometry optimizations of slabs with a *p*(2x2) periodicity have been performed using a Γ-centred k-point grid of 3 x 3 x 1.

The catalysts resting state has been assessed by computing ground energies of clean slabs. Afterwards, the effect of introducing structural modifications, such as the abstraction of lattice oxygen ions in precise positions and different electronic rearrangements has been studied. On the other hand, adsorption energies for CO and H_2 molecules have been computed, too.

References

[1] A. Trovarelli, Catalytic Properties of Ceria and CeO_2-Containing Materials, Catal. Rev. 38 (1996) 439–520.

[2] C.A. Strydom, C.P.J. van Vuuren, The thermal decomposition of cerium(III) nitrate, J. Therm. Anal. 32 (1987) 157–160.

[3] F. Vratny, S. Kern, F. Gugliotta, The thermal decomposition of cerium (III) nitrate hydrate, J. Inorg. Nucl. Chem. 17 (1961) 281–285.

[4] A. Davó-Quiñonero, J. González-Mira, D. Lozano-Castelló, A. Bueno-López, Templated Synthesis of Pr-Doped Ceria with Improved Micro and Mesoporosity Porosity, Redox Properties and Catalytic Activity, Catal. Letters. 148 (2018) 67-79.

[5] X. Zheng, X. Zhang, X. Wang, S. Wang, S. Wu, Preparation and characterization of CuO/CeO2 catalysts and their applications in low-temperature CO oxidation, Appl. Catal. A Gen. 295 (2005) 142–149.

[6] J. Kašpar, R. Di Monte, P. Fornasiero, M. Graziani, H. Bradshaw, C. Norman, Dependency of the Oxygen Storage Capacity in Zirconia–Ceria Solid Solutions upon Textural Properties, Top. Catal. 16 (2001) 83–87.

[7] V. Rico-Pérez, S. Parres-Esclapez, M.J. Illán-Gómez, C. Salinas-Martínez de Lecea, A. Bueno-López, Preparation, characterisation and N_2O decomposition activity of honeycomb monolith-supported $Rh/Ce_{0.9}Pr_{0.1}O_2$ catalysts, Appl. Catal. B Environ. 107 (2011) 18–25.

Universitat d'Alacant
Universidad de Alicante

[8] V. Rico-Pérez, A. Bueno-López, Effect of RhO_x/CeO_2 Calcination on Metal-Support Interaction and Catalytic Activity for N_2O Decomposition, Appl. Sci. 4(3) (2014) 468-481.

[9] R.N. DeGuzman, Y.F. Shen, E.J. Neth, S.L. Suib, C.L. O'Young, S. Levine, J.M. Newsam, Synthesis and characterization of Octahedral Molecular Sieves (OMS-2) having the hollandite structure, Chem. Mater. 6 (1994) 815–821.

[10] I. Atribak, A. Bueno-López, A. García-García, P. Navarro, D. Frías, M. Montes, Catalytic activity for soot combustion of birnessite and cryptomelane, Appl. Catal. B Environ. 93 (2010) 267–273.

[11] M. Tiemann, Repeated Templating, Chem. Mater. 20 (2008) 961–971.

[12] K. Rouquerol, F., Rouquerol, J., Sing, Adsorption by powders and porous solids: principles, methodology and applications, John Wiley & Sons Ltd, 1982.

[13] D.M. Ruthven, Principles of adsorption and adsorption processes, John Wiley & Sons Ltd,1984.

[14] S. Brunauer, P.H. Emmett, E. Teller, Adsorption of Gases in Multimolecular Layers, J. Am. Chem. Soc. 60 (1938) 309–319.

[15] M. Lowell, S., Shields, J.E., Thomas, M.A., Thommes, Characterization of Porous Solids and Powders: Surface Area, Pore Size and Density, Springer Netherlands, Heidelberg, 2004.

[16] Physisorption of gases, with special reference to the evaluation of surface area and pore size distribution (IUPAC Technical Report) , Pure Appl. Chem. 87 (2015) 1051-1069

[17] D. Cazorla-Amorós, J. Alcañiz-Monge, M.A. de la Casa-Lillo, A. Linares-Solano, CO_2 As an Adsorptive To Characterize Carbon Molecular Sieves and Activated Carbons, Langmuir. 14 (1998) 4589–4596.

[18] J. Vicat, E. Fanchon, P. Strobel, D. Tran Qui, The structure of $K_{1.33}Mn_8O_{16}$ and cation ordering in hollandite-type structures, Acta Crystallogr. Sect. B. 42 (1986) 162-167.

[19] P. Scherrer, Bestimmung der Größe und der inneren Struktur von Kolloidteilchen mittels Röntgenstrahlen, Nachrichten von Der Gesellschaft Der Wissenschaften Zu Göttingen, Math. Klasse. 1918 (n.d.) 98–100.

[20] A.W. Burton, K. Ong, T. Rea, I.Y. Chan, On the estimation of average crystallite size of zeolites from the Scherrer equation: A critical evaluation of its application to zeolites with one-dimensional pore systems, Microporous Mesoporous Mater. 117 (2009) 75–90.

[21] G.K. Williamson, W.H. Hall, X-ray line broadening from filed aluminium and wolfram, Acta Metall. 1 (1953) 22–31.

[22] B. Dietzek, D. Cialla, M. Schmitt, J. Popp, Introduction to the Fundamentals of Raman Spectroscopy BT - Confocal Raman Microscopy, in: T. Dieing, O. Hollricher, J. Toporski (Eds.), Springer Berlin Heidelberg, Berlin, Heidelberg, 2011: pp. 21–42.

[23] A. Martínez-Arias, D. Gamarra, A. Hungría, M. Fernández-García, G. Munuera, A. Hornés, P. Bera, J. Conesa, A. Cámara, Characterization of Active Sites/Entities and Redox/Catalytic Correlations in Copper-Ceria-Based Catalysts for Preferential Oxidation of CO in H_2-Rich Streams, Catalysts. 3 (2013) 378–400.

[24] W.Y. Hernández, M. a. Centeno, S. Ivanova, P. Eloy, E.M. Gaigneaux, J. a. Odriozola, Cu-modified cryptomelane oxide as active catalyst for CO oxidation reactions, Appl. Catal. B Environ. 123–124 (2012) 27–35.

[25] P. Burroughs, A. Hamnett, A.F. Orchard, G. Thornton, Satellite structure in the X-ray photoelectron spectra of some binary and mixed oxides of lanthanum and cerium, J. Chem. Soc. Dalt. Trans. (1976) 1686–1698.

[26] M. Romeo, K. Bak, J. El Fallah, F. Le Normand, L. Hilaire, XPS Study of the reduction of cerium dioxide, Surf. Interface Anal. 20 (1993) 508–512.

[27] S. Deshpande, S. Patil, S.V.N.T. Kuchibhatla, S. Seal, Size dependency variation in lattice parameter and valency states in nanocrystalline cerium oxide, Appl. Phys. Lett. 87 (2005) 133113-133117.

[28] M.C. Biesinger, Advanced analysis of copper X-ray photoelectron spectra, Surf. Interface Anal. 49 (2017) 1325–1334.

[29] S. Poulston, P.M. Parlett, P. Stone, M. Bowker, Surface Oxidation and Reduction of CuO and Cu_2O Studied Using XPS and XAES, Surf. Interface Anal. 24 (1996) 811–820.

[30] P. Salvador, J.L.G. Fierro, J. Amador, C. Cascales, I. Rasines, XPS study of the dependence on stoichiometry and interaction with water of copper and oxygen valence states in the $YBa_2Cu_3O_{7-x}$ compound, J. Solid State Chem. 81 (1989) 240–249.

[31] NIST X-Ray Photoelectron Spectroscopy Database, NIST Stand. Ref. Database 20, Version 4.1. (n.d.).

[32] M.C. Biesinger, B.P. Payne, B.R. Hart, A.P. Grosvenor, N.S. McIntryre, L.W. Lau, R.S. Smart, Quantitative chemical state XPS analysis of first row transition metals, oxides and hydroxides, J. Phys. Conf. Ser. 100 (2008) 12025-12029.

[33] G. Moretti, Auger parameter and Wagner plot in the characterization of chemical states by X-ray photoelectron spectroscopy: A review, J. Electron Spectros. Relat. Phenomena. 95 (1998) 95–144.

[34] J.P. Espinós, J. Morales, A. Barranco, A. Caballero, J.P. Holgado, A.R. González-Elipe, Interface Effects for Cu, CuO, and Cu_2O Deposited on SiO_2 and ZrO_2. XPS Determination of the Valence State of Copper in Cu/SiO_2 and Cu/ZrO_2 Catalysts, J. Phys. Chem. B. 106 (2002) 6921–6929.

[35] F. Mariño, C. Descorme, D. Duprez, Noble metal catalysts for the preferential oxidation of carbon monoxide in the presence of hydrogen (PROX), Appl. Catal. B Environ. 54 (2004) 59–66.

[36] M.J. Kahlich, H. a Gasteiger, R.J. Behm, Kinetics of the Selective CO Oxidation in H_2-Rich Gas on Pt/Al_2O_3, J. Catal. 171 (1997) 93–105.

[37] V. Pérez-Dieste, L. Aballe, S. Ferrer, J. Nicolàs, C. Escudero, A. Milán, E. Pellegrin, Near Ambient Pressure XPS at ALBA, J. Phys. Conf. Ser. 425 (2013) 72023-72027.

[38] J.A. Scholl, D.S., Steckel, What is Density Functional Theory?, Density Funct. Theory. (2009) 1–33.

[39] J.C. Cramer, Essentials of Computational Chemistry: Theories and Models, John Wiley & Sons, 2nd Edition, 2004.

[40] P. Hohenberg, W. Kohn, Inhomogeneous Electron Gas, Phys. Rev. 136 (1964) B864–B871.

[41] W. Kohn, L.J. Sham, Self-Consistent Equations Including Exchange and Correlation Effects, Phys. Rev. 140 (1965) A1133–A1138.

[42] G. Kresse, J. Furthmüller, Efficient iterative schemes for ab initio total-energy calculations using a plane-wave basis set, Phys. Rev. B. 54 (1996) 11169–11186.

Universitat d'Alacant
Universidad de Alicante

Universitat d'Alacant
Universidad de Alicante

CHAPTER 3

Into the Preferential Oxidation of CO reaction mechanism over CuO/CeO_2 catalyst

Chapter 3 reviews main significative advances achieved so far into the CO-PROX reaction mechanism study over CuO/CeO_2 catalysts, tested and fully characterized through a battery of techniques: N_2 physisorption at -196ºC, XRD, H_2-TPR and Raman spectroscopy, proving inherent synergistic Cu-Ce effects, which turn beneficial into the ongoing MVK mechanism as demonstrated by pulse O_2-isotopic exchange and *in-situ* Raman spectroscopy. Additionally, cutting-edge experimental techniques for the detailed molecular mechanism dilucidation are presented herein. Namely, CO-PROX *operando* NAP-XPS, and XANES experiments, reveal altogether clear evidences of CeO_2 very surface reduction, assigned to the role of CeO_2 in oxygen assistance to Cu_xO in Cu – Ce interfacial points, when highly reduced Cu_xO particles are inefficiently undertaking direct O_2 uptake at advanced CO-PROX reaction degrees. Finally, complementary DFT calculations confirm that lattice oxygen restitution by O_2 gas phase should be at first directly favored in Cu_xO when partially oxidized, but then via CeO_2 when Cu_xO particles are reduced at surface by the effect of the reaction course. Since reoxidation issues in CO-PROX reaction have been rarely addressed, this Chapter presents relevant insights for the state-of-the-art in the CuO/CeO_2 catalysts study.

Universitat Rovira i Virgili
Universidad de Alicante

3.1 Introduction

CuO/CeO_2 catalysts are well-studied materials with excellent properties towards multiple catalytic applications such as: volatile organic compounds (VOCs) oxidation, water-gas shift (WGS) reaction, low temperature CO oxidation, preferential CO oxidation (CO-PROX) reaction, CO_2 hydrogenation, soot oxidation, selective catalytic reduction (SCR) of NO_x and N_2O decomposition [1–3]. The origin of the great catalytic skills of CuO/CeO_2 relies on the synergistic metal-support interactions, which are rather complex redox effects induced on both CuO and CeO_2 in the interfacial contact points between these phases.

Regarding the particularities of CO-PROX reaction, the specific positive features resulting from Cu – Ce interaction in CuO/CeO_2 catalysts are: the formation of surface oxygen vacancies, the labile electron exchange between Cu^{2+}/Cu^{+} and Ce^{4+}/Ce^{3+} redox pairs, and the promotion and stabilization of Cu^{I} active sites [4–6]. Furthermore, it has been well-reported how CO conversion depends on the ease for the formation of stable and active surface Cu^{+} species, whereas H_2 oxidation is claimed to occur massively when metal Cu entities are present by the effect of the temperature in the reducing CO-PROX atmosphere [4,7–9].

As a consequence, to achieve the optimum CO oxidation rate performance in CO-PROX reaction, it is required to keep an operation temperature with a CO conversion and CO selectivity compromise. In this regard, attempts towards the enhancement into the catalytic CO-PROX reaction operation are focused on the separation along the temperature profile between the on-set of both CO and H_2 oxidation processes, by means of the maximization of the Cu^{+} species stability via different approaches [10,11]. Since Cu^{+} species are being gradually reduced by the effect of the ongoing CO oxidation reaction, their efficient reoxidation by the feeding O_2 gas is crucial to maintain the catalytic performance. Hence, reduction and reoxidation processes occur at the same time during reaction course in quick and labile equilibria. Nevertheless, provided that CO-PROX reaction rate is accelerated with temperature, the average between both processes eventually leads to the extension of the Cu_xO reduction and therefore, the selectivity loss.

Thus, with the aim to improve Cu^{+} stability and endurance to total reduction, the reoxidation step should be studied and facilitated by means of catalyst optimization. In this regard, the strongly interacting CeO_2 support should play a key role given its great lattice oxygen mobility and large oxygen storage capacity (OSC). Nevertheless, few studies are certainly focused on the oxidation process and little is known about the ongoing mechanism of the O restitution route, which could take place wether directly to Cu_xO from O_2 gas or transferred from intimate contacting CeO_{2-x} [12].

Chapter 3 presents a detailed mechanistic study into the conventional CuO/CeO_2 catalytic performance, and compiles the use of multiple complementary advanced *in-situ* techniques to keep the molecular traceability of reactants and products during CO-PROX reaction.

3.2 Experimental details

3.2.1 Catalysts preparation and characterization

The preparation of CeO_2 support and CuO/CeO_2 (5% wt. Cu) catalyst was performed from thermal decomposition of nitrates and incipient wetness impregnation, as detailed in Section 2.2.1 from Chapter 2. These were thoroughly characterized by means of complementary techniques, namely X-ray diffraction (XRD), N_2 adsorption at -196ºC, Raman spectroscopy and temperature programmed reduction with H_2 (H_2-TPR). Further details on experimental settings and specific analysis conditions can be found in Section 2.2.2. from Chapter 2.

3.2.2 CO-PROX activity tests and mechanistic studies

Fixed-bed CO-PROX catalytic tests were performed with 100 ml/min of the He-balanced CO-PROX reactant gas mixture: 2% CO, 2% O_2, 30% H_2 (λ = 2), 150 mg of sample and a heating rate of 2ºC/min from up to 250ºC. Further specifications are described in Section 2.2.3. from Chapter 2.

Isotopic exchange experiments were carried out at selected temperatures with $^{36}O_2$ pulsed by means of an injection valve to a reactor containing 80 mg of sample and a flowing mixture of 20 ml/min of 1% CO, 30% H_2, simulating CO-PROX reaction conditions. The exhaust gases were monitored with MS to track molecular oxygen products after the pulse.

In-situ Raman experiments were performed in a high temperature chamber fed with a regular passing flow of 100 ml/min (He or CO-PROX mixture: 2% CO, 2% O_2, 30% H_2). At selected temperatures: 50, 75, 100, 150, 200 and 250ºC, Raman spectra were recorded in both atmospheres to study structural changes upon exposure to CO-PROX reactant mixture.

Further details are thoroughly provided in specific parts from Section 2.2.2. in Chapter 2.

3.2.3 CO-PROX *operando* NAP-XPS and *operando* XANES

The X-ray photoemission spectra in CO-PROX reaction conditions were recorded at the NAPP branch from CIRCE an modulable beamline at the ALBA Synchrotron Light Source [16]. For each analysis, two different photon energies were used, being: (1) 1082 and 1372 eV for Ce3d and Cu2p

region; (2) 972 and 722 eV for O1s and C1s, providing a variability in the surface sensitivity, according to the inelastic mean free paths. The CO-PROX reacting mixture: 1% CO, 1% O_2, 30% H_2, 30 mL/min balance N_2 was dosed into the analysis chamber containing the CuO/CeO_2 catalyst by means of a leak valve in a controlled gas inlet system. CO-PROX reaction course was monitored with a mass spectrometer (MS), and for each temperature, the spectra were recorded after MS signals stabilization once achieved stationary state.

Near Edge X-ray absorption (NEXAFS or XAS) measurements at the Cu L edge (930-950 eV) were performed at each temperature after the series of NAP-XPS scans using the same experimental conditions. Section 2.2.4 reviews in deep detail these experiments.

3.2.4 Computational activities

Periodic Density Functional Theory (DFT) calculations have been conducted by means of the *Vienna Ab-Initio Simulation Package* code (VASP, version 5.4.1). CuO (111), Cu_2O (111) and CeO_2 (111) surface slabs were built and optimized, and the energies for the oxygen vacancy formation on the surface slabs was calculated by means of the formula given by Equation 3.1:

$$E_{(O\text{-}vac)} = E_{(vac\text{-}slab)} - [E_{(slab)} + ½\ E_{(O2)}] \qquad \text{Eq. 3.1}$$

Where E_i stands for the calculated lowest energy level of the optimized corresponding systems. $E_{(O2)}$, ground energy for the O_2 gas molecules, with complicated electronic structure not properly reproduced by DFT, was set as the DFT-corrected energy of $E_{(O2)}$ = -9.9053 eV, calculated by the formula ruled by Equation 3.2:

$$\text{DFT-corrected } E_{(O2)} = 2 \cdot [E_{(H2O)} - E_{(H2)}] - 2.506 \text{ eV} \qquad \text{Eq. 3.2}$$

The computational part is thoroughly described in Section 2.3.2 from Chapter 2.

3.3 Results and discussion

3.3.1 Catalyst characterization

The CuO/CeO_2 catalyst was characterized by means of several physicochemical techniques and the most relevant results are presented in Table 3.1. Such analyses were focused on the determination of the effect of CuO loading into the prepared CeO_2 support and these are discussed in the following.

Universidad de Alicante

Table 3.1. Main characterization results provided from CeO_2 and CuO/CeO_2 catalyst.

Sample	S_{BET} (m^2/g)	Cell parameter (nm)	Crystallize size (nm)		% Ce^{4+} reduced by H_2 (TPR)	XPS	
			Scherrer	WH		$\%Ce^{3+}$	%Cu
CeO_2	71	0.5420	10	13	20	19.4	-
CuO/CeO_2	65	0.5411	10	15	17	20.0	5.0

Regarding the textural properties provided by N_2 physisorption analysis (Figure 3.1), both CeO_2 and CuO/CeO_2 show a type-IV isotherm, which is a typical feature from mesoporous materials [20]. Moreover, H2(b) hysteresis loop caused by capillary condensation phenomena evidences broad pore size distribution [21], as expected when following the simple nitrate calcination preparation procedure. On the other hand, the lack of a plateau in the last points of adsorption branch also proves the presence of macroporosity. Comparing between CeO_2 and CuO/CeO_2 samples, the presence of CuO produces a lowering in the calculated BET surface [22] from bare CeO_2, in agreement with partial pore blocking upon Cu loading.

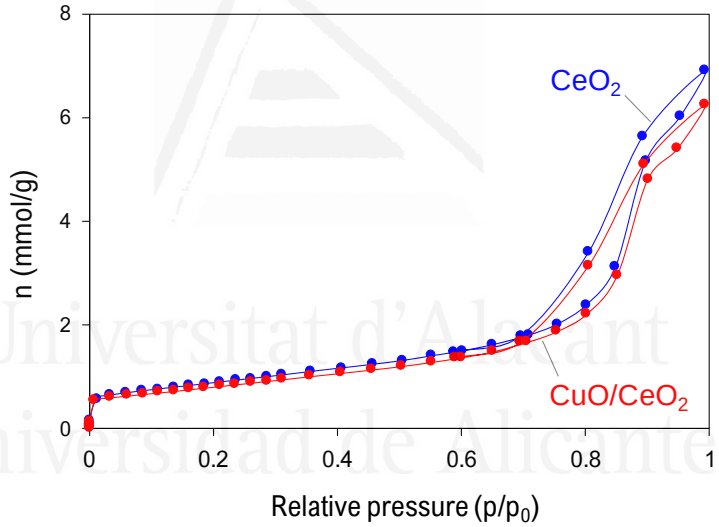

Figure 3.1. N_2 physisorption isotherms (-196ºC) from CeO_2 and CuO/CeO_2 samples.

The crystalline features were studied by means of X-ray diffraction (Figure 3.2), where both CeO_2 and CuO/CeO_2 samples display closely identical diffraction pattern fitting with standard CeO_2 fluorite (JCPDS no. 01-075-0120). The presence of CuO is observed by the appearance of characterisitc CuO tenorite tiny peaks (JCPDS no. 01-089-2529), which evidence good Cu dispersion on the CeO_2 support. On the other hand, attending to the calculated cubic cell parameter using the (111) peak, the Cu deposition leads to a slight lattice contraction, whereas crystallite size remains practically unchanged. These results are in agreement with well-reported values for CeO_2-based materials [23] and allow to infer that CuO is

mainly forming a finely disperse segregated phase on the CeO_2 surface, although minor Cu cations insertion in the CeO_2 lattice cannot be ruled out.

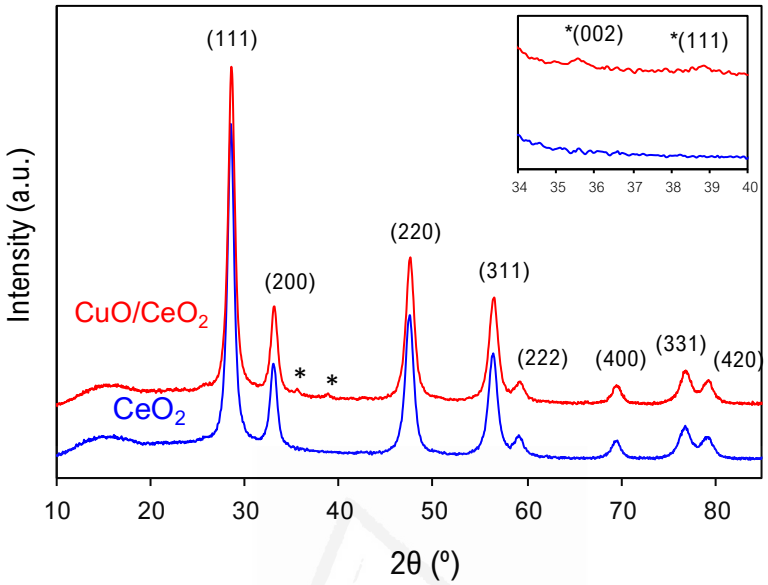

Figure 3.2. X-ray diffractograms recorded for CeO_2 and CuO/CeO_2 catalysts. **(*)** refers to CuO peaks.

Raman spectra of CeO_2 and CuO/CeO_2 samples are presented in Figure 3.3. The intensities have been normalized with the corresponding peak maxima of each spectrum, and since CuO/CeO_2 spectrum data had much less raw intensity, the bands appear broader than when compared to CeO_2.

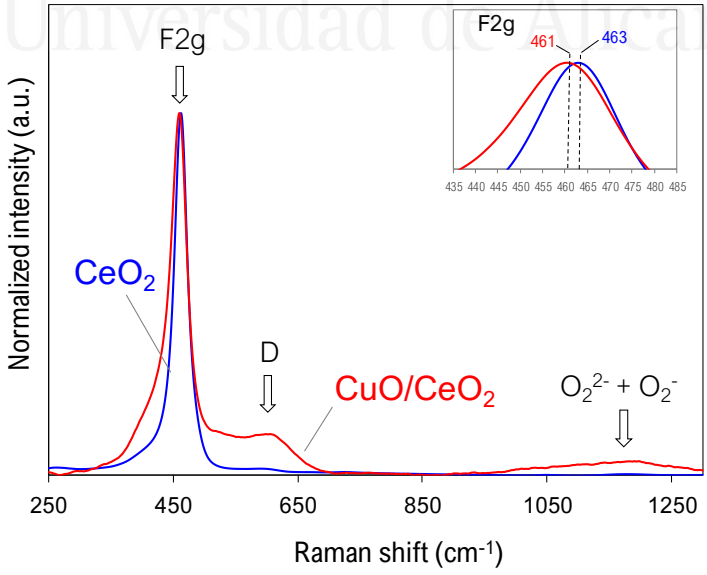

Figure 3.3. Raman spectra corresponding to CeO_2 and CuO/CeO_2 catalysts with main band assignations.

The well-reported characteristic Raman spectrum for CeO_2-based catalysts shows a main Raman line at 463 cm^{-1}, corresponding to the active F_{2g} mode due to the oxygen symmetric breathing vibration around Ce^{4+} ions in the bare fluorite-type CeO_2 lattice [23]. The presence of Cu in CuO/CeO_2 catalyst leads to a red shifting of the F_{2g} band to 461 cm^{-1} which is explained by the fluorite lattice expansion upon Ce^{IV} cations reduction by the Cu^{II}/Cu^{I} – Ce^{IV}/Ce^{III} labile redox interaction [3,24]. In agreement with this, the presence of charge-compensating oxygen vacancies is evidenced by additional bands, namely the D bands positioned around 570-600 cm^{-1}. Additionally, reactive oxygen species such as peroxides (O_2^{2-}) and superoxides (O_2^{-}) are detected in weak broad bands in the 950-1250 cm^{-1} range, which also corroborates the presence of defects in the lattice and the promotion active oxygen upon Cu loading.

In summary, the presence of Cu seems to activate surface lattice oxygen, as well as promotes the formation of defects, which leads to highly active sites with redox enhanced ability. Comparing with XRD data, since XRD and Raman spectroscopy exhibit different depth sensitivity, it can be concluded that the changes observed upon Cu loading are roughly superficial, being CuO forming segregated phase blocking CeO_2 interparticle spaces.

The reducibility of the catalysts was studied by means of H_2 temperature programed reduction experiments (Figure 3.4), and these show large differences between CeO_2 and CuO/CeO_2 behavior. The well-reported H_2-TPR profile from CeO_2 displays two main regions, namely a medium temperature range at *ca.* 550ºC, assigned to surface Ce^{IV} cations reduction; and a high tempertature process at *ca.* 800ºC, attributed to the reduction of bulk Ce^{IV} cations [24], being in both cases Ce^{III} the final state of cerium cations.

Universidad de Alicante

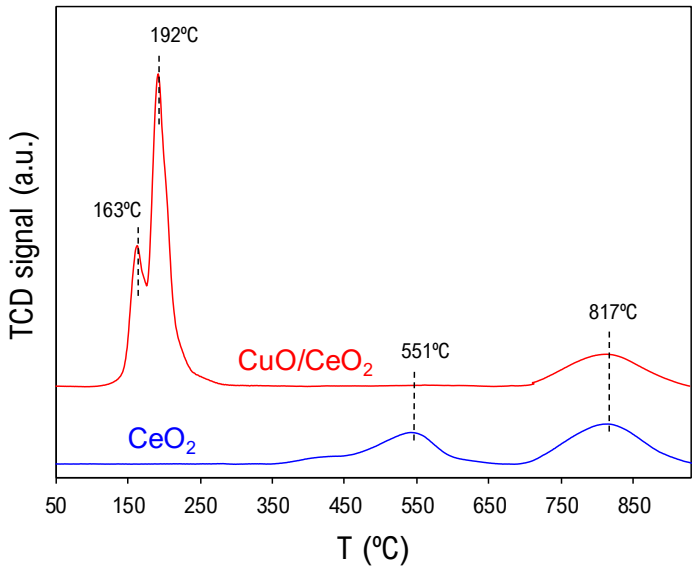

Figure 3.4. H_2-TPR profiles from CeO_2 and CuO/CeO_2 samples.

On the other hand, CuO/CeO_2 shows two sharp reduction peaks at low temperature, around 160 and 190ºC, attributed to the reduction of finely disperse and large CuO particles, respectively [25], although reduction of Cu^{II} in two consecutive steps, first to Cu^{I} and later to Cu^{0}, cannot be ruled out. It should be noticed that bare CuO sample starts reducing in the same conditions around 350ºC, so the anticipated reduction occuring in CuO/CeO_2 catalyst must be related to the synergistic Cu – Ce interaction, promoting the reducibility of copper species. Moreover, the labile redox exchange between Cu and Ce also affects to CeO_2 surface reduction, as it is much anticipated taking place evolved under CuO reduction peaks. The calibrated areas allow to calculate the excess of H_2 consumed in the two first peaks, and thus, eventually to estimate the total Ce^{IV} reduction in the whole profile. As described in Table 3.1, the reduction of CeO_2 does not occur in a higher extent when CuO is present, but in surface it does take place at much lower temperature, shifting from *ca.* 550 to below 200 ºC with concomitant CuO reduction.

In conclusion with the characterization results, the deposition of 5% Cu into the CeO_2 by impregnation conduces to extraordinary redox properties and the facile creation of oxygen vacancies, which are expected to supply great catalytic activity features to the CuO/CeO_2 catalyst.

3.3.1 CO-PROX catalytic activity tests in fixed-bed experiments

Figure 3.5 shows the CO-PROX catalytic activity results of the prepared CuO/CeO_2 catalyst on a first cycle of reaction without any

preteatment, which exhibits an excellent behavior in terms of CO conversion and CO selectivity, in agreement with extensive reported studies [1,26,27]. The different profiles present the expected shape according to the employed CO-PROX reaction conditions of experiment, that is, a stoichiometric O_2 excess of 2 (λ=2) with regards to CO, since it is well-known that λ determines CO oxidation activity and residual H_2 oxidation [28,29]. Provided that bare CeO_2 showed negligible CO conversion in the whole range of CO-PROX experiment, in contrast with CuO/CeO_2, it is not presented neither discussed anymore along the present Chapter.

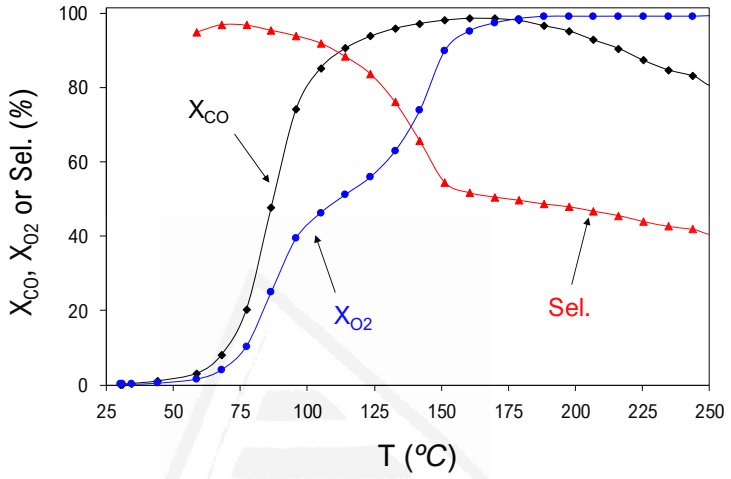

Figure 3.5. CO-PROX catalytic activity performance with CuO/CeO_2 catalyst in terms of **(black):** CO Conversion (X_{CO}); **(blue)** O_2 conversion (X_{O2}); and **(red):** CO selectivity profiles (Sel).

Hence, as described in Chapter 1, two different regions must be discerned from the CO-PROX catalytic response displayed in Figure 3.5, namely the CO selective (below *ca.* 110ºC) and the non-selective CO_2 regime (above *ca.* 110ºC), because of the competitive H_2 oxidation reaction. Such critical temperature is determined by H_2 oxidation on-set, process which presents higher activation energy than for CO oxidation [30]. As a result, when rising the temperature, H_2 oxidation process gains relevance and gradually hampers CO oxidation because of the limited O_2 supply, which eventually causes a CO conversion drop above *ca.* 175ºC. These temperature limits determine CO-PROX reaction course and allow to stablish an optimum temperature of operation with a CO activity and selectivity compromise, particularly suggested as 110ºC for the prepared CuO/CeO_2 catalyst.

Four consecutive CO-PROX reaction cycles were performed and proved the extraordinary stability of the CuO/CeO_2 catalyst along reutilization. Besides, a fifth long time-on-stream experiment allowed to conclude that CuO/CeO_2 also presents excellent stability during continuous CO-PROX operation. Additionally, the inhibition effect by CO_2, H_2O and

CO_2+H_2O mixture to the CO-PROX activity proving the acceptable tolerance and still great stability of CuO/CeO_2 catalyst. All those results will be presented and discussed in detail along Chapter 8 next to a critical comparison of the real opportunities of the potential CuO/Cryptomelane catalyst.

In the following Sections, thorough CO-PROX mechanistic study with CuO/CeO_2 catalyst by means of several complementary techniques is presented.

3.3.2 $^{36}O_2$ pulse isotopic experiments

In order to conduct a detailed study of the enrolment of lattice oxygen towards CO-PROX reaction mechanism, isotopic $^{36}O_2$ pulses were injected in a reactor with CuO/CeO_2 catalyst and flowing CO + H_2 mixture at the set of temperatures: (i) 75ºC, representative for low CO conversion regime; (ii) 100ºC, representative for high CO conversion and high CO selectivity regime; and (iii) 150 ºC, when CO conversion is maximum, but CO selectivity is moderate because of the concomitant H_2 oxidation side reaction.

Figure 3.6 collects quantitative data obtained by the MS analyses after $^{36}O_2$ pulses. First, the overall distribution of the released CO_2 and H_2O gas products is in agreement with results achieved from fixed-bed experiments as H_2O contribution increases with temperature according to gradual CO selectivity loss. On the other hand, for all temperatures tested, no O_2 species release was registered, since the strongly reducing conditions of experiment are setting a highly O-deficient surface in CuO/CeO_2 catalyst, which would act as an oxygen trap for the incoming molecules while restoring O sites.

With regards to CO_2 and H_2O isotopic product distribution, the normalized quantification of each individual isotope molecule has been conducted in separate CO_2 and H_2O mass balances. The specific MS signals followed after the pulse allow to trace the CO and H_2 oxidation path mechanism. Firstly, with regards to CO oxidation, m/Q 44 CO_2 ($^{16}OC^{16}O$ non-isotopic) would involve lattice O abstraction and anionic vacancy formation, as an evidence of CO oxidation taking place via Mars-van Krevelen (MVK) mechanism; whereas when m/Q 46 ($^{18}OC^{16}O$ isotopic), the CO oxidation is taking place involving ^{18}O* species adsorbed in the vicinity of CO; and finally, m/Q 48 ($^{18}OC^{18}O$ isotopic by double exchange) involves a rather complex mechanism consisting of the breakup of a triple C-^{16}O bond, and the creation of two double C-^{18}O bonds by the interaction of ^{18}O* and C* neighboring sorbed species, assuming O_2 dissociative chemisorption. On the other hand, attending to H_2 oxidation products, it has been monitored m/Q 18 signal (non-isotopic $H^{16}OH$), which evidences H_2 oxidation occurring via MVK mechanism; and m/Q 20 signal (isotopic $H^{18}OH$), attributed to H_2 oxidation with adsorbed ^{18}O* species.

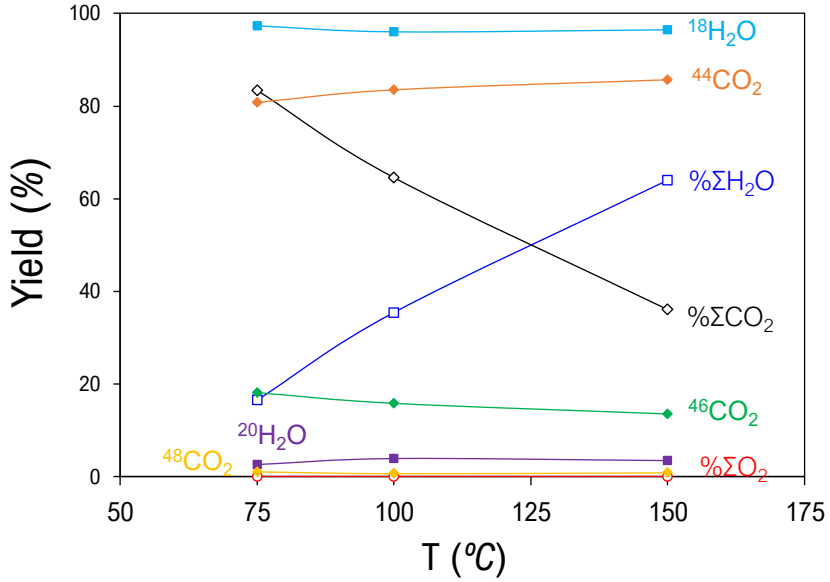

Figure 3.6. MS integrated signals after $^{36}O_2$ pulse in CO-PROX conditions with CuO/CeO_2 catalyst at 75, 100 and 150ºC. **Open symbols:** normalized overall released products (ΣX): CO_2 **(diamonds)**; H_2O **(squares)**; and O_2 **(circles)**. **Solid symbols**: isotopic distribution among CO_2 **(diamonds)** and H_2O **(squares)** species.

According to Figure 3.6, clearly most of the released products are non-isotopic ($^{44}CO_2$ and $^{18}H_2O$) for both CO and H_2 oxidation reactions, which proves, as expected, oxidation mechanisms involving lattice oxygen rather than molecular adsorbed oxygen (MVK). The temperature is due to increase oxygen exchange capacity of the catalyst, *i.e.*, major contribution of non-isotopic products (m/Q 44 + 18) with regard to the isotopic ones (m/Q 46 + 48 + 20), but only a slight increase is observed provided the narrow temperature window for the screening of the pulses.

Nevertheless, the most interesting insights are offered by the analysis of the time-resolved products release since they give relevant information regarding the kinetics of the ongoing processes. Figure 3.7 shows the total O-normalized MS signals evolved after $^{36}O_2$ pulses at 75, 100 and 100 ºC.

In general, according to Figure 3.7, the temperature affects the profiles of the products release by a sharpening in their corresponding evolved curves, which is attributed to a faster desorption. However, the most relevant from these profiles is the clear delay in H_2O release with regards to CO_2, as well as the large broadening of H_2O signal. This is consistent with a major surface retention of water molecules due to a less favored H_2O desorption when compared to CO_2, which suggests certain degree of H_2O accumulation on the CuO/CeO_2 catalyst surface during CO-PROX reaction.

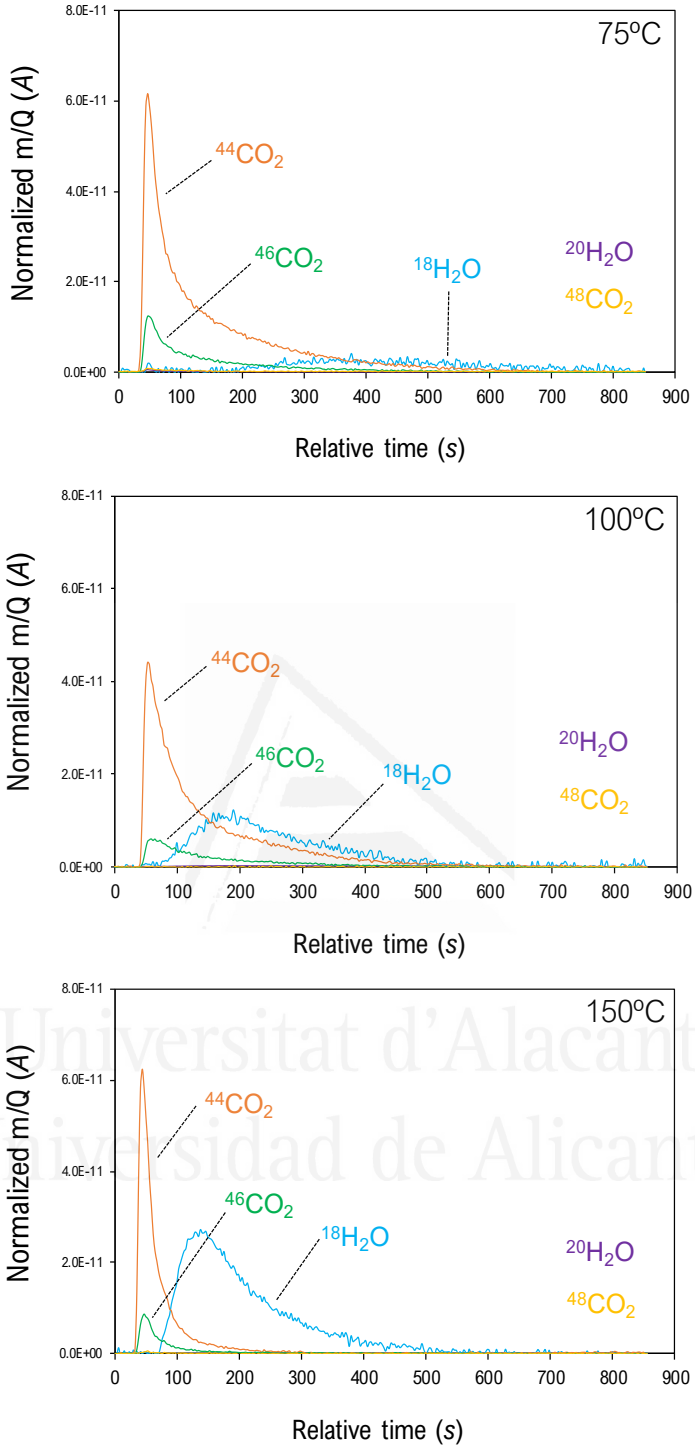

Figure 3.7. MS signals after $^{36}O_2$ pulses in CO-PROX conditions with CuO/CeO_2 catalyst at 75, 100 and 150 ºC. The zero-time has been established after the pulse.

In summary, isotopic pulse experiments allow to unequivocally conclude that CuO/CeO_2 catalyst undergoes MVK mechanism in both CO

and H_2 oxidation reactions occurring in CO-PROX environment, which confirms the active role of lattice oxygen. On the other hand, the CuO/CeO_2 catalyst displays an apparent H_2O retention which could possibly be blocking surface CO oxidation active sites when H_2 oxidation is taking place.

3.3.3 *In-situ* Raman experiments

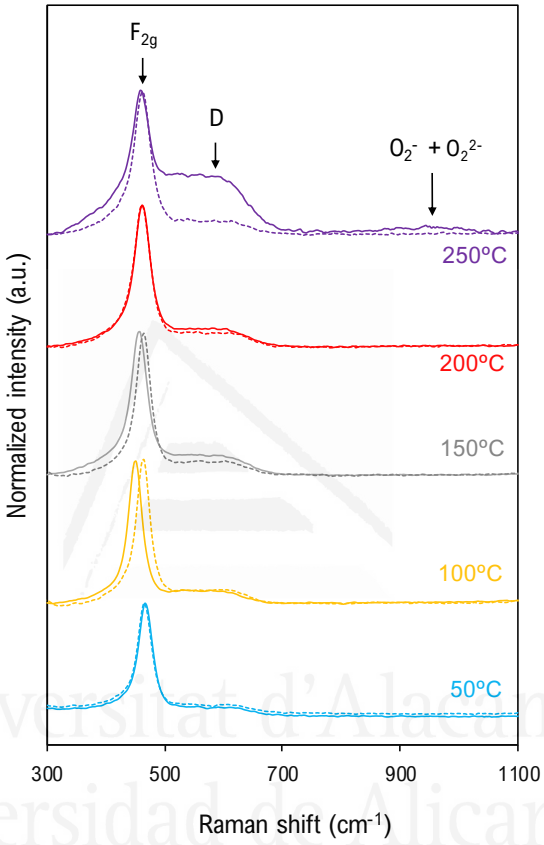

Figure 3.8. Raman spectra for CuO/CeO_2 catalyst recorded at different temperatures in 100 ml/min of He **(dotted lines)**; and CO-PROX conditions **(solid lines).**

Figure 3.8 shows the Raman spectra recorded at different temperatures in He and CO-PROX conditions, showing the characteristic features corresponding to CuO/CeO_2 as described in Section 3.1. The spectra measured in He provide the inherent lattice thermal expansion, which leads to a shift in the F_{2g} band position from 464 to 461 cm^{-1} above 200ºC, and a gradual increase in the D defects band relative intensity, as evidenced in Figure 3.9.

Universitat d'Alacant
Universidad de Alicante

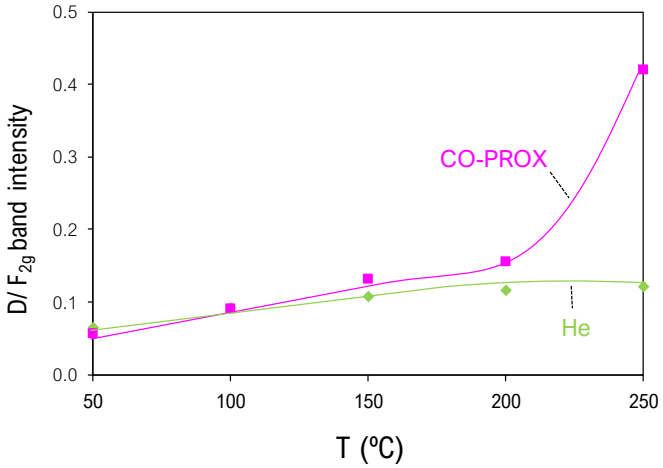

Figure 3.9. D (540-600 cm^{-1}) / F_{2g} (460 cm^{-1}) band intensity ratios from Raman spectra at each temperature in He and CO-PROX conditions.

Regarding the effect of CO-PROX atmosphere, the D band grows substantially once overcome 200ºC, which proves an extensive oxygen vacancy generation in the CeO_2 lattice upon the occurring CO and H_2 oxidation reactions via MVK mechanism in these conditions. Nevertheless, since the on-set for both processes is much lower according to the CO-PROX catalytic activity tests conducted in fixed-bed experiments, it may be tentatively deduced that below certain temperature boundary the O_2 uptake is efficiently restituting lattice oxygen keeping in equilibrium the processes of oxygen vacancy creation and refilling CuO/CeO_2.

On the other hand, the F_{2g} band in CO-PROX conditions shows a more complex behavior with regards to the control spectra in He atmosphere at the same temperatures. Whereas at 50 ºC both spectra are identical, at 100 ºC the CO-PROX spectrum presents a very sharp shifting to the red in the F_{2g} band which evidences lattice expansion upon partial Ce^{IV} reduction. However, this lattice expansion is not encompassed with the detection of oxygen vacancies in a respective D band. Rising the temperature above 100 ºC leads to a lowering into the red-shifting of the F_{2g} band, while D band does not significatively grow. The uncorrelation between the D bands appearance and F_{2g} band shifting can be tentatively explained as the uncoupling of both Ce cations reduction and oxygen vacancy formation phenomena by the uncompensation of CuO/CeO_2 reduction process and lattice oxygen abstraction via MVK mechanism because of an inefficient O_2 uptake. That is to say, at low temperatures the catalyst may be partially more reduced despite O-lattice recovery is taking place. According to this, incoming O would be accommodated in the lattice while Ce cations would remain partially reduced because of the ongoing CO-PROX reaction. When the temperature increases, both processes are better coupled as F_{2g} band is gradually recovering intial position, and eventually at 200 ºC fits with He-recorded

spectrum. Finally, at 250ºC the catalyst is reduced in average because of the high reaction rate and D band is clearly observed while concommitant F_{2g} band red-shifting takes place.

Nevertheless, this observation can be simply anecdotal because of the specific conditions of the experiment, since the sample results locally overheated at the spot irradiated by the laser during the analyses, which may lead to an undefined effect into CeO_2 local reduction, and thus, an overestimation of such process, being more important at lower temperatures. In anycase, the most relevant insights of these characterization results is the observation of extensive CuO/CeO_2 catalyst reduction upon CO-PROX reaction, much after CO and H_2 oxidation reactions begin.

In order to elucidate reversible reduction-oxidation pathways and track the oxidation state of Cu and Ce species in CuO/CeO_2 catalyst during CO-PROX reaction mechanism, NAP-XPS experiments were conducted and the most relevant results are presented in the following Section 3.3.5.

3.3.4 CO-PROX *operando* NAP-XPS experiments

CO-PROX reaction conditions were reproduced in a NAP-XPS analysis chamber up to 100% of O_2 conversion (X_{O2}). It should be taken into account that the catalytic activity dependence with temperature is very different for the CuO/CeO_2 catalyst in the operando NAP-XPS experiment when compared to the fixed-bed reactor catalytic activity tests or in situ Raman experiments, as Figure 3.10 reveals. Thus, in the CO-PROX *operando* NAP-XPS experiment it is necessary to reach much higher temperatures to achieve total O_2 consumption.

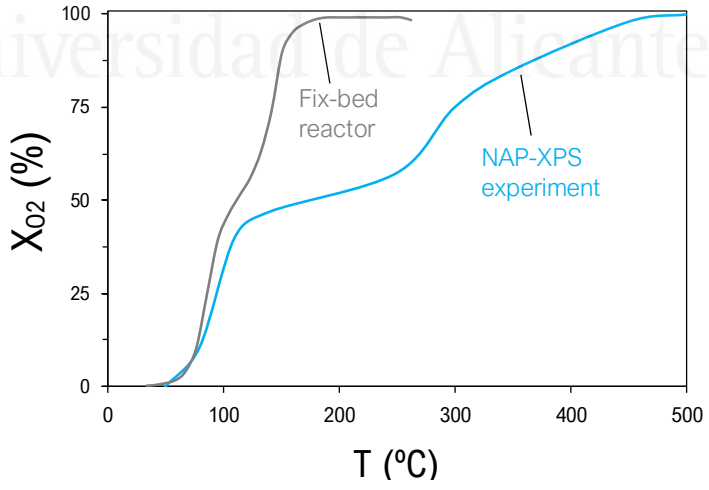

Figure 3.10. O_2 conversion (X_{O2}) profiles along temperature for CuO/CeO_2 catalyst in the CO-PROX reaction conditions: **(grey)** 100 ml/min, 1 bar in the fixed-bed reactor tests; **(blue)** 30 ml/min, $1 \cdot 10^{-3}$ bar in the NAP-XPS experiment.

As previously described, the double S-shaped curve is a consequence of the separate on-sets for CO and H_2 oxidation reactions and the chosen stoichiometric O_2:CO excess of 2 (λ). In the case of the NAP-XPS experiment, the on-set for H_2 oxidation is much delayed probably due to the large difference of total working pressure, while CO oxidation apparently remains selective in a wider temperature window. Accordingly, the following XPS spectra showed in this Section 3.3.5 at the selected temperatures are representative of different reaction stages.

On the other hand, the Ce3d and Cu2p XPS regions were scanned using two different photon energies, namely 1082 and 1372 eV, and the information provided from them should be related to the description of different surface depths in the catalyst according to inelastic mean free path (IMFP) calculations [31–33]. Thus, whereas the differences are moderate, it is well-known that the lower the X-ray energy, the lower the IMFP and then, the depth of the analysis. Nevertheless, for the sake of brevity, only the spectra recorded at 1082 eV energies are plotted, whereas compiled results from both energies are included in Table 3.2. Furthermore, XPS spectra were also measured during the oxidizing pretreatment in O_2/N_2 mixture at 200 ºC for comparative reasons, as an indicator of the initial oxidation state of the catalyst. Conversely, the CO-PROX spectra at 50 ºC did not show good resolution because of the moderate conductivity of the gas mixture in this low temperature situation, resulting in severe surface charging and eventually, diffucult deconvolution fitting because of the broadening of the peaks.

Moreover, the XPS spectra from O1s and C1s regions were measured and analyzed but are not included in the present Chapter for the sake of brevity since their output information is more related to the surface chemistry changes of CuO/CeO_2 catalyst along CO-PROX reaction course, rather than redox processes involved in the mechanism, which is the main topic herein. Briefly, surface oxygen species gain considerably importance during CO-PROX reaction progress, while carbonaceuos species tend to disappear. This observation matches with H_2O accumulation predicted by isotopic experiments, and will be discussed in the following chapters from the results brought by DRIFT spectroscopy, which is the suitable technique to conduct the characterization of sorbed species.

Figure 3.11 shows 3d XPS region (1082 eV) of CuO/CeO_2 catalyst in different conditions and the assignment of the multiple contributions based on the standard nomenclature provided by Burroughs [29]. Hence, the XPS spectrum of the $3d_{5/2}$ Ce level is composed of three compounds for CeO_2 and two compounds for Ce_2O_3, so the proper interpretation of partially reduced CeO_2 samples needs to consider the deconvolution of ten structures under the same spectrum, according to spin-orbit coupling ($3d_{5/2}$ + $3d_{3/2}$) [34]. As it shows, since the energy separation between v and u terms is small, the Ce3d XPS spectrum is quite difficult to analyze.

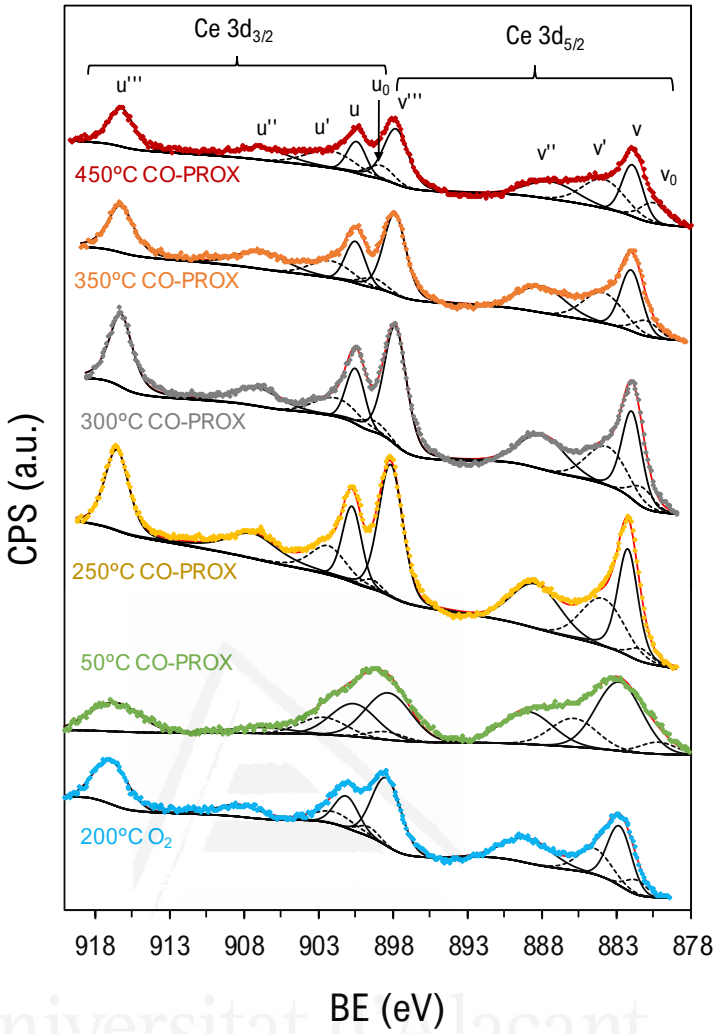

Figure 3.11. Ce3d XPS region of CuO/CeO_2 catalyst in O_2 and CO-PROX reaction conditions at different temperatures. Dotted lines are the contribution of Ce^{3+} species from the average deconvolution fitting [34].

In this regard, according to the type of assignation used, a gradual reduction of CeO_2 will result in the increase of v_0, u_0 and v', u' structures with the expense of the decrease of the rest. Thus, the Ce^{3+} content of the samples can be measured by the formula given by Equation 2.11, introduced in Chapter 2, as a simple percentual calculation for these contributions attributed to Ce^{3+} species among the average [35]. Results of Ce^{3+} estimation on the catalyst in the spectra under both source energies 1082 and 1372 eV, are presented altogether in Table 3.2, which shows that Ce^{3+} content remains constant around 20% until 450 ºC, where partial reduction of the CeO_2 occurs increasing Ce^{3+} up to 33%. Comparing both source X-ray energies, it can be concluded that with the lower energy, it is possible to discern much better this partial reduction, which evidences the very high superficial degree of this reducing process since according to our IMFP

estimations, the target depth difference between both energies should not overcome 0.5 nm [33].

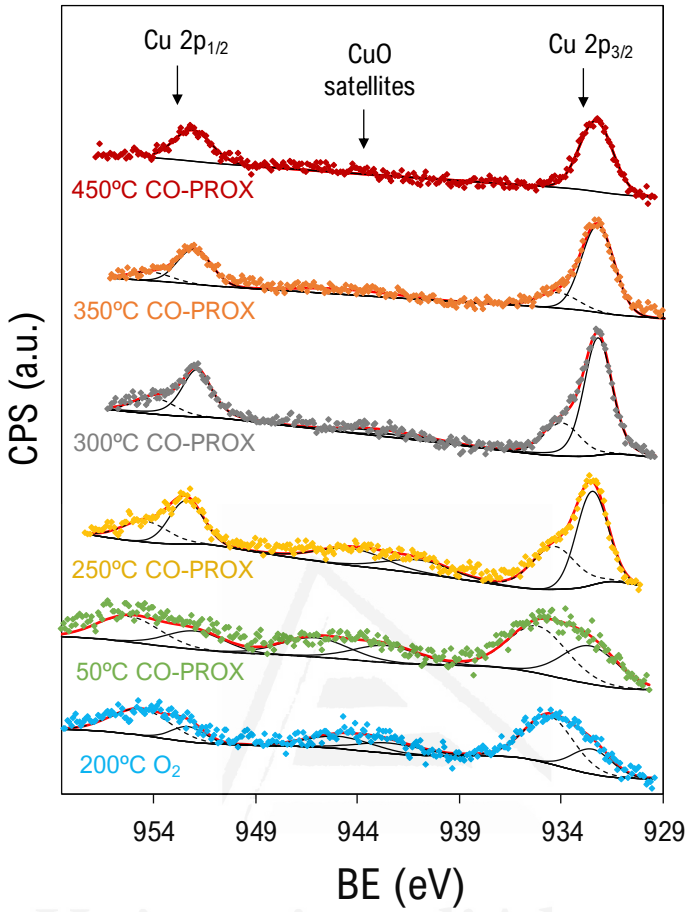

Figure 3.12. Cu2p XPS region of CuO/CeO_2 catalyst in O_2 and CO-PROX reaction conditions at different temperatures. **Caption:** Cu^{2+} contribution **(dotted line)**; Cu^0+Cu^+, or reduced Cu contribution **(solid line)**.

Cu2p XPS spectra (Figure 3.12) show $Cu2p_{3/2}$ and $Cu2p_{1/2}$ peaks, as well as the well-reported shake-up satellite characteristic of Cu^{2+} presence, which is used by some authors to provide qualitative fashion [36,37]. Since $Cu2p_{3/2}$ and $Cu2p_{1/2}$ peaks are well resolved in the Cu2p XPS spectrum, it is possible to analyze and focus on only the $Cu2p_{3/2}$ fraction, which enables much easier analysis when compared to Ce3d region. Thus, $Cu2p_{3/2}$ peak could be theoretically deconvoluted into three components, attributed to Cu^0, Cu^+ and Cu^{2+} contributions, respectively [38,39]. Unfortunately, the statistical separation of the $Cu2p_{3/2}$ peak positions for Cu^0 and Cu^+ is too little to discern between both reduced oxidation states, so it is convenient to perform a two-peak fitting using the precise constraits on BE, FWHM and peak-shape parameters, representative for (1) oxidized copper (CuO); and (2) undistinguisable reduced copper species (Cu and Cu_2O).

It is worth to mention that for total resolution, the Cu $L_3M_{4.5}M_{4.5}$ Auger spectral line should be complementary analyzed and properly presented along with $Cu2p_{3/2}$ in the well-reported Wagner plots [40–42]. However, given the complex nature of the X-ray varying energy NAP-XPS experiments, this Auger line determination was not conducted, and Cu resolution was essentially done through $Cu2p_{3/2}$ fitting analysis. The semi-quantitative estimation of average oxidation state of surface copper species is presented in Table 3.2, showing that copper is gradually being reduced until achieving a total reduced state (Cu^+ and/or Cu^0) at the highest temperature, whereas there is not much influence on the X-ray source energy. Interestingly, even in O_2 conditions during the oxidation pretreatment, there is a significative Cu^I contribution which should be attributed to a promoted reducibility by the redox interplay between Ce and Cu ions.

It should be pointed out that while in CO-PROX conditions both 1082 and 1372 eV energies provide highly correlated results, in O_2/N_2 mixture there are evident discrepancies, being Cu noticeably more reduced in the most external profile. Attending to this, the presence of that large reduced Cu content in CuO/CeO_2 catalyst in such oxidizing conditions is very questionable, given the well-known CuO facile oxidation. Consequently, it can be tentatively described that those differences are due to Cu – Ce synergistic interactions and labile Cu^{2+}/Cu^+ equilibrium upon Ce^{4+}/Ce^{3+} redox exchange in the most external interfacial layers.

Table 3.2. Semi-quantitative determination from Ce3d, Cu2p XPS spectra and Cu L-edge XAS data from XANES analysis.

Conditions	XPS Ce^{3+} (%)		XPS Cu^{2+} (%)		Cu^{2+} (%)
	1082 eV	1372 eV	1082 eV	1372 eV	XANES
O_2/N_2 200ºC	20	22	66	75	88
CO-PROX 50ºC	21	18	58	57	80
250ºC	22	18	38	37	76
300ºC	22	19	30	28	66
350ºC	24	20	21	20	58
450ºC	33	24	0	0	40

Note: Notice differences among XPS and XANES Cu^{II} determination, attributed to the different environments: surface and bulk, respectively.

Cu L-edge XAS measurement of the CuO/CeO_2 catalyst was conducted in complement with NAP-XPS characterization during CO-PROX reaction. The recorded spectra are presented in Figure 3.13, and these exhibit the L_3 and L_2 pre-edge absorption peaks centered at *ca.* 930 and 950 eV, respectively, which correspond to the electric dipole allowed 2p → 3d transition [43,44].

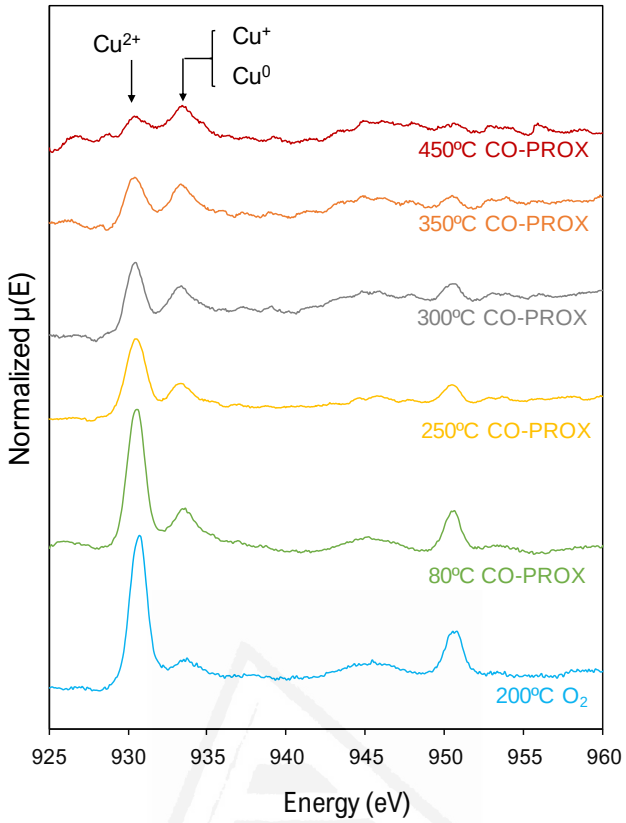

Figure 3.13. Normalized and flattened Cu L-edge XANES spectra of CuO/CeO_2 catalyst in different conditions.

Hence, the resulting L-edge spectrum of the obtained CuO/CeO_2 catalyst is composed of proportional contributions of CuO, Cu_2O and Cu characteristic spectral features. Namely, both CuO and Cu_2O have well-resolved strong L_3 absorption eges, which were assigned with the peaks centered at 930.8 and 933.7 eV, respectively, in agreement with reported values [45,46]. On the contrary, Cu develops an unambiguous fingerprint that allows to identify traces of Cu among an average of mixed Cu_xO species, although L_3 absorption edge would appear overlapped under the corresponding for Cu_2O around 933.5 eV.

Thus, Near Edge XAS characterization provides a measure of the oxidation state of bulk copper particles present in the catalyst during CO-PROX reaction course. In this regard, the intensity ratios between the L_3 components with centers at *ca.* 930.7 and 933.7 eV is used herein as a qualitative indicator of the copper reduction degree and the results are presented in Table 3.2.

Considering that XAS is a bulk characterization analysis, in complement with XPS analysis, provides a combined description of the copper oxidation state along particle depth. Accordingly, as evidenced in

Table 3.2, Cu reduction is partial in the bulk, but total in surface of the Cu-rich particles.

Finally to correlate the XPS results with the CO-PROX catalytic activity, X_{CO} was estimated according to X_{O2}, considering the disagreement between fixed-bed reactor experiments and operando NAP-XPS, and thus, CO selectivity along the temperature profile. Hence, Figure 3.14 gathers Ce^{III} and reduced Cu species evolution determined by NAP-XPS and XANES for the CuO/CeO_2 catalyst plotted against X_{O2}.

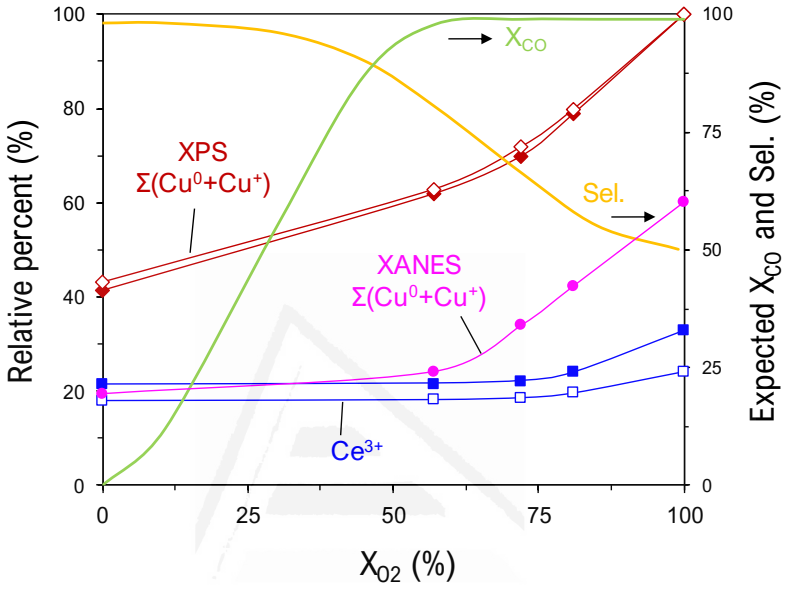

Figure 3.14. Distribution of surface Ce^{3+} **(squares)** and reduced Cu species **(diamonds)** present in the CuO/CeO_2 catalyst during CO-PROX operando NAP-XPS experiment with the irradiation sources of 1082 eV **(solid symbols)**; and 1372 eV **(open symbols).** XANES (bulk) Cu species distribution **(circles)**.

In summary, gradual surface reduction of Cu species occurs along the CO-PROX reaction course, while only moderate and very superficial Ce reduction is observed for the CeO_2 support at the maximum X_{O2}, that is with total X_{CO} and concommitant H_2 oxidation reaction. In agreement with previous studies, the presence of reduced copper is closely connected to H_2 oxidation reaction [4,8,47], as it fits with CO selectivity decay.

Since surface Cu^I abundance is extraordinarily high at the beginning of the CO-PROX reaction, CuO should be partially reduced on surface upon CO contact, resulting in a very anticipated, but limited, CO oxidation activity. Rising the temperature leads to an enhancement of the reaction rate, which occurs via MVK mechanism by means of lattice-O abstraction and eventually provokes a gradual reduction of Cu_xO particles, from the reactant area (surface) to the internal part of the particles (bulk). At the maximum measured temperature with total X_{O2} and yet maximum X_{CO}, there is no trace of CuO on surface, and in this situation, the CuO particles present a (Cu^0/Cu)

mixed reduced surface. It is reasonable to think that Cu^0 component would constantly rise along with temperature increase, so that, overcoming certain reduction degree, H_2 dissociation in Cu sites is more activated and H_2 oxidation reaction is boosted, which additionally would create more reduced Cu sites.

In this scenario, it should be expected that X_{CO} would have decreased at higher temperatures at expenses of higher H_2 oxidation rate by a larger extension on the Cu reduction. Additionally, we would have expected an increasing Cu bulk reduction degree. Unfortunately, we did not go so far at increasing the temperature in the NAP-XPS experiments given the difficulties to reach such high temperatures to overcome by large total X_{O2} point.

On the contrary, CeO_2 remains oxidized in an equilibrium state until surface CuO totally disappears. The disagreement between output from 1082 and 1372 eV energies suggests that Ce reduction is strictly limited to the most external surface, but likewise, would be expected to reach higher extension with higher temperatures as proven by *in situ* Raman experiments. Interestingly, considering that the synergistic Cu – Ce interactions should occur in the periphery of the intimate contacting CeO_2 and Cu_xO particles, *i.e.* the finest surface, this result can be tentatively taken as an evidence of O transference from CeO_2 to the partially reduced Cu_xO particles, acting as an oxygen supply to restitute active O.

Remarkably, this result allows to infer that CuO sites are important to keep a direct O_2 uptake in the O vacancy generation – restitution equilibrium. Since O vacancy generation gains importance with the reaction course, the equilibrium is uncompensated and eventually CuO disappears. In this situation, given the scarcity of active O in the Cu-rich phase, CeO_2 transfers lattice O in the Cu – Ce interfacial points, trying to compensate and prevent total reduction to metal Cu. Consequently, O_2 recovery is meant to occur directly from O_2 gas to the CuO particles, but not in the highly reduced Cu_xO sites, composed mainly of Cu and Cu_2O species. When such reduction degree is achieved, CeO_2 should assist into the lattice O regeneration providing mobile O through the Cu – Ce interface.

In summary, according to the main results presented so far, the CeO_2 support exhibits essentially two important roles: (1) intrinsically stabilizes Cu^I sites in the interfacial points, and thus, enables enhanced and anticipated CO oxidation activity; and (2) aids into O_2 uptake once Cu_xO particles present a reduced state and CuO is no longer on surface to proceed with lattice-O recovery.

3.3.5 Density Functional Theory (DFT) Calculations

As a final remark to be included in this study, DFT calculations were conducted for the modelling of CeO_2(111), CuO(111) and Cu_2O(111)

ssurface slabs, representative for the most abundant facets present in the CuO/CeO_2 catalyst. Figures 3.15a-c show the optimized structures:

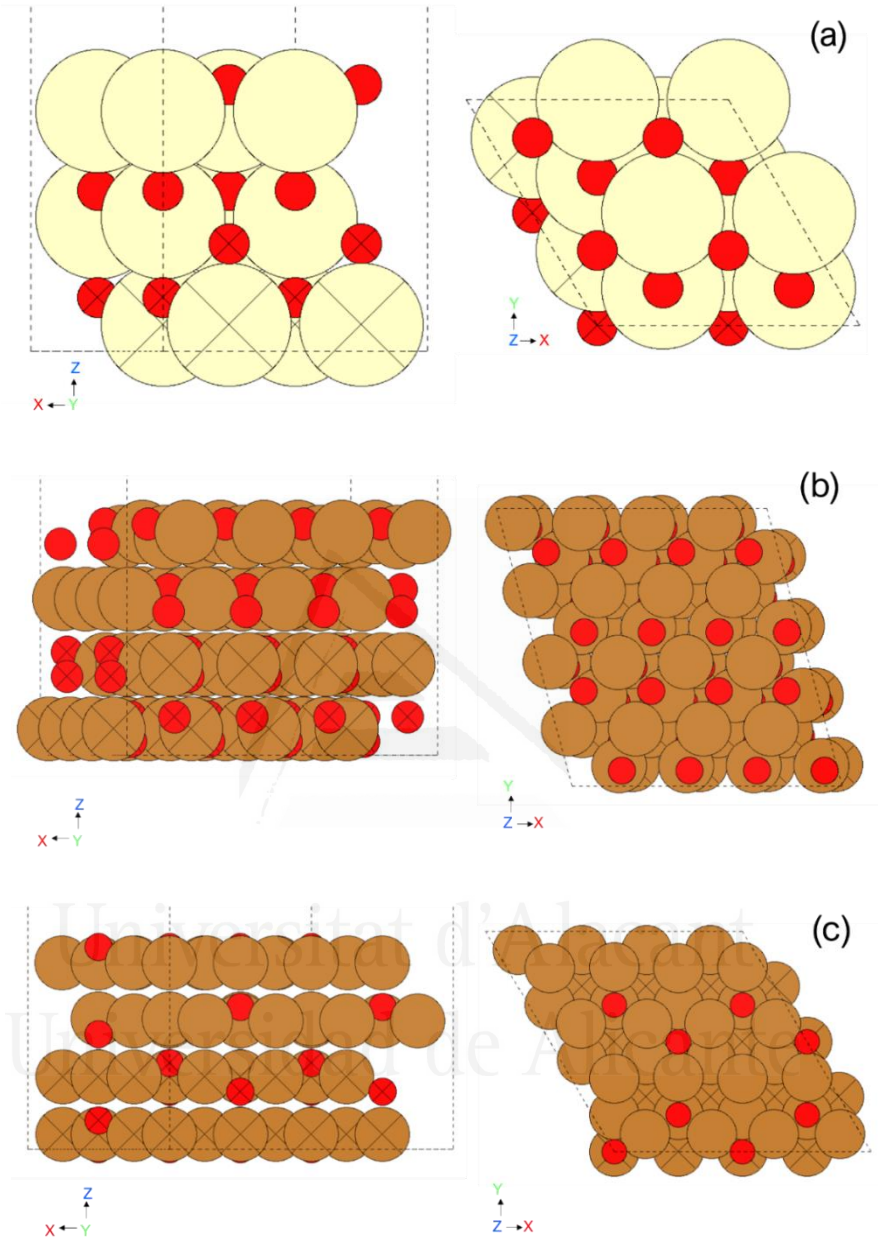

Figure 3.15. (a) $CeO_2(111)$ surface slab with 12 Ce **(yellow)** and 24 O **(red)** ions; **(b)** CuO(111) surface slab with 64 Cu **(brown)** and 64 O ions; **(c)** $Cu_2O(111)$ surface slab, 64 Cu and 32 O ions. **Note:** (X) stands for fixed bulk positions.

Although it is well-known the hetereogenous and imperfect nature of this material, the modelling of the most common surfaces present individually can be taken as a reliable indicative of the properties of each active sites. On each surface slab, a surface oxygen vacancy was created and the slab left

afterwards was optimized searching for the most favorable electronic and ionic configurations. Thus, Table 3.3 collides the lowest energies found for the formation of an O-vacancy on these slabs, showing the trend as follows: CuO(111) > CeO_2(111) > Cu_2O(111).

Table 3.3. Energies for the O vacancy formation in (111) surface slabs of CeO_2, CuO, and Cu_2O crystal structures.

	CeO_2(111)	CuO(111)	Cu_2O(111)
O-vacancy formation energy (eV)	2.22	2.40	1.97

These energies are in agreement with the previously reported values, although they are highly dependent on the localization of the two extra electrons left upon O abstraction [48–50]. On the other hand, it is evident that the higher the energy for the oxygen vacancy formation, the more facile lattice oxygen restitution when the O-deficient slabs are set in contact with O_2 atmosphere. Therefore, attending to the observed trend it is concluded that O-lattice recovery should prevail in CuO, when present, with regards to CeO_2, while once CuO is reduced to Cu_2O as CO-PROX reaction is taking place, the reoxidation through CeO_2 is more favorable.

Hence, in agreement with the experimental approach, the theoretical study corroborates the proposed mechanism for the reoxidation of the CuO/CeO_2 catalyst during CO-PROX reaction course, *i.e.* the O-lattice compensation with incoming O_2 molecules. As a summary, Figure 3.16 presented below shows a graphical abstract of the ongoing processes.

Universitat d'Alacant
Universidad de Alicante

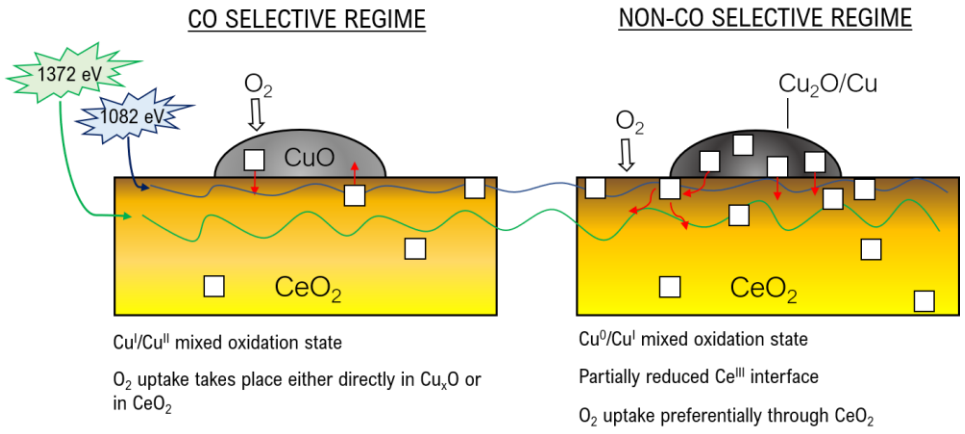

Figure 3.16. Graphical scheme of the molecular processes occurring in the CuO/CeO_2 catalyst in CO-PROX reaction. **Caption: (□)** stands for O vacancy.

3.4 Conclusions

Along the present Chapter, relevant data regarding the CO-PROX reaction mechanism study with CuO/CeO_2 catalyst has been discussed. The main insights and key points aborded are summarized in the following:

(1) The simple preparation of conventional CuO/CeO_2 catalyst through nitrate calcination and impregnation results in an excellent performance in terms of CO conversion and CO selectivity in CO-PROX reaction.

(2) The promoted Cu and Ce reducibilities by means of the synergistic Cu – Ce redox interactions, result in labile electronic exchanges between CuO and CeO_2 phases that activate surface oxygen from the lattice towards the MVK-based catalytic oxidation processes.

(3) The labile Cu^{2+}/Cu^{+} – Ce^{3+}/Ce^{4+} redox interplay allows a great reversibility in the reduction – oxidation balanced processes occuring, and thus, confer to the CuO/CeO_2 catalyst a large stability and cyclability.

(4) The CO oxidation activity is claimed to occurr on Cu^{+} surface states in the surface of CuO particles, whose formation is favored in the active Ce – Cu interface, whereas H_2 oxidation is activated when Cu^{0} sites are present at higher reduction degrees.

(5) In the CuO/CeO_2 catalyst, the role of CeO_2 is to promote the formation and stabilization of Cu^{I} species, which leads to a great activity and a positive broad CO selective regime in CO-PROX reaction.

(6) During CO-PROX process, oxygen vacancies are being created in the CuO_x particles, claimed main active sites, and it is predicted that the catalyst reoxidation occurs directly on these particles via CuO-related sites.

(7) When surface CuO species are not present because of extensive reductionin an advanced CO-PROX reaction degree, CeO_2 assists in the O_2 uptake since it is able to transfer highly mobile lattice O through the Ce – Cu interface to the Cu_xO particles palliating massive copper reduction.

References

[1] M. Konsolakis, The role of Copper–Ceria interactions in catalysis science: Recent theoretical and experimental advances, Appl. Catal. B Environ. 198 (2016) 49–66.

[2] A. Bueno-López, Diesel soot combustion ceria catalysts, Appl. Catal. B Environ. 146 (2014) 1–11.

[3] A. Trovarelli, Catalytic Properties of Ceria and CeO_2-Containing Materials, Catal. Rev. 38 (1996) 439–520.

[4] A. Martínez-Arias, D. Gamarra, A. Hungría, M. Fernández-García, G. Munuera, A. Hornés, P. Bera, J. Conesa, A. Cámara, Characterization of Active Sites/Entities and Redox/Catalytic Correlations in Copper-Ceria-Based Catalysts for Preferential Oxidation of CO in H_2-Rich Streams, Catalysts. 3 (2013) 378–400.

[5] A. Martínez-Arias, M. Fernández-García, J. Soria, J.C. Conesa, Spectroscopic study of a Cu/CeO_2 catalyst subjected to redox treatments in carbon monoxide and oxygen, J. Catal. 182 (1999) 367–377.

[6] X. Tang, B. Zhang, Y. Li, Y. Xu, Q. Xin, W. Shen, CuO/CeO_2 catalysts: Redox features and catalytic behaviors, Appl. Catal. A Gen. 288 (2005) 116–125.

[7] A. Martínez-Arias, A. B. Hungría, G. Munuera, D. Gamarra, Preferential oxidation of CO in rich H_2 over CuO/CeO_2: Details of selectivity and deactivation under the reactant stream, Appl. Catal. B Environ. 65 (2006) 207–216.

[8] C.S. Polster, H. Nair, C.D. Baertsch, Study of active sites and mechanism responsible for highly selective CO oxidation in H_2 rich atmospheres on a mixed Cu and Ce oxide catalyst, J. Catal. 266 (2009) 308–319.

[9] L. Yang, S. Zhou, T. Ding, M. Meng, Superior catalytic performance of non-stoichiometric solid solution $Ce_{1-x}Cu_xO_{2-\delta}$ supported copper catalysts used for CO preferential oxidation, Fuel Process. Technol. 124 (2014) 155–164.

[10] J. Li, Y. Han, Y. Zhu, R. Zhou, Purification of hydrogen from carbon monoxide for fuel cell application over modified mesoporous CuO–CeO_2 catalysts, Appl. Catal. B Environ. 108–109 (2011) 72–80.

[11] A. Hornés, A.B. Hungría, P. Bera, A. López Cámara, M. Fernández-García, A. Martínez-Arias, L. Barrio, M. Estrella, G. Zhou, J.J. Fonseca, J.C. Hanson, J.A. Rodriguez, Inverse CeO_2/CuO catalyst as an alternative to classical direct configurations for preferential oxidation of CO in hydrogen-rich stream., J. Am. Chem. Soc. 132 (2010) 34–35.

[12] J.S. Elias, K.A. Stoerzinger, W.T. Hong, M. Risch, L. Giordano, A.N. Mansour, Y. Shao-Horn, In Situ Spectroscopy and Mechanistic Insights into CO Oxidation on Transition-Metal-Substituted Ceria Nanoparticles, ACS Catal. 7 (2017) 6843–6857.

[13] V. Pérez-Dieste, L. Aballe, S. Ferrer, J. Nicolàs, C. Escudero, A. Milán, E. Pellegrin, Near Ambient Pressure XPS at ALBA, J. Phys. Conf. Ser. 425 (2013) 72023-72027.

[14] M. Lowell, S., Shields, J.E., Thomas, M.A., Thommes, Characterization of Porous Solids and Powders: Surface Area, Pore Size and Density, Springer Netherlands, Heidelberg, 2004.

[15] Physisorption of gases, with special reference to the evaluation of surface area and pore size distribution (IUPAC Technical Report), Pure Appl. Chem. 87 (2015) 1051-1069.

[16] S. Brunauer, P.H. Emmett, E. Teller, Adsorption of Gases in Multimolecular Layers, J. Am. Chem. Soc. 60 (1938) 309–319.

[17] E. Aneggi, D. Wiater, C. de Leitenburg, J. Llorca, A. Trovarelli, Shape-Dependent Activity of Ceria in Soot Combustion, ACS Catal. 4 (2014) 172–181.

[18] H.C. Yao, Y.F.Y. Yao, Ceria in automotive exhaust catalysts: I. Oxygen storage, J. Catal. 86 (1984) 254–265.

[19] G. Avgouropoulos, T. Ioannides, H. Matralis, Influence of the preparation method on the performance of $CuO–CeO_2$ catalysts for the selective oxidation of CO, Appl. Catal. B Environ. 56 (2005) 87–93.

[20] G. Avgouropoulos, T. Ioannides, H.K. Matralis, J. Batista, S. Hocevar, $CuO–CeO_2$ mixed oxide catalysts for the selective oxidation of carbon monoxide in excess hydrogen, Catal. Letters. 73 (2001) 33–40.

[21] D. Gamarra, G. Munuera, A.B. Hungrı, M. Ferna, a Martı, Structure - Activity Relationship in Nanostructured Copper - Ceria-Based Preferential CO Oxidation Catalysts, J. Phys. Chem. C. 111 (2007) 11026–11038.

[22] F. Mariño, C. Descorme, D. Duprez, Noble metal catalysts for the preferential oxidation of carbon monoxide in the presence of hydrogen (PROX), Appl. Catal. B Environ. 54 (2004) 59–66.

[23] M.J. Kahlich, H. a Gasteiger, R.J. Behm, Kinetics of the Selective CO Oxidation in H_2-Rich Gas on Pt/Al_2O_3, J. Catal. 171 (1997) 93–105.

[24] E.D. Park, D. Lee, H.C. Lee, Recent progress in selective CO removal in a H_2-rich stream, Catal. Today. 139 (2009) 280–290.

[25] A. Jablonski, Quantification of surface-sensitive electron spectroscopies, Surf. Sci. 603 (2009) 1342–1352.

[26] C.J. Powell, A. Jablonski, Evaluation of Calculated and Measured Electron Inelastic Mean Free Paths Near Solid Surfaces, J. Phys. Chem. Ref. Data. 28 (1999) 19–62.

[27] M. Krawczyk, M. Holdynski, W. Lisowski, J.W. Sobczak, A. Jablonski, Electron inelastic mean free paths in cerium dioxide, Appl. Surf. Sci. 341 (2015) 196–202.

[28] M. Romeo, K. Bak, J. El Fallah, F. Le Normand, L. Hilaire, XPS Study of the reduction of cerium dioxide, Surf. Interface Anal. 20 (1993) 508–512.

[29] S. Deshpande, S. Patil, S.V.N.T. Kuchibhatla, S. Seal, Size dependency variation in lattice parameter and valency states in nanocrystalline cerium oxide, Appl. Phys. Lett. 87 (2005) 133113-133117.

[30] S. Poulston, P.M. Parlett, P. Stone, M. Bowker, Surface Oxidation and Reduction of CuO and Cu_2O Studied Using XPS and XAES, Surf. Interface Anal. 24 (1996) 811–820.

[31] P. Salvador, J.L.G. Fierro, J. Amador, C. Cascales, I. Rasines, XPS study of the dependence on stoichiometry and interaction with water of copper and oxygen valence states in the $YBa_2Cu_3O_{7-x}$ compound, J. Solid State Chem. 81 (1989) 240–249.

[32] M.C. Biesinger, Advanced analysis of copper X-ray photoelectron spectra, Surf. Interface Anal. 49 (2017) 1325–1334.

[33] M.C. Biesinger, B.P. Payne, B.R. Hart, A.P. Grosvenor, N.S. McIntryre, L.W. Lau, R.S. Smart, Quantitative chemical state XPS analysis of first row transition metals, oxides and hydroxides, J. Phys. Conf. Ser. 100 (2008) 12025-12029.

[34] J.P. Espinós, J. Morales, A. Barranco, A. Caballero, J.P. Holgado, A.R. González-Elipe, Interface Effects for Cu, CuO, and Cu_2O Deposited on SiO_2 and ZrO_2. XPS Determination of the Valence State of Copper in Cu/SiO_2 and Cu/ZrO_2 Catalysts, J. Phys. Chem. B. 106 (2002) 6921–6929.

[35] G. Moretti, Auger parameter and Wagner plot in the characterization of chemical states by X-ray photoelectron spectroscopy: A review, J. Electron Spectros. Relat. Phenomena. 95 (1998) 95–144.

Universidad de Alicante

[36] G.E. Wagner, C.D., Riggs, W.M., Davis, L.E., Moulder, J.F., Mullenberg, Handbook of X-Ray Photoelectron Spectroscopy, Perkin-Elmer Corp., Physical Electronics Division, Eden Prairie, Minnesota, USA, 1979.

[37] R. Sarangi, N. Aboelella, K. Fujisawa, W.B. Tolman, B. Hedman, K.O. Hodgson, E.I. Solomon, X-ray Absorption Edge Spectroscopy and Computational Studies on $LCuO_2$ Species: Superoxide−CuII versus Peroxide−CuIII Bonding, J. Am. Chem. Soc. 128 (2006) 8286–8296.

[38] S.J. George, M.D. Lowery, E.I. Solomon, S.P. Cramer, Copper L-edge spectral studies: a direct experimental probe of the ground-state covalency in the blue copper site in plastocyanin, J. Am. Chem. Soc. 115 (1993) 2968–2969.

[39] P. Jiang, D. Prendergast, F. Borondics, S. Porsgaard, L. Giovanetti, E. Pach, J. Newberg, H. Bluhm, F. Besenbacher, M. Salmeron, Experimental and theoretical investigation of the electronic structure of Cu_2O and CuO thin films on Cu(110) using x-ray photoelectron and absorption spectroscopy, J. Chem. Phys. 138 (2013) 24704-24710.

[40] K. Shimizu, H. Maeshima, H. Yoshida, A. Satsuma, T. Hattori, Deconvolution Analysis of Cu L-edge XANES for Quantification of Copper (II) Coordinations in Copper-aluminate Catalysts, Jpn. J. Appl. Phys. 38 (1999) 44-46.

[41] D. Gamarra, G. Munuera, A.B. Hungria, M. Fernandez-Garcia, J.C. Conesa, P.A. Midgley, X.Q. Wang, J.C. Hanson, J.A. Rodriguez, A. Martinez-Arias, Structure-Activity Relationship in Nanostructured Copper-Ceria-Based Preferential CO Oxidation Catalysts, J. Phys. Chem. C. 111 (2007) 11026–11038.

[42] M.V. Ganduglia-Pirovano, J.L.F. Da Silva, J. Sauer, Density-Functional Calculations of the Structure of Near-Surface Oxygen Vacancies and Electron Localization on CeO_2 (111), Phys. Rev. Lett. 102 (2009) 26101-26105.

[43] M. Nolan, S.D. Elliott, The p-type conduction mechanism in Cu_2O: a first principles study, Phys. Chem. Chem. Phys. 8 (2006) 5350–5358.

[44] P.A. Korzhavyi, B. Johansson, Literature review on the properties of cuprous oxide Cu_2O and the process of copper oxidation, Sweden, 2011.

.

Universidad de Alicante

CHAPTER 4

Role of hydroxyl groups in CO-PROX reaction over CuO/CeO_2 catalysts

Chapter 4 presents a thorough Diffuse Reflectance Infra-red Fourier Transformed (DRIFT) spectroscopic study on CO-PROX reaction with model $CuO/Ce_{0.8}X_{0.2}O_{\delta}$ catalysts (with X =Ce, Zr, La, Pr, or Nd). These have been fully characterized exhibiting different chemical features that correlate with catalytic activity. The CO oxidation rate over CuO/CeO_2 catalysts correlates with the formation of the $Cu^{+}-CO$ carbonyl above a critical temperature (90 °C for the experimental conditions in this study) because copper−carbonyl formation is the rate-limiting step. Above this temperature, CO oxidation capacity depends on the redox properties of the catalyst. However, decomposition of adsorbed intermediates is the slowest step below this threshold temperature. The hydroxyl groups on the catalyst surface play a key role in determining the nature of the carbon-based intermediates formed upon CO chemisorption and oxidation. Hydroxyls favor the formation of bicarbonates with respect to carbonates, and catalysts forming more bicarbonates produce faster CO oxidation rates than those which favour carbonates.

Davó-Quiñonero et al., *ACS Catalysis*, **6(3)** (2016) 1723-1731

4.1 Introduction

Chapter 3 has presented experimental and theoretical evidences that corroborate the excellent performance of CuO/CeO_2 catalysts towards the Preferential Oxidation of CO (CO-PROX) reaction. Attempts to improve this catalytic activity are not trivial as the range of improvement is very little provided the outstanding primary features from the bare CuO/CeO_2 conventional catalyst. With this aim, the doping of CeO_2 lattice with different elements such as Zr, Sm, Pr or La is, apparently, an interesting approach provided the inherent positive doping-effect into oxygen storage capacity, redox properties or crystalline size of the support. Nevertheless, widely reported studies show how ceria doping results in detrimental towards the catalytic activity of $CuO/Ce_{1-\delta}X_\delta O_2$ catalysts for every δ varying content. The general explanation accepted for this negative effect are attributed to the loss of synergistic redox interactions existing among Cu^{2+}/Cu^{+} – Ce^{+4}/Ce^{+3} pairs as doping cations block the necessary interfacial contact and hinder the redox interplay for the formation and stabilization of Cu^{+} states.

However, solid evidences that reinforce these arguments are not abundant given the complex nature of the synergistic Cu – Ce interactions and, in addition, very little has been addressed the ceria-doping effect into the surface chemistry evolution during CO-PROX reaction. In this scenario, in this Chapter a series of $CuO/Ce_{0.8}X_{0.2}O_\delta$ catalysts (with X = Ce, Zr, La, Pr, or Nd) has been prepared in order to obtain materials with different chemical features, and these have been tested on CO-PROX *operando* DRIFT spectroscopy. The objectives were to understand the role of the carbon-containing intermediates in the CO oxidation reaction, to determine whether the hydroxyl groups on the catalyst influence the formation of bicarbonates in preference to carbonates, and to provide evidence to support a hypothesis that catalysts which preferentially form bicarbonates are able to oxidize CO faster than those forming carbonate-type species.

4.2 Experimental section

4.2.1 Catalysts preparation

Five metal oxides with composition $Ce_{0.8}X_{0.2}O_\delta$ (X = Ce, Zr, La, Pr or Nd) were prepared by decomposition of the corresponding metal nitrates aqueous dissolution dissolved in the proper amounts, using “flash” calcination protocol, as described in Section 2.2.1 from Chapter 2. $CuO/Ce_{0.8}X_{0.2}O_\delta$ catalysts (5 wt. % Cu) were prepared by impregnation followed by flash calcination in the same protocol as for the support preparation.

4.2.2 Catalysts characterization

Samples were characterized by means of X-Ray Diffraction (XRD) for the calculation of average crystallite size of the mixed oxide supports by means of Williamson-Hall's equation. The specific surface areas, pore volumes and pore sizes were determined from N_2 physisorption analysis. Raman spectra were recorded with Nd-YAG laser source (1064 nm), instead of He-Ne as in the rest of the Thesis, in attempts to avoid fluorescence effect from certain dopants. The catalysts reducibility was measured by means of temperature programmed reduction with H_2 (H_2-TPR) experiments, as described in Section 2.2.2 from Chapter 2.

4.2.3 CO-PROX activity tests

The prepared $CuO/Ce_{0.8}X_{0.2}O_{\delta}$ catalyst series was tested in CO-PROX catalytic tests according to the experimental settings and specific conditions as stated in Section 2.2.3. Briefly, 100 ml/min of the CO-PROX gas mixture consisting in 2% CO, 2% O_2, 30% H_2 in He balance ($\lambda = 2$) was fed to the reactor with 150 mg of sample, and the experiment was conducted following heating rate of 2ºC/min from 25 to 250ºC.

4.2.4 *Operando* DRIFTS-MS experiments.

The reaction mechanism was studied by means of Diffuse Reflectance Infra-red Fourier Transform spectroscopy (DRIFTs), performed in CO-PROX reaction conditions (*operando*) coupled to MS. The reaction gas mixture was set in 50 ml/min of 2% CO, 2% O_2, 58% H_2 balanced with He; passing through the pre-treated catalyst bed (100 mg), and the temperature was raised at 5ºC/min while infrared spectra were recorded at 10ºC intervals. Further details on the specific settings are provided in Section 2.2.4.1 from Chapter 2.

4.3 Results

4.3.1 Textural and crystalline catalysts characterization

The crystalline structure and porosity of the catalysts was characterized by XRD, N_2 adsorption, and Raman spectroscopy. The X-ray diffractograms are compiled in Figure 4.1 and the crystallite sizes and cell parameters calculated for the ceria-based supports are compiled in Table 4.1.

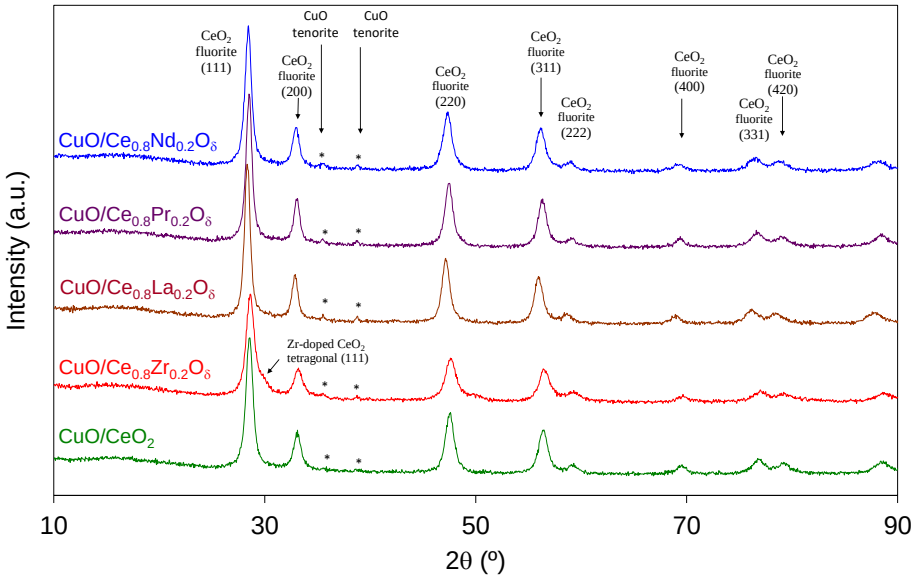

Figure 4.1. X-Ray diffractograms of the catalysts.

All diffractograms show the typical reflexions of the fluorite structure of ceria, and also tiny peaks of CuO at 35.7 and 39.0º seem to be present in most catalyst. Evidence of other crystalline phase are only identified for the $CuO/Ce_{0.8}Zr_{0.2}O_{\delta}$ catalyst, which shows a shoulder at the right-hand side of the (111) fluorite peak at 29.0º that is consistent with the presence of a Zr-rich tetragonal phase (peak 111). Evidence of segregated phases of La, Pr or Nd was not observed in the diffractograms.

Table 4.1. Results of the catalysts characterization by N_2 adsorption, XRD and Raman spectroscopy.

Catalyst	S_{BET} (m^2/g)	V_{DR} (cm^3/g)	PSD BJH (nm)	Crystal size (nm)	Lattice constant (nm)	F_{2g} Raman shift (cm^{-1})
CuO/CeO_2	58	0.021	12	13	0.5407	441
$CuO/Ce_{0.8}Zr_{0.2}O_{\delta}$	60	0.020	12	13	0.5392	457
$CuO/Ce_{0.8}La_{0.2}O_{\delta}$	40	0.015	17	26	0.5448	446
$CuO/Ce_{0.8}Pr_{0.2}O_{\delta}$	35	0.013	12	27	0.5411	450
$CuO/Ce_{0.8}Nd_{0.2}O_{\delta}$	45	0.016	12	16	0.5429	453

The cell parameter calculated for the ceria bare support (0.5407 nm) is consistent with values typically obtained for this material [3], and doping with some cations affect this value. The cell parameter does not change significantly upon ceria doping with Pr, which is not surprising because the sizes of the Ce cations (0.097 nm for Ce^{4+} and 0.114 nm for Ce^{3+}) are almost equal to those of Pr cations (0.096 nm for Pr^{4+} and 0.113 nm for Pr^{3+}) [4]. On

the contrary, Zr doping decreases the cell parameter of ceria while doping with La or Nd increases the cell parameter. The cell parameter contraction upon Zr doping is expected considering the smaller size of Zr^{4+} (0.084 nm) with regard to Ce^{4+}, and the cell expansion upon La or Nd doping is consistent with the bigger size of their cations (0.116 nm for La^{3+} and 0.112 nm for Nd^{3+}). These modifications of the cell parameters of ceria upon doping provide evidence that the foreign cations are actually located into the parent ceria framework. However, it cannot be ruled out that, in addition to the amount introduced into the ceria lattice, Zr is partially segregated, since evidence of such segregated phase is observed in the diffractograms, as mentioned.

The pore size (12-17 nm) and pore volume (0.013-0.021 cm^3/g) values are quite similar for all catalysts. The crystallite sizes of the ceria supports are in the 13-27 nm range (see Table 4.1), and the smallest sizes are obtained for undoped and Zr-doped ceria. These two supports also have the largest specific surface areas (58-60 m^2/g), these values being in good agreement with those typically obtained for cerium oxides exposed to a similar thermal history [3]. Ceria doping with La, Pr or Nd leads to a decrease of the specific surface area and an increase of the crystallite size, which means that these dopants induce sintering. It is known that the effect of dopants on ceria sintering depends on the temperature of the thermal treatments [5]. As a rule of thumb, dopants partially hinder ceria sintering for high temperature calcination (above 800-900ºC) while they have no effect or promote sintering for mild temperature calcination (500-600ºC). The argument postulated to explain such behavior is that the surface defects created upon doping decrease the energy required for crystals to merge, and therefore dopants promote sintering if there are energy restrictions, as occurring at mild temperature. On the contrary, if the temperature is high enough to overcome such energy restrictions to sintering, the effect of dopants is the opposite, partially hindering sintering because they do not allow long-range structural order into the ceria crystals.

Raman spectroscopy (Figure 4.2) provides additional information about the structure of the catalysts. All catalysts show the F_{2g} band around 450 cm^{-1}, typical feature of the ceria-based oxides [6,7]. This band has been attributed to the oxygen breathing frequency around the Ce^{4+} cations [8,9]. The position of this band provides information about the introduction of foreign cations into the ceria lattice. The position of the F_{2g} band in pure ceria is usually ca 464 cm^{-1} [3], and the position obtained for all $CuO/Ce_{0.8}X_{0.2}O_{\delta}$ catalysts is well below this value (see data in Table 4.1). The shift of the F_{2g} band towards low values is attributed to the presence of foreign cations into the lattice larger than Ce^{4+}, while the shift towards high values is assigned to the presence of smaller cations. Therefore, the low values obtained for our catalysts suggest the presence of large cations. In the CuO/CeO_2 catalyst, the large cations could be Ce^{3+} and a potential explanation would be that the energy of the laser used to obtain the Raman spectra is sufficiently high to

partially reduce the surface. Copper seems to play a key role in this reduction, because this effect is not observed in copper-free ceria catalysts [19]. In catalysts with dopants larger than Ce^{4+}, like La^{3+}, Pr^{3+} and Nd^{3+}, the shift of the F_{2g} band below 464 cm^{-1} must be additionally attributed to the introduction of such cations into the ceria lattice. It is also reasonable to think that Ce^{4+} reduction (and also Pr^{4+} in the case of $CuO/Ce_{0.8}Pr_{0.2}O_{\delta}$) is additionally taking place.

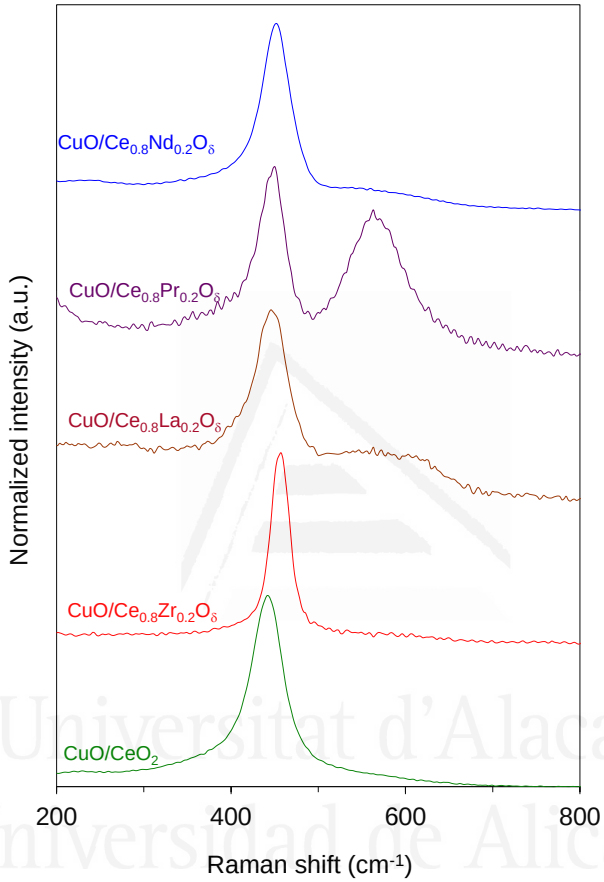

Figure 4.2. Raman spectra of the catalysts. The spectra were normalized by dividing the intensity of each spectrum between the intensity of its F_{2g} band maximum.

In addition to the F_{2g} band, another band or shoulder appears in some Raman spectra at 540 cm^{-1}, which has been assigned to oxygen vacancies. The relative intensity of this band with regard to the maximum of the F_{2g} band is highest for the Pr-containing catalyst, being much lower for the La- or Nd-doped catalysts and negligible for the remaining samples. The formation of oxygen vacancies is expected upon Ce^{4+} substitution by trivalent cations, like La^{3+} or Nd^{3+}, while is not expected to be relevant upon isovalent substitution of Ce^{4+} by Zr^{4+}. The prominent vacancies band observed in $CuO/Ce_{0.8}Pr_{0.2}O_{\delta}$ has been attributed to the easy reduction of the Pr^{4+} cations, which could be even reduced due to the local heating produced by the laser used to excite the samples and obtain the Raman spectra, as previously reported.[20] The

presence of Ce^{3+} cations, as previously proposed considering the position of the F_{2g} band, is also expected to lead to the formation of oxygen vacancies. However, the band due to these vacancies is negligible in spectra of CuO/CeO_2, for instance, suggesting that the partial reduction of Ce^{4+} under measurements conditions is high enough to shift the position of the F_{2g} band but not for the band due to the vacancies to grow. This is not surprising because, usually, the position of the Raman bands is much more sensitive to changes in the physical chemical features of solids than the intensity of the bands, which is affected by other variables like crystal size or radiation absorption.

In conclusion, these characterization results confirm that, in the $CuO/Ce_{0.8}X_{0.2}O_\delta$ catalysts prepared, the doping cations are actually located into the parent ceria framework. Only the $CuO/Ce_{0.8}X_{0.2}O_\delta$ catalyst shows certain evidences of the formation of a segregated Zr-rich phase, but even in this case, it can be confirmed that part of the Zr dopant is located into the ceria lattice.

4.3.2 Catalysts characterization by H_2-TPR.

The TCD signals monitored during the H_2-TPR experiments are plotted on Figure 4.3, and all catalysts show a main feature in the 120-300ºC range, which consist of double peaks or a main peak with a shoulder at low temperature. Also, a small band is shown in some profiles around 800ºC, which can be assigned to the reduction of the particles bulk.

The position of the low-temperature reduction bands indicates that $CuO/Ce_{0.8}Zr_{0.2}O_\delta$ and CuO/CeO_2 are reduced at the lowest temperature, and that the behavior of these two catalysts is quite similar to each other. Different events are taking place within the reduction bands in the 120-300ºC range, and the dual-mode shape reported for MO/CeO_2 catalysts (MO = Metal Oxide) has been related to the reduction of the supported metal oxide (MO) and ceria in close contact with MO at the lowest temperature, and to surface ceria reduction which is not directly in contact with MO at higher temperature [10]. In the case of CuO catalysts, the reduction of Cu^{2+} to Cu^0 in two consecutive steps, Cu^{2+} to Cu^+ first and Cu^+ to Cu^0 afterwards cannot be ruled out. In the $CuO/Ce_{0.8}Pr_{0.2}O_\delta$ catalyst it must be additionally taken into account that Pr^{4+} is also reduced to Pr^{3+}. Quantitative values calculated from the H_2-TPR experiments are compiled in Table 4.2:

Universidad de Alicante

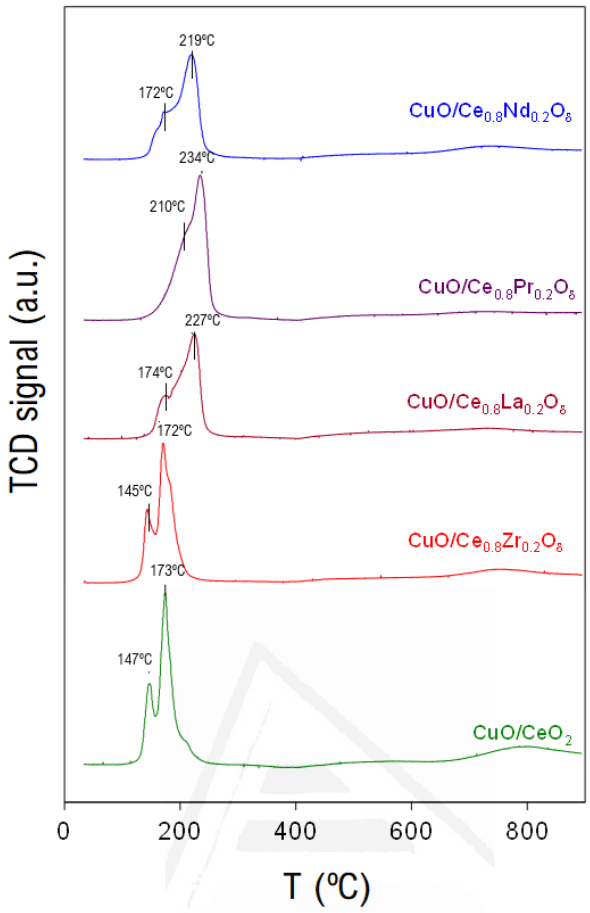

Figure 4.3. H_2-TPR profiles of the catalysts.

Table 4.2. Quantitative values calculated from the H_2-TPR experiments. [a]In the $CuO/Ce_{0.8}Pr_{0.2}O_\delta$ catalyst, the percentage of Ce^{4+} reduced is actually Ce^{4+} + Pr^{4+}.

Catalyst	H_2 consumed mol/CuO mol	Ce^{4+} reduced (%)
CuO/CeO_2	1.7	20
$CuO/Ce_{0.8}Zr_{0.2}O_\delta$	1.6	22
$CuO/Ce_{0.8}La_{0.2}O_\delta$	1.6	23
$CuO/Ce_{0.8}Pr_{0.2}O_\delta$	1.9	27[a]
$CuO/Ce_{0.8}Nd_{0.2}O_\delta$	1.8	28

In all cases, the moles of H_2 consumed are higher than those of CuO on the catalysts, and this provides experimental evidence that not only is CuO being reduced but also the ceria supports. Considering total reduction of Cu^{2+} to Cu^0, the percentages of Ce^{4+} reduced to Ce^{3+} are in the 20-28 % range for all catalysts.

These H_2-TPR experiments allow concluding that the presence of dopants affect the reducibility of the CuO-Ceria system, and

$CuO/Ce_{0.8}Zr_{0.2}O_\delta$ and CuO/CeO_2 are reduced more easily than the remaining catalysts. This affects the temperature required for catalysts reduction by H_2, but differences in the extent of the reduction are not very relevant once totally accomplished.

4.3.3 Catalytic tests in a fixed-bed reactor

Figure 4.4 shows the oxidation of CO (Figure 4.4a) and the CO selectivity (Figure 4b) obtained in the fixed-bed reactor PROX experiments, where it is observed that the catalysts with the undoped and Zr-doped supports are active and selective at lower temperature than catalysts containing La, Pr or Nd.

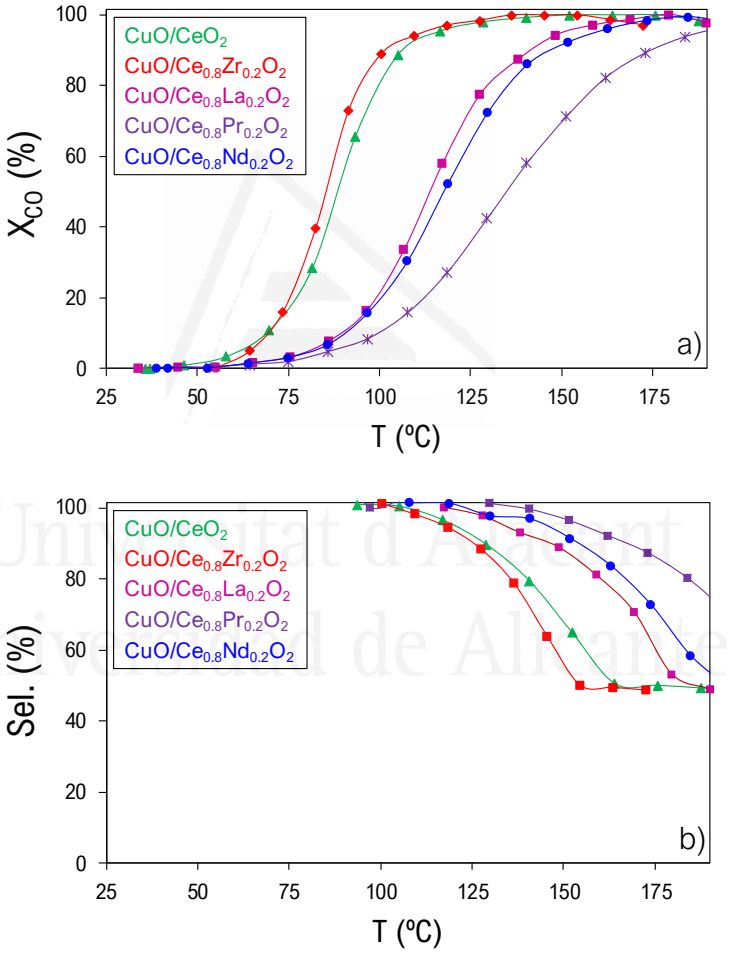

Figure 4.4. CO-PROX reactions performed in a fixed-bed reactor. **(a)** CO conversion (X_{CO}) and (b) CO selectivity (Sel.)

The results on Figure 4.4, together with the previous H_2-TPR characterization, confirm that the reducibility of the catalyst plays an important role in CO oxidation, since the catalytic processes are based on

redox cycles taking place on the catalyst surface. In accordance with the well accepted role of the different copper species in the PROX reactions [11,12], the oxidation of CO starts at temperatures (~ 50ºC) lower than those required for the massive reduction of the catalyst by H_2 (see H_2-TPR in Figure 4.3). This is in agreement with the hypothesis supporting that the active sites for CO oxidation are Cu^+ sites located at the CuO-Ceria interface. In addition, the selectivity drops (Figure 4.4b) when temperature approaches the onset temperature for massive reduction of the catalysts (see H_2-TPR in Figure 4.3), supporting that H_2 oxidation takes place on reduced metal sites.

4.3.4 *Operando* DRIFTS-MS experiments.

In order to investigate the nature of the carbon intermediates and to demonstrate that the catalyst hydroxyl groups play a critical role in the formation of bicarbonates and in the CO oxidation rate, which is the main goal of the study, *operando* DRIFTS-MS experiments were carried out.

Figure 4.5 shows, as representative examples, spectra obtained with $CuO/Ce_{0.8}Zr_{0.2}O_\delta$ and $CuO/Ce_{0.8}La_{0.2}O_\delta$. DRIFT spectra were recorded between 4000-1000 cm^{-1}, but the main features are located in three main regions. Figures 4.5a and 4.5d show the 1650-1150 cm^{-1} range, where several vibration/stretching modes corresponding to carbonates, bicarbonates and formates are identified. Figures 4.5b and 5e show the 2250-1950 cm^{-1} range, where a single band corresponding to the Cu^+-CO carbonyl is observed. Figures 4.5c and 4.5d show the 3850-2450 cm^{-1} range, where hydroxyl groups show their main features.

Universitat d'Alacant
Universidad de Alicante

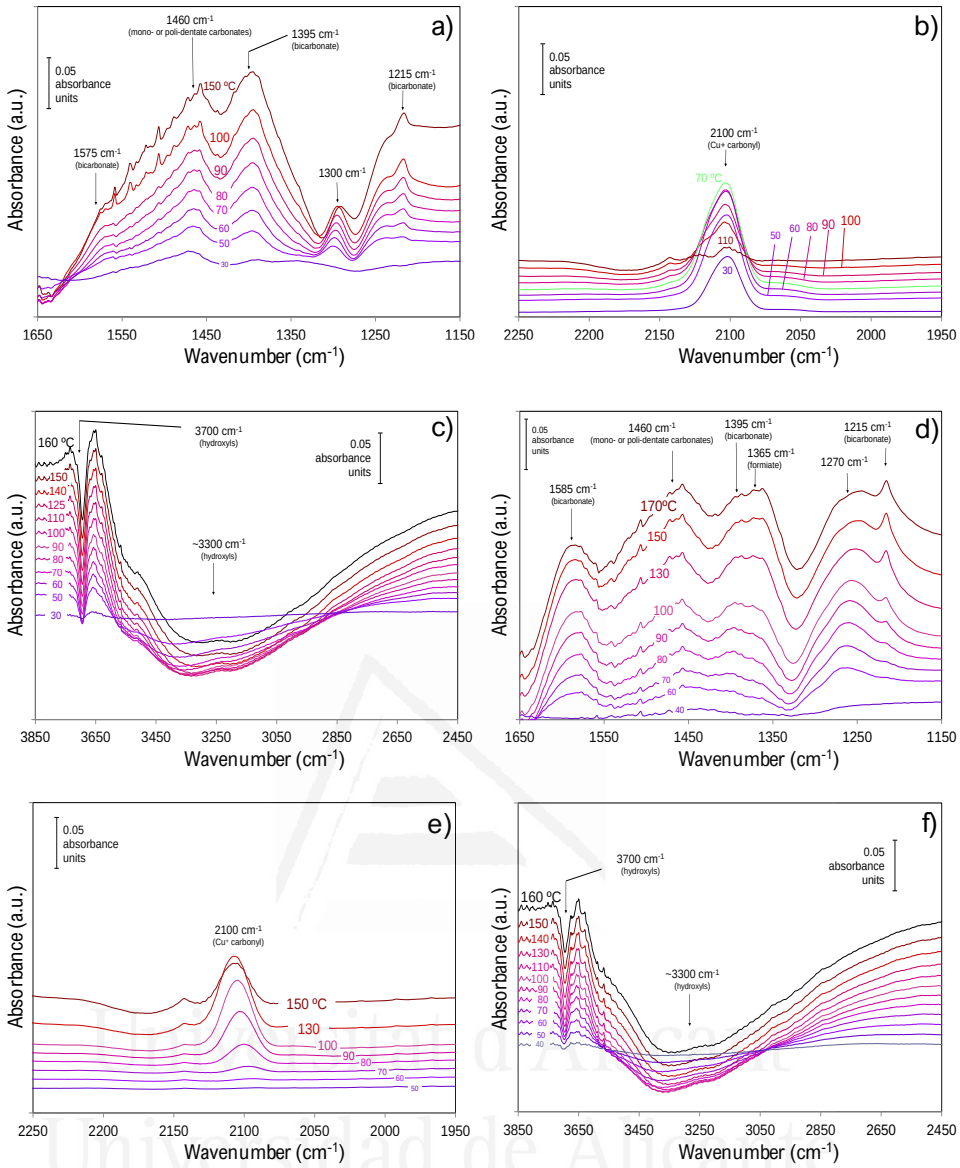

Figure 4.5. DRIFT spectra obtained as a function of temperature under operando PROX conditions with **(a,b,c)** $CuO/Ce_{0.8}Zr_{0.2}O_{\delta}$ and **(d,e,f)** $CuO/Ce_{0.8}La_{0.2}O_{\delta}$.

4.3.4.1 Role of the catalyst hydroxyls groups

The main carbon-containing reaction intermediates accumulated on the catalysts surface during the PROX reaction are carbonates and bicarbonates, as is observed in the DRIFT spectra of Figure 4.5. Figure 4.6 shows the ratio between the band maxima due to bicarbonates (at 1395 cm^{-1}) and carbonates (at 1460 cm^{-1}) bands as a function of temperature for all catalysts.

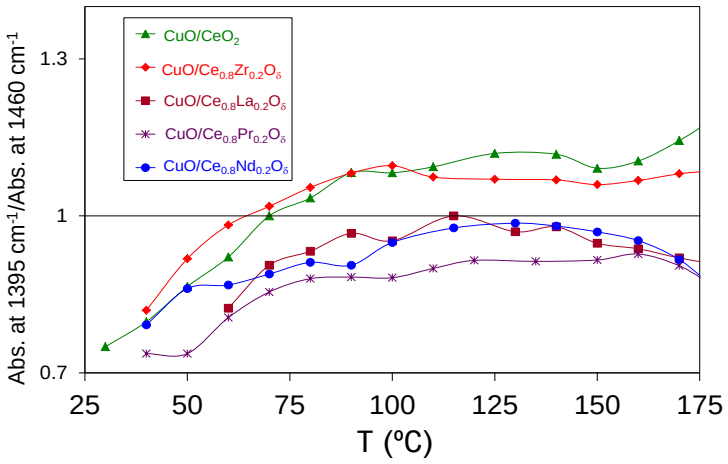

Figure 4.6. Ratio between the absorbance at 1395 cm^{-1} (bicarbonates) and the absorbance and 1460 cm^{-1} (carbonates) as a function of temperature.

The most active catalysts (CuO/CeO_2 and $CuO/Ce_{0.8}Zr_{0.2}O_\delta$) favor the formation of surface bicarbonates in preference of carbonates, while catalysts with lower CO-PROX activity (X= La, Pr or Nd) accumulate more carbonates on the surface. The positive effect on the CO oxidation rate of surface bicarbonates formation as reaction intermediates with regards to carbonates could be related to the lower thermal stability of the former species, which would lead to a faster desorption of CO_2 leaving the surface available for further chemisorbing other reaction intermediates more rapidly. This would suggest that, in some circumstances, the slow step of the reaction mechanism is the surface intermediates desorption, and this hypothesis is discussed afterwards in more detail.

Catalysts hydroxyls are involved in the formation of surface bicarbonates, as it is deduced from Figure 4.7 where the intensity of the bicarbonates band at 1395 cm^{-1} is plotted as a function of the area of the hydroxyls band (3600-2500 cm^{-1} range). Note that the area of the hydroxyls band shows negative values because hydroxyls are consumed during the reactions. Linear relationships between the consumption of hydroxyls and the formation of bicarbonates are observed for all catalysts suggesting that the two processes are related to each other.

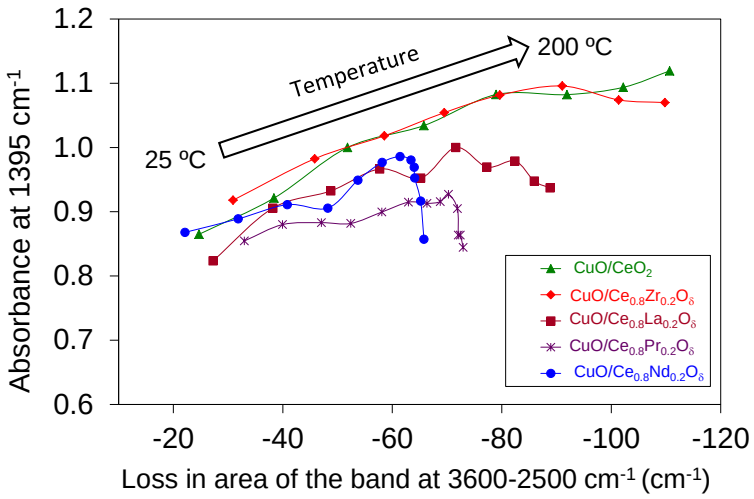

Figure 4.7. Relationship between bicarbonates formation (band at 1395 cm^{-1}) and hydroxyls consumption (band in the 2500-3600 cm^{-1} range).

Figure 4.7 also shows that the linear trend is valid for the whole range of temperatures studied (25-200 ºC) for the most active catalysts (CuO/CeO_2 and $CuO/Ce_{0.8}Zr_{0.2}O_\delta$) but not for those with lower activity (X= La, Pr or Nd). Catalysts with X= La, Pr or Nd show a deviation from the trend line of Figure 4.7 above a certain temperature, and according to results of Figure 4.4b, this deviation occurs at a stage where the CO selectivity decreases, that is, where the onset of H_2 oxidation begin. A vertical drop in Figure 4.7 indicates that the amount of surface hydroxyls remains constant above a certain temperature while surface bicarbonates are depleted, that is, once the oxidation of H_2 is initiated the formation of carbonate-like intermediates is favored with respect to bicarbonates.

According to these results and the background literature, our proposed CO oxidation mechanism is as follows:

$2CuO + CO \rightarrow Cu_2O\text{-}O\text{-}CO$ Step 1

$Cu_2O\text{-}O\text{-}CO + *\text{-}O \rightarrow Cu_2O + *\text{-}CO_3$ Step 2a

$Cu_2O\text{-}O\text{-}CO + *\text{-}OH \rightarrow Cu_2O + *\text{-}CO_2OH$ Step 2b

$Cu_2O + 1/2O_2 \rightarrow 2CuO$ Step 3

$*\text{-}CO_3 \rightarrow *\text{-}O + CO_2$ Step 4a

$*\text{-}CO_2OH \rightarrow *\text{-}OH + CO_2$ Step 4b

where CuO are active sites for CO chemisorption at the copper oxide-cerium oxide interface, $Cu_2O\text{-}O\text{-}CO$ represents the Cu^+-CO carbonyl, *-O are chemisorption sites where surface carbonates ($*\text{-}CO_3$) are formed and *-OH are chemisorption sites where surface bicarbonates ($*\text{-}CO_2OH$) are formed.

Universidad de Alicante

The CO oxidation reaction mechanism starts with CO chemisorption at the copper oxide-cerium oxide interface and formation Cu^{+}-CO carbonyls (step 1), and it has been proposed that chemisorbed CO is oxidized to CO_2 following a Mars van Krevelen mechanism using the Cu^{2+}/Cu^{+} redox cycle [13]. Then, CO_2 is transferred from the copper oxide-cerium oxide interface to other surface sites, probably on the ceria support, forming bicarbonates (step 2a) and carbonates (step 2b), and molecular oxygen reoxidizes the reduced sites via steps 3. Surface hydroxyls are involved in the formation of bicarbonates (step 2b). Finally, CO_2 is desorbed following steps 4a and 4b.

4.3.4.2 Products poisoning versus Cu^{+}-CO carbonyl

The contribution to the CO oxidation rate of the copper oxide-cerium oxide interface reducibility and of the carbon products desorption has been analyzed.

Figure 4.8 shows the area of the Cu^{+}-CO carbonyl peak monitored under CO-PROX reaction conditions for all $CuO/Ce_{0.8}X_{0.2}O_{\delta}$ catalysts as a function of the reaction temperature, where it is observed that the room temperature formation of the Cu^{+}-CO carbonyl obtained with the Zr-containing catalyst is about three times higher to that formed on the undoped CuO/CeO_2 counterpart, and that the Cu^{+}-CO carbonyl formation is delayed to higher temperatures for catalysts with X = La, Pr or Nd.

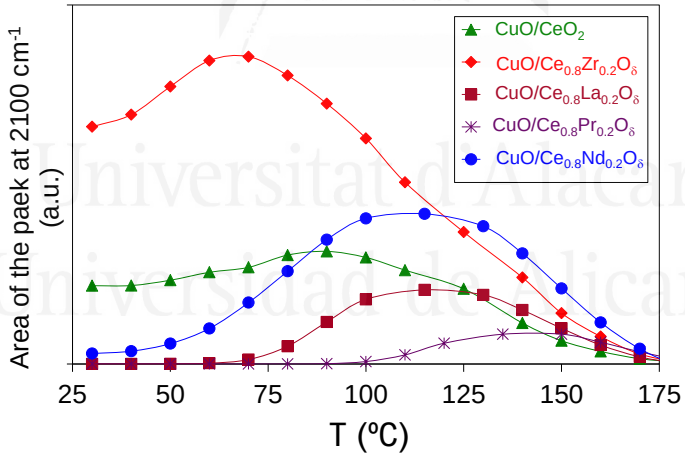

Figure 4.8. Integrated area of the Cu^{+}-CO carbonyl band at 2100 cm^{-1} as a function of the reaction temperature.

The temperature of maximum carbonyl coverage has been determined from Figure 4.8, and these temperatures correlate to the CO oxidation rates. Figure 4.9 shows the relationship between the CO oxidation rate and the formation of the Cu^{+}-CO carbonyl in the CO-PROX experiments. The data for most $CuO/Ce_{0.8}X_{0.2}O_{\delta}$ catalysts lie on a straight line, confirming the important role of the reducibility of the copper oxide-cerium oxide interface.[15]

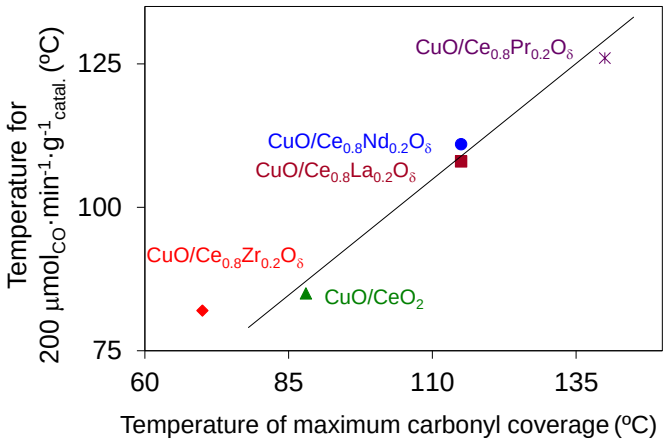

Figure 4.9. Relationship between CO oxidation rate and temperature corresponding to the maximum absorbance due to Cu^+-CO carbonyl.

However, the CO oxidation rate obtained with the Zr-containing catalyst is lower than that predicted by its Cu^+-CO carbonyl population. These results indicate that the Cu^+-CO carbonyl formation (step 1) is the rate limiting step for temperatures above a certain threshold (above 90 ºC approximately for the experimental conditions of this study) but, below this temperature, the accumulation of reaction products on the catalyst surface must also be taken into account because desorption of reaction intermediates (steps 4a and 4b) becomes the slowest step of the mechanism.

The area of a broad DRIFTS band envelope with several contributions appearing in the 1650-1300 cm^{-1} range has been calculated. This band can be attributed to surface carbonates and bicarbonates (and formats, in particular cases). Figure 4.10 shows the area of this band as a function of the reaction temperature for all catalysts.

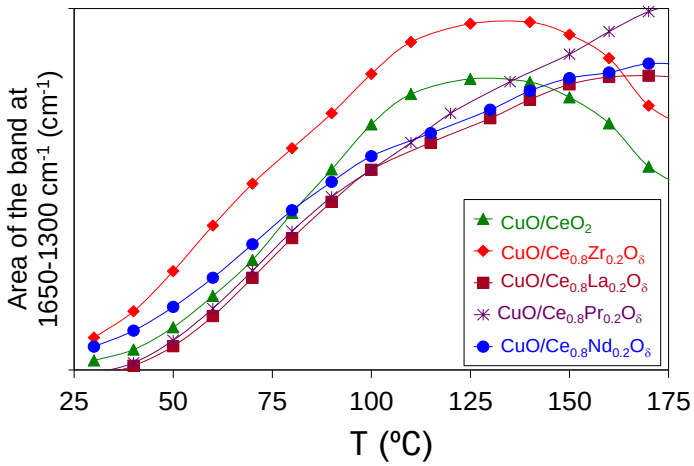

Figure 4.10. Integrated area of the band due to carbon containing products (carbonates + bicarbonates + formates) in the 1650-1300 cm^{-1} range as a function of the reaction temperature.

The accumulation of carbon containing reaction products is highest for the Zr-containing catalyst, its area of the 1650-1300 cm^{-1} band being, for instance, twice that of CuO/CeO_2 at 50 ºC. The poisoning by the formation of carbon containing adsorbed intermediates explains why the CO oxidation rate of the $CuO/Ce_{0.8}Zr_{0.2}O_\delta$ catalyst does not follow the trend predicted by the formation of the Cu^+-CO carbonyl (Figure 4.9). Comparison of the CuO/CeO_2 and $CuO/Ce_{0.8}Zr_{0.2}O_\delta$ behavior is interesting because both catalysts show similar CO-PROX activity, the latter more readily forming the Cu^+-CO carbonyl at low temperature but also suffering much stronger inhibition by adsorbed products. Therefore, the contribution to the CO oxidation rate of the Cu^+-CO carbonyl formation and carbon products desorption oppose each other at low temperature. Taking the trend of Figure 4.9 into account, poisoning by reaction products becomes of special relevance at temperatures below *ca.* 90 ºC for the experimental conditions used in this study.

The CO-PROX experiments performed in this study show that ceria doping with foreign cations has either no effect or a negative impact on the activity, and this observation has been also reported by many authors [10].There have been only reported few examples of improved CO-PROX activity of copper oxide-cerium oxide activity upon ceria doping [14–16], but the reasoning why some authors observe the positive effect of ceria doping while most do not has not been fully explained. It has been proposed that the incorporation of foreign cations into the ceria lattice hinders the extent of copper oxide-cerium oxide interaction and it is this interface where the most active sites for CO oxidation are located [16,17]. Temperature programmed reduction experiments performed with H_2, (Figure 4.3), also indicate that the onset reduction temperature is lowest for the most active catalysts in the CO-PROX reaction (CuO/CeO_2 and $CuO/Ce_{0.8}Zr_{0.2}O_\delta$), that is, most dopants (X = La, Pr or Nd) retard CO oxidation with regard to CuO/CeO_2 and $CuO/Ce_{0.8}Zr_{0.2}O_\delta$ because they delay the onset in the reduction temperature.

Universitat d'Alacant
Universidad de Alicante

4.3.4.3 Comparing CO-PROX with other catalytic reactions

The observed lack of influence or negative effect of ceria doping in the CO-PROX activity is in disagreement with the general behavior of ceria in most catalyzed reactions, such as in Three Way Catalysts (TWC) where ceria doping by Zr^{4+} enhances the oxygen storage capacity, the redox properties, and overall, the catalytic performance [18]. The positive effect of ceria doping has been also reported for ceria-catalyzed diesel soot combustion [19–21] or NO_x storage and Reduction (NSR) on Pt/Ceria catalysts [22], for instance, where the redox properties of ceria play an important role.

An important difference between the CO-PROX reaction and the other applications where the doping of ceria has a positive effect is the range of temperatures where the reactions take place. Ceria doping with foreign

cations usually has a positive effect on the activity for catalytic applications occurring at medium or high temperatures (around 200-300ºC for TWC and NSR or > 400 ºC for soot combustion, for instance). Dopants improve the thermal stability, oxygen storage capacity and/or some other physic-chemical properties of the ceria-based oxide, and therefore the catalytic activity, but the potential stabilization of the reaction intermediates on the catalyst has a minor effect on the reaction rate because the temperature is high enough to encourage desorption of the reaction products. On the other hand, the CO-PROX reaction takes place below ca 100ºC, and desorption of reaction products becomes a critical step. Therefore, the challenge for CO-PROX is to prepare copper oxide-cerium oxide catalysts which are readily reducible at low temperature but that, at the same time, also desorb the reaction products at low temperature, and the participation of catalyst hydroxyls in the formation of bicarbonates as reaction intermediates has a positive effect.

4.4 Conclusions

In summary, it can be concluded that the CO oxidation rate accelerated by copper oxide-cerium oxide catalysts in CO-PROX conditions correlates to the formation of the Cu^+-CO carbonyl above a critical temperature (90ºC for the experimental conditions of this study) because Step 1 (copper carbonyl formation) is the rate limiting one. However, desorption of carbon products (Steps 4a and 4b) is the slowest step below this threshold temperature. The hydroxyl groups on the catalyst surface play a key role in determining the nature of the carbon-based intermediates formed upon CO chemisorption and oxidation. Hydroxyls favor the formation of bicarbonates with respect to carbonates, and catalyst forming more bicarbonates reach faster CO oxidation rates than those which favor carbonates.

Universidad de Alicante

References

[1] G.K. Williamson, W.H. Hall, X-ray line broadening from filed aluminium and wolfram, Acta Metall. 1 (1953) 22–31.

[2] A.W. Burton, K. Ong, T. Rea, I.Y. Chan, On the estimation of average crystallite size of zeolites from the Scherrer equation: A critical evaluation of its application to zeolites with one-dimensional pore systems, Microporous Mesoporous Mater. 117 (2009) 75–90.

[3] N. Guillén-Hurtado, A. Bueno-López, A. García-García, Surface and structural characterisation of coprecipitated $Ce_xZr_{1-x}O_2$ ($0 \leq x \leq 1$) mixed oxides, J. Mater. Sci. 47 (2012) 3204–3213.

[4] K. Krishna, A. Bueno-López, M. Makkee, J.A. Moulijn, Potential rare earth modified CeO_2 catalysts for soot oxidation: I. Characterisation and catalytic activity with O_2, Appl. Catal. B Environ. 75 (2007) 189–200.

[5] A. Bueno-López, I. Such-Basáñez, C. Salinas-Martínez de Lecea, Stabilization of active Rh_2O_3 species for catalytic decomposition of N_2O on La-, Pr-doped CeO_2, J. Catal. 244 (2006) 102–112.

[6] A. Mineshige, T. Taji, Y. Muroi, M. Kobune, S. Fujii, N. Nishi, M. Inaba, Z. Ogumi, Oxygen chemical potential variation in ceria-based solid oxide fuel cells determined by Raman spectroscopy, Solid State Ionics. 135 (2000) 481–485.

[7] L.N. Ikryannikova, A.A. Aksenov, G.L. Markaryan, G.P. Murav'eva, B.G. Kostyuk, A.N. Kharlanov, E. V Lunina, The red–ox treatments influence on the structure and properties of M_2O_3–CeO_2–ZrO_2 (M=Y, La) solid solutions, Appl. Catal. A Gen. 210 (2001) 225–235.

[8] J.R. McBride, K.C. Hass, B.D. Poindexter, W.H. Weber, Raman and x-ray studies of $Ce_{1-x}RE_xO_{2-y}$, where RE=La, Pr, Nd, Eu, Gd, and Tb, J. Appl. Phys. 76 (1994) 2435–2441.

[9] J.E. Spanier, R.D. Robinson, F. Zhang, S.-W. Chan, I.P. Herman, Size-dependent properties of CeO_{2-y} nanoparticles as studied by Raman scattering, Phys. Rev. B. 64 (2001) 245407-245414.

[10] P. Fornasiero, R. Dimonte, G.R. Rao, J. Kaspar, S. Meriani, A. Trovarelli, M. Graziani, Rh-Loaded CeO_2-ZrO_2 Solid-Solutions as Highly Efficient Oxygen Exchangers: Dependence of the Reduction Behavior and the Oxygen Storage Capacity on the Structural-Properties, J. Catal. 151 (1995) 168–177.

[11] D. Gamarra, G. Munuera, a B. Hungrı, M. Ferna, a Martı, Structure - Activity Relationship in Nanostructured Copper - Ceria-Based Preferential CO Oxidation Catalysts, J. Phys. Chem. C. 111 (2007) 11026–11038.

[12] A. Martínez-Arias, D. Gamarra, A. Hungría, M. Fernández-García, G. Munuera, A. Hornés, P. Bera, J. Conesa, A. Cámara, Characterization of Active Sites/Entities and Redox/Catalytic Correlations in Copper-Ceria-Based Catalysts for Preferential Oxidation of CO in H_2-Rich Streams, Catalysts. 3 (2013) 378–400.

[13] D. Gamarra, C. Belver, M. Fernández-García, A. Martínez-Arias, Selective CO Oxidation in Excess H_2 over Copper−Ceria Catalysts: Identification of Active Entities/Species, J. Am. Chem. Soc. 129 (2007) 12064–12065.

[14] I. López, T. Valdés-Solís, G. Marbán, An attempt to rank copper-based catalysts used in the CO-PROX reaction, Int. J. Hydrogen Energy. 33 (2008) 197–205.

[15] J.S. Moura, J. da S.L. Fonseca, N. Bion, F. Epron, T. de F. Silva, C.G. Maciel, J.M. Assaf, M. do C. Rangel, Effect of lanthanum on the properties of copper, cerium and zirconium catalysts for preferential oxidation of carbon monoxide, Catal. Today. 228 (2014) 40–50.

[16] E. Moretti, L. Storaro, A. Talon, P. Riello, A.I. Molina, E. Rodríguez-Castellón, 3-D flower like Ce–Zr–Cu mixed oxide systems in the CO preferential oxidation (CO-PROX): Effect of catalyst composition, Appl. Catal. B Environ. 168–169 (2015) 385–395.

[17] L. Gong, Z. Huang, L. Luo, N. Zhang, Promoting effect of MnO_x on the performance of CuO/CeO_2 catalysts for preferential oxidation of CO in H_2-rich gases, React. Kinet. Mech. Catal. 111 (2014) 489–504.

[18] M. Manzoli, R. Di Monte, F. Boccuzzi, S. Coluccia, J. Kašpar, CO oxidation over CuO_x-CeO_2-ZrO_2 catalysts: Transient behaviour and role of copper clusters in contact with ceria, Appl. Catal. B Environ. 61 (2005) 192–205.

[19] J. Kašpar, P. Fornasiero, M. Graziani, Use of CeO_2-based oxides in the three-way catalysis, Catal. Today. 50 (1999) 285–298.

[20] A. Bueno-López, K. Krishna, M. Makkee, J.A. Moulijn, Enhanced soot oxidation by lattice oxygen via La^{3+}-doped CeO2, J. Catal. 230 (2005) 237–248.

[21] E. Aneggi, C. de Leitenburg, G. Dolcetti, A. Trovarelli, Promotional effect of rare earths and transition metals in the combustion of diesel soot over CeO_2 and CeO_2–ZrO_2, Catal. Today. 114 (2006) 40–47.

[22] R. Strobel, F. Krumeich, S.E. Pratsinis, A. Baiker, Flame-derived $Pt/Ba/Ce_xZr_{1-x}O_2$: Influence of support on thermal deterioration and behavior as NO_x storage-reduction catalysts, J. Catal. 243 (2006) 229–238.

Universitat d'Alacant
Universidad de Alicante

Universitat d'Alacant
Universidad de Alicante

CHAPTER 5

CuO/Cryptomelane catalyst for preferential oxidation of CO in the presence of H_2

Non-RE metal-based, Cryptomelane and CuO/Cryptomelane catalysts have been tested in CO-PROX reaction, paying special attention to deactivation and regeneration issues. Cryptomelane was stable during CO-PROX reactions in ramp experiments until 200ºC and in a long-term isothermal experiment, exhibiting after use no changes neither in crystallinity nor H_2 reducibility. On the contrary, CuO/Cryptomelane, though being much more active, deactivated in consecutive CO-PROX reaction cycles performed until 200ºC, but the catalytic activity was partially restored reoxidising the catalyst at 200ºC or 400ºC, the latter temperature being more effective. After four cycles of reaction, stable behavior was achieved, and then CuO/Cryptomelane demonstrated higher catalytic activity than that of Cryptomelane, even after its deactivation along cycles. Such deactivation has been attributed to potential causes: cryptomelane structure collape into the cyrstallization of new phases (hausmannite (Mn_3O_4) and/or hopcalite ($CuMn_2O_4$)); segregation of potassium and decrease of the copper cations reducibility, whereas possible changes in the porous texture of CuO/Cryptomelane was ruled out.

Davó-Quiñonero et al., *Catalysis Science & Technology*, **6(14)** (2016) 5684-5691

Universitat d'Alacant
Universidad de Alicante

5.1 Introduction

As stated and demonstrated in this Project Thesis, CuO/CeO_2 system, allows to provide excellent catalytic features while skipping the high expenses of noble metals and the lack of stability of Au-based catalysts, gaining big opportunities on their extended implementation into CO-PROX technologies [1,2]. The outstanding performance of the CuO/CeO_2 catalysts in CO-PROX is related to the strong interaction between CuO and CeO_2 and to the oxygen storing/releasing capacity of ceria, which leads to an important mobilization of active lattice oxygen [3,4]. Thus, in previous Chapters 3 and 4, the unique properties of the CuO/CeO_2 catalyst have been well described, besides a thorough study of the reaction mechanism and such oxygen activation process has been conducted. As it was proven, and/or elsewhere reported, apart from its excellent activity and selectivity to CO oxidation in the low temperature range of CO-PROX reaction conditions, CuO/CeO_2 systems possess great qualities such as certain CO_2 and H_2O compatibility, or large stability in cyclability and long-time operation catalytic tests [5], for which CuO/CeO_2 and derived materials are ideal catalysts for this application.

However, the supply of cerium oxide is limited and subjected to geopolitical interests, since Rare Earths (RE) mineral sources are heterogeneously distributed over the planet and their extraction costs are very high not only economically but also environmentally [6]. In this regard, there is a deep, but not patent yet, problematic in RE metals use, which are nowadays present in nearly every electronic device and their demand is dramatically rising [7]. Therefore, the implementation of ceria-based catalytic technologies in CO-PROX reaction is only partially practicable since near-future strategies are meant to restrict RE use whenever efficient substitutes are available [8]. As a result, potential catalytic alternatives to cerium oxide materials are a need, and manganese oxides are claimed to be potential candidates for that purpose.

Manganese oxides are a very promising option to replace ceria due to their natural abundance, high oxygen mobility and oxygen storage capacity, apart from their low cost, environmental compatibility and non-toxicity [9,10]. The mineral oxide cryptomelane is based on a well-defined 2 x 2 tunnel structure (tunnel size of 0.46 nm × 0.46 nm) consisting of double chains of edge-shared MnO_6 octahedra and corner-sharing of the double chains [11,12], which gives rise to its general name “Octahedral Molecular Sieve” (OMS) [13]. Typically, the average manganese oxidation state in cryptomelane is around 3.8, which is a consequence of the coexistence of Mn^{4+} cations with small amounts of Mn^{3+} and Mn^{2+} [14], and the charge imbalance generated by partial reduction of Mn^{4+} is compensated by interstitial cations, such as K^+ and water species. Among manganese oxides, cryptomelane has presented an exceptional catalytic activity in a wide range of reactions [15–22],

The unique versatility over cryptomelane-based materials relies on the high porosity, acidity, hydrophobicity, electronic and ionic conductivities, and easy removal of lattice oxygen and recovery [15,23,24]. In addition, it is has been well-reported that cryptomelane catalytic properties are improved by means of the introduction of different framework dopants, such as Cu [32–36], attributed to the weakening of the Mn–O bond in Mn–O–Cu bridges, resulting in the mobility and reactivity of the active oxygen species. [32,37–39].

Interestingly, another approach to improve catalytic performance is to disperse CuO particles on the external facets of cryptomelane structure via precursor copper salts deposition, seeking the formation of a binary catalytic system composed of CuO supported on cryptomelane (CuO/Cryptomelane) [40], in analogy to the outstanding well-reported CuO/CeO_2 catalysts, where special interfacial redox properties by means of synergistic effects result in an excellent performance [41,42].

Therefore, the goal of the current study presented herein along Chapter 5 deals with the critical investigation of CuO/Cryptomelane catalyst as an alternative to CuO/CeO_2 catalyst towards CO-PROX reaction. To this aim, cyclability and stability tests were conducted in order to study CuO/Cryptomelane performance and activity loss, besides the mechanism of deactivation and possible strategies to prevent such negative process to guarantee a feasible operation in CO-PROX reaction.

5.2 Experimental details

5.2.1 Catalyst synthesis

The synthesis of Cryptomelane catalyst was conducted following the well-reported reflux route [5], and the latter Cu loading (5% wt. Cu) by impregnation followed by calcination led to the preparation of CuO/Cryptomelane catalyst. Further details regarding procedures have been presented in Section 2.1.1 from Chapter 2.

5.2.2 CO-PROX catalytic activity tests

Cryptomelane and CuO/Cryptomelane catalysts were tested in CO-PROX catalytic tests according to the experimental settings and specific conditions as stated in Section 2.2.3. Briefly, 100 ml/min of the CO-PROX gas mixture consisting in 2% CO, 2% O_2, 30% H_2 in He balance ($\lambda = 2$) was fed to the reactor with 150 mg of sample, and the experiment was conducted following heating rate of 2ºC/min from 25 to 200ºC. Consecutive catalytic cycles were performed in order to evaluate the stability of the catalysts, and after each catalytic cycle the catalysts were treated at 200ºC or 400ºC for 1 hour (heating rate 5ºC/min) in 20 ml/min of 10% O_2/He. Afterwards, the

reactor was cooled down to room temperature and a new catalytic cycle was conducted.

After four consecutive ramp CO-PROX experiments, a further isothermal CO-PROX experiment was also carried out using the same gas mixture (2 % CO, 2 % O_2, 30 % H_2, balance He). The temperatures were selected to obtain *ca.* 75 % CO conversion at the beginning of the isothermal experiments.

5.2.3 Catalysts characterization

Catalysts were characterized before and after the catalytic tests by means of X-ray photoelectron spectroscopy (XPS), Temperature programmed reduction with H_2 (H_2-TPR), X-ray diffraction (XRD) and N_2 adsorption at -196ºC, using DFT method for the determination of pore size distributions. All these techniques and procedures are explained in detail in Section 2.2.2 from Chapter 2.

5.3 Results and discussion

5.3.1 CO-PROX catalytic tests

Figure 5.1 shows results obtained with fresh catalysts in the CO-PROX reaction. Cryptomelane accelerates CO oxidation above 75ºC and CuO loading lowers the onset temperature, CuO/Cryptomelane showing CO oxidation even at room temperature. This improvement of the cryptomelane performance upon CuO loading was already reported by Hernández et al.[26], and was attributed to a high lattice oxygen mobility due to the formation of Cu-O-Mn bridges.

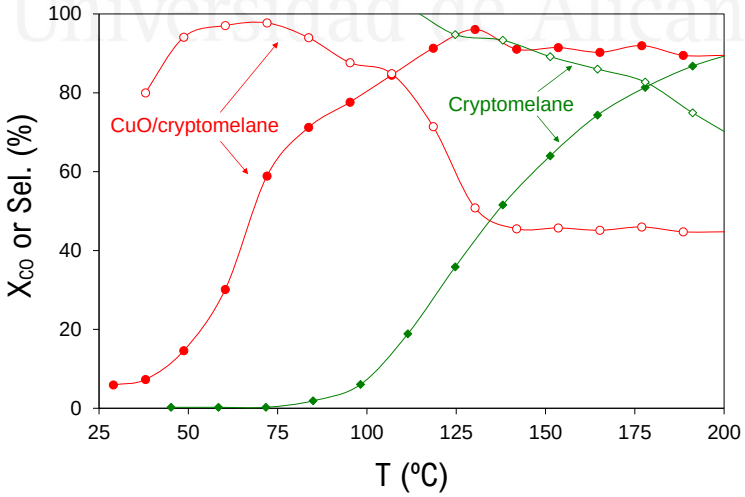

Figure 5.1. CO conversion (X_{CO}) in **(solid symbols)**; and CO selectivity (Sel.) in **(hollow symbols)** obtained in CO-PROX experiments performed with fresh catalysts.

The CO conversion profile of CuO/Cryptomelane reached a maximum value near 100% at 130ºC, and then decreased slowly with temperature. This drop of the CO conversion at high temperatures was already reported by other authors and was attributed to the competition between H_2 and CO oxidation and to the formation of hot spots (or higher local temperatures) as a consequence of the exothermic CO and H_2 oxidation reactions, which leads to the reversed WGS reaction and the subsequent CO formation [43,44].

Thus, the lower activation energy for CO oxidation when comparing to H_2 oxidation favours the preferential process only up to a critical temperature [42]. The selectivity profile of CuO/Cryptomelane reached a very high value (~96%) at relatively low temperature, and then decreased until an almost constant value of about 41%. It is important to highlight that a selectivity of 50% means that equal amounts of CO_2 (desired reaction) and H_2O (side reaction) would be produced and that this is the maximum selectivity achievable at total O_2 consumption in the experimental conditions used (excess oxygen with λ=2). Thus, even the relatively low selectivity remaining at high temperatures is high enough to obtain adequate fuel efficiency [44].

Once confirmed the excellent behaviour of the CuO/Cryptomelane catalyst, the stability was studied and four consecutive reaction cycles were performed with the CuO/Cryptomelane catalyst under the same experimental conditions used with the fresh catalyst (those indicated in the caption of Figure 5.1). For comparison, consecutive reaction cycles were also carried out with cryptomelane. As indicated in Section 5.2.2 from the present Chapter, after each reaction cycle the catalysts were reoxidized in 10% O_2/He for 1 h. The reoxidation temperature was 200ºC for cryptomelane while two temperatures were tested for CuO/Cryptomelane, 200 and 400ºC.

The catalytic performance in four successive runs was studied for each reoxidation pre-treatment, and registered $T_{50\%}$ temperatures, which is the temperature required to achieve 50% CO oxidation, are plotted in Figure 5.2.

Universitat d'Alacant
Universidad de Alicante

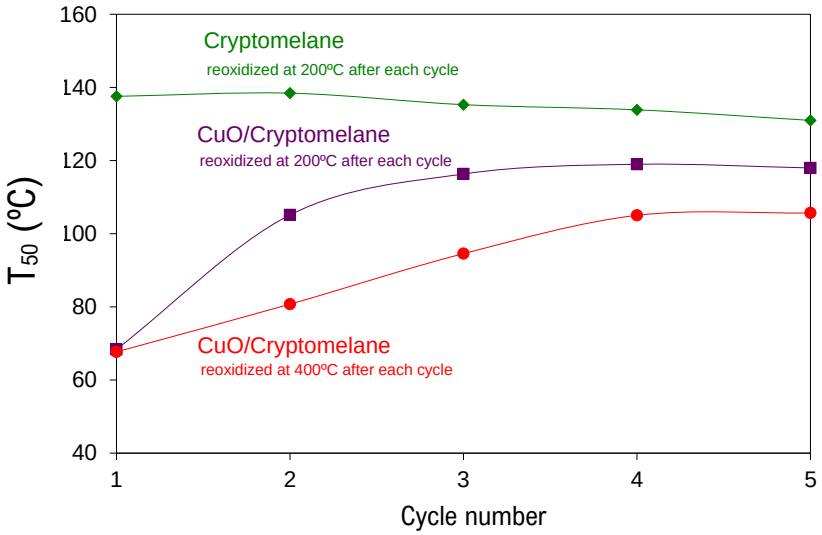

Figure 5.2. Temperature for 50% CO conversion in consecutive CO-PROX reaction cycles.

Cryptomelane kept the same activity during the five consecutive reaction cycles, evidencing the high stability of this catalyst. On the contrary, CuO/Cryptomelane partially deactivated in consecutive cycles, and the temperature of the reoxidation step played an important role. Reoxidation of CuO/Cryptomelane at 400ºC was more efficient than reoxidation at 200ºC, and both temperatures allowed obtaining stable T_{50} values after the fourth CO-PROX reaction cycle. Despite the CuO/Cryptomelane deactivation in consecutive cycles, the stable T_{50} values obtained with the copper-containing catalyst in the fourth and fifth cycles were lower than those of cryptomelane, and the lowest values were obtained by reoxidation at 400ºC.

These results in Figure 5.2 suggest that the decrease of the CO oxidation capacity of CuO/Cryptomelane, once used in the CO-PROX reaction, is related to changes in the copper species, since cryptomelane is stable. This hypothesis was also postulated by other authors [40,45] and will be discussed in more detail in the following sections.

5.3.2 Long-term catalytic tests

In order to evaluate the stability of the catalysts at constant temperature under CO-PROX reaction condition, long-term experiments were conducted after the forth cycle. The temperatures of the isothermal experiments were selected to obtain *ca*. 75 % CO conversion.

The CO conversion, CO selectivity and temperature monitored during more than 10 hours are shown in Figure 5.3a for CuO/cryptomelane and in Figure 5.3b for cryptomelane, and both catalysts maintained quite stable behaviours. Only the CuO/Cryptomelane catalyst suffered a small drop of

CO conversion (~ 6 %) at the beginning of the experiment, which could be related to the presence of copper species because is not observed in copper-free cryptomelane.

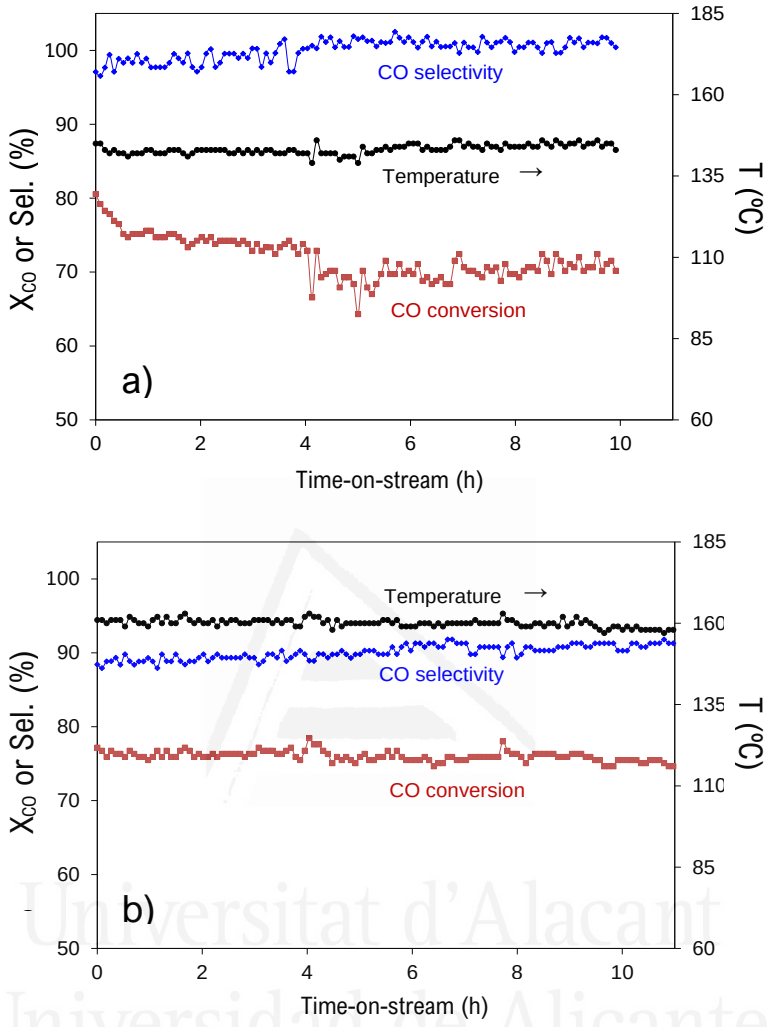

Figure 5.3. Long-term CO-PROX experiments performed with **(a)** CuO/Cryptomelane and **(b)** Cryptomelane.

In conclusion, the ramp experiments showed that cryptomelane is stable while CuO/Cryptomelane partially deactivates in consecutive CO-PROX reaction cycles performed from room temperature up to 200ºC. This deactivation was quite small in the long-term experiment performed at 145ºC, indicating that transformations leading to partial deactivation occur above this temperature. The catalytic activity of CuO/Cryptomelane was partially restored reoxidizing the catalyst, and 400ºC reoxidation was more effective than 200ºC reoxidation.

Universitat d'Alacant
Universidad de Alicante

5.3.3 XPS characterization

The ramp CO-PROX experiments suggested that changes in the copper species was the reason of the activity decay of the CuO/Cryptomelane catalyst in consecutive cycles, and XPS was used to analyze these changes during the experiments. Figure 5.4 shows the Cu2p region for fresh CuO/Cryptomelane and for this catalyst used in consecutive CO-PROX cycles with reoxidation treatments at 200ºC or 400ºC in between (XPS measurements were done after the fifth CO-PROX cycle). It is worth noting that the used catalyst was not reoxidized after the last CO-PROX cycle.

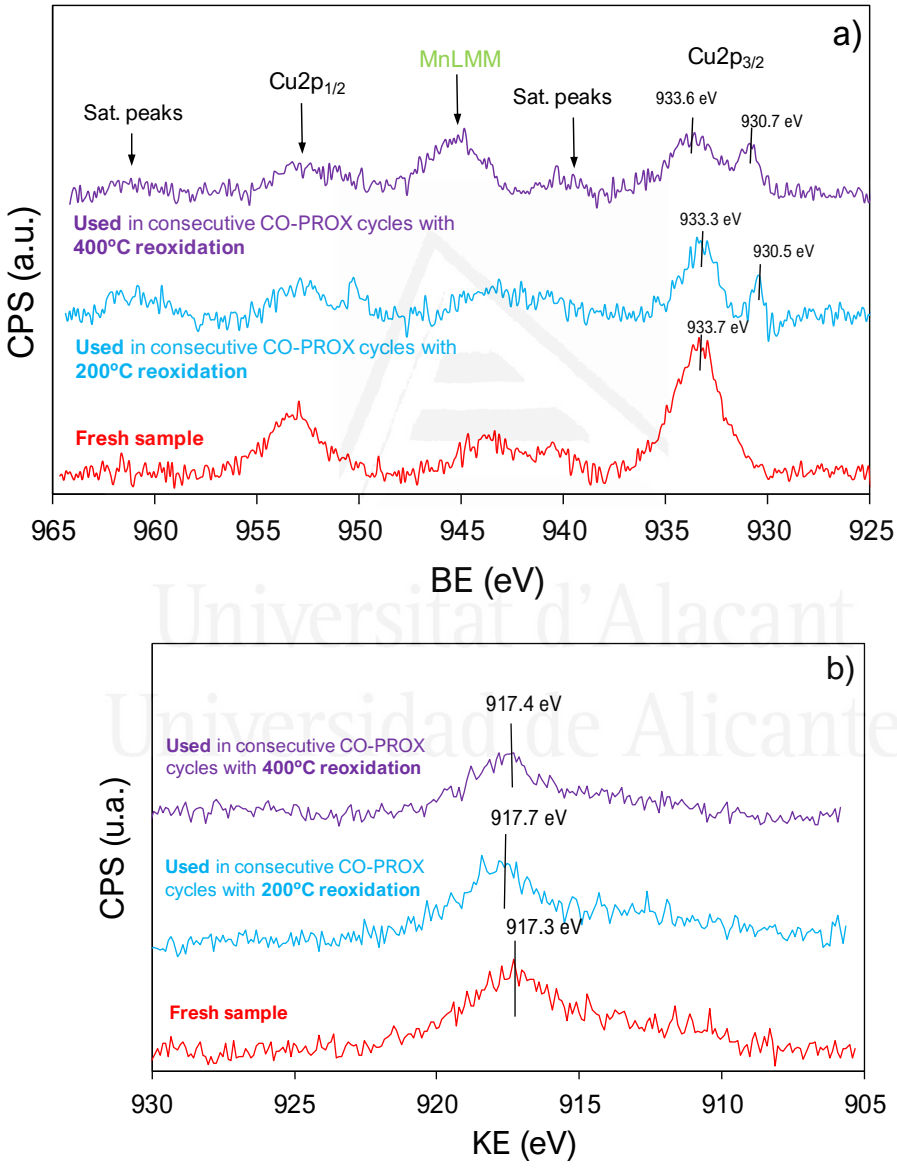

Figure 5.4. XPS spectra of CuO/Cryptomelane. **(a)** Cu2p region and **(b)** CuLMM Auger range.

Universitat d'Alacant
Universidad de Alicante

The Cu $2p_{3/2}$ photoemission of fresh catalyst showed a main contribution at 933.7 eV, typical of CuO [46], and the used catalyst additionally showed another contribution at 930.5-930.7 eV that must be assigned to copper species with different negative charge density. These low binding energy values have been reported for Cu-Mn mixed oxide with hopcalite structure ($CuMn_2O_4$) [47–49]. The main cations on hopcalite are Cu^{2+} and Mn^{3+}, but the presence of Cu^{+} has been postulated due to the equilibrium $Cu^{2+} + Mn^{3+} \leftrightarrow Cu^{+} + Mn^{4+}$. Evidences of the formation of hopcalite after the catalytic tests have been also obtained in the current study by XRD, as it will be discussed below.

These XPS results suggest that copper was fully oxidised as CuO on the fresh catalyst, which is not surprising because it was calcined for copper precursor decomposition, and part of this CuO was introduced into the hopcalite structure during the ramp CO-PROX experiments while part remained as CuO. The CuLMM Auger transition (Figure 4b) is quite similar in all spectra, being consistent with the presence of Cu(II). However, the relative contribution of the Cu^{2+} satellite peak at 944 eV (Figure 5.4a) with regard to the $Cu2p_{3/2}$ peak at ~ 933.5 eV increases on the spectra obtained with the used catalyst reoxidized at 400ºC with regard to that reoxidized at 200ºC. This suggests higher population of Cu(II) cations upon 400ºC reoxidation. Nevertheless, identification of the copper species by XPS is complex [50–53], and much more concluding evidences where obtained by H_2-TPR, as discussed below.

The surface composition of the cryptomelane and CuO/Cryptomelane catalysts was also analyzed by XPS, and Table 5.1 compiles results of the K/Mn and Cu/Mn ratios obtained.

Universitat d'Alacant
Universidad de Alicante

Table 5.1. Atomic surface composition of Cryptomelane and CuO/Cryptomelane determined by XPS.

Catalyst	K/Mn	Cu/Mn
Cryptomelane fresh	0.64	-
Cryptomelane used (Used in consecutive CO-PROX cycles with 200ºC reoxidation in between)	0.52	-
CuO/Cryptomelane fresh	0.58	0.19
CuO/Cryptomelane used (without reoxidation)	0.59	0.23
CuO/Cryptomelane (Used in consecutive CO-PROX cycles with 200ºC reoxidation in between)	0.65	0.12
CuO/Cryptomelane (Used in consecutive CO-PROX cycles with 400ºC reoxidation in between)	0.83	0.06

The K/Mn ratio of cryptomelane slightly decreased after the CO-PROX ramp experiment, but this small surface modification does not affect the

catalytic performance. On the contrary, the K/Mn atomic ratio of CuO/Cryptomelane remained constant after the CO-PROX ramp experiment (without reoxidation) and increased during the consecutive CO-PROX experiments with reoxidation treatments in between, suggesting certain segregation of potassium to the surface. These results indicate that the segregation of K to the surface mainly occurs during the reoxidation treatments when copper is present. This segregation of K to the surface was similarly suggested by Veprek et al. [47] for commercial hopcalite tested as CO oxidation catalyst. Furthermore, Hu et al. [54] also described this phenomenon for silver-doped cryptomelane, and in our CuO/Cryptomelane catalyst occurred in a higher extent when the reoxidation between cycles was performed at 400ºC than when was reoxidized at 200ºC.

In addition, the Cu/Mn ratio decreased after the CO-PROX reactions performed with reoxidation treatments in between, and the minimum value was obtained for the catalyst reoxidized at 400ºC between cycles. The reduction of this parameter can be an evidence of copper sintering.

These XPS results allowed concluding that the CuO/Cryptomelane catalyst suffered segregation of potassium to the surface and copper sintering, which could explain that the initial activity of the fresh catalyst was not fully recovered (see Figure 5.2) after the reoxidation treatments. More information about these transformations was obtained by complementary characterization techniques that are discussed in the coming sections.

5.3.4 H_2-TPR characterization

Since the redox processes occurring on CuO/Cryptomelane seem to be behind the partial deactivation of this catalyst in consecutive CO-PROX ramp experiments, H_2-TPR characterization was carried out to get further insight into such processes. Figure 5.5 compiles the H_2 reduction profiles obtained with the cryptomelane and CuO/Cryptomelane catalysts tested as prepared (fresh) and after CO-PROX experiments (after the fifth CO-PROX cycle).

The H_2-TPR profiles obtained with fresh and used cryptomelane are equal (top profiles in Figure 5.5), with a single peak with maxima at 400ºC and a low-temperature shoulder evidencing that several events were taking place. This is consistent with the high stability of this material in consecutive ramp CO-PROX experiments (Figure 5.2). Note that the onset H_2 reduction temperature in H_2-TPR experiments (~ 270ºC) was well above the maximum temperature achieved in the ramp CO-PROX experiments (200ºC).

The consumption of H_2 by cryptomelane in H_2-TPR experiments is attributed to the reduction of manganese cations, initially present mainly in +4 and +3 oxidation states, giving MnO as the final product of the reduction processes [55]. It is known that the reduction progresses throughout the following sequence: $MnO_2 \rightarrow Mn_2O_3 \rightarrow Mn_3O_4 \rightarrow MnO$, though it is not easy

to discern each step due to the experimental conditions and to the local environment of the reducible species [9,26,56]. Hence, cryptomelane has a complex reduction profile with several chemical transformations appearing under the same peak [32,33,57,58]. Typically, the H_2 reduction profiles of cryptomelane described in bibliography, which are similar to those on Figure 5.5, consist of a shoulder at about 340ºC, assigned to the reduction of surface cations, followed by a main peak attributed to bulk transformations of MnO_2/Mn_2O_3 to Mn_3O_4, and Mn_3O_4 to MnO, which overlap in the H_2-TPR profile.

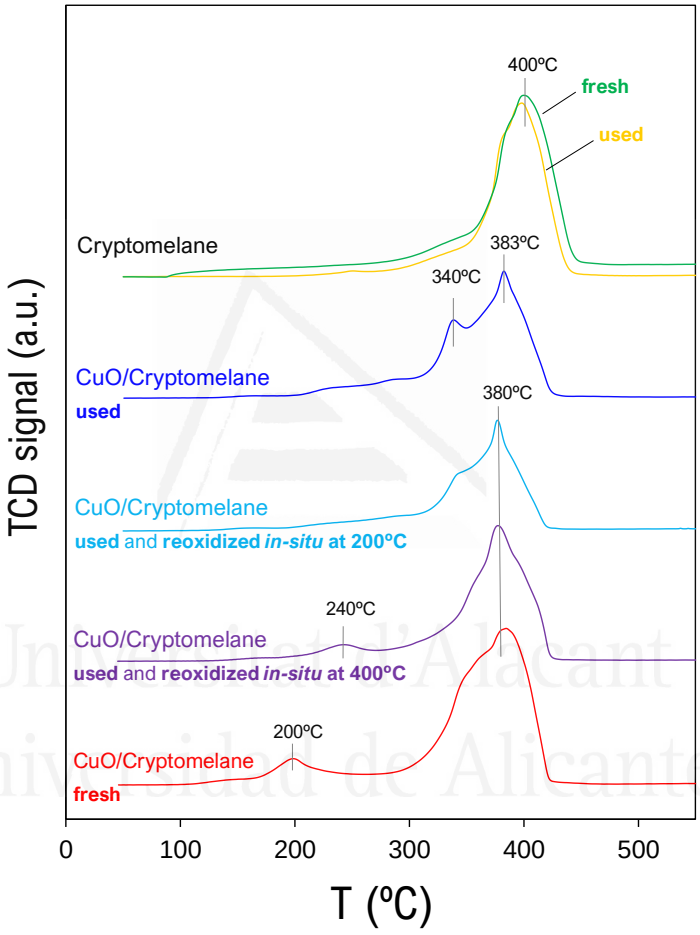

Figure 5.5. H_2 reduction profiles obtained with Cryptomelane and CuO/Cryptomelane catalysts tested as prepared (fresh) and after CO-PROX experiments (after the fifth CO-PROX cycle). In some cases, the used CuO/Cryptomelane catalyst was reoxidized in situ (in the H_2-TPR device) at 200 or 400ºC (at the same temperature used in each case in consecutive CO-PROX cycles for reoxidation between cycles).

The H_2 reduction profile of fresh CuO/Cryptomelane (bottom curve on Figure 5.5) had some differences with regard to that of bare cryptomelane (top curve on Figure 5.5). A H_2 consumption peak was observed at 200ºC associated to the reduction of disperse CuO particles. It must be taken into account that bulk CuO is reduced above 350ºC [46], and the shift to lower

temperature in CuO/Cryptomelane must be attributed to the effect of the cryptomelane support [59,60]. In addition, the reduction of cryptomelane also took place at lower temperature in CuO/Cryptomelane (maximum at 380ºC) than in bare cryptomelane (400ºC). It has been reported that the addition of copper leads to the creation of Cu^{2+}-O-Mn^{y+} entities that promote the oxygen lability with partial delocalization of the Mn – O bond, improving manganese reducibility [9,26,32,33,40]. Such lability is related to a high structural and superficial oxygen mobility, and this is positive for oxidation reactions occurring throughout a Mars-van Krevelen (MVK) mechanism, which is usually accepted for these kind of catalysts [30,40,61]. In the reaction studied in this article, it is expected that CO was oxidised by catalyst oxygen forming oxygen vacancies that were filled up by gas phase molecular oxygen afterwards [62].

Moreover it has been reported that metallic Cu has a catalytic effect on the dissociation of the H_2 molecule, and enhances the reduction of interfacial manganese cations by hydrogen *spillover* [32,60,63].This effect is strongly dependent on the CuO dispersion [64,65]. The catalytic effect of metallic copper would explain the shift of the main manganese reduction peak from 400 to 380ºC.

The H_2 reduction profile of fresh CuO/Cryptomelane changed after the ramp CO-PROX reaction (see reduction profile of used CuO/Cryptomelane in Figure 5). The peak at 200ºC associated to the reduction of highly dispersed CuO species disappeared, indicating that CuO was reduced under the reaction conditions of the CO-PROX ramp experiments. Instead, two little reduction events were identified at 240 and 280ºC, probably due to the reduction of CuO aggregates with two different sizes [40] that remained oxidised after the CO-PROX experiments. Additionally, the main band at 380-400ºC attributed to manganese cations reduction was also different for fresh and used CuO/Cryptomelane. The low-temperature shoulder observed in the fresh catalyst became a well-defined peak in the used catalyst. This could indicate that oxygen species were accumulated on the catalyst surface during the CO-PROX reaction, which would be reduced in the H_2-TPR experiments, and the desorption of carbonate/bicarbonate species accumulated on the catalyst as CO oxidation intermediates cannot be ruled out.

The reoxidation of the used CuO/Cryptomelane catalyst at 200ºC had a little effect on the H_2 reduction profile. The low temperature CuO reduction peak remained missing, evidencing that this temperature was not high enough to reoxidize copper. The main difference in the H_2 reduction profiles of the used CuO/Cryptomelane catalyst before and after reoxidation at 200ºC was the decrease of the peak at 340ºC, which would indicate that this reoxidation treatment removed surface species accumulated during the CO-PROX reaction.

Nevertheless, used CuO/Cryptomelane reoxidation at 400ºC leads to the oxidation of reduced copper, and a H_2 reduction peak appeared at 240ºC. This temperature was higher than that on the fresh catalyst (200ºC), and the worse reducibility of CuO after reduction and reoxidation would explain the partial decrease of the CO oxidation capacity in consecutive CO-PROX cycles (see Figure 5.2). This delay of the CuO reduction peak after reoxidation at 400ºC could be due to the worse CuO-crytomelane interaction [48,66,67] and would be consistent with the evidences of copper sintering provided by XPS (see Table 5.1).

5.3.5 Characterization by XRD and N_2 adsorption-desorption

The structural transformations of the catalysts during the ramp CO-PROX experiments were studied, and Figure 5.6 shows the X-Ray powder diffraction (XRD) patterns of fresh and used cryptomelane and CuO/Cryptomelane. All diffractograms showed the main reflexions of the Cryptomelane structure, while evidences of the CuO peaks were not observed in the diffractograms of CuO/Cryptomelane. This indicated that CuO aggregates must consist of small crystallites [68].

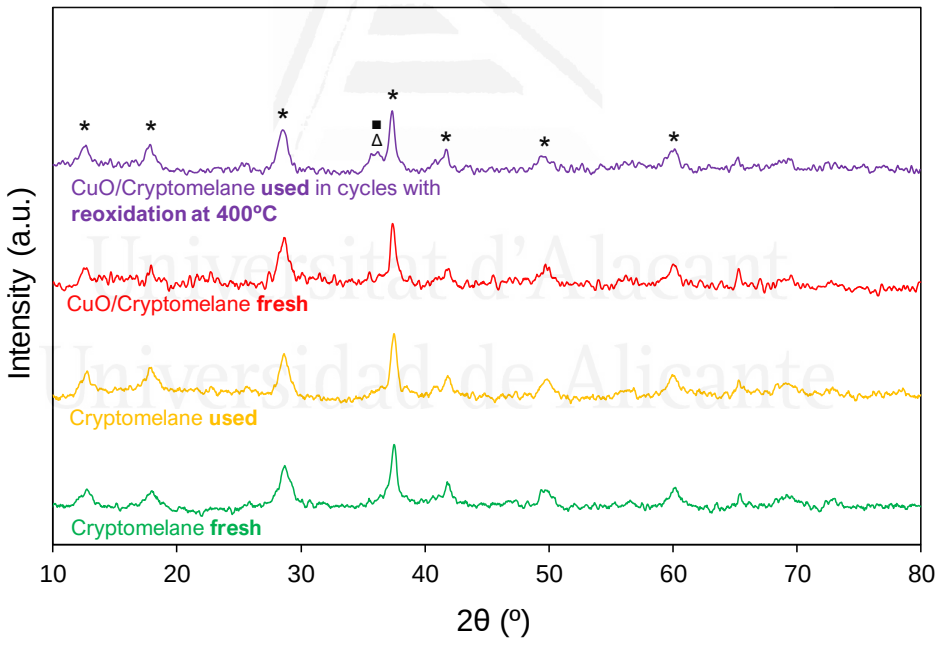

Figure 5.6. X-Ray powder diffraction patterns for fresh and spent Cryptomelane-based catalysts. Caption: (*) Cryptomelane (JCPDS card no. 29-1020); (Δ) $CuMn_2O_4$, (JCPDS card no. 45-0505); (■) Mn_3O_4, Hausmannite (JCPDS card no. 24-0734); (□) CuO (JCPDS card no. 80-1268).

The cryptomelane catalyst showed the same diffractogram before and after the ramp CO-PROX experiments, which was in good agreement with the high stability of this material under reaction conditions (see Figure 5.2).

On the contrary, an additional peak appeared on the diffractogram of CuO/Cryptomelane after the CO-PROX experiments that could be attributed to hausmannite (Mn_3O_4) and/or to hopcalite ($CuMn_2O_4$). Cryptomelane, hausmannite and hopcalite are based on tetragonal structures, and seldom transitions can take place as a consequence of partial reduction of manganese cations and/or due to the sintering of copper particles to form copper-manganese mixed oxide aggregates. These transformations are in agreement with the surface restructuration observed by XPS (Table 5.1) and with the delay of the copper species reduction peak in H_2-TPR experiments to higher temperatures (Figure 5.5), and also explain why the CO oxidation capacity of CuO/Cryptomelane was not fully recovered after reoxidation at 400ºC (Figure 5.2).

Finally, selected samples were characterized by N_2 adsorption-desorption at -196. Figure 5.7 includes the N_2 adsorption–desorption isotherms for fresh Cryptomelane, fresh CuO/Cryptomelane and CuO/Cryptomelane used in 5 consecutive CO-PROX cycles with 400ºC reoxidation in between. The obtained specific surface areas and pore volumes are compiled in Table 5.2.

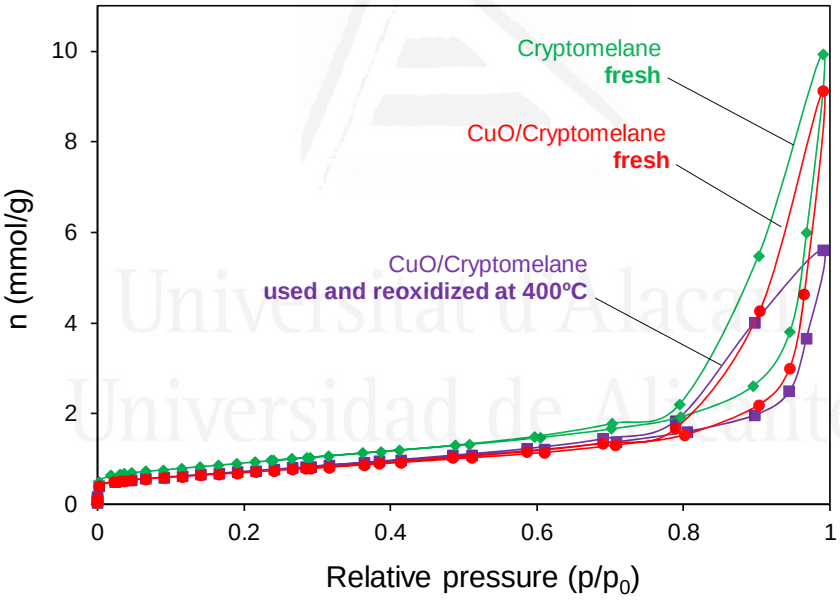

Figure 5.7. N_2 adsorption–desorption isotherms (-196ºC) characterization for fresh Cryptomelane, fresh CuO/Cryptomelane and used CuO/Cryptomelane in 5 consecutive CO-PROX cycles with 400ºC reoxidation in between.

Table 5.2. Catalyst characterization by gas adsorption–desorption

Catalyst	S_{BET} (m^2/g)	V_{DR} (N_2) (cm^3/g)	V_{DR} (CO_2) (cm^3/g)
Cryptomelane fresh	73	0.03	0.02
CuO/Cryptomelane fresh	59	0.02	0.01
CuO/Cryptomelane (Used in consecutive CO-PROX cycles with 400ºC reoxidation in between)	55	0.02	-

Cryptomelane showed a type IV N_2 adsorption isotherm, with a hysteresis loop in the high relative pressure range, which according to the IUPAC classification is typical of mesoporous materials. Cryptomelane-based materials show a type H3 hysteresis, as it does not exhibit any limiting adsorption at high P/P_0, and this is typical of non-rigid aggregates of plate-like particles giving rise to slit-shaped pores [69].

The N_2 adsorption-desorption isotherms of fresh and used CuO/Cryptomelane were qualitatively similar to that of cryptomelane, but with a slightly lower adsorption at low relative partial pressures. This decrease must be attributed to the partial porosity blocking by CuO. The surface area values are also consistent with the decrease produced upon CuO loading, being 73 m^2/g for Cryptomelane and 59 m^2/g for CuO/Cryptomelane, and these values are in agreement with those reported by other authors [21,30,40,70]. Further changes in the porosity of the CuO/Cryptomelane catalyst during the ramp CO-PROX reactions were negligible, indicating that the restructuration detected by XPS and XRD does not affect the porosity.

Universitat d'Alacant
Universidad de Alicante

5.4 Conclusions

In conclusion, the study of Cryptomelane and CuO/Cryptomelane catalysts in the CO-PROX reaction, paying special attention to deactivation and regeneration, has shown that:

(1) Cryptomelane was stable during CO-PROX reactions in ramp experiments until 200ºC and in a long-term isothermal experiment (10 h). Changes neither in the H_2 reducibility and porosity nor in the crystalline phases detected by XRD were observed.

(2) CuO/Cryptomelane partially deactivated in consecutive CO-PROX reaction cycles performed until 200ºC, and the catalytic activity was partially restored reoxidising the catalyst at 200ºC or 400ºC, the latter temperature being more effective.

(3) In spite of the CuO/Cryptomelane partial deactivation, the catalytic CO-PROX activity of this catalyst was higher to that of Cryptomelane once a stable behaviour was achieved.

(4) The partial deactivation of CuO/Cryptomelane was related to the segregation of crystalline phases (hausmannite (Mn_3O_4) and/or to hopcalite ($CuMn_2O_4$)), with segregation of potassium to the surface and decrease of the copper cations reducibility. The potential contribution to deactivation of changes in the porous texture of the CuO/Cryptomelane catalyst has been ruled out.

As these results bring promising opportunities for CuO/Cryptomelane catalyst when the appropriate reoxidation treatment is conducted. The following Chapter focuses on the study of CuO/Cryptomelane catalyst in real CO-PROX operation conditions, including H_2O and CO_2 in the reaction mixture together with CO and H_2.

References

[1] N. Bion, F. Epron, M. Moreno, F. Mariño, D. Duprez, Preferential oxidation of carbon monoxide in the presence of hydrogen (PROX) over noble metals and transition metal oxides: Advantages and drawbacks, Top. Catal. 51 (2008) 76–88.

[2] A. Mishra, R. Prasad, A review on preferential oxidation of carbon monoxide in hydrogen rich gases, Bull. Chem. React. Eng. Catal. 6 (2011) 1-14.

[3] E. Aneggi, M. Boaro, C. de Leitenburg, G. Dolcetti, A. Trovarelli, Insights into the redox properties of ceria-based oxides and their implications in catalysis, J. Alloys Compd. 408–412 (2006) 1096–1102.

[4] A. Bueno-López, Diesel soot combustion ceria catalysts, Appl. Catal. B Environ. 146 (2014) 1–11.

[5] D. Gamarra, C. Belver, M. Fernández-García, A. Martínez-Arias, Selective CO Oxidation in Excess H_2 over Copper−Ceria Catalysts: Identification of Active Entities/Species, J. Am. Chem. Soc. 129 (2007) 12064–12065.

[6] B. Zhou, Z. Li, C. Chen, Global Potential of Rare Earth Resources and Rare Earth Demand from Clean Technologies, Miner. 7 (2017) 203-217.

[7] S. Massari, M. Ruberti, Rare earth elements as critical raw materials: Focus on international markets and future strategies, Resour. Policy. 38 (2013) 36–43.

[8] N.T. Nassar, X. Du, T.E. Graedel, Criticality of the Rare Earth Elements, J. Ind. Ecol. 19 (2015) 1044–1054.

[9] K. Ramesh, L. Chen, F. Chen, Y. Liu, Z. Wang, Y.F. Han, Re-investigating the CO oxidation mechanism over unsupported MnO, Mn_2O_3 and MnO_2 catalysts, Catal. Today. 131 (2008) 477–482.

[10] R. Craciun, B. Nentwick, K. Hadjiivanov, H. Knözinger, Structure and redox properties of MnO_x/Yttrium-stabilized zirconia (YSZ) catalyst and its used in CO and CH_4 oxidation, 243 (2003) 67–79.

[11] H.C. Genuino, Y. Meng, D.T. Horvath, C.H. Kuo, M.S. Seraji, A.M. Morey, R.L. Joesten, S.L. Suib, Enhancement of catalytic activities of octahedral molecular sieve manganese oxide for total and preferential co oxidation through vanadium ion framework substitution, ChemCatChem. 5 (2013) 2306–2317.

Universidad de Alicante

[12] S.L. Suib, Microporous manganese oxides, Curr. Opin. Solid State Mater. Sci. 3 (1998) 63-70.

[13] Y.F. Shen, R.P. Zerger, R.N. DeGuzman, S.L. Suib, L. McCurdy, D.I. Potter, C.L. O'Young, Manganese oxide octahedral molecular sieves: Preparation, characterization, and applications, Science. 260 (1993) 511–515.

[14] R.N. DeGuzman, Y.F. Shen, E.J. Neth, S.L. Suib, C.L. O'Young, S. Levine, J.M. Newsam, Synthesis and characterization of Octahedral Molecular Sieves (OMS-2) having the hollandite structure, Chem. Mater. 6 (1994) 815–821.

[15] J. Luo, Q. Zhang, A. Huang, S.L. Suib, Total oxidation of volatile organic compounds with hydrophobic cryptomelane-type octahedral molecular sieves, Microporous Mesoporous Mater. 35–36 (2000) 209–217.

[16] H.C. Genuino, S. Dharmarathna, E.C. Njagi, M.C. Mei, S.L. Suib, Gas-Phase Total Oxidation of Benzene, Toluene, Ethylbenzene, and Xylenes Using Shape-Selective Manganese Oxide and Copper Manganese Oxide Catalysts, J. Phys. Chem. C. 116 (2012) 12066–12078.

[17] H. Tian, J. He, X. Zhang, L. Zhou, D. Wang, Facile synthesis of porous manganese oxide K-OMS-2 materials and their catalytic activity for formaldehyde oxidation, Microporous Mesoporous Mater. 138 (2011) 118–122.

[18] S. Ching, D.A. Kriz, K.M. Luthy, E.C. Njagi, S.L. Suib, Self-assembly of manganese oxide nanoparticles and hollow spheres. Catalytic activity in carbon monoxide oxidation, Chem. Commun. 47 (2011) 8286–8288.

[19] J. Chen, J. Li, H. Li, X. Huang, W. Shen, Facile synthesis of Ag–OMS-2 nanorods and their catalytic applications in CO oxidation, Microporous Mesoporous Mater. 116 (2008) 586–592.

[20] S. Wagloehner, M. Nitzer-Noski, S. Kureti, Oxidation of soot on manganese oxide catalysts, Chem. Eng. J. 259 (2015) 492–504.

[21] I. Atribak, A. Bueno-López, A. García-García, P. Navarro, D. Frías, M. Montes, Catalytic activity for soot combustion of birnessite and cryptomelane, Appl. Catal. B Environ. 93 (2010) 267–273.

[22] T. Jakubek, W. Kaspera, P. Legutko, P. Stelmachowski, A. Kotarba, How to Efficiently Promote Transition Metal Oxides by Alkali Towards Catalytic Soot Oxidation, Top. Catal. 59 (2016) 1083–1089.

[23] Y. Ding, X. Shen, S. Sithambaram, S. Gomez, R. Kumar, V.M.B. Crisostomo, S.L. Suib, M. Aindow, Synthesis and Catalytic Activity of Cryptomelane-Type Manganese Dioxide Nanomaterials Produced by a Novel Solvent-Free Method, Chem. Mater. 17 (2005) 5382–5389.

[24] J. Luo, Q. Zhang, J. Garcia-Martinez, S.L. Suib, Adsorptive and acidic properties, reversible lattice oxygen evolution, and catalytic mechanism of cryptomelane-type manganese oxides as oxidation catalysts, J. Am. Chem. Soc. 130 (2008) 3198–3207.

[25] P. Stelmachowski, A.H.A. Monteverde Videla, T. Jakubek, A. Kotarba, S. Specchia, The Effect of Fe, Co, and Ni Structural Promotion of Cryptomelane (KMn_8O_{16}) on the Catalytic Activity in Oxygen Evolution Reaction, Electrocatalysis. 9 (2018) 762–769.

[26] W.Y. Hernández, M. a. Centeno, F. Romero-Sarria, S. Ivanova, M. Montes, J.A. Odriozola, Modified cryptomelane-type manganese dioxide nanomaterials for preferential oxidation of CO in the presence of hydrogen, Catal. Today. 157 (2010) 160–165.

[27] Y. Li, Z. Fan, J. Shi, Z. Liu, J. Zhou, W. Shangguan, Modified manganese oxide octahedral molecular sieves M′-OMS-2 (M′=Co,Ce,Cu) as catalysts in post plasma-catalysis for acetaldehyde degradation, Catal. Today. 256 (2015) 178–185.

[28] X. Chen, Y.-F. Shen, S.L. Suib, C.L. O'Young, Characterization of Manganese Oxide Octahedral Molecular Sieve (M−OMS-2) Materials with Different Metal Cation Dopants, Chem. Mater. 14 (2002) 940–948.

[29] G.G. Xia, Y.G. Yin, W.S. Willis, J.Y. Wang, S.L. Suib, Efficient stable catalysts for low temperature carbon monoxide oxidation, J. Catal. 185 (1999) 91–105.

[30] M. Özacar, A.S. Poyraz, H.C. Genuino, C.-H. Kuo, Y. Meng, S.L. Suib, Influence of silver on the catalytic properties of the cryptomelane and Ag-hollandite types manganese oxides OMS-2 in the low-temperature CO oxidation, Appl. Catal. A Gen. 462–463 (2013) 64–74.

[31] M. Polverejan, J.C. Villegas, S.L. Suib, Higher Valency Ion Substitution into the Manganese Oxide Framework, J. Am. Chem. Soc. 126 (2004) 7774–7775.

[32] W.Y. Hernández, M.A. Centeno, S. Ivanova, P. Eloy, E.M. Gaigneaux, J. a. Odriozola, Cu-modified cryptomelane oxide as active catalyst for CO oxidation reactions, Appl. Catal. B Environ. 123–124 (2012) 27–35.

[33] Y. Yang, J. Huang, S. Zhang, S. Wang, S. Deng, B. Wang, G. Yu, Catalytic removal of gaseous HCBz on Cu doped OMS: Effect of Cu location on catalytic performance, Appl. Catal. B Environ. 150–151 (2014) 167–178.

[34] R. Kumar, J. Mittal, N. Kushwaha, B. V Rao, S. Pandey, C.-P. Liu, Room temperature carbon monoxide gas sensor using Cu doped OMS-2 nanofibers, Sensors Actuators B Chem. 266 (2018) 751–760.

[35] A.L. Ramstad, Ø. Mikkelsen, Structural characterisation of copper-containing manganese oxide octahedral molecular sieve (Cu-OMS-2) materials by X-ray absorption spectroscopy and cyclic voltammetry, J. Mol. Struct. 697 (2004) 109–117.

[36] Y. Shen, Cu Containing Octahedral Molecular Sieves and Octahedral Layered Materials, J. Catal. 161 (1996) 115–122.

[37] M. Sun, L. Yu, F. Ye, G. Diao, Q. Yu, Z. Hao, Y. Zheng, L. Yuan, Transition metal doped cryptomelane-type manganese oxide for low-temperature catalytic combustion of dimethyl ether, Chem. Eng. J. 220 (2013) 320–327.

[38] Y.G. Yin, W.Q. Xu, R. DeGuzman, S.L. Suib, C.L. O'Young, Studies of stability and reactivity of synthetic cryptomelane-like manganese oxide octahedral molecular sieves, Inorg. Chem. 33 (1994) 4384-4389.

[39] C.K. King'ondu, N. Opembe, C. Chen, K. Ngala, H. Huang, A. Iyer, H.F. Garcés, S.L. Suib, Manganese Oxide Octahedral Molecular Sieves (OMS-2) Multiple Framework Substitutions: A New Route to OMS-2 Particle Size and Morphology Control, Adv. Funct. Mater. 21 (2011) 312–323.

[40] X.S. Liu, Z.N. Jin, J.-Q. Lu, X.X. Wang, M.F. Luo, Highly active CuO/OMS-2 catalysts for low-temperature CO oxidation, Chem. Eng. J. 162 (2010) 151–157.

[41] M. Konsolakis, The role of Copper–Ceria interactions in catalysis science: Recent theoretical and experimental advances, Appl. Catal. B Environ. 198 (2016) 49–66.

[42] D. Gamarra, A.L. Cámara, M. Monte, S.B. Rasmussen, L.E. Chinchilla, A.B. Hungría, G. Munuera, N. Gyorffy, Z. Schay, V.C. Corberán, J.C. Conesa, A. Martínez-Arias, Preferential oxidation of CO in excess H_2 over CuO/CeO_2 catalysts: Characterization and performance as a function of the exposed face present in the CeO_2 support, Appl. Catal. B Environ. 130–131 (2013) 224–238.

[43] X. Ouyang, R. Besser, Effect of reactor heat transfer limitations on CO preferential oxidation, J. Power Sources. 141 (2005) 39–46.

[44] M.J. Kahlich, H. a Gasteiger, R.J. Behm, Kinetics of the Selective CO Oxidation in H_2-Rich Gas on Pt/Al_2O_3, J. Catal. 171 (1997) 93–105.

[45] Y.I. Hasegawa, R.U. Maki, M. Sano, T. Miyake, Preferential oxidation of CO on copper-containing manganese oxides, Appl. Catal. A Gen. 371 (2009) 67–72.

[46] J. Giménez-Mañogil, A. Bueno-López, A. García-García, Preparation, characterisation and testing of $CuO/Ce_{0.8}Zr_{0.2}O_2$ catalysts for NO oxidation to NO_2 and mild temperature diesel soot combustion, Appl. Catal. B Environ. 152–153 (2014) 99–107.

[47] S. Vepek, Mechanism of the deactivation of Hopcalite catalysts studied by XPS, ISS, and other techniques, J. Catal. 100 (1986) 250–263.

[48] M. Krämer, T. Schmidt, K. Stöwe, W.F. Maier, Structural and catalytic aspects of sol–gel derived copper manganese oxides as low-temperature CO oxidation catalyst, Appl. Catal. A Gen. 302 (2006) 257–263.

[49] H. Chen, X. Tong, Y. Li, Mesoporous Cu–Mn Hopcalite catalyst and its performance in low temperature ethylene combustion in a carbon dioxide stream, Appl. Catal. A Gen. 370 (2009) 59–65.

[50] G.E. Wagner, C.D., Riggs, W.M., Davis, L.E., Moulder, J.F., Mullenberg, Handbook of X-Ray Photoelectron Spectroscopy, Perkin-Elmer Corp., Physical Electronics Division, Eden Prairie, Minnesota, USA, 1979.

[51] A. Martínez-Arias, M. Fernández-García, J. Soria, J.C. Conesa, Spectroscopic study of a Cu/CeO_2 catalyst subjected to redox treatments in carbon monoxide and oxygen, J. Catal. 182 (1999) 367–377.

[52] G. Moretti, Auger parameter and Wagner plot in the characterization of chemical states by X-ray photoelectron spectroscopy: A review, J. Electron Spectros. Relat. Phenomena. 95 (1998) 95–144.

[53] J.P. Espinós, J. Morales, A. Barranco, A. Caballero, J.P. Holgado, A.R. González-Elipe, Interface Effects for Cu, CuO, and Cu_2O Deposited on SiO_2 and ZrO_2. XPS Determination of the Valence State of Copper in Cu/SiO_2 and Cu/ZrO_2 Catalysts, J. Phys. Chem. B. 106 (2002) 6921–6929.

[54] R. Hu, C. Yan, L. Xie, Y. Cheng, D. Wang, Selective oxidation of CO in rich hydrogen stream over Ag/OMS-2 catalyst, Int. J. Hydrogen Energy. 36 (2011) 64–71.

[55] F. Kapteijn, L. Singoredjo, A. Andreini, J.A. Moulijn, Activity and selectivity of pure manganese oxides in the selective catalytic reduction of nitric oxide with ammonia, Appl. Catal. B Environ. 3 (1994) 173–189.

[56] M. Piumetti, D. Fino, N. Russo, Mesoporous manganese oxides prepared by solution combustion synthesis as catalysts for the total oxidation of VOCs, Appl. Catal. B Environ. 163 (2015) 277–287.

[57] V.P. Santos, M.F.R. Pereira, J.J.M. Órfão, J.L. Figueiredo, The role of lattice oxygen on the activity of manganese oxides towards the oxidation of volatile organic compounds, Appl. Catal. B Environ. 99 (2010) 353–363.

[58] L.M. Martínez, F. Romero-Sarria, W.Y. Hernández, M.A. Centeno, J.A. Odriozola, Gold supported cryptomelane-type manganese dioxide OMS-2 nanomaterials deposited on AISI 304 stainless steels monoliths for CO oxidation, Appl. Catal. A Gen. 423–424 (2012) 137–145.

[59] E.C. Njagi, H.C. Genuino, C.K. King'Ondu, C.H. Chen, D. Horvath, S.L. Suib, Preferential oxidation of CO in H_2-rich feeds over mesoporous copper manganese oxides synthesized by a redox method, Int. J. Hydrogen Energy. 36 (2011) 6768–6779.

[60] K. Qian, Z. Qian, Q. Hua, Z. Jiang, W. Huang, Structure-activity relationship of CuO/MnO2 catalysts in CO oxidation, Appl. Surf. Sci. 273 (2013) 357–363.

[61] C.H. Chen, S.L. Suib, Control of catalytic activity via porosity, chemical composition, and morphology of nanostructured porous manganese oxide materials, J. Chinese Chem. Soc. 59 (2012) 465–472.

[62] W. Gac, The influence of silver on the structural, redox and catalytic properties of the cryptomelane-type manganese oxides in the low-temperature CO oxidation reaction, Appl. Catal. B Environ. 75 (2007) 107–117.

[63] K. Liu, A. Wang, T. Zhang, Recent Advances in Preferential Oxidation of CO Reaction over Platinum Group Metal Catalysts, ACS Catal. 2 (2012) 1165–1178.

[64] F.C. Buciuman, F. Patcas, T. Hahn, A spillover approach to oxidation catalysis over copper and manganese mixed oxides, Chem. Eng. Process. Process Intensif. 38 (1999) 563–569.

[65] J. Ashok, P.S. Reddy, G. Raju, M. Subrahmanyam, A. Venugopal, Catalytic Decomposition of Methane to Hydrogen and Carbon Nanofibers over Ni−Cu−SiO_2 Catalysts, Energy & Fuels. 23 (2009) 5–13.

[66] E.C. Njagi, C.H. Chen, H. Genuino, H. Galindo, H. Huang, S.L. Suib, Total oxidation of CO at ambient temperature using copper manganese oxide catalysts prepared by a redox method, Appl. Catal. B Environ. 99 (2010) 103–110.

[67] A.A. Mirzaei, H.R. Shaterian, M. Kaykhaii, The X-ray photoelectron spectroscopy of surface composition of aged mixed copper manganese oxide catalysts, Appl. Surf. Sci. 239 (2005) 246–254.

[68] M. Monte, D. Gamarra, A. López Cámara, S.B. Rasmussen, N. Gyorffy, Z. Schay, A. Martínez-Arias, J.C. Conesa, Preferential oxidation of CO in excess H_2 over CuO/CeO_2 catalysts: Performance as a function of the copper coverage and exposed face present in the CeO_2 support, Catal. Today. 229 (2014) 104–113.

[69] M. Lowell, S., Shields, J.E., Thomas, M.A., Thommes, Characterization of Porous Solids and Powders: Surface Area, Pore Size and Density, Springer Netherlands, Heidelberg, 2004.

[70] C. Almquist, M. Krekeler, L. Jiang, An investigation on the structure and catalytic activity of cryptomelane-type manganese oxide materials prepared by different synthesis routes, Chem. Eng. J. 252 (2014) 249–262.

Universitat d'Alacant
Universidad de Alicante

CHAPTER 6

Effect of CO_2 and H_2O in the catalytic performance of CuO/Cryptomelane for the preferential oxidation of CO

The catalytic activity of CuO/Cryptomelane in CO-PROX reaction has been studied in the absence and presence of H_2O and CO_2, paying special attention to the catalyst stability and to changes on its physical-chemical properties. For fresh CuO/cryptomelane catalyst, the presence of CO_2 and/or H_2O in the CO-PROX feed partially inhibits CO oxidation due to chemisorption of H_2O and CO_2 on the catalyst. H_2O chemisorption on CuO/Cryptomelane is stronger than CO_2 chemisorption, and simultaneous CO_2 and H_2O adsorption has a synergistic effect that enhances co-adsorption and significantly hinders CO oxidation. On the contrary, the presence of CO_2 + H_2O in the CO-PROX reaction mixture has a positive effect in the CuO/Cryptomelane stability upon several consecutive reaction cycles in the 25-200ºC range. XRD showed that chemisorbed CO_2 + H_2O species partially prevent the catalyst deactivation due to cryptomelane reduction to hausmannite (Mn_3O_4) under the strongly reductive environment of the CO-PROX reaction, and H_2-TPR and Raman spectroscopy characterization support that the cryptomelane structure is less damaged under CO-PROX conditions in the presence of CO_2 and H_2O than in the absence of these species. Therefore, interestingly under CO_2 + H_2O environment (realistic CO-PROX conditions) CuO/Cryptomelane catalyst performs an improved catalytic activity once stable behavior is reached.

A. Davó-Quiñonero et al., *Appl. Catal. B Env.* **217** (2017) 459–465

Universitat Rovira i Virgili
Universitat de Barcelona

6.1 Introduction

In the previous Chapter, a CuO/Cryptomelane catalyst was tested in CO-PROX reaction with a CO + H_2 + O_2 gas mixture, and an exceptional performance was found [1]. However, its catalytic activity lowered in successive cycles of reaction, despite regeneration steps were conducted between cycles. Such deactivation was associated to partial collapse of cryptomelane structure produced by potassium segregation and copper sintering under CO-PROX reaction conditions. Despite this loss of activity, the remaining activity of CuO/Cryptomelane catalyst showed a good potential for CO-PROX oxidation under the reaction conditions of that study.

The effect of CO_2 and H_2O in the CO-PROX reaction feed in the activity, selectivity and stability of CuO/Cryptomelane was not evaluated in our previous study [1], and it is known the detrimental effect of these inhibitors in many CO-PROX catalysts, such as CuO/Ceria [2]. The study from Hernández et al. [3] was pioneer in undergoing CO-PROX real conditions using Cryptomelane. These authors evaluated the activity of Cu-modified cryptomelane for CO-PROX reaction with the addition of CO_2, H_2O and CO_2 + H_2O in the reaction mixture, concluding that CO_2 partially inhibits the activity while H_2O inhibits or enhances the activity depending on the reaction temperature. The inhibiting effect of CO_2 and H_2O was attributed to the blockage of CO chemisorption sites while the positive effect of H_2O above a critical temperature was explained appealing to the thermodynamics of parallel reactions that could take place in presence of water, such as the Reverse Water Gas Shift reaction [4], and to the formation of labile intermediates of fast desorption by means of the surface hydroxyl groups. As far as we know, the stability of CuO/Cryptomelane catalysts under CO-PROX reaction conditions including CO_2 and H_2O in the reaction mixture has not been studied so far, and this is a critical issue for the potential application of this promising catalysts in real devices. Therefore, the goal of this study is to analyse the stability of CuO/Cryptomelane catalyst under realistic CO-PROX conditions including CO_2, H_2O and CO_2 + H_2O in the gas mixture, not only paying attention to the effect of these species on the chemical processes occurring under reaction conditions but also to changes on the physical-chemical properties of the catalyst in consecutive reaction tests.

6.2 Experimental details

The synthesis of CuO/Cryptomelane catalyst (5% wt. Cu) was conducted following the well-reported reflux route [5] according to the previously procedure detailed in Section 2.1.1 from Chapter 2.

. The prepared CuO/Cryptomelane was tested in CO-PROX catalytic tests according to the experimental settings and specific conditions as stated in Section 2.2.3. Briefly, 100 ml/min of the CO-PROX gas mixture consisting

in 2% CO, 2% O_2, 30% H_2 in He balance (λ = 2) was fed to the reactor with 150 mg of sample, and the experiment was conducted following heating rate of 2ºC/min from 25 to 200ºC. The effect of inhibitors was studied, too, performing different catalytic cycles in the set of conditions: $CO+H_2+O_2$; $CO+H_2+O_2+CO_2$; $CO+H_2+O_2+H_2O$; and $CO+H_2+O_2+CO_2+H_2O$, conducted by means of the introduction, either separated or together, of 9% CO_2 and 5% H_2O in the reactant gas mixture feeding.

The chemical adsorption of CO_2 and H_2O on CuO/Cryptomelane catalysts was studied by means of temperature programmed desorption (TPD), performing saturation steps over pre-treated sample in 100 ml/min of 10% CO_2/Ar (for CO_2-TPD), 5% H_2O/Ar (for H_2O-TPD) or 10% CO_2 + 5%H_2O/Ar (for CO_2+H_2O-TPD). Fresh and spent catalyst samples were analyzed by means of temperature programmed reduction with H_2 (H_2-TPR), X-ray diffraction (XRD), and Raman spectroscopy. Further details regarding the experimental settings can be found in Section 2.2.2 from Chapter 2.

6.3 Results and discussion

6.3.1 CO-PROX reaction catalytic tests

Figure 6.1 shows the CO conversion (Figure 6.1a) and CO selectivity (Figure 6.1b) profiles in the ramp experiments conducted in CO-PROX conditions for the fresh CuO/Cryptomelane catalyst (first run) under the different atmospheres tested.

According to Figure 6.1, the gas mixture composition strongly affects the catalytic activity. The catalyst showed the best performance when tested under CO + H_2 + O_2 mixture, reaching its maximum CO conversion of 95% at 125ºC and keeping after that temperature a stable conversion of 88%. Such CO conversion decay coincides with a loss of CO oxidation selectivity towards the competitive reaction of H_2 oxidation, which reaches an acceptable constant value of 44% (being 50% the maximum selectivity that can be achieved given the O_2 stoichiometric excess, λ=2). This was the expected behaviour of this catalyst for these experimental conditions, as discussed in the previous chapter, and is in good agreement with the behaviour previously reported on literature [3,6]

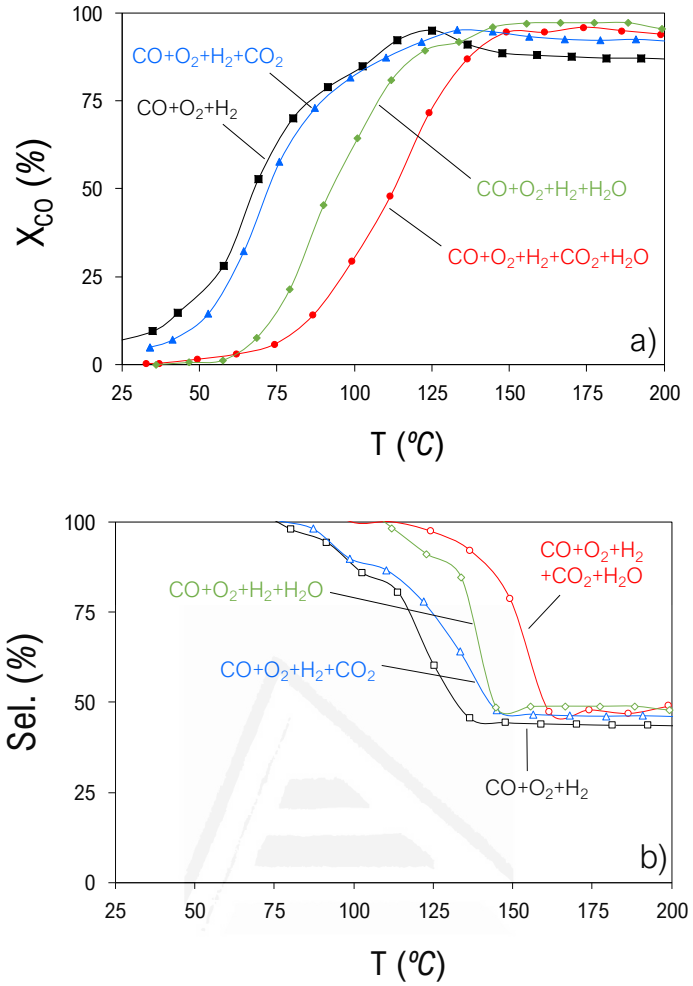

Figure 6.1. CO-PROX experiments performed with fresh catalyst (first run for each gas mixture) under gas mixtures of different composition. **(a)** CO conversion (X_{CO}) and **(b)** CO selectivity (Sel.).

The addition of CO_2 to the reactant mixture slightly decreases the catalytic activity, shifting the CO conversion and CO selectivity profiles towards higher temperatures. The inhibitor effect of CO_2 in many CO-PROX catalysts is well-known [3,7], but in this case, our CuO/Cryptomelane catalyst is only minimally affected. On the contrary, results on Figure 1 evidence that H_2O strongly affects CO oxidation, delaying the CO oxidation curve about 25ºC, and the experiment performed with $CO + H_2 + O_2 + CO_2 + H_2O$ reveals a synergy between the CO_2 and H_2O inhibiting effects.

Some authors suggested that the presence of H_2O and/or CO_2 in the CO-PROX reaction mixture does not affect the mechanism of reaction for transition metal (Co, Cr, Cu, Ni, Zn) catalysts supported on oxides with very different nature (MgO, La_2O_3, SiO_2–Al_2O_3, CeO_2,$Ce_{0.63}Zr_{0.37}O_2$), as CO selectivity profile is not modified in any case, just shifting in temperature in the same way than CO conversion [8]. These conclusions are also in agreement with those of Hernández et al. [16] for Cu-modified Cryptomelane

CO-PROX catalysts, but these authors additionally reported the contribution of parallel reactions involving H_2O above a certain temperature.

Assuming that the inhibition processes can be associated to chemisorption of H_2O and CO_2 on the CuO/Cryptomelane catalyst, our results indicate that H_2O chemisorption on CuO/Cryptomelane is stronger than CO_2 chemisorption. H_2O chemisorption could take place both in the external surface of cryptomelane and/or into the channels. External chemisorption of H_2O (and CO_2) is expected to compete with CO chemisorption, while H_2O chemisorption into the channels will increase the amount of structural water decreasing the population of oxygen vacancies and oxygen mobility.

According to literature results obtained for other CO-PROX catalysts [29], surface CO_2 chemisorption probably leads to the formation of mono- and/or bidentate carbonates on the catalyst surface, H_2O is expected to lead to the formation of hydroxyl groups, and simultaneous CO_2 and H_2O chemisorption will probably form a mixture of carbonate and bicarbonate species [9]. Unfortunately, all our attempts to identify such chemisorbed species by *in situ* DRIFTS experiments failed due to the high adsorption of IR radiation by the CuO/Cryptomelane catalyst because of its dark black colour.

In order to check the stability of the CuO/Cryptomelane catalyst under the catalytic conditions tested, four consecutive cycles of reaction were carried out (without any regeneration treatment between cycles). The CO conversion and selectivity profiles obtained were qualitatively similar to those compiled in Figure 6.1, and only changed the temperatures depending on the gas mixture and run number. Figure 6.2 compiles the temperatures for 50% CO conversion in these experiments.

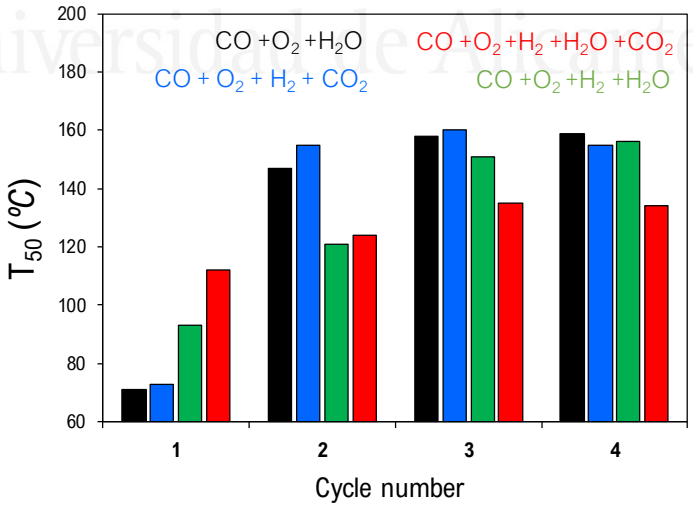

Figure 6.2. Temperature for 50% of CO conversion in consecutive reaction cycles under gas mixtures of different composition.

In accordance to our previous conclusions [24], the catalytic activity in CO + H_2 + O_2 decreases after the first run, and this was attributed to the segregation of crystalline phases (hausmannite (Mn_3O_4) and/or hopcalite ($CuMn_2O_4$)), with the segregation of potassium to the surface and decrease in the copper cations' reducibility. Figure 6.2 shows that the effect of adding CO_2 to the reaction atmosphere in CO oxidation in consecutive cycles is negligible.

On the contrary, deactivation in consecutive cycles occurs more gradually in the presence of H_2O, leading to a steady state in the fourth cycle similar to that achieved with CO + H_2 + O_2 (with and without CO_2). Therefore, the presence of H_2O seems to affect the kinetics of changes occurring on the catalyst leading to partial deactivation. Such positive impact is even more evident when CO_2 and H_2O are added simultaneously, since the catalyst reaches a stable behaviour after the third cycle with a T_{50} temperature lower to that achieved under all other gas mixtures tested. In the presence of CO_2 + H_2O, the catalytic activity is clearly inhibited on the first run, but the moderate deactivation occurring along further cycles leads to the best performance after four cycles of reaction. Hence, in these conditions, CO_2 is facilitating H_2O-cryptomelane interaction, which is being positive for the maintenance of the catalyst integrity. Thus, despite the negative blocking of the catalyst surface by CO_2 and H_2O and the consequent initial inhibition of the catalytic activity, the incorporation of CO_2 and H_2O is, in the end, positive to perform CO-PROX in CuO/Cryptomelane in further reaction cycles.

6.3.2 Temperature Programmed Desorption (TPD) experiments

In order to study the CO_2 and H_2O chemisorption on CuO/Cryptomelane, TPD experiments were conducted after saturation of the catalyst with CO_2 (CO_2-TPD), H_2O (H_2O-TPD), and CO_2 + H_2O (CO_2+H_2O-TPD). Additionally, a control experiment was carried out omitting the saturation step previous to TPD. The control experiment allows discerning the effect of the saturation steps from the inherent decomposition of the fresh material. Figure 6.3 shows the results obtained in all TPD experiments conducted, following by mass spectrometry the m/z signals 44, 18 and 32, corresponding to CO_2, H_2O and O_2, respectively.

Two regions must be distinguished on Figure 6.3, below and above 450ºC approximately. Cryptomelane structure starts decomposing to Mn_2O_3 at temperatures around 500ºC, the actual temperature depending on the atmosphere and particle size [10]. This is consistent with the release of O_2 observed in Figure 3c, and previous saturation of the catalysts with CO_2 and/or H_2O has a minor effect on the release of O_2 in the experimental conditions of these experiments. Below 500ºC, the cryptomelane structure is maintained but a loss of the water bounded to the cryptomelane nanofibers takes place together with desorption of the chemisorbed species.

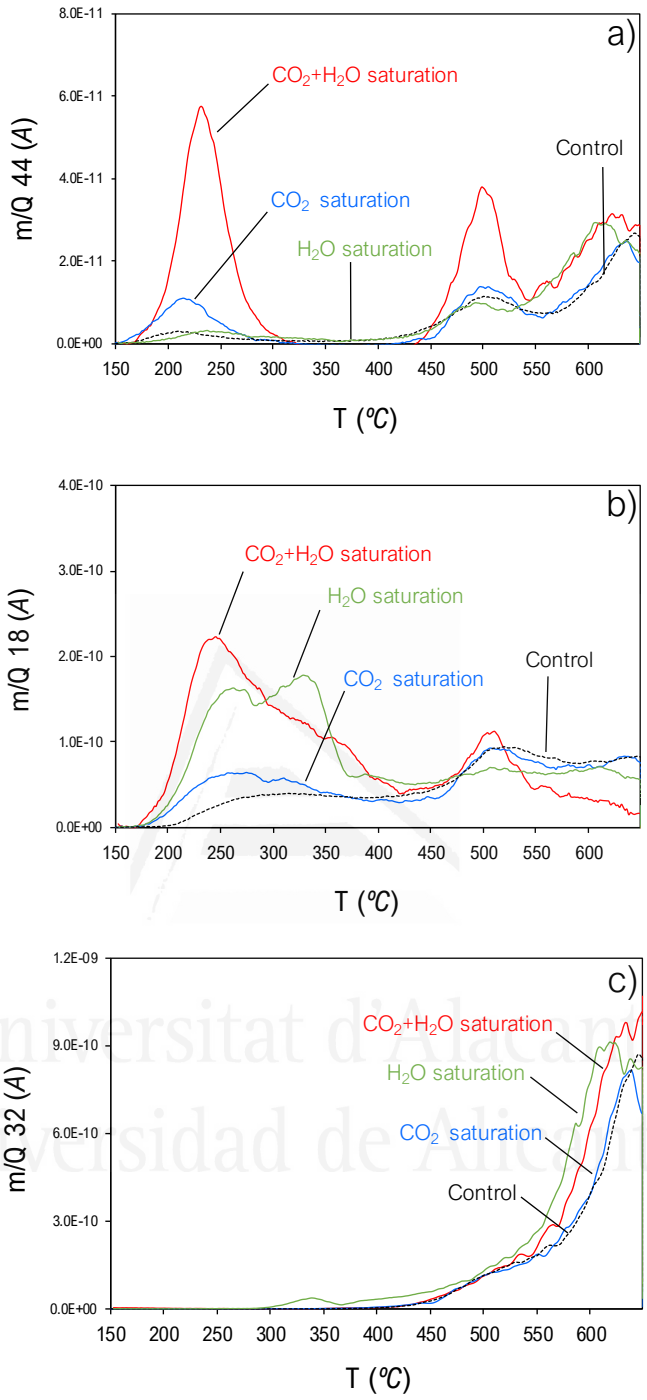

Figure 6.3. TPD experiments performed in Ar after saturation of the CuO/Cryptomelane catalyst with CO_2, H_2O, or CO_2+H_2O (control = no previous saturation). **(a)** CO_2 release, **(b)** H_2O release and **(c)** O_2 release.

After saturation with CO_2, a CO_2 evolution peak centred at 215ºC is observed on the TPD profile (Figure 6.3a), which is associated to the decomposition of carbonates formed during the saturation step. The intensity of this peak increases drastically upon saturation with a mixture of CO_2 +

H_2O, indicating that the presence of H_2O significantly enhances CO_2 chemisorption.

Besides, it can be discerned in Figure 6.3b two types of chemisorbed H_2O species that are desorbed in the ranges 150-300ºC and 300-375ºC, corresponding to the evolution of surface-related water and water bounded inside the 2x2 tunnels, respectively. On the other hand, CO_2-TPD and H_2O-TPD experiments show that cryptomelane has a clear preference towards water interaction and is capable to chemisorb water in the narrow tunnel with strong adsorption potential due to the micropore filling, which is in agreement with the study of Kijima et al. [11].

When CO_2 and H_2O are added simultaneously in the saturation step, the emission profiles for the signals 44 and 18 change in a great measure, displaying a coupled CO_2 and H_2O evolution and evidencing the magnification of the chemisorption capacity of cryptomelane towards these species when added together rather than in separate environments. Below 450ºC, the sharp CO_2 peak can be matched to the H_2O evolution in the same temperature window, which is associated to the desorption of bicarbonate species that are thermodynamically less stable and more labile than carbonates [9]. The preferential formation of bicarbonates rather than carbonates in the presence of H_2O upon CO_2 chemisorption gives rise to a different interaction with the catalyst, which improves its chemisorption capacity towards carbon-based species. Thus, the m/z 18 peak in the 300-375ºC range observed in the experiment with H_2O saturation, which is assigned to H_2O occluded inside the tunnels, is not visible upon $CO_2 + H_2O$ co-chemisorption, suggesting that H_2O is instead forming bicarbonate intermediates that cannot enter the narrow pores of the structure.

As a conclusion, TPD experiments have shown the synergistic effect between CO_2 and H_2O towards the formation of chemisorbed species, which can be critical in the catalytic process. These TPD results (Figure 6.3) are in agreement with the observed catalytic activities during the first cycle of CO-PROX experiments performed under different gas mixtures (Figure 6.1), where CO_2 has almost no influence, H_2O inhibits the activity by blocking active sites and/or decreasing oxygen vacancies and CO_2+H_2O inhibit in higher extent by means of forming a larger amount of chemisorbed species with stronger interaction with cryptomelane. However, this negative effect of CO_2 and H_2O co-chemisorption during the first cycle of catalytic tests (see Figure 2) becomes positive effect in further cycles, and the reasons are discussed in the coming section.

6.3.3 Characterization of fresh and used catalysts

Figure 6.4 shows X-Ray diffraction patterns for the fresh CuO/Cryptomelane catalyst and once used in four consecutive reactions with $CO + H_2 + O_2 + CO_2 + H_2O$ and with $CO + H_2 + O_2$. In all cases, the CuO

tenorite diffraction peaks are not distinguished, but important changes in the diffraction pattern of the cryptomelane support are observed in the fresh and used samples.

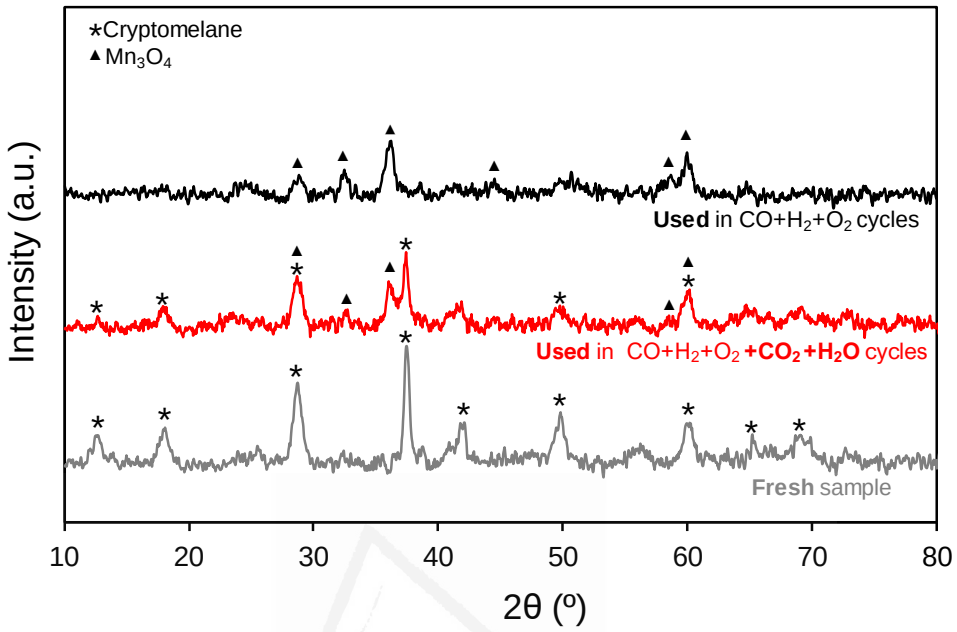

Figure 6.4. XRD diffraction patterns for the CuO/Cryptomelane catalysts**.** Caption: (□) Cryptomelane: JCPDS card no. 29-1020; (▲) Hausmannite: JCPDS card no. 24-0734.

The X-Ray diffraction patterns shown in Figure 6.4 prove that the deactivation of the CuO/Cryptomelane catalyst depends on the reaction gas mixture composition. Once the catalyst was used in CO-PROX cycles in absence of CO_2 and H_2O, the main crystallite phase is not cryptomelane, but hausmannite (Mn_3O_4). This indicates that the strongly reductive environment of the CO-PROX reaction at the maximum temperature is able to reduce the manganese in the cryptomelane ($K_xMn_8O_{16-x}$) structure up to some extent.

Previously, in Chapter 5 [1], it has been discussed the deactivation process and the possible strategies of regeneration of the CuO/Cryptomelane catalyst in CO-PROX reaction, concluding that partial recovery is achieved by reoxidation pre-treatments at 400ºC in between. In addition, the presence of CuO nanoparticles on the surface was critical for the catalyst performance, which improved its catalytic activity when comparing to raw cryptomelane, but the stability was dramatically affected during the reactions. Accordingly, the reducibility of CuO/Cryptomelane was largely increased with regards to bare Cryptomelane, so its catalytic activity, but also the susceptibility to deactivation by reduction under CO-PROX conditions. Thus, even undertaking the reoxidation treatments between cycles, it was not possible to restore completely the original catalytic activity, as a consequence of the partial collapse of cryptomelane structure by means of K segregation and the collateral sintering of CuO nanoparticles, occurring at the high temperature of such regeneration procedures.

In this particular study, however, the regeneration issues are not taken into account, and the catalyst was tested during four reaction cycles without any pre-treatment between them in all the series conducted. According to Figure 6.3, CuO/Cryptomelane catalyst is less damaged after used in reaction when CO_2 and H_2O are present in the gas mixture, as cryptomelane peaks are still observed in the diffractogram. Then, the better performance after several uses in these conditions is necessarily associated to the catalyst stability and, consequently, reutilisation, aspects that have been studied for the first time in Cryptomelane-based catalysts under real CO-PROX reaction.

The H_2-TPR characterization of the CuO/Cryptomelane catalyst, both fresh and used, evidence as well a higher stability during CO-PROX experiments performed with CO_2 + H_2O in the feed (results shown in Figure 6.4¡5), which is in agreement with the XRD characterization.

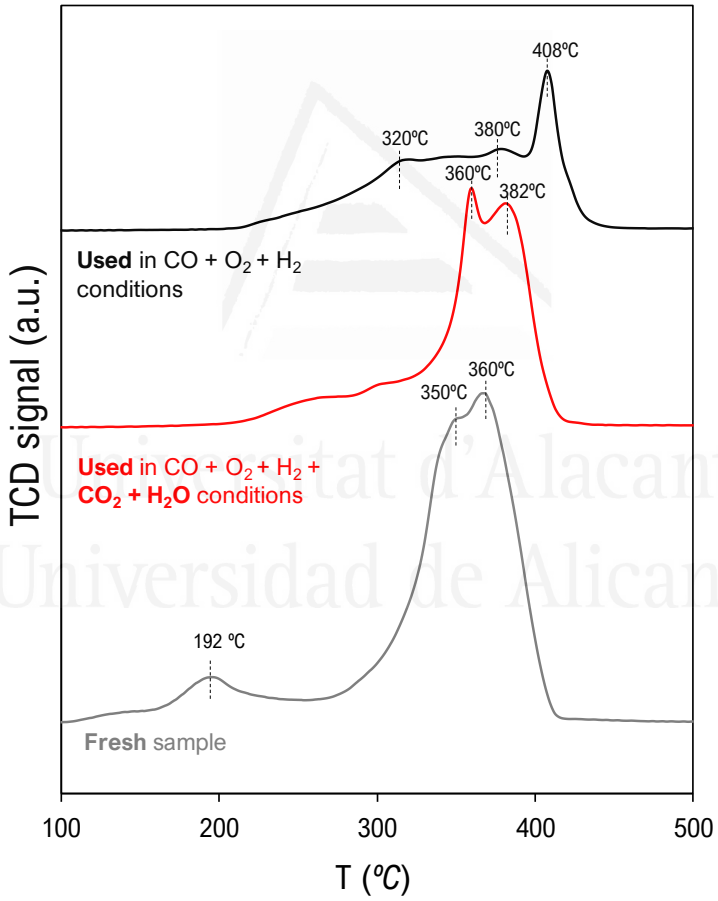

Figure 6.5. H_2-TPR results for the CuO/Cryptomelane samples. 40 mg of catalyst, 40 ml/min 5% H_2/Ar, 10ºC/min.

It is well known that cryptomelane presents a H_2 reduction profile which is based on multiple reduction steps until the final state of 2+ for manganese [12]. The presence of copper oxide modifies the reduction profile observable

by the shift towards lower temperatures, produced by means of a synergistic effect between Cu and Mn. As well, CuO is also more easily reduced when it is finely dispersed onto cryptomelane support, when comparing to bulk CuO [1]. Hence, in fresh CuO/Cryptomelane can be distinguished a reduction peak with maxima at 192ºC, which corresponds to the anticipated reduction of the CuO dispersed phase. This reduction peak is characteristic from the initial dispersion of CuO present in the catalyst at the beginning of the reaction. This CuO reduction peak is not discernible in the profiles for the used samples, which is shifted towards higher temperatures and overlapped under the reduction of bulk manganese, giving rise to the mixed reduction peaks centred between 265ºC and 320ºC in the used samples. This suggests that, under CO-PROX reaction conditions, the CuO phase is partially sintered, lowering the Cu-Mn interaction [13], or reduced to a degree.

Nevertheless, the most explicit differences between the reduction profiles are relative to the reduction process for manganese in cryptomelane. The H_2 reduction profile of the catalysts used in CO-PROX experiments performed with CO_2 and H_2O in the feed is qualitatively similar to the one for the fresh sample, but with lower area. The two main peaks observed in these profiles are assigned to the reduction of cryptomelane in two steps: (i) to Mn_2O_3/Mn_3O_4; (ii) to MnO. On the contrary, the H_2 reduction profile of the sample tested in CO-PROX experiments in absence of CO_2 and H_2O presents totally different shape. The sharp peak centred at 408ºC is an evidence of the loss of Cu-Mn interaction and of the formation of Mn_3O_4, which is reduced in one step to MnO.

As a conclusion, H_2-TPR characterization confirms the greater stability of CuO/Cryptomelane during CO-PROX reactions performed with $CO_2 + H_2O$ in the feed, which presents partial degradation but keeps cryptomelane integrity up to an extent, which is not shown by the sample tested in CO-PROX experiments under the CO_2- and H_2O-free stream.

Raman spectra compiled on Figure 6.6 are consistent with these conclusions, and also support the higher stability of the CuO/Cryptomelane catalyst during the CO-PROX experiments performed with CO_2 and H_2O in the feed. The interpretation of the entire Raman spectra for cryptomelane-based crystalline structure is not trivial, as well as for the wide range of existing manganese oxides [14,15].

Universitat d'Alacant
Universidad de Alicante

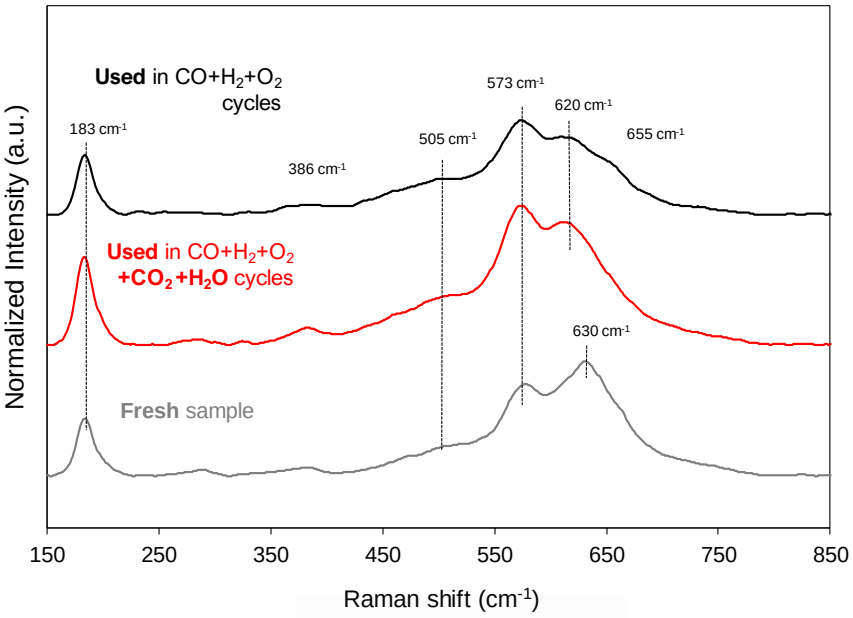

Figure 6.6. Raman spectra of the fresh and used samples for CuO/Cryptomelane catalyst.

Cryptomelane is based on a body-centered tetragonal structure with space group I4/m [16] and its Raman spectrum features four main contributions at 183, 386, 574 and 634 cm^{-1}, regarding the Mn-O vibrations within the MnO_6 octahedral double chains, along with some weak bands recorded at 287 and 505 cm^{-1} [17]. Particularly, the low frequency Raman band at 183 cm^{-1} has been assigned to an external vibration derived from the translational motion of the MnO_6 octahedra and the Raman band at 386 cm^{-1} has been attributed to the Mn-O bending vibrations. On the other hand, the bands at 574 and 634 cm^{-1} are due to symmetrical Mn-O vibrations, being assigned to vibrations in the along direction of the MnO_6 octahedral double chains, and in the perpendicular direction, respectively. Thus, the broadening, relative intensity and definition of the latter can be an indicative of the degree of development of the (2x2) tunnelled structure.

In the case of fresh CuO/Cryptomelane, the bands at 574 and 634 cm^{-1} are not well defined, evidencing a poor crystallinity, as well as the relative intensities show a short length of nanofibers but a good definition of 2x2 channel size [15]. Attending to the used samples, the Raman spectra presents some differences between these bands in terms of Raman shift and relative intensities, which is consistent with changes in the crystalline periodicity of cryptomelane phase, and the connection between the MnO_6 octahedra. In both cases, the band located at 634 cm^{-1} is shifted towards lower wavenumber, up to 615 cm^{-1}, which can be associated to a higher Mn^{3+}/Mn^{4+} ratio in the network formed by MnO_6 octahedra [18,19]. Additionally, there can be discerned a shoulder at 655 cm^{-1} in the CuO/Cryptomelane sample used in CO-PROX cycles in absence of CO_2 +

H_2O, that can be ascribed as the band characteristic for the symmetric stretching of Mn-O lattice for Mn_3O_4 [20].

Thus, Raman characterization suggests that used samples are based on a distorted cryptomelane structure formed by MnO_6 octahedra whose manganese has in average a more reduced oxidation state compared to the fresh sample. The reduction of manganese in the cryptomelane structure is possible by means of the formation of O^{2-} vacancies and/or by the insertion of a greater proportion of K species in the intratunnel space. However, such reduction cannot overcome certain boundaries due to the electrostatic repulsion of the hosted K species, which may provoke a segregation into Mn_3O_4 and a K-enriched cryptomelane phases [10]. Comparing both used samples, Raman characterization evidences a higher development of Mn_3O_4 phase in the sample used in absence of CO_2 and H_2O in the catalytic tests.

In conclusion, the better performance of CuO/Cryptomelane catalyst after several CO-PROX experiments performed in the presence of CO_2 and H_2O is related to its enhanced stability. In absence of CO_2 and H_2O in the CO-PROX reaction feed, the catalyst is reduced leading to the formation of the phase Mn_3O_4, which decreases the catalytic activity up to a steady level. On the contrary, when CO_2 and H_2O are present in the CO-PROX feed, their chemisorption maintains the tunnelled structure of cryptomelane.

6.4 Conclusions

The catalytic activity of CuO/Cryptomelane for the preferential oxidation of CO in H_2-rich streams has been studied in the absence and presence of H_2O and CO_2, and the following conclusions can be summarised:

(1) For fresh CuO/cryptomelane catalyst, the presence of CO_2 and/or H_2O in the CO-PROX feed partially inhibits CO oxidation due to chemisorption of H_2O and CO_2 on the catalyst. H_2O chemisorption on CuO/Cryptomelane is stronger than CO_2 chemisorption and simultaneous CO_2 and H_2O feed has a synergetic effect that enhances co-adsorption.

(2) On the contrary, the presence of CO_2 + H_2O in the CO-PROX reaction mixture has a positive effect in the CuO/Cryptomelane stability upon several consecutive reaction cycles in the 25-200ºC range.

(3) XRD showed that CO_2 + H_2O co-chemisorption partially prevents catalyst deactivation due to cryptomelane reduction to hausmannite (Mn_3O_4) under the strongly reductive environment of the CO-PROX reaction.

(4) Additionally, H_2-TPR and Raman spectroscopy characterization support that the cryptomelane structure is less damaged under CO-PROX conditions in the presence of CO_2 and H_2O than in the absence of these species.

Therefore, this greater stability of CuO/Cryptomelane in realistic conditions (CO_2 and H_2O presence) is eventually minimising the catalyst deactivation in CO-PROX reaction cycles and leads to the best catalytic performance after 4 cycles of reaction, which is a very interesting peculiarity of this material for the studied application.

References

[1] A. Davó-Quiñonero, M. Navlani-García, D. Lozano-Castelló, A. Bueno-López, CuO/cryptomelane catalyst for preferential oxidation of CO in the presence of H_2: Deactivation and regeneration, Catal. Sci. Technol. 6 (2016) 5684-5692.

[2] D. Gamarra, A. Martínez-Arias, Preferential oxidation of CO in rich H_2 over CuO/CeO_2: Operando-DRIFTS analysis of deactivating effect of CO_2 and H_2O, J. Catal. 263 (2009) 189–195.

[3] W.Y. Hernández, M. A. Centeno, S. Ivanova, P. Eloy, E.M. Gaigneaux, J. A. Odriozola, Cu-modified cryptomelane oxide as active catalyst for CO oxidation reactions, Appl. Catal. B Environ. 123–124 (2012) 27–35.

[4] G.K. Reddy, P.G. Smirniotis, Water Gas Shift Reaction: Research Developments and Applications, Elsevier, Amsterdam, 2015.

[5] Y.F. Shen, R.P. Zerger, R.N. DeGuzman, S.L. Suib, L. McCurdy, D.I. Potter, C.L. O'Young, Manganese oxide octahedral molecular sieves: Preparation, characterization, and applications, Science. 260 (1993) 511-515.

[6] G.G. Xia, Y.G. Yin, W.S. Willis, J.Y. Wang, S.L. Suib, Efficient stable catalysts for low temperature carbon monoxide oxidation, J. Catal. 185 (1999) 91–105.

[7] A. Martínez-Arias, D. Gamarra, A. Hungría, M. Fernández-García, G. Munuera, A. Hornés, P. Bera, J. Conesa, A. Cámara, Characterization of Active Sites/Entities and Redox/Catalytic Correlations in Copper-Ceria-Based Catalysts for Preferential Oxidation of CO in H_2-Rich Streams, Catalysts 3 (2013) 378–400.

[8] F. Mariño, C. Descorme, D. Duprez, Supported base metal catalysts for the preferential oxidation of carbon monoxide in the presence of excess hydrogen (PROX), Appl. Catal. B Environ. 58 (2005) 175–183.

[9] A. Davó-Quiñonero, M. Navlani-García, D. Lozano-Castelló, A. Bueno-López, J.A. Anderson, Role of Hydroxyl Groups in the Preferential Oxidation of CO over Copper Oxide-Cerium Oxide Catalysts, ACS Catal. 6 (2016) 1723–1731.

[10] T. Gao, P. Norby, Frame stability of tunnel-structured cryptomelane nanofibers: The role of tunnel cations, Eur. J. Inorg. Chem. 28 (2013) 4948-4957.

[11] N. Kijima, H. Yasuda, T. Sato, Y. Yoshimura, Preparation and characterization of open tunnel oxide α-MnO_2 precipitated by ozone oxidation, J. Solid State Chem. 159 (2001) 94-102.

[12] W. Gac, The influence of silver on the structural, redox and catalytic properties of the cryptomelane-type manganese oxides in the low-temperature CO oxidation reaction, Appl. Catal. B Environ. 75 (2007) 107–117.

Universidad de Alicante

[13] K. Qian, Z. Qian, Q. Hua, Z. Jiang, W. Huang, Structure-activity relationship of CuO/MnO_2 catalysts in CO oxidation, Appl. Surf. Sci. 273 (2013) 357–363.

[14] C. Julien, M. Massot, R. Baddour-Hadjean, S. Franger, S. Bach, J.P. Pereira-Ramos, Raman spectra of birnessite manganese dioxides, Solid State Ionics. 159 (2003) 345-356.

[15] T. Gao, H. Fjellvåg, P. Norby, A comparison study on Raman scattering properties of α- and β-MnO_2, Anal. Chim. Acta. 648 (2009) 235–239.

[16] J. Vicat, E. Fanchon, P. Strobel, D. Tran Qui, The structure of $K_{1.33}Mn_8O_{16}$ and cation ordering in hollandite-type structures, Acta Crystallogr. Sect. B. 42 (1986) 162-167.

[17] T. Gao, M. Glerup, F. Krumeich, R. Nesper, H. Fjellvâg, P. Norby, Microstructures and spectroscopic properties of cryptomelane-type manganese dioxide nanofibers, J. Phys. Chem. C. 112 (2008) 13134-13140.

[18] M.-C. Bernard, A.H.-L. Goff, Electrochemical science and technology: Electrochromic Reactions in Manganese Oxides: I. Raman Analysis, J. Electrochem. Soc. 140 (1993) 3065-3070.

[19] F. Buciuman, F. Patcas, R. Craciun, D.R.T. Zahn, Vibrational spectroscopy of bulk and supported manganese oxides, Phys. Chem. Chem. Phys. 1 (1999) 185-190.

[20] F. Kapteijn, L. Singoredjo, A. Andreini, J.A. Moulijn, Activity and selectivity of pure manganese oxides in the selective catalytic reduction of nitric oxide with ammonia, Appl. Catal. B Environ. 3 (1994) 173–189.

[21] M.J. Kahlich, H.A Gasteiger, R.J. Behm, Kinetics of the Selective CO Oxidation in H_2-Rich Gas on Pt/Al_2O_3, J. Catal. 171 (1997) 93–105.

[22] X. Ouyang, R. Besser, Effect of reactor heat transfer limitations on CO preferential oxidation, J. Power Sources. 141 (2005) 39–46.

[23] D. Gamarra, A.L. Cámara, M. Monte, S.B. Rasmussen, L.E. Chinchilla, A.B. Hungría, G. Munuera, N. Gyorffy, Z. Schay, V.C. Corberán, J.C. Conesa, A. Martínez-Arias, Preferential oxidation of CO in excess H_2 over CuO/CeO_2 catalysts: Characterization and performance as a function of the exposed face present in the CeO_2 support, Appl. Catal. B Environ. 130–131 (2013) 224–238.

[24] X.S. Liu, Z.N. Jin, J.Q. Lu, X.X. Wang, M.F. Luo, Highly active CuO/OMS-2 catalysts for low-temperature CO oxidation, Chem. Eng. J. 162 (2010) 151–157.

[25] Y.I. Hasegawa, R.U. Maki, M. Sano, T. Miyake, Preferential oxidation of CO on copper-containing manganese oxides, Appl. Catal. A Gen. 371 (2009) 67–72.

[26] J. Giménez-Mañogil, A. Bueno-López, A. García-García, Preparation, characterisation and testing of CuO/$Ce_{0.8}Zr_{0.2}O_2$ catalysts for NO oxidation to NO_2 and mild temperature diesel soot combustion, Appl. Catal. B Environ. 152–153 (2014) 99–107.

[27] S. Vepek, Mechanism of the deactivation of Hopcalite catalysts studied by XPS, ISS, and other techniques, J. Catal. 100 (1986) 250–263.

[28] M. Krämer, T. Schmidt, K. Stöwe, W.F. Maier, Structural and catalytic aspects of sol–gel derived copper manganese oxides as low-temperature CO oxidation catalyst, Appl. Catal. A Gen. 302 (2006) 257–263.

[29] H. Chen, X. Tong, Y. Li, Mesoporous Cu–Mn Hopcalite catalyst and its performance in low temperature ethylene combustion in a carbon dioxide stream, Appl. Catal. A Gen. 370 (2009) 59–65.

Universidad de Alicante

[30] C.D. Wagner, W.M. Riggs, L.E.R. Davis, J.F. Moulder, G.E. Mullenberg, Handbook of X-Ray Photoelectron Spectroscopy, Perkin-Elmer Corp., Physical Electronics Division, Eden Prairie, Minnesota, USA, 1981.

[31] A. Martínez-Arias, M. Fernández-García, J. Soria, J.C. Conesa, Spectroscopic study of a Cu/CeO_2 catalyst subjected to redox treatments in carbon monoxide and oxygen, J. Catal. 182 (1999) 367–377.

[32] G. Moretti, Auger parameter and Wagner plot in the characterization of chemical states by X-ray photoelectron spectroscopy: A review, J. Electron Spectros. Relat. Phenomena. 95 (1998) 95–144.

[33] J.P. Espinós, J. Morales, A. Barranco, A. Caballero, J.P. Holgado, A.R. González-Elipe, Interface Effects for Cu, CuO, and Cu_2O Deposited on SiO_2 and ZrO_2. XPS Determination of the Valence State of Copper in Cu/SiO_2 and Cu/ZrO_2 Catalysts, J. Phys. Chem. B. 106 (2002) 6921–6929.

[34] R. Hu, C. Yan, L. Xie, Y. Cheng, D. Wang, Selective oxidation of CO in rich hydrogen stream over Ag/OMS-2 catalyst, Int. J. Hydrogen Energy. 36 (2011) 64–71.

[35] W.Y. Hernández, M. a. Centeno, F. Romero-Sarria, S. Ivanova, M. Montes, J.A. Odriozola, Modified cryptomelane-type manganese dioxide nanomaterials for preferential oxidation of CO in the presence of hydrogen, Catal. Today. 157 (2010) 160–165.

[36] K. Ramesh, L. Chen, F. Chen, Y. Liu, Z. Wang, Y.F. Han, Re-investigating the CO oxidation mechanism over unsupported MnO, Mn_2O_3 and MnO_2 catalysts, Catal. Today. 131 (2008) 477–482.

[37] M. Piumetti, D. Fino, N. Russo, Mesoporous manganese oxides prepared by solution combustion synthesis as catalysts for the total oxidation of VOCs, Appl. Catal. B Environ. 163 (2015) 277–287.

[38] W.Y. Hernández, M. a. Centeno, S. Ivanova, P. Eloy, E.M. Gaigneaux, J. a. Odriozola, Cu-modified cryptomelane oxide as active catalyst for CO oxidation reactions, Appl. Catal. B Environ. 123–124 (2012) 27–35.

[39] Y. Yang, J. Huang, S. Zhang, S. Wang, S. Deng, B. Wang, G. Yu, Catalytic removal of gaseous HCBz on Cu doped OMS: Effect of Cu location on catalytic performance, Appl. Catal. B Environ. 150–151 (2014) 167–178.

[40] V.P. Santos, M.F.R. Pereira, J.J.M. Órfão, J.L. Figueiredo, The role of lattice oxygen on the activity of manganese oxides towards the oxidation of volatile organic compounds, Appl. Catal. B Environ. 99 (2010) 353–363.

[41] L.M. Martínez T., F. Romero-Sarria, W.Y. Hernández, M. a. Centeno, J. a. Odriozola, Gold supported cryptomelane-type manganese dioxide OMS-2 nanomaterials deposited on AISI 304 stainless steels monoliths for CO oxidation, Appl. Catal. A Gen. 423–424 (2012) 137–145.

[42] E.C. Njagi, H.C. Genuino, C.K. King'Ondu, C.H. Chen, D. Horvath, S.L. Suib, Preferential oxidation of CO in H2-rich feeds over mesoporous copper manganese oxides synthesized by a redox method, Int. J. Hydrogen Energy. 36 (2011) 6768–6779.

[43] M. Özacar, A.S. Poyraz, H.C. Genuino, C.-H. Kuo, Y. Meng, S.L. Suib, Influence of silver on the catalytic properties of the cryptomelane and Ag-hollandite types manganese oxides OMS-2 in the low-temperature CO oxidation, Appl. Catal. A Gen. 462–463 (2013) 64–74.

[44] C.H. Chen, S.L. Suib, Control of catalytic activity via porosity, chemical composition, and morphology of nanostructured porous manganese oxide materials, J. Chinese Chem. Soc. 59 (2012) 465–472.

[45] K. Liu, A. Wang, T. Zhang, Recent Advances in Preferential Oxidation of CO Reaction over Platinum Group Metal Catalysts, ACS Catal. 2 (2012) 1165–1178.

[46] F.C. Buciuman, F. Patcas, T. Hahn, A spillover approach to oxidation catalysis over copper and manganese mixed oxides, Chem. Eng. Process. Process Intensif. 38 (1999) 563–569.

[47] J. Ashok, P.S. Reddy, G. Raju, M. Subrahmanyam, A. Venugopal, Catalytic Decomposition of Methane to Hydrogen and Carbon Nanofibers over Ni−Cu−SiO_2 Catalysts, Energy & Fuels. 23 (2009) 5–13.

[48] E.C. Njagi, C.-H. Chen, H. Genuino, H. Galindo, H. Huang, S.L. Suib, Total oxidation of CO at ambient temperature using copper manganese oxide catalysts prepared by a redox method, Appl. Catal. B Environ. 99 (2010) 103–110.

[49] A.A. Mirzaei, H.R. Shaterian, M. Kaykhaii, The X-ray photoelectron spectroscopy of surface composition of aged mixed copper manganese oxide catalysts, Appl. Surf. Sci. 239 (2005) 246–254.

[50] M. Monte, D. Gamarra, A. López Cámara, S.B. Rasmussen, N. Gyorffy, Z. Schay, A. Martínez-Arias, J.C. Conesa, Preferential oxidation of CO in excess H_2 over CuO/CeO_2 catalysts: Performance as a function of the copper coverage and exposed face present in the CeO_2 support, Catal. Today. 229 (2014) 104–113.

[51] M. Lowell, S., Shields, J.E., Thomas, M.A., Thommes, Characterization of Porous Solids and Powders: Surface Area, Pore Size and Density, Springer, Heidelberg, 2004.

[52] I. Atribak, A. Bueno-López, A. García-García, P. Navarro, D. Frías, M. Montes, Catalytic activity for soot combustion of birnessite and cryptomelane, Appl. Catal. B Environ. 93 (2010) 267–273.

[53] C. Almquist, M. Krekeler, L. Jiang, An investigation on the structure and catalytic activity of cryptomelane-type manganese oxide materials prepared by different synthesis routes, Chem. Eng. J. 252 (2014) 249–2.

Universitat d'Alacant
Universidad de Alicante

Universitat d'Alacant
Universidad de Alicante

CHAPTER 7

Into the Preferential Oxidation of CO reaction mechanism over CuO/Cryptomelane catalyst

CuO/Cryptomelane catalyst was subjected to a mechanistic study over CO-PROX reaction by means of indirect techniques by the preparation, advanced characterization and testing of catalysts with different Cu nominal contents. Their CO-PROX catalytic activity has been tested in CO-PROX reaction and evaluated according to Cu dispersion and synergistic interaction between copper and manganese-rich phases. This work entails the use of conventional characterization techniques such as XRD, Raman, XPS and Auger spectroscopies, as well as complementary basic DFT simulation. Additionally, it is reported for the first time, *in-situ* Work Function measurements over CO and O_2 interaction in CuO/Cryptomelane catalysts. Results reveal a strong influence in the electronic properties of CuO/Cryptomelane depending on CuO-cryptomelane interaction at the interface contact points, which stabilize Cu^{+} states upon Cu^{+2}/Cu^{+} and Mn^{3+}/Mn^{4+} redox interplay. The optimal performance is achieved by the efficient participation of two active species: (1) interfacial Cu^{+}–Mn pairs, as the active sites for CO oxidation; and (2) CuO bulky particles for the efficient O_2 refilling. Thus, these results bring the conclusion the that clear analogies exist within the ongoing CO-PROX mechanism involving copper species in CuO/Cryptomelane and the well-reported CuO/CeO_2 catalysts.

Universitat d'Alacant
Universidad de Alicante

7.1 Introduction

Along Chapters 5 and 6, a CuO/Cryptomelane catalyst was evaluated in CO-PROX reaction, and despite the moderate stability of the material in a continuous operation in reaction conditions, the activity of the CuO/Cryptomelane catalyst resulted very promising. Besides, provided its H_2O and CO_2 compatibility, which turns into a major stability and activity maintenance in real CO-PROX operation conditions, CuO/Cryptomelane catalysts are truly interesting for practical reasons and a further study over particular mechanistic aspects is a must.

Hence, although CuO/Cryptomelane had already previously demonstrated an outstanding catalytic activity in CO-PROX reaction, mechanistic studies provided so far are truly limited when compared to CuO/CeO_2 catalysts [1–4]. Apart from the more extended use and the well-known excellent performance of CuO/CeO_2 materials in catalytic applications, which turn into a very large list of related reported literature, CuO/CeO_2 systems are more facile to analyse by means of conventional characterization techniques and the good track record provided brings a deep understanding of the ongoing mechanism [5,6]. In particular, *operando* CO-PROX DRIFT spectroscopy allowed to identify Cu^+ species as CO oxidation active sites, besides the enrolment of carbonaceous intermediate species, the role of OH surface groups, and the relevant Cu – Ce interfacial properties that determine Cu^+ carbonyl formation and stabilization [7].

In addition, along this Project Thesis the state-of-the-art into CuO/CeO_2 studies over CO-PROX reaction has been expanded by the novel operando NAP-XPS experiments complemented with in-situ Raman spectroscopy and Density Functional Theory calculations upon CeO_2 surfaces. It is complicated, tough, to stablish analogue analyses into CuO/Cryptomelane provided its great crystallographic complexity and mixed nature with potassium species and intra-channel bounded water on the MnO_2 network [8]. On the one hand, Mn XPS analyses are not trivial, given the many multiplet-split components of Mn2p peaks, which hinder substantially the interpretation of such region in the average spectra of Mn mixed species present in cryptomelane [9]. On the other hand, such complex crystallographic assembly in MnO_6 octahedra 2 x 2 channel arrays results in an entangled characteristic Raman spectra [10], from which it is difficult to retain critical information. And last, but not least, probably because of the characteristic black-colored nature of CuO/Cryptomelane catalyst, infrared spectroscopic *operando* CO-PROX analyses present flat spectra that do not allow to get mechanistic insights from this powerful technique [11].

In this scenario, some authors have reported a Mars van Krevelen (MVK) mechanism occurring when cryptomelane-based catalysts are used for oxidation reactions, such as in Volatile Organic Compounds (VOC) oxidation [12–14], or CO oxidation [11,15,16], based on indirect evidences such as O1s XPS region measurements or H_2-TPR experiments. However,

to the best of my knowledge, the establishment of a proper CO-PROX reaction mechanism for the promising CuO/Cryptomelane formulation with *in-situ* techniques is still pending.

Therefore, the study presented along this Chapter deals with a proposed alternative methodology to study CO-PROX mechanism over CuO/Cryptomelane catalysts based on the multidisciplinary use of potential advanced complementary techniques. Namely, *in-situ* Work Function (WF) measurements were conducted [17], which offer a powerful tool and a novel approach for this mechanistic purpose. Additionally, the effect of Cu loading and CuO particle size has been critically included in the present Chapter.

7.2 Experimental details

7.2.1 Catalysts preparation

The synthesis of CuO/Cryptomelane was conducted according to procedure detailed in Section 2.1.1 from Chapter 2. In this particular Chapter, a battery of CuO/Cryptomelane catalysts with different Cu loadings were prepared.

7.2.2 CO-PROX activity tests

The prepared CuO/Cryptomelane series was tested in CO-PROX catalytic tests according to the experimental settings and specific conditions as stated in Section 2.2.3. Briefly, 100 ml/min of the CO-PROX gas mixture consisting in 2% CO, 2% O_2, 30% H_2 in He balance ($\lambda = 2$) was fed to the reactor with 150 mg of sample, and the experiment was conducted following heating rate of 2ºC/min from 25 to 250ºC.

Universidad de Alicante

7.2.3 Catalysts characterization

CuO/Cryptomelane catalysts were characterized by means of N_2 physisorption at -196ºC, X-Ray Diffraction (XRD), Temperature Programmed Reduction with H_2 (H_2-TPR), and X-ray photoelectron spectroscopy (XPS) analysis. Specific conditions of such measurements were detailed in Section 2.2.2 from Chapter 2. Accordingly, surface area was calculated by using the BET equation (S_{BET}), micropore volume (<2 nm) with the Dubinin-Radushkevich equation (DR), while Cryptomelane (α-MnO_2) crystallite size determined by means of the Scherrer equation considering the (211) peak.

Since cryptomelane is known to emit potassium at elevated temperatures [20,21], potassium thermal desorption was investigated by measuring the potassium atom flux from pelletized samples (100 mg, 13 mm diameter) heated in a vacuum chamber. Due to the low ionization potential of potassium (I = 4.3 eV) from solid surfaces potassium is typically thermally

emitted in the form of atoms and ions. The samples were biased with a positive potential of +5 V to prevent the thermal emission of electrons during a heating program up to ~500 °C. For each temperature the resultant positive current was averaged over 10 independent data points and measure with the use of Keithley 6512 digital electrometer.

7.2.4 *In-situ* Work Function measurements

Work function measurements were carried out under room conditions of atmosphere and temperature with the calcined and pelletized samples (6 MPa, 10 mm diameter). The contact potential difference (CPD) measurements were carried out by the dynamic condenser method of Kelvin with a KP6500 probe (McAllister Technical Services), and the reference electrode was a standard stainless-steel plate with a diameter of 3 mm (Φ_{ref} = 4.3 eV) provided by the manufacturer. During the measurements, the gradient of the peak-to-peak versus backing potential was set to 0.2 V, whereas the vibration frequency and amplitude was set to 120 Hz and 40 a.u. The final CPD value was an average of 60 independent points using two backing potentials. The work function values were obtained from a simple relation CPD = Φ_{ref} –Φ_{sample}. *In-situ* WF measurements over CuO/cryptomelane catalysts were conducted at 200 and 300ºC after a thermal treatment up to 450 ºC in vacuum conditions. The atmosphere was switched among vacuum (below 10^{-6} atm), O_2 (Air Products, 99.9998%) and 5% CO/He at two different chamber pressures: $3.5 \cdot 10^{-5}$ and $8.0 \cdot 10^{-5}$ atm.

7.2.5 Density Functional Theory (DFT) Calculations

DFT calculations were conducted by means of the CP2K package in its 4.1 version using the QUICKSTEP module [49]. Dispersion corrected (D3)[50] GGA-PBE[51] exchange correlation functional under periodic boundary conditions (PBS) were used for all simulations. CO and H_2 molecules were positioned close the surface of Cu(111), Cu_2O(111) and CuO(111) slabs of 320 atoms, 180 atoms and 160 atoms respectively and the systems were allowed to relax. Adsorption energies were calculated by using the equations:

$$E_{CO,ads} = E_{slab + CO,ads} - (E_{slab} + E_{CO(g)})$$

$$E_{H2,ads} = E_{slab + H2,ads} - (E_{slab} + E_{H2(g)})$$

Additional information on the computational approach can be found in Section 2.3 from Chapter 2.

7.3 Results and discussion

7.3.1 Catalyst characterization

Textural, crystallographic and chemical characterization results for Cryptomelane and CuO/Cryptomelane catalysts are presented in Table 7.1, as a screening of Cu loading effect towards the physicochemical features and catalytic activity. The nominal Cu content was determined by means of XRF, and this result provided the denomination for each CuO/Cryptomelane catalyst, namely: 4% CuO/Cryptomelane, 7% CuO/Cryptomelane and 11% of CuO/Cryptomelane loading, which, for the sake of simplicity, are named henceforward in the present Chapter as 4% Cu/CR, 7% Cu/CR and 11% of Cu/CR, respectively.

Table 7.1. Compiled results of characterization by N_2 adsorption, XRF (bulk) and XPS (surface) quantification.

Catalyst	S_{BET} (m^2/g)	V_{DR} (cm^3/g)	[a]wt.% Cu	[a]Cu/Mn	[b]% C	[b]Cu/M
CR	72	0.041	-	0.000	42	0.000
4% Cu/CR	63	0.034	3.7	0.036	29	0.403
7% Cu/CR	56	0.034	7.2	0.073	30	0.677
11% Cu/CR	55	0.033	11.2	0.118	31	0.830

[a]From XRF characterization; [b]From XPS analysis.

On the other hand, the calculated BET surface of the catalysts decreases by increasing Cu content, whereas the micropore volume (V_{DR}) is lowered in a constant degree for all Cu/CR catalysts. Since N_2 physisorption technique is limited at providing information in the ultra micro-pore range (< 0.7 nm), as in the case of cryptomelane tunnel size (0.65 nm diameter), the micropore volume determined does not consider intra-channel space [22]. Thus, textural results reveal that Cu lowers cryptomelane specific surface by porosity blocking upon CuO deposition, although partial tunnel insertion or framework substitution cannot be ruled out.

The chemical quantification by XRF analysis reveals real Cu content in the Cu/CR catalysts, whereas XPS shows surface composition. Considering the equivalent atomic Cu/Mn bulk ratios, this parameter shows a proportional linear trend upon Cu loading. On the contrary, analogue atom ratios provided by XPS analysis showed surface Cu enrichment in all cases. Furthermore, among the Cu/CR catalysts, Cu surface content is not monotonically coupled to Cu nominal values. This deviation suggests the formation of larger CuO particles by copper sintering as Cu loading increases. This effect is identified by XPS as a lowering in the Cu content. On the other hand, surface % C decreases in Cu/CR samples with respect to CR, which is a reported side-

effect of the impregnation with acid copper precursor solution based on structural and surface carbonate dissolution [23].

XRD characterization (Figure 7.1) showed a pattern for all the catalysts consisting of the characteristic diffraction peaks of cryptomelane (JCPDS no. 29-1020). The presence of CuO tenorite phase (JCPDS no. 80-1268) is only detected in 11% Cu/CR catalyst, which is indicating that in lower contents, CuO may be highly dispersed, and its crystallite size is below the threshold detection limit of the XRD apparatus. On the other hand, important crystallite size changes upon Cu loading on bare cryptomelane phase were discarded by means of calculations using the Scherrer equation and lattice parameters considering tetragonal phase (Table 2.2) [24,25].

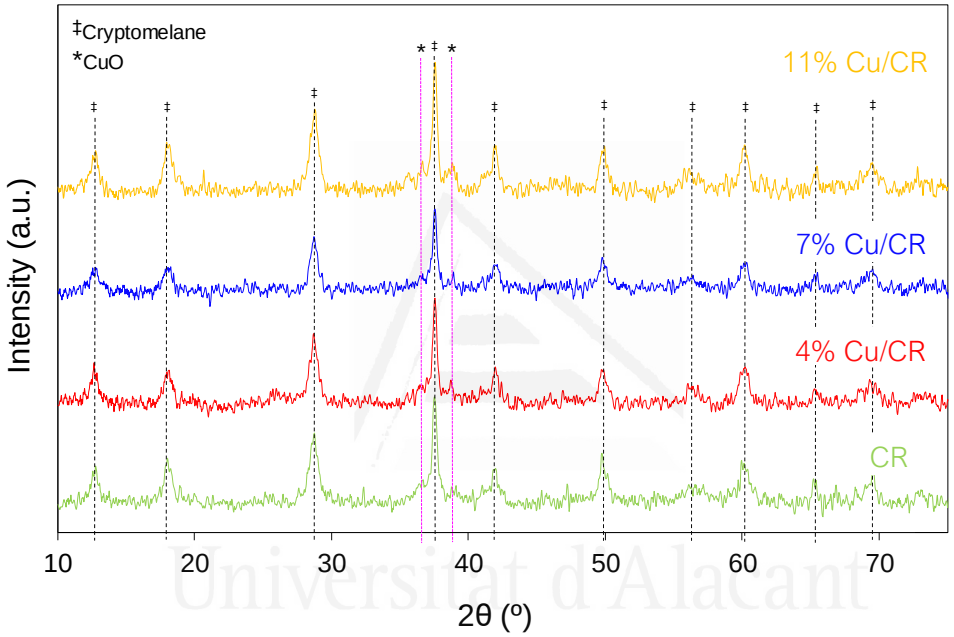

Figure 7.1. X-Ray diffractograms for CR and Cu/CR catalysts with peak markers for characteristic diffraction patterns of cryptomelane (‡) and CuO (*) structures.

Table 2.2. Crystallite size and cryptomelane lattice dimensions by XRD using (211) and (310) diffraction peaks.

Catalyst	$D_{Scherrer}$ (nm)	Lattice constant "a" (nm)	Lattice constant "c" (nm)	Cell volume (A^3)
CR	22	0.9811	0.2403	231
4% Cu/CR	23	0.9828	0.2400	232
7% Cu/CR	27	0.9811	0.2397	231
11% Cu/CR	24	0.9795	0.2397	230

In conclusion, Cu loading is not altering the basic MnO_x framework structure of cryptomelane, in agreement with the expected low degree of Cu lattice insertion by following an impregnation procedure. The decrease in

BET surface should be attributed to the formation of CuO particles deposited mainly on the external surface of cryptomelane that partially block the porosity. The higher the Cu content, the larger the CuO particle size, which is detected as a crystalline phase in 11% Cu/CR. Thus, according to these results, it may be inferred that 4% Cu/CR presents the higher Cu dispersion, 7% Cu/CR should be composed of medium-sized particles with good dispersion, too, and finally in 11% Cu/CR CuO presents the largest particle size with lower dispersion.

7.3.2 CO-PROX catalytic activity tests

Bare cryptomelane (CR), bulk CuO and the prepared CuO/Cryptomelane (Cu/CR) catalysts were tested in CO-PROX reaction activity experiments and results are presented in Figure 7.2.

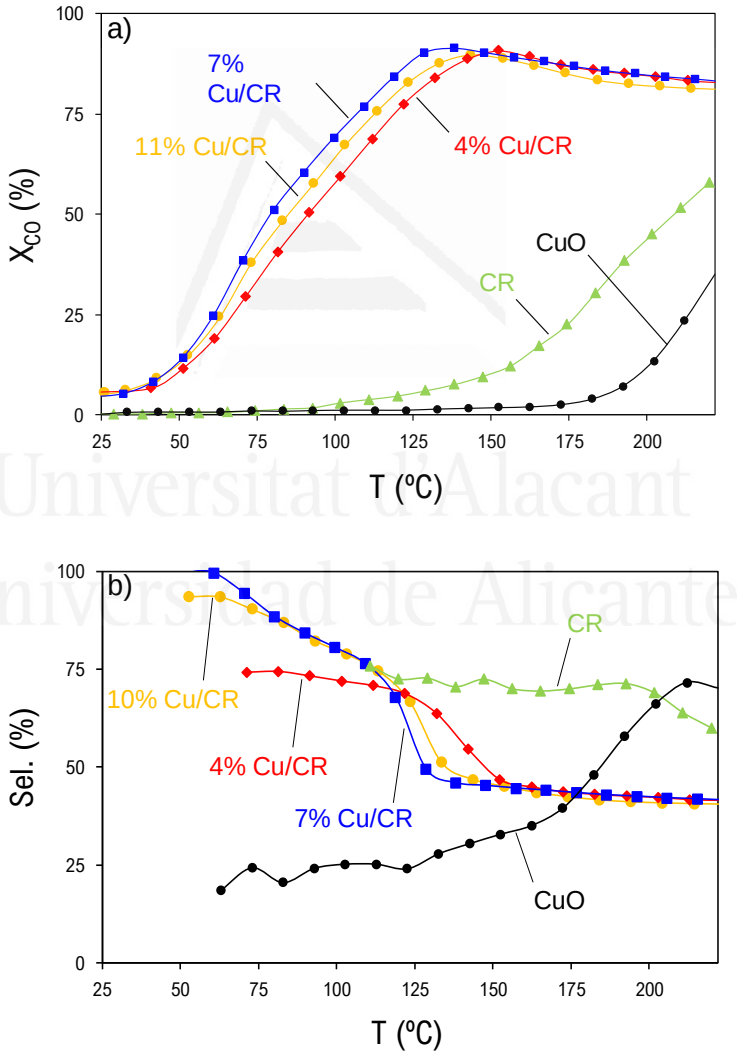

Figure 7.2. (a) CO conversion; and **(b)** CO selectivity profiles in CO-PROX activity tests conducted with the prepared catalysts. 150 mg, 2 ºC/min,100 ml/min 2% CO, 2% O_2, 30% H_2 balance He.

The beneficial effect of Cu loading into cryptomelane in the Cu/CR catalysts performance with regards to bare CR and CuO samples is clear and evidenced by a dramatic lowering in the temperature range over CO conversion profiles, roughly shifted *ca.* 100ºC lower for Cu/CR catalysts. Such enhancement, reported elsewhere, is attributed to the synergistic effect between MnO_x from cryptomelane (CR) and CuO phases, which brings about a large increase of lattice oxygen mobility, as a result of the formation of Cu-O-Mn bridges which partially delocalize electron density in Mn-O bonds [26–28]. Furthermore, the labile redox interplay Cu^{2+}/Cu^{+} on the reducible MnO_x surface promotes the creation of defects such as oxygen vacancies in the cryptomelane framework via Mn^{2+} substitution in the interface points. Hence, the presence of such defects increases the lattice oxygen activation and reactivity [12,29] which may accelerate CO oxidation rate occurring by means of Mars-van Krevelen (MVK) mechanism with the participation of surface oxygen [30].

According to MVK mechanism, lattice oxygen is directly involved in the oxidation process of chemisorbed CO species, and, as a result, oxygen vacancies are created upon the reaction course. Those oxygen vacancy defects are replenished by O_2 gas dissociation and incorporation in balanced equilibria, keeping stable the average oxidation state of the catalyst. In the case of Cryptomelane catalyst, CO oxidation should take place upon the labile redox Mn^{3+}/Mn^{4+} interplay, whereas in CuO/Cryptomelane catalysts, CuO can additionally undergo analogue redox processes involving partial reduction to state Cu(I). Attending to this, since CuO presents large stability on its oxidized state, which facilitates lattice oxygen recovery, besides an enhanced CO chemisorption capacity, it could be inferred that processes attained to CuO participation is more favourable for the achievement of higher CO oxidation rates. However, provided the catalytic testing of pure CuO presents negligible CO oxidation activity in the temperature threshold of interest, catalytic activity of CuO phase is only relevant when dispersed on a MnO_x surface in CuO/Cryptomelane samples. As a result, a synergistic effect between CuO – Cryptomelane contact points at the interface should be activating the oxygen lattice evolution in both phases, as stated before. Thus, the changes of catalyst features such as CuO dispersion, particle size and distribution in the cryptomelane support are expected to have large effects on the catalytic activity.

Conversely, the differences are moderate among the series of CuO/Cryptomelane catalysts, which reach the maximum CO conversion (~90 %) in a narrow temperature range, following the trend 7% Cu/CR > 11% Cu/CR > 4% Cu/CR. Nevertheless, in terms of CO selectivity, 7% Cu/CR and 11% Cu/CR catalysts present the best behavior with region of complete CO selectivity at low temperatures and the typical selectivity decay up to (~40 %), by the competitive H_2 oxidation on-set. Such selectivity value is acceptable to guarantee a good CO-PROX catalytic performance, provided the experimental conditions of $\lambda=2$ for O_2 [31]. Therefore, 7% Cu is assessed

as the optimum loading in Cu/CR catalysts, but in close similarity to the 4 and 11%. As a result, 7% Cu/CR catalyst, with an inferred intermediate CuO particle size, presents the preferential chemical features. In order to get further insights regarding those optimum properties in terms of CuO – CR interactions and redox properties of CuO/Cryptomelane catalysts, H_2-TPR and XPS analysis were conducted.

7.3.3 CuO – Cryptomelane redox interaction study

Figure 7.3 displays the H_2-temperature programmed reduction profiles of the tested catalysts, showing that their different susceptibility for H_2 reduction is affected by the interaction of C and CuO phases.

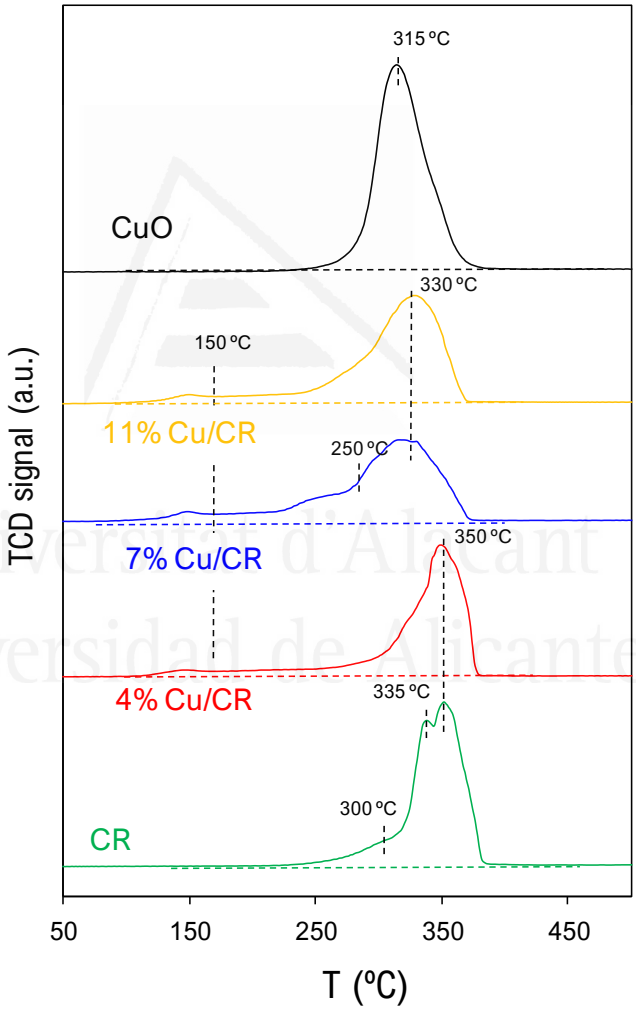

Figure 7.3. H_2-Temperature Programmed Reduction profiles of Cryptomelane, CuO/Cryptomelane and CuO catalysts.

In the case of cryptomelane phase, manganese species achieve the final oxidation state of +2 under the reduction treatment [32–34]. For pure

cryptomelane, CR profile presents three main reduction events assigned to the redox processes: (i) $MnO_2 \rightarrow Mn_2O_3$; (ii) $Mn_2O_3 \rightarrow Mn_3O_4$; and (iii) $Mn_3O_4 \rightarrow MnO$, seen in broad peaks centred at 300, 335 and 350ºC, respectively [28,29]. The introduction of 4% Cu produces little changes in the average reduction of cryptomelane framework, presenting an overlapping of the manganese reduction processes occurring in the same temperature range as in bare CR. Nevertheless, an extra peak at 150ºC assigned to finely dispersed CuO species is detected in the reduction profile. Since reduction of pure bulk CuO occurs above 300ºC according to the H_2-TPR profile of CuO sample, also shown in Figure 7.3, this anticipated CuO reduction evidences a Cu – Mn synergistic effect by means of the formation of labile Cu^{2+} - O- Mn^{y+} entities [35–37]. As a consequence, the anticipated partial MnO_2 reduction is gradually taking place as well, evidenced by the permanent sloping signal above 150ºC after small size CuO particles reduction. In contrast, the effect of Cu is much more evident in the 7 and 11% Cu/CR catalysts by shifting the maxima towards lower temperatures of the overall cryptomelane reduction processes (from 350 to 330ºC). This shifting proves the superior Cu – Mn interaction in 7% Cu/CR and 11% Cu/CR catalysts, and the effective promotion of Mn^{4+}/Mn^{3+} redox interplay. The reduction peak attributed to the anticipated reduction of CuO disperse particles is also observed. The 7% Cu/CR catalyst displays the greatest area and peak definition, while in 11% Cu/CR, a hindered reduction and limited Cu – Mn contact by the larger CuO particles can be observed, since bulky CuO reduction may be overlapping with MnO_x reduction processes at higher temperatures. Furthermore, the broadening of the reduction profile and the appearance of an anticipated manganese reduction peak centred at 250ºC evidences the more labile manganese redox properties in 7% Cu/CR catalyst than in the other two Cu/CR catalysts.

Figure 7.4a, shows that Cu2p 3/2 spectra are broad and composed of multiple copper species with two main contributions, the first at lower binding energy (931.5 – 932.0 eV), and the second higher binding energy (933.6 – 933.8 eV). On the other hand, although overlapped under Mn LMM lines characteristic Cu(II) satellite peaks are observed in all cases.

Universitat d'Alacant
Universidad de Alicante

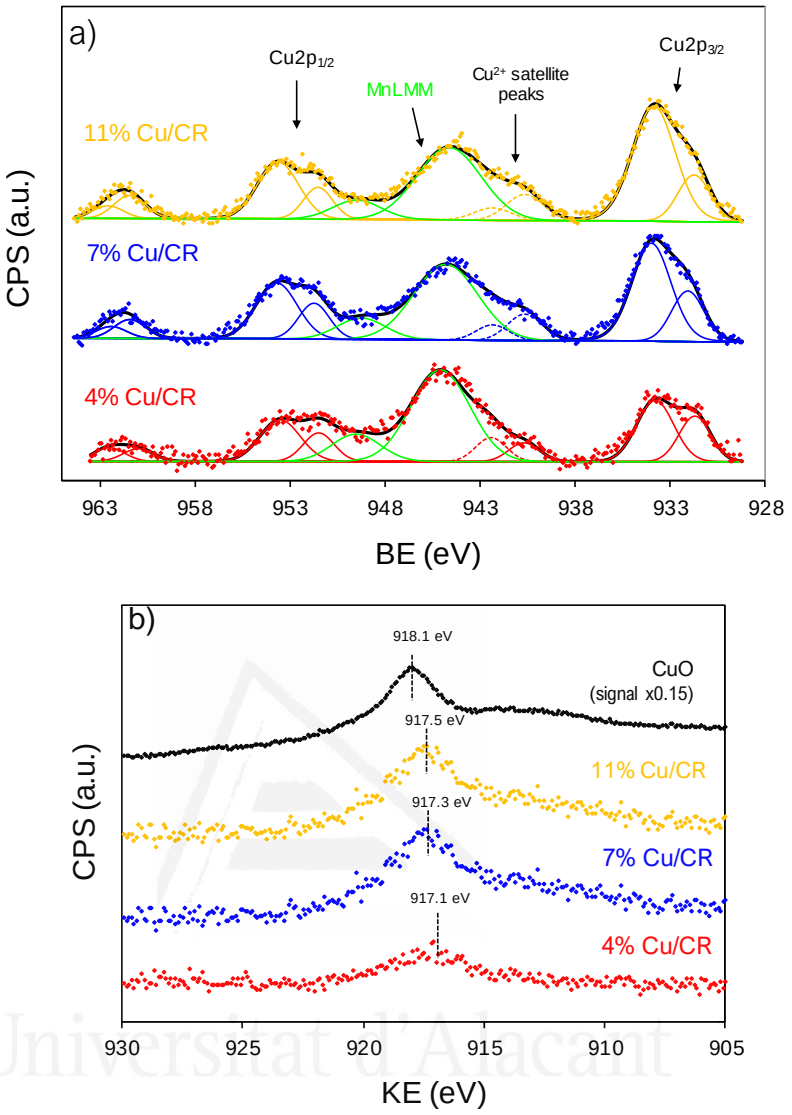

Figure 7.4. (a) Deconvoluted XPS Cu2p$_{3/2}$ photoemission region. **(b)** Cu $L_3M_{4.5}M_{4.5}$ Auger spectra of CuO and Cu/CR prepared catalysts

The detailed analysis of XPS and Auger spectra for CuO and Cu/CR catalysts, presented, allows to conclude that Cu $^{2+}$ is the main copper species present, although two different electronic environments are found and assigned to: (i) the higher BE contribution: Cu^{2+} species belonging to CuO particles (ii) the lower BE contribution: Cu^{2+} in intimate contact with the support and enhanced reducibility by means of Cu^{2+} – O – Mn^{y+} bridges. The abundance relation between both type of species is tentatively associated to the degree of copper oxide – cryptomelane interaction, which results significantly higher in the case of 4% Cu/CR, when compared to 7 and 11% catalysts (Table 7.3). Likewise, 4% Cu/CR catalyst presents the highest percentage of reducible copper, which is a sign that evidences the stronger CuO-CR interaction [40].

Universitat d'Alacant
Universidad de Alicante

Table 7.3. Modified Auger parameter and Cu distribution percentages for Cu/CR catalysts based on XPS and Auger characterization. [*] Using for calculation main 2p contribution.

Catalyst	α' (eV) [*]	% Cu(I) + % Cu(0)	% Cu^{2+}
4% Cu/CR	1850.7	39	61
7% Cu/CR	1851.1	29	71
11% Cu/CR	1851.2	22	78

On the other hand, neither Mn 2p region nor O1s region analyses (not shown results) presented have shown significative differences in the Mn average oxidation state (AOS) or in the oxygen species in the CR and Cu/CR catalysts. These results are in contrast with other authors' who reported an increased Mn AOS in cryptomelane by Cu substitution or deposition [11,32,42], as well as a greater population of loosely bound oxygen species [28,42]. Therefore, unfortunately we cannot confirm by this technique the effect of copper at the promotion of Mn redox properties in the Cu/CR catalysts, but conversely, the presence of Cu species with a more negative electron environment following the trend 11% Cu/CR < 7% Cu/CR < 4% Cu/CR can be an evidence of the CuO-CR interaction.

To get further insights, work function (WF) measurements of the Cryptomelane and Cu/Cryptomelane catalysts and a CuO reference were conducted, and the results are presented in Figure 7.5a. This technique provides information about the energy required to extract electrons from the solids, and the lower WF of a material indicates higher electron availability, which leads to a higher reactivity of such catalysts in the reactions where electron transfer from the catalyst surface to reacting molecule plays a key role [43]. The compiled data are consistent and show close values for bare cryptomelane (CR) and copper oxide(II), which hinders to establish a simple correlation among the series of Cu/CR prepared catalysts. Nevertheless, it is clearly observed a decrease in work function for 7% Cu/CR catalyst, even when compared to both pure phases CuO and Cryptomelane, which is an evidence of electrodonor properties in this sample because of a promoted Cu-Mn interaction. Thus, a lower work function value could be roughly associated to the higher facility towards reduction of the material and in this case 7% Cu/CR presents the strongest effect, in-line with the H_2-TPR results.

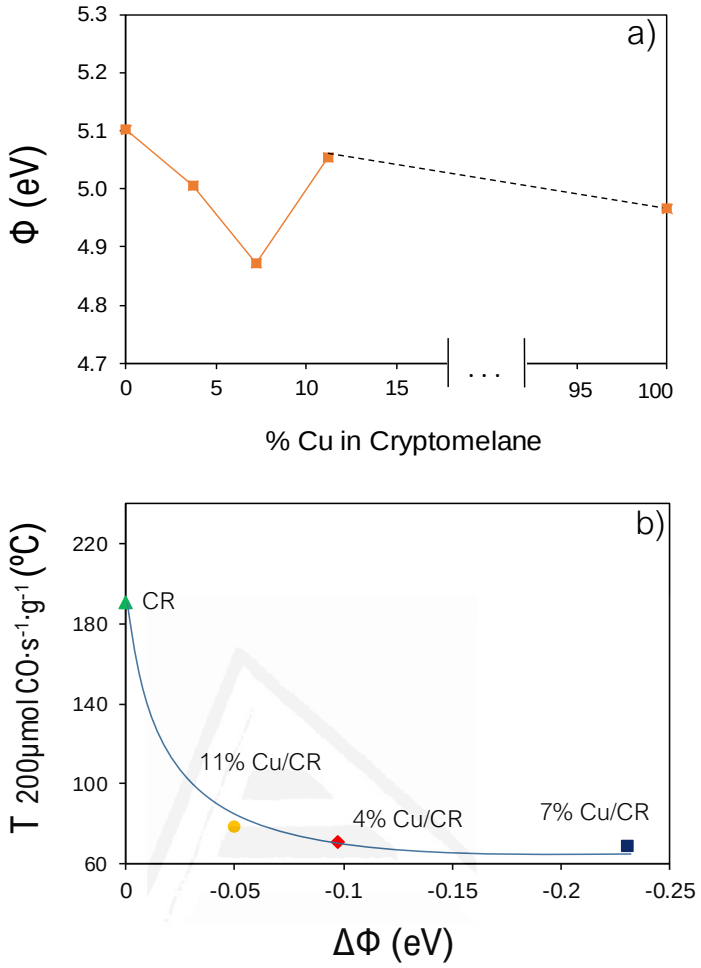

Figure 7.5. (a) Work Function (Φ) measurements of CR, Cu/CR prepared samples and CuO reference (100% Cu in X-axis) in air and room temperature conditions. **(b)** Temperature for 200 µmol CO/s·g of reaction rate plotted against Work Function differences ($\Delta\Phi = \Phi_{Cu/CR} - \Phi_{CR}$) by the effect of copper loading.

Nevertheless, taking into account the conditions of the measurements, and the prior state of samples after calcination in air, the presence of chemisorbed carbonates, hydroxyls and surface groups is important and its effect in work function values should not be ruled out. This surface chemistry affects the electrical properties by the formation of diffuse surface dipoles and electron density transference, which is evidenced by a work function lowering [44,45]. Thus, the behavior observed with regard to work function is representative of the abundance of oxygen surface species, which are present at the beginning of the CO-PROX activity experiments, as well. These oxygen containing groups (carbonates, bicarbonates, formates and hydroxyls) are not only spectators, but also take part in the CO-PROX mechanism suggested elsewhere [7]. Therefore, for 7% Cu/CR catalyst, which presents the lowest work function value, it can be inferred that the maximum degree of electronic surface distortion with atmospheric

components occurs, matching its better catalytic performance. In this regard, Figure 7.5b shows the work function decrease of Cu/CR catalysts compared to bare cryptomelane and its correlation with the reaction rate at low CO conversion by means of the characteristic temperature for 200 µmol CO/s· g in CO-PROX experiment.

The trend is clear, showing that reaction rate is accelerated with the lowering of the catalyst work function, establishing eventually a plateau below 0.1 eV of decrease. Thus, according to CuO – Cryptomelane interaction quantified by means of work function decrease, 7% Cu/CR catalyst presents the strongest synergistic effect towards reduction and oxygen groups chemisorption, which should be related to the presence of randomly dispersed CuO particles.

7.3.4 Role of K in CuO – CR interaction

One key factor for the understanding of the great activity of cryptomelane-based catalysts is the role of potassium in the electronic promotion of copper and manganese towards reduction and oxygen donor capacity. In this regard, specific analysis techniques have been performed in order to stablish appropriate determination of such properties. First of all, XPS analysis of K2p photoemission region presented in Figure 7.6, confirms there are no significant differences among potassium electronic states in the prepared catalysts, as deviations in peak maxima are below XPS sensitivity threshold (0.2 eV), in the $2p_{3/2}$ peaks centred, on average, at *ca.* 291.5 eV, which are values reported for cryptomelane [46]. Comparing with ionic potassium compounds, which present a sharp peak centred at 292.9 eV [47], such particularly low BE results are an evidence of potassium electronic enrichment by MnO_x donation in the narrow confinement inside cryptomelane tunnels. Thus, as this BE shifting is present in all Cryptomelane-based catalysts, it can be concluded that K electronic density is not dependent on copper content, showing that most probably copper and potassium are not directly interacting electronically.

Universidad de Alicante

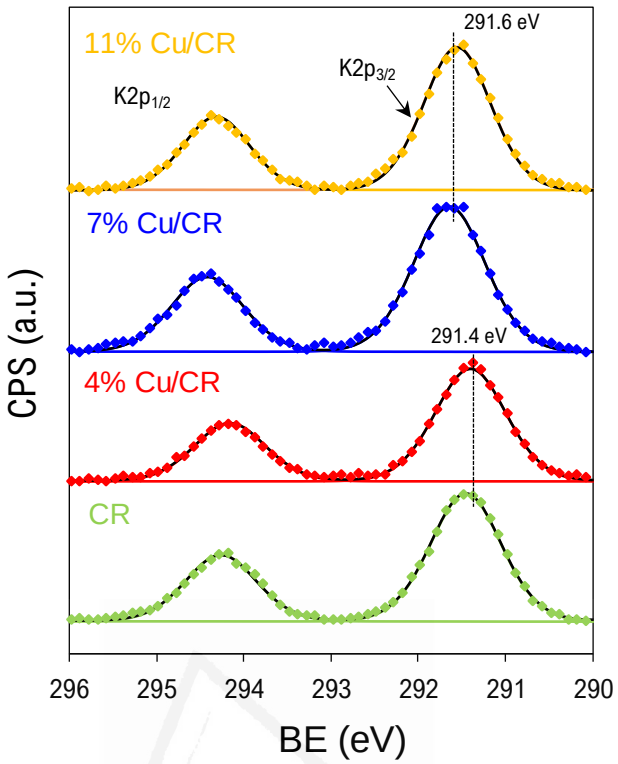

Figure 7.6. XPS K2p photoemission region for CR and Cu/CR prepared catalysts.

Additionally, the stability of potassium species was studied by thermal desorption tests, measuring the potassium atom flux from the samples heated in a vacuum chamber (Figure 7.7). Potassium thermal desorption measurements reveal that the process takes place over 400 ºC, thus at temperatures much higher than the CO-PROX catalytic activity. The linear part in the Arrhenius' plot corresponds to typical activation barriers for desorption of 2.1 eV without significant differences for CR and 7% Cu/CR catalysts. It means that the structure of cryptomelane, and thus the state of potassium, is not altered by the addition of copper oxide particles.

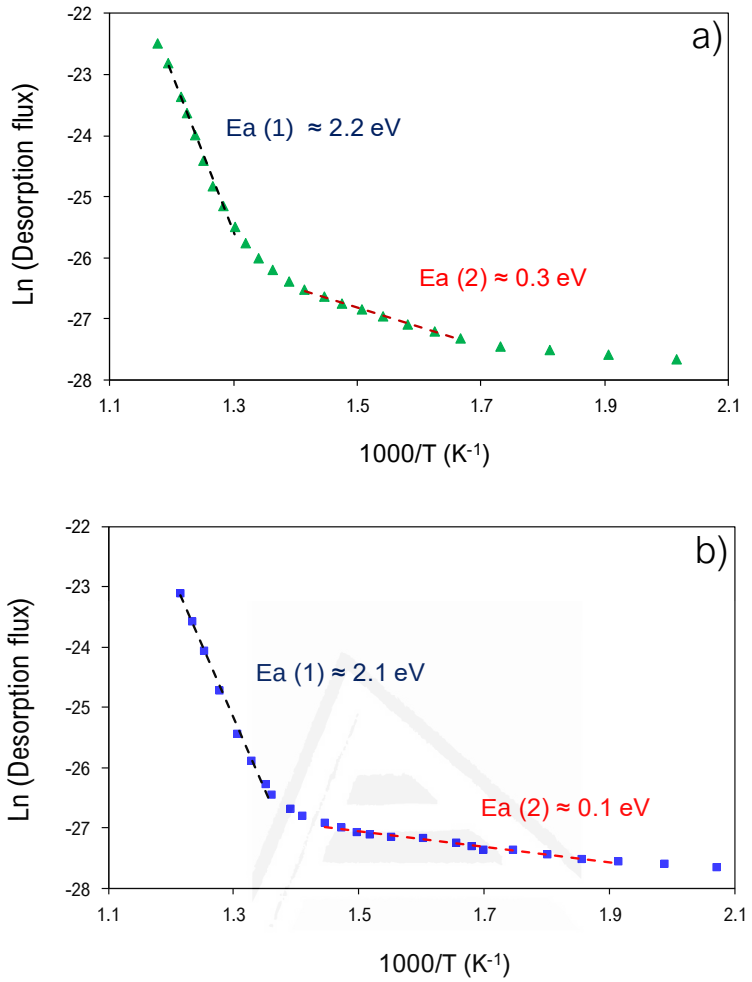

Figure 7.7. Potassium desorption as a function of temperature for **(a)** CR and **(b)** 7% Cu/CR catalyst.

In conclusion, potassium species play essentially a structural role in Cu/CR catalysts, stabilizing cryptomelane tunnels via electronic interaction with MnO_6 octahedra. Conversely, there is not an electronic promotion or activation of the dispersed copper oxide particles upon K interaction, which is not an unexpected conclusion since potassium remains inside the tunnels, whereas CuO is located at the periphery covering the external surface of cryptomelane. Therefore, since K – CuO interaction is scarce and occurs only by means of MnO_x intermediation, the particular contribution of K species in the catalytic activity should be equivalent for Cryptomelane and CuO/Cryptomelane catalysts, for which is not further considered in the present discussion.

7.3.5 Study of CO/H_2 interaction with Cu/CR catalysts

Since it is truly complex to obtain mechanistic data for CuO/Cryptomelane catalysts when compared to other studied catalysts,

such as ceria-based ones, with a thorough studies of well-known interpretation [5,7], in order to get analogue mechanistic information for cryptomelane-based catalysts, instrumental and methodological alternatives must be considered.

7.3.5.1 Density Functional Theory (DFT) calculations

Simple DFT calculations for the energy of adsorption of CO and H_2 gas molecules onto copper substrates in different oxidation states were conducted. Thus, the aim of this study is to discern the adsorption affinities of CO and H_2 at the different copper-based structures, representative of the catalyst state during reaction course.

Figure 7.8 compiles adsorption energies for CO and H_2 gas molecules onto copper-based slabs in their most favourable cases, considering dissociative or non-dissociative adsorption at different surface sites (Figure 7.9a-f).

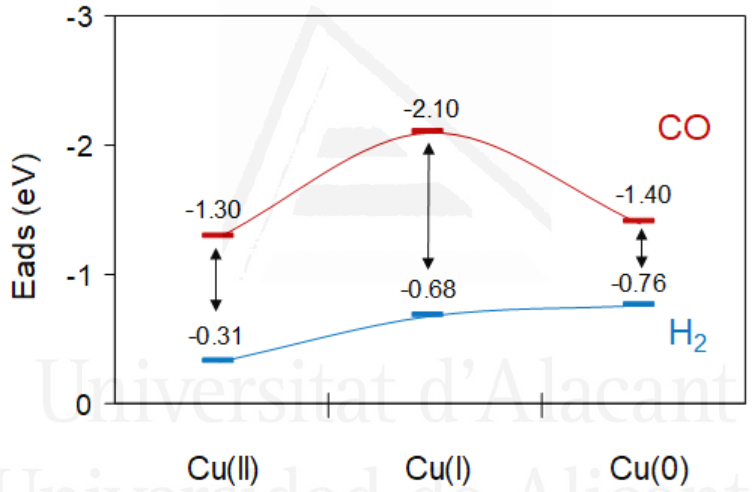

Figure 7.8. Energy of adsorption (eV) for CO and H_2 gas molecules onto slabs of CuO, Cu_2O and Cu, respectively.

Universitat d'Alacant
Universidad de Alicante

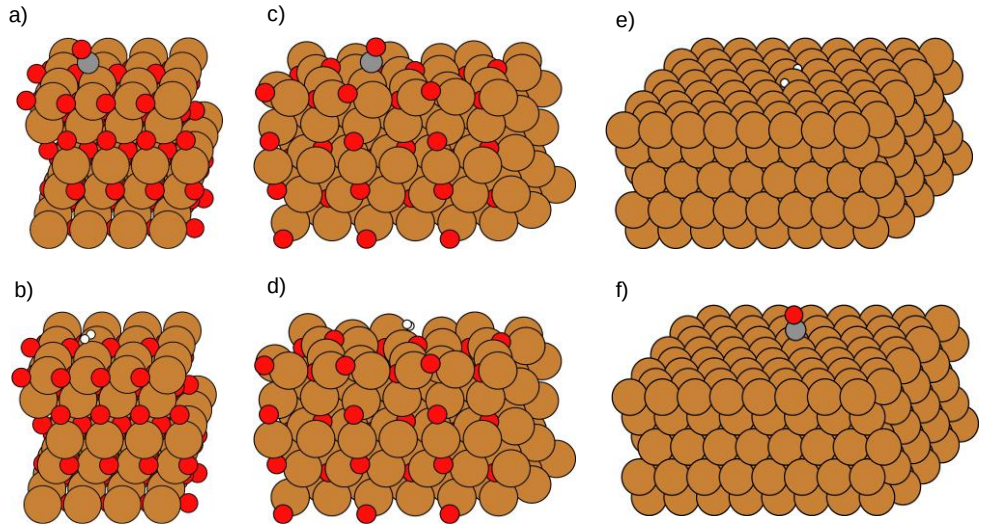

Figure 7.9. (a,b) CuO(111), **(c,d)** Cu_2O(111) and **(e,f)** Cu(111) surface slabs in the most favourable interaction with **(a,c,e)** CO; **(b,d,f)** H_2.

By the assumption that adsorption of gas molecules on the surface of the active sites is the first key step for catalytic reaction to occur, the difference between the energetics of these processes can be tentatively related to the CO-PROX selectivity for each copper-based surface. Therefore, by simple subtraction, it can be established that Cu(I) surface presents the highest energy difference for CO and H_2 adsorption, so the best selectivity is achieved when copper is partially reduced.

When it comes to the whole data comparison, Figure 6 shows that for CuO, initial state of the catalyst, the adsorption of H_2 presents quite low energy, whereas CO is significantly higher. In this case, CO-PROX reaction is based on a truly selective CO oxidation. Such activity is enlarged when CuO is partially reduced to Cu_2O, as energy of adsorption rises from -1.30 to -2.10 eV. In the same way, the surface doubles the affinity for H_2 adsorption, going from -0.31 eV for Cu(II) to -0.68 eV for the Cu(I) surface. This change can be related with the onset of H_2 oxidation reaction and therefore a loss in selectivity loss from the maximum values. Finally, when Cu_2O is reduced to Cu, the difference between energies of adsorption of CO and H_2 notably decreases, which is may be the cause of poor selectivity and a strong competition.

Despite the fact that the description of adsorption energetics profile matches that of experimental data, it must be taken into account that not all adsorption interactions are necessarily translated into chemical reaction, as a high percentage of adsorptive processes are not efficient and eventually lead to desorption in an adsorption-desorption pseudo-equilibrium situation. However, the energy of adsorption can be an indicator of average reaction process taking place as the relative population of CO and H_2 coverage is

affected, and then, the probability of reaction. Furthermore, the higher coverage of CO and H_2 is blocking the adsorption of their counterpart, as competitive adsorption is assumed according to this model.

In this environment, considering that the support MnO_x is stabilizing the Cu(I) particles by means of Cu-Mn synergistic interaction on CuO – MnO_x interface, it can be concluded that the best activity is obtained when the catalyst maximizes Cu – Mn interaction. As it was described before along the manuscript, this interaction is the strongest for 7% Cu/CR, according to H_2-TPR analysis and work function measurements. On the other hand, despite for 4% Cu/CR catalyst, Cu – Mn interface is maximized and copper species present a partially reduced state up to a higher extent, synergy at Cu and Mn reducibility is not clearly observed. Therefore, it is the cyclability of redox processes between Cu(II)/Cu(I) the driving force that induces the best catalytic performance, as lattice oxygen is actively participating in the reaction mechanism. So, for the lowest Cu loading (4%), CuO particles are too small to stabilize Cu(II)/Cu(I) mixed states, conceived as bulky CuO particles with surface reduction.

7.3.5.2 In-situ Work Function measurements

Thus, in order to check reactivity of Cu – Mn interfaces, *in-situ* work function measurements in an evacuated chamber with further addition of O_2 or CO gases were conducted to check WF changes in those atmospheres. WF is a highly sensitive surface reactivity descriptor and a useful measurable parameter, as it is claimed that surfaces undergo work function changes upon interaction with selected gases according to different sensing/reaction schemes [17,48]. In the case of semiconducting materials, the strength of interaction is directly reflected in WF change, assigned to the depletion/restitution of electrons from the conduction band (CB). The effect can be discussed in terms of the interaction of probe molecules with the surface: (1) O_2, by O- ionosorption (Equation 7.1); and (2) CO, by surface reduction (Equation 7.2), as particular cases for CO sensing materials. The description of these processes can be done according to the following scheme, where S represents surface sites [17,49,50]:

$$\tfrac{1}{2}\, O_2 \text{ gas} + e^- \text{ CB} + S \rightarrow O^- \text{ ads} \qquad \text{Eq. 7.1}$$

$$CO \text{ gas} + O^- \text{ ads} \rightarrow CO_2 \text{ gas} + e^- \text{ CB} + S \qquad \text{Eq. 7.2}$$

Equations 7.1 and 7.2 suggest that atmospheric oxygen thermally dissociates at the semiconducting sensor surface and is adsorbed as atomic ions by trapping conduction electrons. On the other hand, reducing gases, such as CO can undergo catalytic oxidation removing the ad-oxygen and releasing the captured electron back into the CB. Process from (1) leads to a work function rise as oxygen concentration yields surface negative charge, enlarging surface barrier and depletion degree. Whereas process (2) is generally observed as a weaker interaction consuming partially adsorbed/surface oxygen and releasing some captured electrons in the CB,

providing a slight work function lowering, since CB electrons do not influence directly into work function of the material, but its conductivity.

Therefore, WF measurements under O_2 and CO atmospheres at temperatures at which the catalysts present activity towards CO oxidation, can provide valuable information about catalyst – adsorbate interaction. In order to conduct these analyses, the measurement chamber was heated to 200ºC and the studied gasses were added to increase the total pressure in two steps, using: (1) bare cryptomelane; (2) 7% CuO/cryptomelane; and (3) pure CuO; which are representative for MnO_x surface; Cu – Mn interface and CuO surface; respectively. Figure 7.10 compiles these results.

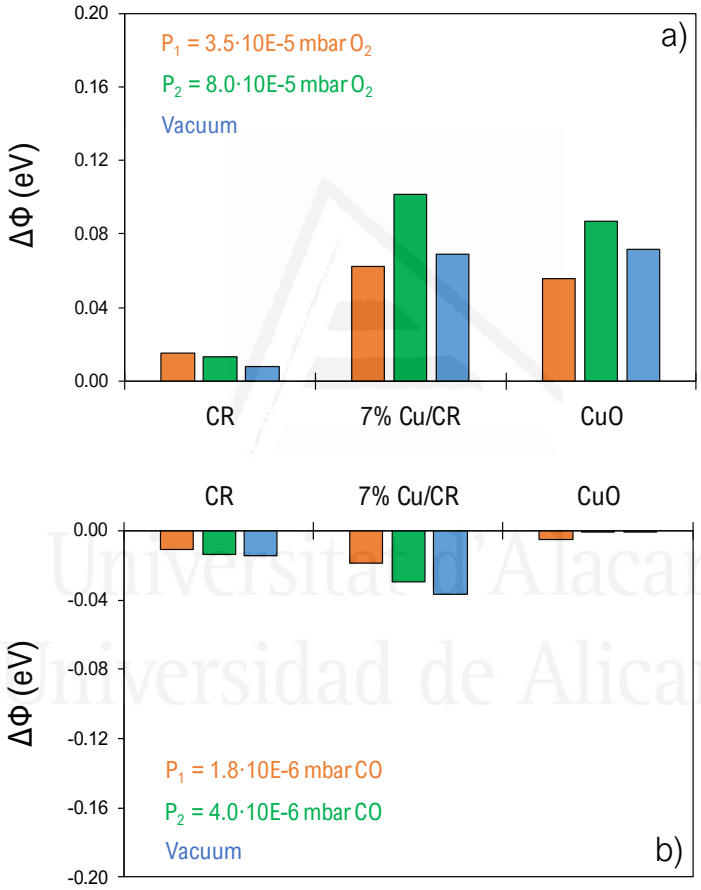

Figure 7.10. WF differences ($\Delta\Phi = \Phi_{p,i} - \Phi_{vac}$) measured at 200ºC by the effect of **(a)** O_2; **(b)** CO, on clean pretreated surfaces (500ºC, 30 min vacuum) of cryptomelane (CR), 7% CuO/cryptomelane (7% Cu/CR) and pure CuO.

Figures 7.10a and 7.10b evidence important differences in the behavior of the tested samples, as well as between interacting probe molecules. When it comes to O_2 interaction, WF rises with O_2 concentration in the chamber, as previously explained, according to the theoretical model.

In all cases, this interaction is mainly non-reversible, as vacuum measurement after O_2 contact does not bring back original work function values. Comparing between samples, 7% Cu/CR and CuO show a sharp work function change upon O_2 interaction, while CR shows much poorer response. These results reveal that the copper-rich phase is active for O_2 ionosorption and lattice oxygen vacancy replacement, but not MnO_x. However, CuO – CR contact phases occurring at 7% Cu/CR catalyst maximizes O_2 interaction, and therefore, oxygen restitution during reaction. It has to be taken into account that prior to analysis, samples were pretreated at 450ºC for 30 min in vacuum, which generally produce structural oxygen release and partial reduction, from CuO to $CuO_{1-\delta}$ and MnO_x to $MnO_{x-\delta}$. Thus, the great ability of CuO to undergo easy reduction when compared to MnO_x makes it more susceptible to accept oxygen species from the gas phase, which is observed by a large work function change response. However, it occurs at a higher extent in the case of 7% Cu/CR sample, where a synergistic effect is clearly promoting oxygen restoration in the catalyst. In a possible mechanism, partially reduced $CuO_{1-\delta}$ particles would act as O_2 caption sites, facilitating then, by a spillover effect at the interface, their transport towards MnO_x, and releasing again $CuO_{1-\delta}$ sites for new coming O_2 molecules. Thus, changes are more significant in Cu/CR as MnO_x takes part as oxygen receptor as well, increasing average oxygen capacity. Besides, given the promoted reduction of MnO_x and CuO in 7% Cu/CR catalyst, it is rational to expect higher extent in vacancy formation, leading to a higher oxygen uptake, and then, a larger work function change.

Regarding Figure 7.10b, a negative change in work function is observed by the effect of CO – surface interaction, assigned to the release of an electron into the CB as a product of CO oxidation, and removal of surface oxygen dipoles. Taking into account that the temperature of measurement is 200ºC in chamber (~150ºC on sample surface), this modification should necessarily be related to the catalyst activity in CO oxidation at such range of temperatures: 7% Cu/CR (~90% conv. CO) >> CR (~10% conv. CO) > CuO (~2% conv. CO). Despite the fact that the changes are much weaker when compared to O_2 measurements, the trend observed is clear, showing that for 7% Cu/CR the interaction is the strongest, whereas for reference CuO the electron affinity is not modified. Another important fact which is observable on Figure 7.10b is the non-reversible CO electronic effect, observed by a maintenance or even slight increase in work function modification after chamber evacuation back to vacuum, which is rather expected as the effect is related to chemical reaction and not merely an adsorption process.

Universidad de Alicante

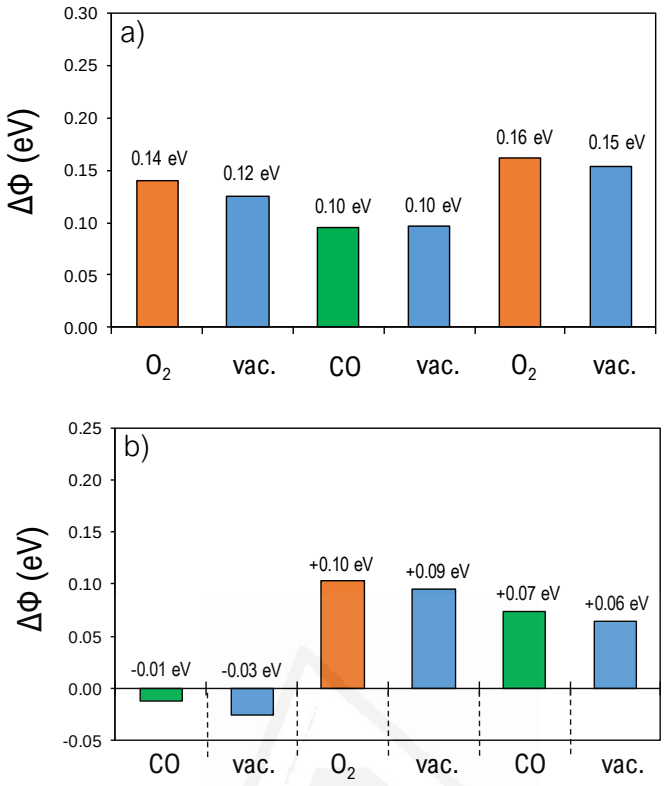

Figure 7.11. Work Function differences ($\Delta\Phi = \Phi_{p,i} - \Phi_{vac}$) measured at 200 ºC over 7% Cu/CR catalyst by the effect of switching atmospheres (i) pO_2: $8 \cdot 10^{-5}$ mbar, for 30 minutes; (ii) p CO: $4 \cdot 10^{-6}$ mbar, for 60 minutes, following the sequence: **(a)** O_2-CO-O_2; **(b)** CO-O_2-CO.

Finally, as complementary characterization using Kelvin Probe instrument, *in-situ* work function measurement experiments with switching O_2/CO atmospheres were conducted on 7% Cu/CR catalyst, results of which are presented in Figure 7.11.

The conducted gas switching experiments reveal that the presence of O_2 prevails over CO due to stronger interaction with the surface of the catalysts in the initial uptake, even though the pressure gap between O_2 and CO steps has been compensated by a longer CO exposure. Independent of whether O_2 or CO is supplied first, according to Figure 9a,b on average their introduction conduces to an increase of +0.13 eV, and decrease of -0.02 eV, respectively, in a quite good cyclability. Additionally, turning back to vacuum does not recover in any case work function values from the beginning, probing the non-reversible effect of such gas-surface interaction as described above. Whereas O_2 is refilling vacancies and abstracting electrons from CB, CO is providing electrons to CB and removing lattice O_2-, back and forth in an imbalanced cycle with superior O_2 interaction. So, as a final remark, lattice oxygen must be necessarily involved in CO oxidation mechanism according to MVK mechanism.

Compiling these data, it must be concluded that it is in CuO/Cryptomelane where both O_2 ionosorption and CO oxidation are maximised, ultimately observed by means of a greater catalytic activity. In the case of Cryptomelane, despite presenting interaction with CO, O_2 restoration is a severe limiting step towards restitution of active oxygen to participate in CO oxidation reaction, thus presenting poor catalytic activity. In this sense, copper-rich phase aids O_2 storage and release in CuO/Cryptoemale catalyst, skipping such barrier with a good Cu – Mn interaction under tight contact of both constituent phases. On the other hand, on CuO_x surface, CO interaction is not observed as work function change, but given the nature of electron transference is based on CO oxidation process, CO chemisorption cannot be ruled out. In fact, according to DFT calculations on CuO_x surfaces, it is predicted a strong CO chemisorption, however, without the appropriate oxygen assistance supply in absence of O_2 at the atmosphere, this CO sorption does not lead to effective catalytic activity in the oxygen-poor pure CuO_x.

It can therefore be concluded that cryptomelane would act as an oxygen restitution reservoir towards CuO, stabilizing partially reduced particles at the Cu – Mn interface, enabling CO oxidation to take place. It is, thus a solid evidence of the role of active interface points between MnO_x and CuO dispersed clusters in Cu/CR type catalysts in CO oxidation reaction, as well as a proof of Mars van Krevelen mechanism.

7.4 General discussion

From the Cu/CR prepared catalysts, 7% Cu/CR resulted the optimum and the characterization of this material revealed that it is constituted by well dispersed CuO particles on the cryptomelane support, leading to a good Cu – Mn interaction. The Cu – Mn interaction was observed by means of an enhanced reducibility when compared to separate MnO_x and CuO materials.

The strong effect of copper loading into CO-PROX activity performance was attributed to the gain in CO / O_2 interaction with the catalytic surface on the Cu – O – Mn sites, which promotes Cu(I) states with the predicted maximum selective CO chemisorption compared to that of H_2. The synergistic Cu – Mn effect relies on the labile oxygen transference and replacement from O_2 phase, crucial in MVK mechanism oxidation reactions. On the one hand, CR shows a measurable CO interaction, but O recovery is not efficient, while CuO, which is prone to reoxidation with O_2, and chemisorbs CO with no changes in WF. The synergism found in Cu/CR catalysts allow us to predict the reaction mechanism for CO oxidation, represented by the following scheme:

$Cu^{2+}–O^{2-}–Cu^{2+}–O^{2-}–Mn^{4+} + CO \rightarrow$

$Cu^{2+}–O^{2-}–Cu^{+}–□–Mn^{3+} + CO_2$ Step 1

$Cu^{2+}–O^{2-}–Cu^{+}–□–Mn^{3+} + ½\ O_2 \rightarrow$

$Cu^{2+}–O^{2-}–Cu^{2+}–O^{2-}–Mn^{4+}$ Step 2a

$Cu^{2+}–O^{2-}–Cu^{+}–□–Mn^{3+} + CO \rightarrow$

$Cu^{+}–□–Cu^{0}–□–Mn^{3+} + CO_2$ Step 2b

$Cu^{+}–□–Cu^{0}–□–Mn^{3+} + ½\ O_2 \rightarrow Cu^{+}\text{-}□–Cu^{+}–O^{2-}–Mn^{4+}$ Step 3b

$Cu^{+}–□–Cu^{+}–O^{2-}–Mn^{4+} \rightarrow Cu^{2+}–O^{2-}–Cu^{+}–□–Mn^{3+}$ Step 4b

First, CO oxidation takes place in the interfacial O from CuO – MnO_x (Step 1) since the redox interaction of Cu – Mn bonding provides an extra charge density in Cu^{2+} species, which present the highest CO chemisorption energy. Secondly, the O vacancy created upon CO oxidation, could be immediately refilled by O_2 gas (Step 2a), recovering its initial state, or alternatively, the active Cu^{+} formed could oxidize another CO molecule, achieving a more reduced state by the formation of another oxygen vacancy (Step 2b). The catalyst would undergo one pathway or another depending on the temperature. Presumably at lower temperatures, Step 2a would prevail over Step 2b, while at higher temperatures of reaction in CO-PROX conditions, Step 2b would be faster, keeping the catalyst in a reduced state. Then, with ambient oxygen, the catalyst recovers a partially oxidized state (Step 3b), and it is predicted that the first oxygen vacancy to be refilled may be the one located at the Cu – Mn interface, since it was proven that O_2 interaction was maximised for Cu/CR catalyst when compared to pure CuO sample.

Finally, the catalysts could undergo a further CO oxidation step with interfacial oxygen, or promote its transference towards the Cu-rich phase to recover partially recover the Cu(II) oxidized state (Step 4b) and ultimately produce again CO oxidation. Since it was checked that in 7% and 11% Cu/CR catalysts Mn reducibility was improved, it is expected that this process gains importance when CuO particles are larger, ensuring the formation of stable CuO bulky sites. Anyhow, both lattice oxygen sites (interfacial and from the CuO bulk) should present good CO oxidation capacity, and specially at high temperatures the accelerated reaction rate would make both sites indistinguishable.

7.5 Conclusions

The CO-PROX reaction mechanism has been studied for CuO/Cryptomelane catalysts and it has been disentangled the individual role of CuO particles and the cryptomelane support, as well as the synergistic effect of the active Cu – Mn interface. The main conclusions achieved may be summarized as follows:

(1) When Cu is deposited in a cryptomelane substrate for the preparation of CuO/Cryptomelane catalysts, it mainly forms a segregated phase of dispersed CuO particles between cryptomelane nanorods.

(2) These particles present good contact with Mn-phase of the support at surface, leading to a positive Cu – Mn synergistic effect, whereas there is no interaction with K intratunnel species from cryptomelane.

(3) The presence of medium-sized CuO particles dispersed in cryptomelane in Cu/CR catalyst turns into the best performance for 7% Cu/CR in CO-PROX reaction, when compared to smaller and larger CuO particles, as in 4% Cu/CR and 11% Cu/CR, respectively.

(4) The most enhanced reducibility of 7% Cu/CR correlates well with its best CO-PROX catalytic activity, and the largest change in WF by the effect of Cu loading into cryptomelane, too. Both are signs of the strongest Cu – Mn interaction, which are indirect evidences of the maximization of Cu(I) states in the contact points to MnO_x phase from cryptomelane support.

(5) According to *in situ* Work Function measurements, Cu/CR catalyst maximizes both O_2 uptake and CO interaction with regards to pure CuO and CR catalysts, evidencing the active role of interfacial labile Cu – O – Mn entities.

(6) On the other hand, whereas CuO_x phase enhances O_2 restitution capacity in Cu/CR catalyst, cryptomelane promotes surface Cu(I) states that increase CO interaction with the catalytic surface.

(7) The presence of medium-sized CuO particles exhibits a compromise between sufficient active Cu – Mn interface for the maximization of Cu(I) species, and stable CuO bulky sites for the efficient O_2 recovery upon MVK CO-PROX ongoing mechanism.

(8) Hence, for CuO/Cryptomelane, certain analogy with CuO/CeO_2 catalyst can be established since both supports are reducible oxides that promote interfacial Cu(I) active states by means of strong synergistic effect.

(9) The results presented herein evidence the large potential of cryptomelane as an active support for Cu-based catalysts towards CO-

Universidad de Alicante

PROX reaction application, although the stability of this material is not as good as in CuO/CeO_2 catalyst, but partially kept in CO_2 + H_2O reaction conditions, in which CuO/Cryptomelane results particularly interesting.

Next Chapter 8 deals with a direct comparison between CuO/CeO_2 and CuO/Cryptomelane materials for catalytic CO-PROX application, in order to rationalize real opportunities of this alternative material, when compared to the well-established CuO/CeO_2 catalyst.

References

[1] C.S. Polster, H. Nair, C.D. Baertsch, Study of active sites and mechanism responsible for highly selective CO oxidation in H_2 rich atmospheres on a mixed Cu and Ce oxide catalyst, J. Catal. 266 (2009) 308–319.

[2] J.L. Ayastuy, A. Gurbani, P. Gonza, M. a Gutie, Kinetics of Carbon Monoxide Oxidation over CuO Supported on Nanosized CeO_2, (2010) 5633–5641.

[3] E.-Y. Ko, E.D. Park, K.W. Seo, H.C. Lee, D. Lee, S. Kim, A comparative study of catalysts for the preferential CO oxidation in excess hydrogen, Catal. Today. 116 (2006) 377–383.

[4] H.C. Lee, D.H. Kim, Kinetics of CO and H_2 oxidation over $CuO-CeO_2$ catalyst in H_2 mixtures with CO_2 and H_2O, Catal. Today. 132 (2008) 109–116.

[5] A. Martínez-Arias, D. Gamarra, A. Hungría, M. Fernández-García, G. Munuera, A. Hornés, P. Bera, J. Conesa, A. Cámara, Characterization of Active Sites/Entities and Redox/Catalytic Correlations in Copper-Ceria-Based Catalysts for Preferential Oxidation of CO in H_2-Rich Streams, Catalysts. 3 (2013) 378–400.

[6] J.S. Elias, K.A. Stoerzinger, W.T. Hong, M. Risch, L. Giordano, A.N. Mansour, Y. Shao-Horn, In Situ Spectroscopy and Mechanistic Insights into CO Oxidation on Transition-Metal-Substituted Ceria Nanoparticles, ACS Catal. 7 (2017) 6843–6857.

[7] A. Davó-Quiñonero, M. Navlani-García, D. Lozano-Castelló, A. Bueno-López, J.A. Anderson, Role of Hydroxyl Groups in the Preferential Oxidation of CO over Copper Oxide-Cerium Oxide Catalysts, ACS Catal. 6 (2016) 1723-1731.

[8] X. Chen, Y.-F. Shen, S.L. Suib, C.L. O'Young, Characterization of Manganese Oxide Octahedral Molecular Sieve (M−OMS-2) Materials with Different Metal Cation Dopants, Chem. Mater. 14 (2002) 940–948.

[9] M.C. Biesinger, B.P. Payne, A.P. Grosvenor, L.W.M. Lau, A.R. Gerson, R.S.C. Smart, Resolving surface chemical states in XPS analysis of first row transition metals, oxides and hydroxides: Cr, Mn, Fe, Co and Ni, Appl. Surf. Sci. 257 (2011) 2717–2730.

[10] T. Gao, M. Glerup, F. Krumeich, R. Nesper, H. Fjellvâg, P. Norby, Microstructures and spectroscopic properties of cryptomelane-type manganese dioxide nanofibers, J. Phys. Chem. C. 112 (2008) 13134-13140.

[11] X.-S. Liu, Z.-N. Jin, J.-Q. Lu, X.-X. Wang, M.-F. Luo, Highly active CuO/OMS-2 catalysts for low-temperature CO oxidation, Chem. Eng. J. 162 (2010) 151–157.

[12] J. Hou, Y. Li, L. Liu, L. Ren, X. Zhao, Effect of giant oxygen vacancy defects on the catalytic oxidation of OMS-2 nanorods, J. Mater. Chem. A. 1 (2013)

6736–6741.

[13] H.C. Genuino, S. Dharmarathna, E.C. Njagi, M.C. Mei, S.L. Suib, Gas-Phase Total Oxidation of Benzene, Toluene, Ethylbenzene, and Xylenes Using Shape-Selective Manganese Oxide and Copper Manganese Oxide Catalysts, J. Phys. Chem. C. 116 (2012) 12066–12078.

[14] M. Sun, L. Yu, F. Ye, G. Diao, Q. Yu, Z. Hao, Y. Zheng, L. Yuan, Transition metal doped cryptomelane-type manganese oxide for low-temperature catalytic combustion of dimethyl ether, Chem. Eng. J. 220 (2013) 320–327.

[15] W.Y. Hernández, M. a. Centeno, S. Ivanova, P. Eloy, E.M. Gaigneaux, J. a. Odriozola, Cu-modified cryptomelane oxide as active catalyst for CO oxidation reactions, Appl. Catal. B Environ. 123–124 (2012) 27–35.

[16] M. Özacar, A.S. Poyraz, H.C. Genuino, C.-H. Kuo, Y. Meng, S.L. Suib, Influence of silver on the catalytic properties of the cryptomelane and Ag-hollandite types manganese oxides OMS-2 in the low-temperature CO oxidation, Appl. Catal. A Gen. 462–463 (2013) 64–74.

[17] A. Oprea, N. Bârsan, U. Weimar, Work function changes in gas sensitive materials: Fundamentals and applications, Sensors Actuators B Chem. 142 (2009) 470–493.

[18] R.N. DeGuzman, Y.F. Shen, E.J. Neth, S.L. Suib, C.L. O'Young, S. Levine, J.M. Newsam, Synthesis and characterization of Octahedral Molecular Sieves (OMS-2) having the hollandite structure, Chem. Mater. 6 (1994) 815–821.

[19] I. Atribak, a. Bueno-López, a. García-García, P. Navarro, D. Frías, M. Montes, Catalytic activity for soot combustion of birnessite and cryptomelane, Appl. Catal. B Environ. 93 (2010) 267–273.

[20] P. Stelmachowski, P. Legutko, T. Jakubek, A. Kotarba, Phase evolution and electronic properties of cryptomelane nanorods, J. Alloys Compd. 767 (2018) 592–599.

[21] P. Stelmachowski, P. Legutko, T. Jakubek, P. Indyka, Z. Sojka, L. Holmlid, A. Kotarba, Emission of highly excited electronic states of potassium from cryptomelane nanorods, Phys. Chem. Chem. Phys. 17 (2015) 26289–26294.

[22] D. Cazorla-Amorós, J. Alcañiz-Monge, M.A. de la Casa-Lillo, A. Linares-Solano, CO_2 As an Adsorptive To Characterize Carbon Molecular Sieves and Activated Carbons, Langmuir. 14 (1998) 4589–4596.

[23] V. Alcalde-Santiago, A. Davó-Quiñonero, D. Lozano-Castelló, A. Bueno-López, On the soot combustion mechanism using 3DOM ceria catalysts, Appl. Catal. B Environ. 234 (2018) 187-197.

[24] A.W. Burton, K. Ong, T. Rea, I.Y. Chan, On the estimation of average crystallite size of zeolites from the Scherrer equation: A critical evaluation of its application to zeolites with one-dimensional pore systems, Microporous Mesoporous Mater. 117 (2009) 75–90.

[25] P. Scherrer, Bestimmung der Größe und der inneren Struktur von Kolloidteilchen mittels Röntgenstrahlen, Nachrichten von Der Gesellschaft Der Wissenschaften Zu Göttingen, Math. Klasse. 1918 (n.d.) 98–100.

[26] A. Davó-Quiñonero, M. Navlani-García, D. Lozano-Castelló, A. Bueno-López, CuO/cryptomelane catalyst for preferential oxidation of CO in the presence of H_2: Deactivation and regeneration, Catal. Sci. Technol. 6 (2016) 5684-5692.

[27] H. Huang, Y. Meng, A. Labonte, A. Dobley, S.L. Suib, Large-Scale Synthesis of Silver Manganese Oxide Nanofibers and Their Oxygen Reduction

Properties, J. Phys. Chem. C. 117 (2013) 25352–25359.

[28] W.Y. Hernández, M. a. Centeno, S. Ivanova, P. Eloy, E.M. Gaigneaux, J. a. Odriozola, Cu-modified cryptomelane oxide as active catalyst for CO oxidation reactions, Appl. Catal. B Environ. 123–124 (2012) 27–35.

[29] V.P. Santos, M.F.R. Pereira, J.J.M. Órfão, J.L. Figueiredo, The role of lattice oxygen on the activity of manganese oxides towards the oxidation of volatile organic compounds, Appl. Catal. B Environ. 99 (2010) 353–363.

[30] P. Mars, D.W. van Krevelen, Oxidations carried out by means of vanadium oxide catalysts, Chem. Eng. Sci. 3 (1954) 41–59.

[31] M.J. Kahlich, H.A. Gasteiger, R.J. Behm, Kinetics of the Selective CO Oxidation in H_2 -Rich Gas on Pt/Al_2O_3, J. Catal. 171 (1997) 93–105.

[32] W.Y. Hernández, M.A. Centeno, F. Romero-Sarria, S. Ivanova, M. Montes, J.A. Odriozola, Modified cryptomelane-type manganese dioxide nanomaterials for preferential oxidation of CO in the presence of hydrogen, Catal. Today. 157 (2010) 160–165.

[33] K. Ramesh, L. Chen, F. Chen, Y. Liu, Z. Wang, Y.F. Han, Re-investigating the CO oxidation mechanism over unsupported MnO, Mn_2O_3 and MnO_2 catalysts, Catal. Today. 131 (2008) 477–482.

[34] M. Piumetti, D. Fino, N. Russo, Mesoporous manganese oxides prepared by solution combustion synthesis as catalysts for the total oxidation of VOCs, Appl. Catal. B Environ. 163 (2015) 277–287.

[35] A. Davó-Quiñonero, D. Lozano-Castelló, A. Bueno-López, Unexpected stability of CuO/Cryptomelane catalyst under Preferential Oxidation of CO reaction conditions in the presence of CO_2 and H_2O, Appl. Catal. B Environ. 217 (2017) 459-465.

[36] E.C. Njagi, H.C. Genuino, C.K. King'Ondu, C.H. Chen, D. Horvath, S.L. Suib, Preferential oxidation of CO in H_2-rich feeds over mesoporous copper manganese oxides synthesized by a redox method, Int. J. Hydrogen Energy. 36 (2011) 6768–6779.

[37] K. Qian, Z. Qian, Q. Hua, Z. Jiang, W. Huang, Structure-activity relationship of CuO/MnO_2 catalysts in CO oxidation, Appl. Surf. Sci. 273 (2013) 357–363.

[38] G. Moretti, Auger parameter and Wagner plot in the characterization of chemical states by X-ray photoelectron spectroscopy: A review, J. Electron Spectros. Relat. Phenomena. 95 (1998) 95–144.

[39] J.P. Espinós, J. Morales, A. Barranco, A. Caballero, J.P. Holgado, A.R. González-Elipe, Interface Effects for Cu, CuO, and Cu_2O Deposited on SiO_2 and ZrO_2. XPS Determination of the Valence State of Copper in Cu/SiO_2 and Cu/ZrO_2 Catalysts, J. Phys. Chem. B. 106 (2002) 6921–6929.

[40] M.C. Biesinger, Advanced analysis of copper X-ray photoelectron spectra, Surf. Interface Anal. 49 (2017) 1325–1334.

[41] NIST X-Ray Photoelectron Spectroscopy Database, NIST Stand. Ref. Database 20, Version 4.1. (n.d.).

[42] M. Sun, L. Yu, F. Ye, G. Diao, Q. Yu, Z. Hao, Y. Zheng, L. Yuan, Transition metal doped cryptomelane-type manganese oxide for low-temperature catalytic combustion of dimethyl ether, Chem. Eng. J. 220 (2013) 320–327.

[43] G. Grzybek, P. Stelmachowski, S. Gudyka, J. Duch, K. Ćmil, A. Kotarba, Z. Sojka, Insights into the twofold role of Cs doping on deN_2O activity of cobalt spinel catalyst—towards rational optimization of the precursor and loading, Appl. Catal. B Environ. 168–169 (2015) 509–514.

[44] M. Batzill, U. Diebold, The surface and materials science of tin oxide, Prog. Surf. Sci. 79 (2005) 47–154.

[45] N. Barsan, U. Weimar, Understanding the fundamental principles of metal oxide based gas sensors; the example of CO sensing with SnO_2 sensors in the presence of humidity, J. Phys. Condens. Matter. 15 (2003) R813–R839.

[46] T. Soejima, K. Nishizawa, R. Isoda, Monodisperse manganese oxide nanoparticles: Synthesis, characterization, and chemical reactivity, J. Colloid Interface Sci. 510 (2018) 272–279.

[47] G.E. Wagner, C.D., Riggs, W.M., Davis, L.E., Moulder, J.F., Mullenberg, Handbook of X-Ray Photoelectron Spectroscopy, Perkin-Elmer Corp., Physical Electronics Division, Eden Prairie, Minnesota, USA, 1979.

[48] P. Legutko, T. Jakubek, W. Kaspera, P. Stelmachowski, Z. Sojka, A. Kotarba, Strong Enhancement of deSoot Activity of Transition Metal Oxides by Alkali Doping: Additive Effects of Potassium and Nitric Oxide, Top. Catal. 60 (2017) 162–170.

[49] D.E. Williams, Semiconducting oxides as gas-sensitive resistors, Sensors Actuators B Chem. 57 (1999) 1–16.

[50] H. Windischmann, P. Mark, A Model for the Operation of a Thin-Film SnO_x Conductance-Modulation Carbon Monoxide Sensor, J. Electrochem. Soc. . 126 (1979) 627–633.

Universitat d'Alacant
Universidad de Alicante

Universitat d'Alacant
Universidad de Alicante

CHAPTER 8

Comparative analysis between CuO/CeO_2 and CuO/Cryptomelane: real opportunities in CO-PROX application

Chapter 8 compiles main remarks referring to CuO/CeO_2 and CuO/Cryptomelane catalysts utilization in the Preferential CO Oxidation reaction and the most relevant outcomes achieved along the development of this Project Thesis are presented altogether for their direct comparison. With fresh sample on the reactor, CuO/Cryptomelane shows better performance than CuO/CeO_2 on a first catalytic run, but latter CuO/Cryptomelane deactivation on successive reaction cycles flips their relative activities. Nevertheless, in CO_2+H_2O environment, the enhanced stability of CuO/Cryptomelane allows to reach a much more active state after the succession of catalytic runs, which sets closer the CuO/CeO_2 and CuO/Cryptomelane performances, up to the point that the latter shows big competitive potential.

Universitat Rovira i Virgili
Universidad de Alicante

8.1 Introduction

During this Project Thesis, CuO/Cryptomelane and CuO/CeO_2 catalysts have been prepared, fully characterized and tested in the Preferential CO Oxidation (CO-PROX) reaction in presence of large H_2 excess. The results achieved from the research work presented so far clearly reveal the large potential of CuO/Cryptomelane catalyst and its promising real opportunities to leverage CeO_2-based catalysts substitution for the sake of a more sustainable approach into the exhaustive catalytic CO clean-up required for H_2 purification. Nonetheless, stability issues attributed to partial collapse of cryptomelane structure evidenced, by the segregation into Mn_3O_4 and $CuMn_2O_4$ crystalline phases, forced by ongoing oxidation – reduction cycles, is a strong limiting barrier towards the widespread utilization of CuO/Cryptomelane, although regeneration treatments have demonstrated to partially prevent this deactivation [1].

In Chapter 6, though, it was checked that when CO-PROX reaction test is performed in CO_2+H_2O presence, CuO/Cryptomelane was less prone to deactivation on each catalytic run, and it was not even necessary to undertake any regeneration intermediate pre-treatment in between cycles [2]. Interestingly, the introduction of CO_2+H_2O, potential inhibitors in CO-PROX catalysts, lead to an improved stability over CuO/Cryptomelane, which was attributed to the partial relocation of intra-tunnel water species, with structural stabilizing effect, that hold back cryptomelane collapse into the inactive segregated phases. Furthermore, the co-presence of CO_2 leads to a magnified H_2O and CO_2 retention capacity with regards to standalone H_2O and CO_2 addition, which tentatively involves different mechanisms of adsorption/incorporation on the CuO/Cryptomelane surface. Namely, the effect of carbonate formation and its participation in H_2O co-adsorption mechanism via bicarbonates, with higher affinity with the acid cryptomelane surface than carbonates. Yet, the blocking effect of CO_2 molecules, which impedes redox exchange in Cu – O – Mn entities leading to a reducibility loss, which is negative for the catalytic activity, but positive for the stability since it restrains the deactivating redox cycling and eventually maintains the intrinsic good H_2O affinity of better-kept cryptomelane.

Conversely, CuO/CeO_2 catalysts are reported to be affected by CO_2+H_2O presence, although they exhibit absolute stability upon cyclability in successive CO-PROX catalytic runs, as well as good performance in long time-on-stream CO-PROX tests, as it was confirmed in Chapter 4 [3]. The enhanced stability is attributed to the large lattice adaptability upon changes in Ce^{3+}/Ce^{4+} ratios, allowing the easy oxygen vacancy formation that leads to excellent catalytic activity, but more importantly, the facile lattice oxygen re-accommodation with incoming O_2 molecules from the gas phase. The latter is a key feature, since enables entire reversibility in the reduction – oxidation processes over CeO_2 catalysts, in contrast the inefficient oxygen restitution from Cryptomelane catalysts.

At this stage, having presented all along this Thesis parallel studies on CuO/CeO_2 and CuO/Cryptomelane catalyst by separate, Chapter 8 aims to compile main relevant outcomes from the separate studies, while providing at the same time, further coordinate characterization results for the sake of their direct benchmarking.

8.2 Experimental Section

The synthesis of CuO/Cryptomelane and CuO/CeO_2 catalysts (5% wt. Cu) was conducted according to procedure detailed in Section 2.1.1 from Chapter 2, which is repeatedly followed all along the Project Thesis.

Both prepared materials were tested in CO-PROX catalytic tests according to the experimental settings and specific conditions as stated in Section 2.2.3, which include stability tests upon cyclability in the set of conditions: CO+H_2+O_2; CO+H_2+O_2+CO_2; CO+H_2+O_2+H_2O; and CO+H_2+O_2+CO_2+H_2O, conducted by means of the introduction, either separated or together, of 9% CO_2 and 5% H_2O in the reactant gas mixture feeding.

CuO/Cryptomelane and CuO/CeO_2 catalysts were characterized in fresh and spent samples by means of several techniques as presented in Chapter 2. Namely, N_2 adsorption at -196ºC for the assessment of textural properties (Section 2.2.2.1); X-Ray Diffraction (XRD) for the crystalline characterization (Section 2.2.2.2); Temperature Programmed Reduction with H_2 (H_2-TPR), as explained in Section 2.2.2.4; and Temperature Programmed Desorption (TPD) experiments, CO_2-, H_2O-, and CO_2+H_2O-TPD, as detailed in Section 2.2.2.5.

Finally, results from isotopic $^{36}O_2$ pulse experiments conducted over CuO/CeO_2 and CuO/Cryptomelane are herein presented and discussed. Instrumental details and specifications regarding these experiments were exposed in Section 2.2.4.3.

8.3 Results

8.3.1 CO-PROX activity tests

8.3.1.1 Effect of CO_2, H_2O and CO_2+H_2O

Figure 8.1 gathers the CO-PROX activity results in a first run in different set of experimental conditions for CuO/CeO_2 and CuO/Cryptomelane catalysts in Figures 8.1a,b) and 8.1c,d) respectively. Accordingly, the inhibiting effect of CO_2, H_2O and CO_2+H_2O mixture in the reactor feeding stream into each catalyst is observed.

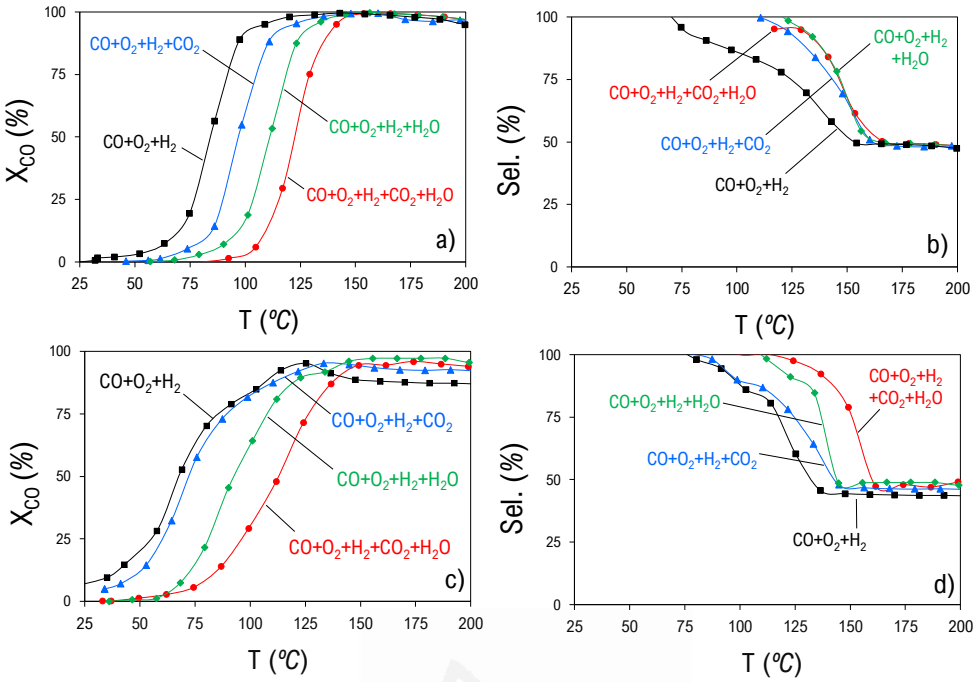

Figure 8.1. CO-PROX activity results in terms of **(a,c)** CO conversion (%); and **(b,d)** CO selectivity (%) with **(a,b)** CuO/CeO_2; and **(c,d)** CuO/Cryptomelane catalysts.

As thoroughly discussed along Chapter 6, the CO-PROX catalytic activity of CuO/Cryptomelane is not much affected by CO_2 presence, but is highly sensitive to H_2O, and the combined CO_2+H_2O feeding is the most detrimental condition, as expected. The irregular S-shape of the CO conversion profiles is tentatively assigned to structural and redox redistributions in the CuO/Cryptomelane catalyst along the reaction course, while in CO_2+H_2O conditions this observation is not applicable provided the major stability of the catalyst. The CO selectivity profiles are affected by H_2O presence, showing a sharper lowering after H_2 oxidation reaction *on-set* as inhibitor of H_2 oxidation reaction in H_2O and CO_2+H_2O conditions.

On the contrary, for CuO/CeO_2 catalyst, the CO conversion profiles presented in Figure 1a show for the whole set of tested conditions identical well-defined sigmoidal shapes but moved along the temperature range according to their particular degree of inhibition, which correlates as follows: CO_2 < H_2O < CO_2+H_2O. On the other hand, the presence of CO_2, H_2O and CO_2+H_2O mixture in the feeding shifts equally the CO selectivity profiles shown in Figure 1b which appear overlapped in these three conditions. That is to say, the CO/H_2 competition is kept constant with independence of whether CO_2 or H_2O is present, which is an interesting remark that leads to the conclusion that the main inhibition mechanism is due to surface blocking rather than thermodynamic aspects of the oxidation reactions by equilibria shifting, in contrast with CuO/Cryptomelane catalyst.

Thus, in agreement to the discussion presented in Chapter 4, CO_2 forms in a large extent stable carbonate, formate and bicarbonate species in

the CuO/CeO_2 catalyst surface that would hinder interfacial Cu – Ce interaction and eventually block active sites for both CO and H_2 oxidation. In the first case, because of the decrease in the abundance of partially reduced Cu^+ species (CO oxidation active sites) as a result of the hampered Cu – Ce interaction; and in the second case, because the stabilization of carbonaceous surface groups would prevent catalyst reduction up to Cu^0 state (H_2 oxidation site).

On the other hand, it is expected that H_2O may be massively physisorbed as molecular water, besides forming surface hydroxyls that would partially reduce the CeO_2 surface. According to the discussion presented in Chapter 4, the presence of surface hydroxyls turns in positive for CO oxidation activity at low temperatures by the preferential formation of hydrogen-based carbonaceous species with lower thermal stability and faster active site release. However, the presence of ample OH-covered surfaces is detrimental, apart from the surface blocking and reactants limited access, by the large reduction extension of the CeO_2 surface, which shifts the redox Cu^{2+}/Cu^+ - Ce^{3+}/Ce^{4+} interplay stabilizing Cu^{2+} with regard to Cu^+. Hence, despite the presence of surface Ce(III) cations is generally attributed to be positive since the concomitant formation of O vacancy defects, which induce a higher oxygen mobility and eventually more active oxygen, the Ce(IV) reduction by OH formation does not bring such positive consequence as the extra electron is well-located in the Ce^{3+} –O– H ends.

Additionally, comparing the results of CO_2 and H_2O addition into CO-PROX conversion profiles, H_2O causes more damage to CO conversion than CO_2, which proves the very large affinity of the basic CeO_2 surface to get hydroxylated and covered by water molecules. Finally, the combined CO_2+H_2O addition to the reactor leads to the worst performance, being additive the detrimental effects of their individual action, probably, as in the case of CuO/Cryptomelane, because of the major surface coverage provided by the enhanced CO_2/H_2O co-adsorption [2].

Universidad de Alicante

8.3.1.2 Catalysts stability in CO-PROX reaction conditions

The stability and cyclability of CuO/CeO_2 and CuO/Cryptomelane catalysts was evaluated conducting several reaction runs in the different CO-PROX ambient conditions. Figures 8.2a and 8.2b show the temperature for the 50% of CO conversion (T_{50}) along 4 catalytic runs without pre-treatment in between.

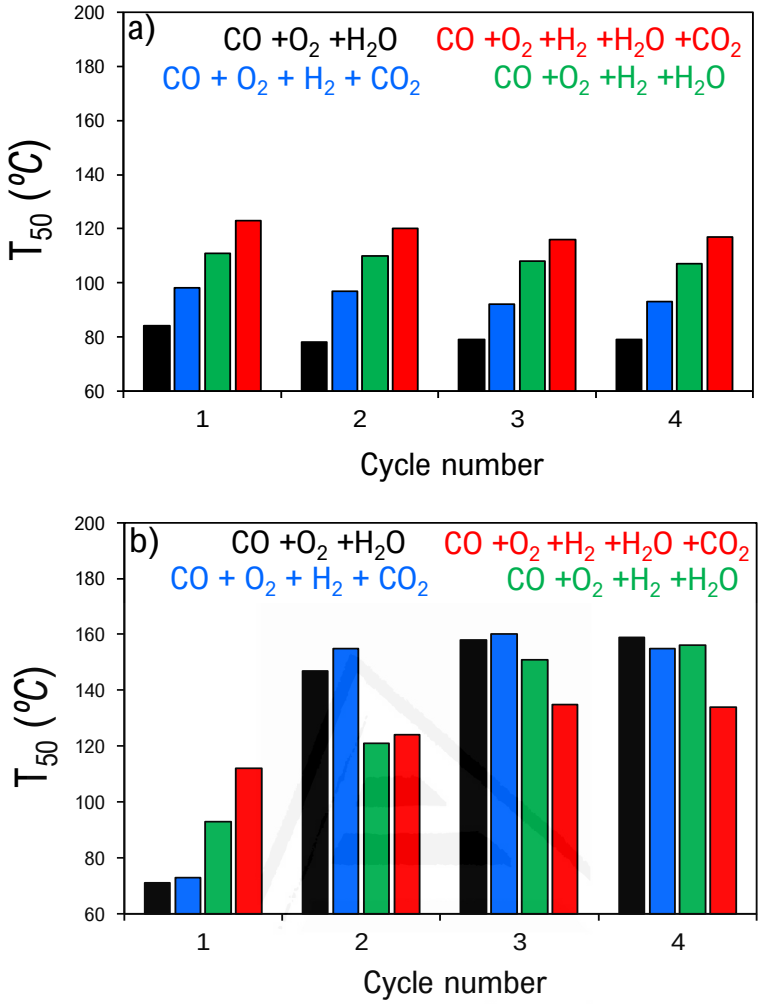

Figure 8.2. Temperature for the 50% of CO conversion (T_{50}) in 1-4 cycles of CO-PROX reaction in different environment mixtures with **(a)** CuO/CeO_2; and **(b)** CuO/Cryptomelane catalysts.

Comparing in qualitative view Figures 8.2a and 8.2b, CuO/CeO_2 presents a stable behavior along 4 cycles of reaction for each and every condition tested, whereas CuO/Cryptomelane suffers from a deactivating process of different magnitude depending on the reaction environment, as thoroughly detailed in Chapter 5. In particular, at the first run CuO/Cryptomelane presents an enhanced catalytic activity with regards to CuO/CeO_2, which is evidenced by a lower T_{50} for all the set of conditions. However, the severe deactivation of CuO/Cryptomelane and the excellent stability of CuO/CeO_2 lead to the opposite trend after the second cycle of reaction. Thus, when CuO/Cryptomelane reaches a stationary performance on its cyclability, CuO/CeO_2 presents a better performance. Nevertheless, as it was concluded in Chapter 7, the catalytic performance of CuO/Cryptomelane in the, apparently, most detrimental conditions (CO_2+H_2O), representative of real CO-PROX reaction operation, allows to achieve relevant CO conversion and CO selectivities in the convenient

temperature ranges of this application, overcoming the catalytic performance than when free of both or either CO_2 or H_2O.

This particular feature of CuO/Cryptomelane, attributed to an enhanced stability of Cryptomelane material with CO_2+H_2O presence in CO-PROX reaction environment, leads to a comparable performance to CuO/CeO_2 in the same reaction settings, which are the most detrimental. As a result, CuO/Cryptomelane catalyst is a potential competitor to CuO/CeO_2 when real CO-PROX operation conditions are tested, including CO_2 and H_2O in the reactor feeding stream, although CuO/CeO_2 still presents an improved performance.

This conclusion leads to important consequences since Cryptomelane material is inexpensive, natural and abundant, and therefore is not involved in any environmentally-damaging extraction process as it occurs with cerium-based materials under the umbrella of geopolitical RE metal interests. Therefore, new opportunities for Cryptomelane-based catalyst may arise given its multiple advantages and its excellent performance in real conditions of CO-PROX operation.

In order to shed some more light in the inhibition mechanism and CO_2/H_2O relative affinities of both CuO/CeO_2 and CuO/Cryptomelane catalysts, temperature programmed desorption experiments are presented in next Section.

8.3.2 Temperature Programmed Desorption (TPD) experiments

Figure 8.3 shows the TPD profiles for CuO/CeO_2 and CuO/Cryptomelane after different conditioning pre-treatments, namely: CO_2 saturation (CO_2-TPD), H_2O saturation (H_2O-TPD) and CO_2+H_2O saturation (CO_2+H_2O-TPD). Results corresponding to CuO/Cryptomelane were previously presented in Figures 6.3 from Chapter 6.

Universidad de Alicante

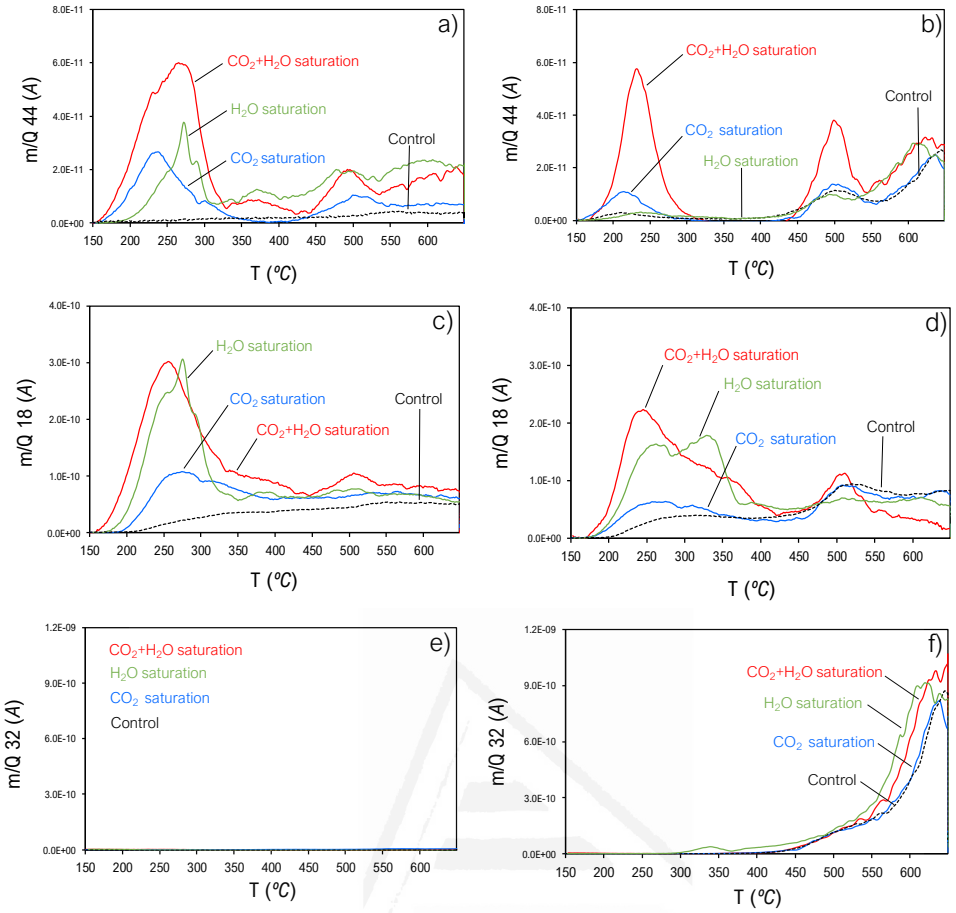

Figure 8.3. Monitored MS signals **(a,b)** 44, CO_2; **(c,d)** 18, H_2O; and **(e,f)** 32, O_2 for **(a,c,e)** CuO/CeO_2; and **(b,d,f)** CuO/Cryptomelane catalysts in CO_2-TPD; H_2O-TPD and (CO_2 + H_2O)-TPD experiments.

Comparing CuO/CeO_2 with CuO/Cryptomelane, it is evidenced in Figures 8.3a-f how CuO/CeO_2 is thermally more stable, since the control experiment (with no saturation pre-treatment) presents a flat product release. Moreover, no O_2 is released in the heating up to 650ºC (Figure 3e), in contrast with CuO/Cryptomelane (Figure 8.3f) which starts decomposing above 450ºC to Mn_2O_3 [5].

Firstly, CO_2 saturation pre-treatment turns into a larger CO_2 release, which is compatible with the more basic nature of CeO_2 support and its great capacity to stabilize carbonaceous species on surface. On the other hand, H_2O product is also observed after this treatment, in a non-coupled release with regards to CO_2, which could be explained by the forced hydroxyl decomposition upon carbonate formation by CO_2 contact.

Nevertheless, in the opposite way this effect is maximized since H_2O saturation pre-treatment leads to a larger CO_2 release than even after CO_2 treatment. Interestingly, this CO_2 desorption is retarded with regard to CO_2-TPD profile, but coupled with H_2O desorption, which could be tentatively ascribed as the decomposition of bicarbonate species formed when intrinsic

and stable carbonates in CeO_2 surface interact with incoming H_2O molecules. Thus, H_2O interaction in CuO/CeO_2 catalyst forces CO_2 release of stable carbonates, and such effect is even more clearly observed in the concomitant $CO_2 + H_2O$ saturation mixture, leading to the maximum product evolution in CO_2/H_2O coupled profiles, in analogy with CuO/Cryptomelane. Therefore, it may be a common feature for both the preferential formation of bicarbonate species or hydrogenated carbon intermediates as carboxylates, or formates when CO_2 and H_2O co-adsorb in the catalytic surface. In the case of CuO/Cryptomelane, its low affinity towards CO_2 chemisorption leads a very impressive growth in CO_2 release, driving to the conclusion that bicarbonates can be stabilized into cryptomelane acidic surface, but not much carbonates, in contrast with CeO_2.

As a result, TPD experiments prove that CuO/CeO_2 catalyst presents a great thermal stability and a higher sensitivity to CO_2 and H_2O exposure, accommodating easily carbonates, adsorbed water and other intermediate products upon the saturation treatments. The larger product emission when compared to CuO/Cryptomelane, indicates that CuO/CeO_2 is more susceptible to surface blocking upon CO_2 and H_2O pre-treatments, from which the latter shows most intense effect. This trend explains the catalytic activity observed in the first cycle in the different conditions tested for CuO/CeO_2, where H_2O leads to a larger inhibition than CO_2, and it should be attributed to a higher surface blockage. In contrast, acid Cryptomelane surface has no affinity to retain CO_2, for which the catalytic performance of CuO/Cryptomelane catalyst is not much affected by CO_2 presence, whereas H_2O is deactivating in a large extent.

On the other hand, to study in detail the reason for the different evolution of the catalytic activity along cycles for CuO/CeO_2 and CuO/Cryptomelane in each of the experimental settings tested, physicochemical characterization of fresh and spent samples is presented in the following section. For the sake of brevity, only the used samples from the tests in $CO+O_2+H_2$ and $CO+O_2+H_2+CO_2+H_2O$ conditions were analyzed, besides the fresh samples.

8.3.3 Physicochemical characterization of fresh and spent samples

8.3.3.1 X-Ray diffraction (XRD)

Figures 8.4a and 8.4b show XRD results from CuO/CeO_2 and CuO/Cryptomelane fresh and spent samples.

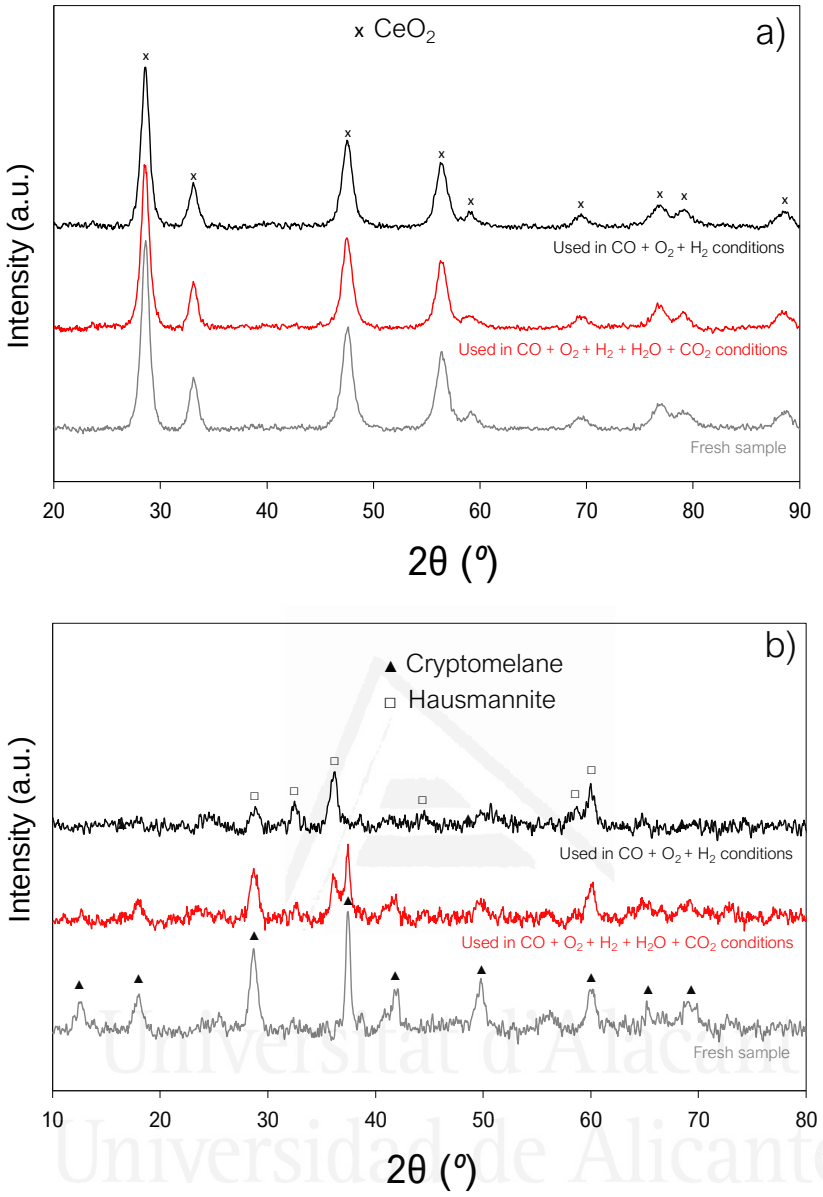

Figure 8.4. X-Ray diffractograms for **(a)** CuO/CeO_2 and **(b)** CuO/Cryptomelane fresh and used catalysts.

Figure 8.4a exhibits a clear stable maintenance of CuO/CeO_2 catalyst crystalline structure, displaying a typical X-Ray diffractogram of CeO_2 fluorite lattice. The presence of CuO tenorite phase is not detected in any case, for which significative CuO sintering is tentatively ruled out. On the other hand, as Table 8.1 displays, there are no important differences in the crystallite size calculated by means of Debye-Scherrer equation [6–8] and Williamson-Hall (WH) [9,10], and the calculated lattice parameter correlates well with the characteristic CeO_2 cell unit. In conclusion, CuO/CeO_2 is stable and presents identical crystalline features before and after reaction.

Table 8.1. Crystallographic features of CuO/CeO_2 samples fresh and used in different conditions. Scherrer calculations and lattice constant "a" are referred to (111) peak from cubic fluorite structure.

CuO/CeO_2 sample	Lattice constant (nm)	Crystal Scherrer (nm)	Crystal size WH (nm)
Fresh	0.5392	10	14
Used in CO+O_2+H_2 conditions	0.5401	9	15
Used in CO+O_2+H_2 +CO_2+H_2O conditions	0.5411	10	14

On the contrary, CuO/Cryptomelane displays a poor stability upon CO-PROX reaction course in CO + O_2 + H_2 conditions, where Mn_3O_4 hausmannite phase is the main crystalline phase detected by XRD. As previously explained in detail in Chapter 6, cryptomelane structure is not stable upon reduction and oxidation cycles ongoing during CO-PROX reaction mechanism. However, the co-addition of CO_2 + H_2O to the CO-PROX gas reactant mixture leads to an improved stability of cryptomelane phase, that also results in the best catalytic performance at the forth cycle.

The ratio between the intensities of (211) peaks from cryptomelane phase centred at 37.45º and (211) from hausmannite centred at 36.1º, allows to roughly measure the degree of transformation. Table 8.2 also shows the calculated crystallite size using Scherrer equation for the (211) peak and cell parameters (a) and (c) according to cryptomelane tetragonal unit cell for the fresh and used samples. Both parameters correlate well with reported values of cryptomelane structure (α-MnO_6), being (a) 9.866 A; and (c) 2.872 A [11]. In the case of Mn_3O_4 lone phase observed in CuO/Cryptomelane used sample in CO + O_2 + CO conditions, the cell parameter values fit as well with reported literature [12].

Table 8.2. Crystallographic features of CuO/Cryptomelane samples fresh and used in different conditions. % α-MnO_2 calculated by peak intensity ratios Scherrer calculations are referred to (211) peak from tetragonal phase.

CuO/Cryptomelane sample	% α-MnO_2	Crystallite size Scherrer (nm)	"a" (nm)	"c" (nm)
Fresh	100	17	9.811	2.861
Used in CO+O_2+H_2 conditions	0	11	-	-
Used in CO+O_2+H_2 +CO_2+H_2O conditions	60	19	9.828	2.869

Universitat d'Alacant
Universidad de Alicante

8.3.3.2 *Temperature Programmed Reduction with H_2 (H_2-TPR)*

The interaction strength and synergistic effect from CuO and the support in CuO/CeO_2 and CuO/Cryptomelane catalyst can be determined by means of reducibility studies provided by H_2-TPR for the fresh and spent samples, as shown in Figures 8.5a and 8.5b.

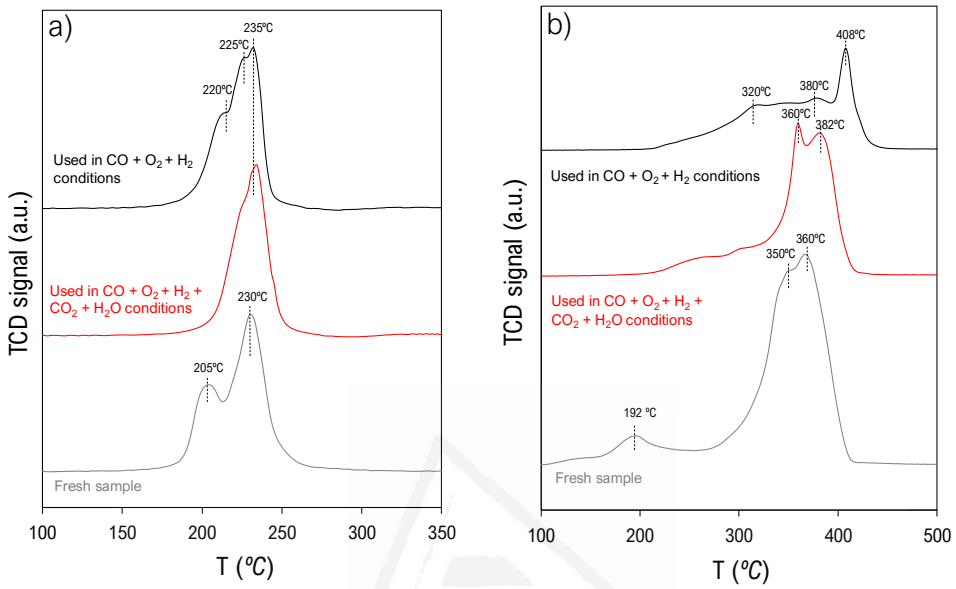

Figure 8.5. H_2-TPR profiles for **(a)** CuO/CeO_2 and **(b)** CuO/Cryptomelane fresh and used catalysts.

Regarding Figure 8.5a, the reduction profiles for CuO/CeO_2 catalyst are presented only for the low temperature region, where CuO and the promoted surface Ce^{4+} reduction take place in two separate peaks that may be assigned to (1) finely dispersed CuO particles and (2) bulky CuO particles in concomitant reduction with interfacial Ce^{4+} ions [13]. The profiles of the used CuO/CeO_2 samples show slight differences, which evidences changes in Cu – Ce interaction after the CO-PROX reaction cycles, by shifting the low temperature peak towards higher temperatures. The shifting is much more obvious in the sample used in CO_2 + H_2O conditions, where the low temperature peak is overlapped under the evolved high temperature peak. These results provide hints of certain CuO sintering or Cu – Ce contact modification upon reaction course. Nevertheless, partial reduction of the fine CuO nanoparticles cannot be ruled out.

On the other hand, the reduction profiles for CuO/Cryptomelane samples exhibit large differences depending on the catalyst state, which were discussed in detail in Chapter 6. The characteristic H_2-reduction profile of CuO/Cryptomelane catalyst with anticipated reduction of CuO particles and MnO_2 reduction in two steps towards MnO has been previously described and well-reported [1]. Thus, whereas the spent sample in CO_2 + H_2O conditions shows discrepancies with fresh sample, such as the

disappearing CuO reduction event, the manganese reduction events roughly keep the shape and position along temperature profile. However, for the sample used in the experiments free of CO_2 + H_2O, the reduction profile presents a very different aspect, which can be attributed to the cryptomelane phase distortion and reduction towards hausmannite phase, in agreement with XRD results. Therefore, important crystalline and structural changes occur in the CuO/Cryptomelane catalyst undergoing CO-PROX reaction, and CO_2 + H_2O conditions prevent from such deactivating processes.

In conclusion, the physicochemical characterization of fresh and used catalysts confirms the great stability of CuO/CeO_2, while provides insights into the CuO/Cryptomelane deactivation mechanism. On the contrary, CuO/CeO_2 catalyst is active, selective and perfectly stable despite the slight differences observed, which do not reflect into activity loss after CO-PROX cyclability tests. The real opportunities for CuO/Cryptomelane catalyst in real CO-PROX operation would depend on the overcome of several challenges in terms of the maintenance of cryptomelane integrity, as proven in Chapter 5, a reoxidation treatment at high temperatures is a solution that partially hinders this deactivation process, as well as the presence of CO_2 + H_2O in the reactor environment [2].

Finally, in order to complete this critical review analysis for the comparison of CuO/CeO_2 and CuO/Cryptomelane catalyst, the mechanism of CO-PROX reaction is studied using $^{36}O_2$ isotopic pulse experiments, results presented and discussed in the following section.

8.3.3 Isotopic $^{36}O_2$ pulse experiments

Pulse oxygen isotopic experiments in CO-PROX conditions: 1% CO, 50% H_2 in 20 ml/min balanced He flow over 80 mg of catalyst were conducted at critical temperatures for both CuO/CeO_2 and CuO/Cryptomelane samples and the results are presented in Figure 8.6 and Figure 8.7, respectively. Regarding Figure 8.6, the results corresponding to the study over CuO/CeO_2 catalyst have been previously shown in Chapter 3, but for comparatively reasons are presented again in this section.

As discussed in Chapter 3, CuO/CeO_2 catalyst displays a behaviour typical for Mars-van Krevelen (MVK) mechanism, involving non-isotopic lattice oxygen in the CO oxidation and H_2 oxidation mechanisms at the three studied temperatures. The distribution of products CO_2 to H_2O ratios correlates well with the selectivity profiles observed during fixed-bed catalytic tests, being fully selective to CO oxidation at 75ºC, and the following decay with regards to H_2 oxidation at the rising temperature. On the other hand, the effect of the temperature towards the exchange capacity is not much relevant, given the narrow range of temperatures tested, resulting in a constant but high exchange capacity and the formation of mainly non-isotopic products. As commented previously in Chapter 3, whereas $^{20}H_2O$ is not detected, the release of $^{18}H_2O$ is observed in delay with regards to CO_2

products, which is attributed to major desorption limitations of H_2O from the surface of CeO_2.

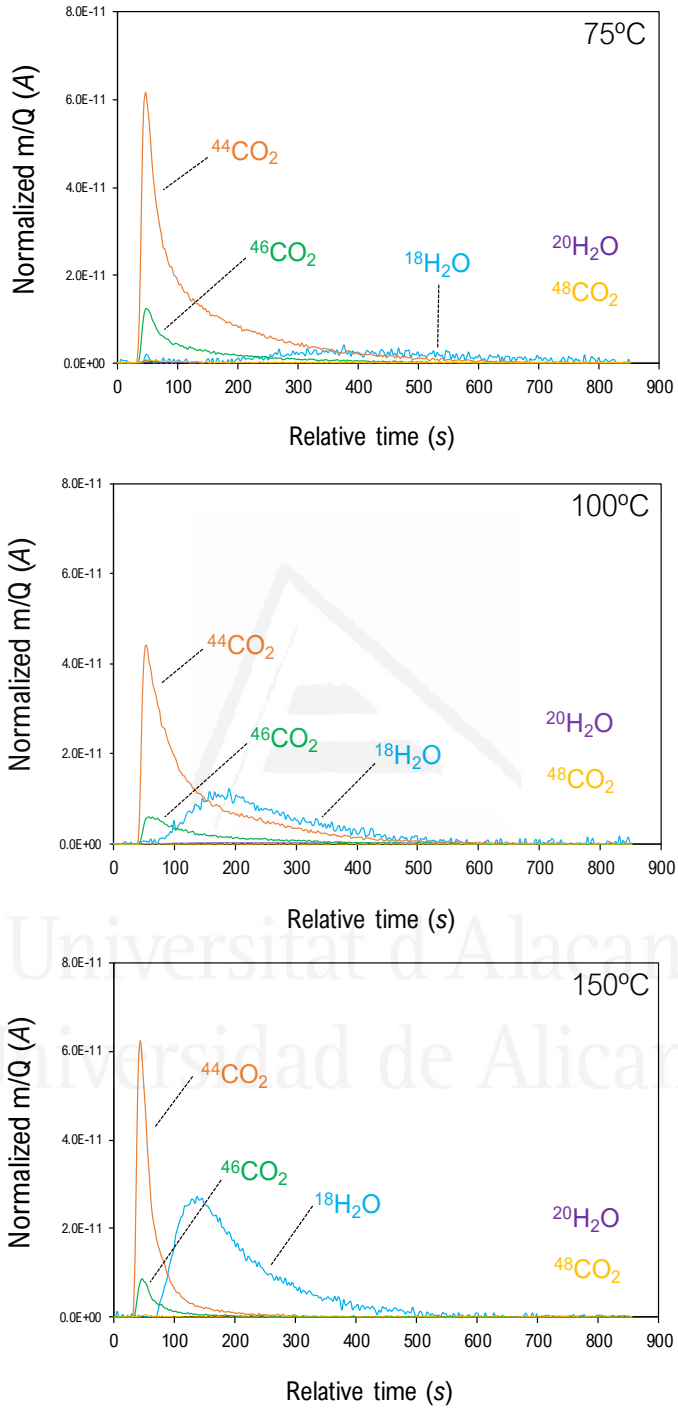

Figure 8.6. MS monitored signals after $^{36}O_2$ pulses in CO-PROX conditions with CuO/CeO_2 catalyst at 75, 100 and 150ºC.

Worth to mention that for all the tested temperatures, O_2 signals were not detected after the pulses, which indicates that the oxygen-poor environment of the experiments in the highly reducing $CO+H_2$ atmosphere

leads to a great population of anionic vacancies creation into the CuO/CeO_2 catalyst. In this state, the catalyst absorbs the pulse of $^{36}O_2$, accommodating oxygen into the lattice and recovering partially the network, which eventually destabilises the adsorbed CO and H_2 molecules, and produces their oxidation in the adsorption sites with non-isotopic lattice oxygens.

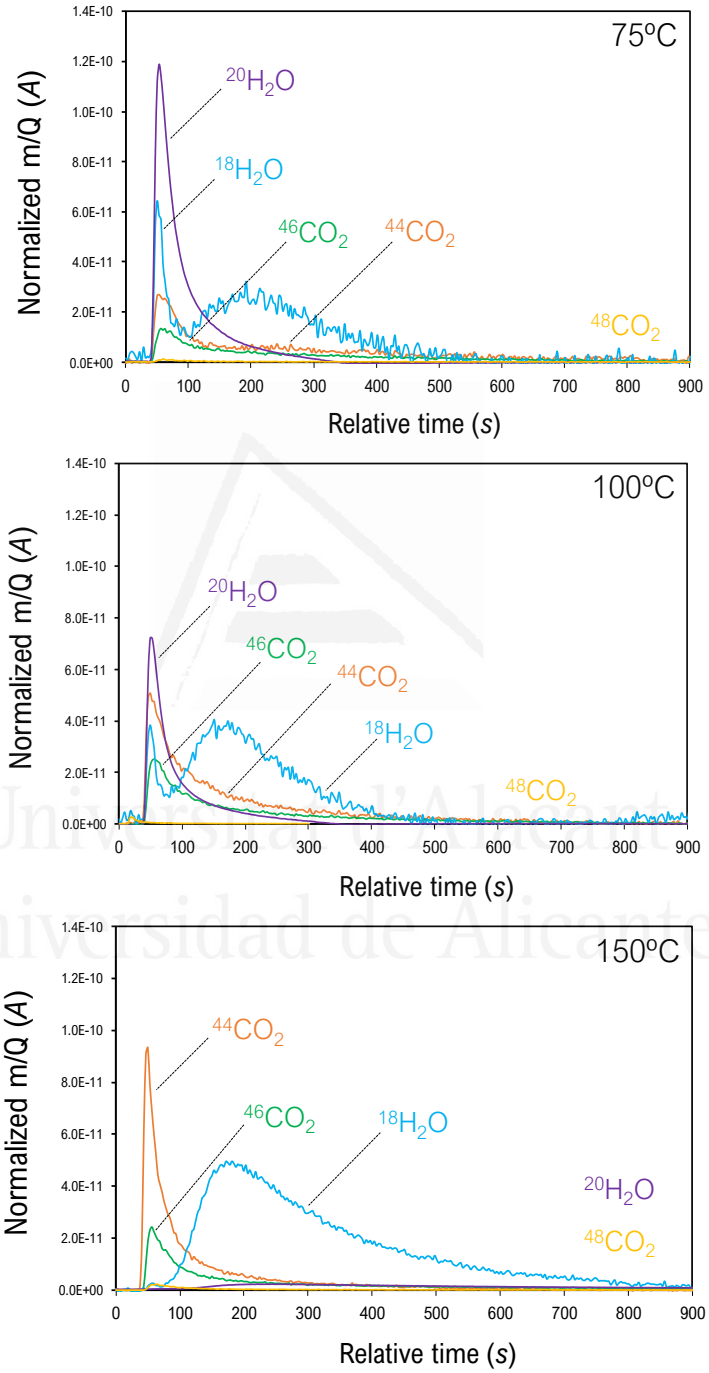

Figure 8.7. MS monitored signals after $^{36}O_2$ pulses in CO-PROX conditions with CuO/Cryptomelane catalyst at 75, 100 and 150ºC.

On the contrary, Figure 8.7 shows analogue results obtained for the CuO/Cryptomelane isotopic pulse experiments, and significative differences with regards to CuO/CeO_2 are observed. In order to accurately interpret and discern CuO/CeO2 and CuO/Cryptomelane behaviour, the MS signals were integrated and normalized in terms of total O species (CO_2 + H_2O + O_2) after the pulse.

Figures 8.8a and 8.8b present for CuO/CeO_2 and CuO/Cryptomelane, respectively, the integrated signals for the released products from H_2O and CO_2 formation upon H_2 and CO oxidation after the pulse (solid symbols), as well as the overall outlet H_2O, CO_2 and O_2 measured (open symbols). Hence, CO_2 and H_2O product distribution ratio is more complex for CuO/Cryptomelane and relevant differences arise according to the pulse temperature.

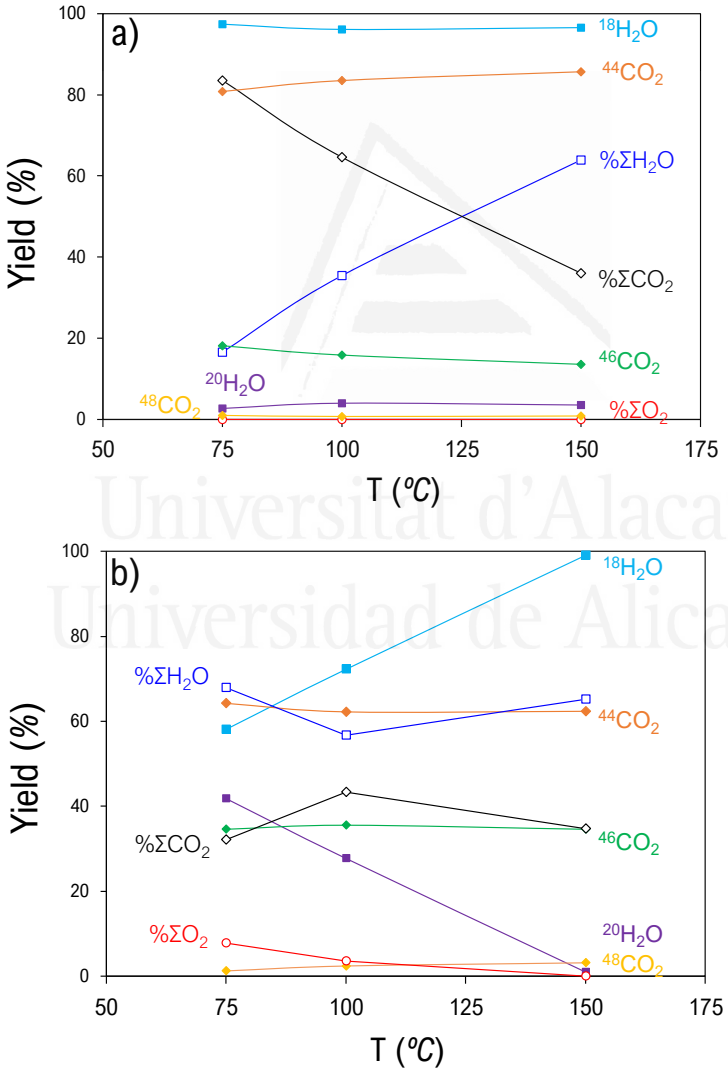

Figure 8.8. MS integrated signals after $^{36}O_2$ pulse in CO-PROX conditions with CuO/CeO_2 catalyst at 75, 100 and 150ºC. **Open symbols:** normalized overall released products (ΣX): CO_2 **(diamonds)**; H_2O **(squares)**; and O_2 **(circles)**. **Solid symbols**: isotopic distribution among CO_2 **(diamonds)** and H_2O **(squares)** species. **(a)** CuO/CeO_2; **(b)** CuO/Cryptomelane.

Universitat d'Alacant
Universidad de Alicante

The release of a large amount of H_2O at low temperatures disrupts the well-correlated CO selectivity profiles of pulse experiments to fix-bed catalytic tests as in CuO/CeO_2 catalyst. Furthermore, the distribution of CO_2 and H_2O products is a mixture between isotopic and non-isotopic, rather than clearly non-isotopic as for CuO/CeO_2, which demonstrates the poorer oxygen exchange capacity of CuO/Cryptomelane.

In agreement with such statement, in contrast with CuO/CeO_2, CuO/Cryptomelane releases O_2 species after the pulse, which evidences its lower re-oxidation capacity and, thus, lower oxygen mobility. In this regard, Figure 8.9 displays the amount of O_2-type species after the pulse for CuO/Cryptomelane catalyst, and it shows that it is only at 150ºC when all the pulsed O_2 is absorbed by the catalyst into the recovery of lattice oxygen.

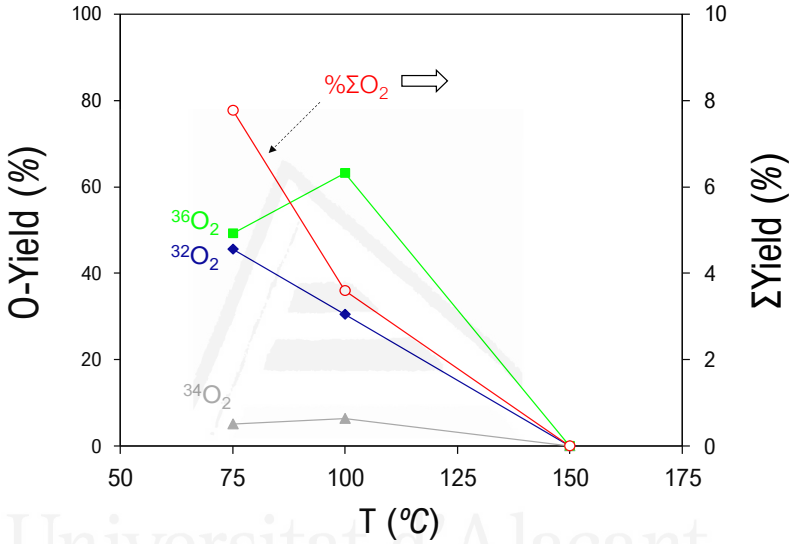

Figure 8.9. MS monitored normalized signals after $^{36}O_2$ pulses in CO-PROX conditions with CuO/Cryptomelane catalyst at 75, 100 and 150ºC. **(Solid symbols):** overall O_2 released species in the outlet flow; **(open symbols):** isotopic distribution among H_2O and CO_2 species.

Meanwhile, from 75 to 100ºC, the release of O_2 species is lowered and the isotopic contribution grows, suggesting major O_2 absorption that does not result in an apparent exchange capacity improvement with the low temperature increase. Compared to CuO/CeO_2, which does not present evolved O_2 signals after the pulses, CuO/Cryptomelane has much less active O_2 mobility, being unable to accommodate the integrity of the incoming O_2 molecules in its oxygen-deficient crystalline network by the highly reducing conditions of the experiment. Additionally, most of the O_2 released is of isotopic nature, originally coming from the $^{36}O_2$ pulse, confirming the lower oxygen exchange capacity of CuO/Cryptomelane.

Therefore, most of incoming isotopic $^{36}O_2$ molecules react with the highly abundant surface hydroxyl groups present by the effect of H_2-rich environment, producing isotopic $^{20}H_2O$ that is quickly released and detected

in the MS in very important proportion. On the other hand, the O_2 pulse destabilizes HO and H_2O molecules formed upon O lattice interaction, resulting in a significative non-isotopic $^{18}H_2O$ co-emission. Interestingly, two contributions of $^{18}H_2O$ release can be discerned, being the first anticipated and concomitant with $^{20}H_2O$ and CO_2 release, and the second, delayed, in analogue manner, to H_2O released when CuO/CeO_2 catalyst pulse experiments. These results must be compared to H_2O-TPD profiles (Figure 8.3d), where CuO/Cryptomelane would exhibit two types of H_2O release in the low temperature region, attributed to surface-related water and water bounded inside the 2 x 2 tunnels.

In this case, since the release of surface H_2O is retarded because of its limited desorption rate when compared to CO_2, as it occurs in CuO/CeO_2 catalyst, the first H_2O contribution must be tentatively assigned to intratunnel water molecules, that quickly partially exchange part of O with incoming $^{36}O_2$ molecules, resulting in a sharp co-emission of $^{18}H_2O$ and $^{20}H_2O$ coupled to O_2 pulse. As it was studied previously, the great activity of CuO/Cryptomelane catalyst is related to the presence of highly mobile water species hosted in the tunnels, which provide good ionic mobility and stabilize the cryptomelane framework. Thus, it is unfair to conclude preliminary that CuO/Cryptomelane has a much poorer oxygen exchange capacity, since its crystalline nature and activity depend on such intratunnel-bounded H_2O molecules, as partial O exchange in water is indeed observed.

As a final remark, the lowering of anticipated H_2O release with the rising of temperature is in agreement with XRD and TPR characterization, which suggest cryptomelane collapse towards the formation of the average reduced Mn_3O_4 spinel phase, probably by the massive water loss in the redox cycles suffered in CO-PROX reaction conditions. So that, when temperature is higher in the reducing CO-PROX conditions of the pulse experiments, the CuO/Cryptomelane catalyst is more reduced and consequently, the amount of released water decreases, until at 150ºC, cryptomelane is in overall reduced. In such state, such intra-tunnel water species are not found or the remaining keep so tightly bounded that are not mobilized after the pulse.

It is only at 150ºC when outlet water comes only from H_2 oxidation reaction, and, in comparison with CuO/CeO_2, the release of such delayed H_2O release has a clear more important contribution in the overall $CO_2 + H_2O$ distribution products, as shown in Figure 8b. This apparent lower CO selectivity of CuO/Cryptomelane has to be critically rationalized, given the large affinity of CuO/Cryptomelane for water and the strong driving force for its favored release in the highly reducing conditions of the experiment.

Nevertheless, the isotopic CO_2 components are free of this masking effect from cryptomelane intrinsic water, and compared to CuO/CeO_2, CuO/Cryptomelane exhibits less contribution for the non-isotopic $^{44}CO_2$ species, that is, lower participation in the Mars van Krevelen mechanism, and accordingly, less active lattice oxygen species.

As a result, whereas CuO/CeO_2 promotes catalyst reoxidation with the incoming O_2 pulse molecules, being efficiently absorbed in the anionic lattice vacancies, CuO/Cryptomelane exchanges in first instance, O from intratunnel labile water molecules, and is unable to accommodate the integrity of O_2 pulse provided its lower ionic mobility. Thus, at 75 and 100ºC, the O uptake from the pulse is high, but not 100%, since the preferred interaction with intratunnel water molecules with regards to O lattice restoration in the MnO_6 octahedra framework. In this scenario, only once the catalyst is fully reduced, cryptomelane accommodates or consumes the whole O_2 species from the pulse, but the temperature is high enough so that in this condition, the non-selective regime still leads to a very large H_2O emission with regards to CO_2, and therefore, H_2O products are always majority in CuO/Cryptomelane, in contrast with CuO/CeO_2.

These results provide interesting conclusions and evidence the very important role of the intratunnel water species in the catalytic activity of CuO/Cryptomelane material. These are, not only the reoxidation key sites, but also the oxygen labile species in cryptomelane framework and the stabilizing anchors beside K intratunnel species. Therefore, when H_2O is supplied (or co-supplied next to CO_2) in the reactor feeding for the CO-PROX catalytic tests, CuO/Cryptomelane keeps better performance along catalytic cycles, given its faster reoxidation capacity by the H_2O restitution. Nevertheless, a positive complementary effect of CO_2 cannot be ruled out since the best performance at the forth cycle occurs in CO_2 + H_2O conditions, as shown in Figure 8.2b. A possible explanation is the promotion of the H_2O retention capacity and the maximization of H_2O interaction with cryptomelane surface when H_2O and CO_2 are co-supplied, as TPD results in Figure 8.3b show. According to this, CO_2+H_2O saturation leads to the preferential formation of low temperature desorbed water (150-300ºC) in detrimental to the higher temperature desorbed water contribution (300-375ºC), previously attributed to surface water and intratunnel water, respectively. In a critical overview, it may be inferred that CO_2 presence aids to stabilize intratunnel water, preventing its release after CO_2 + H_2O contact with regards to lone H_2O, and thus, cryptomelane structure stability is improved. The characteristic redox features is better maintained with the co-addition of CO_2, as well as CO_2 retention is enlarged in the stabilization of hydrogen-carbonated intermediates. This substantial coating of labile carbonaceous intermediates with an ease desorption should protect O-lattice abstraction and cryptomelane reduction upon CO and H_2 oxidation reactions, resulting in a hindered activity, but eventually a greater stability.

8.4 Conclusions

The catalytic performance and CO-PROX occurring mechanism in CuO/CeO_2 and CuO/Cryptomelane catalysts have been compared in the present Chapter, as a convergent study of the particular insights obtained in

the separate studies presented along previous chapters in this Project Thesis. The overview of this direct comparison allows to stablish important conclusions regarding the critical use for CO-PROX operation of both promising materials, which are herein collected in the following lines:

(1) In a first cycle of CO-PROX reaction, the catalytic activity of CuO/CeO_2 and CuO/Cryptomelane catalysts is comparable, being both excellent materials for this application even in real operation conditions, including $CO_2 + H_2O$ in the feeding stream.

(2) Initially, the individual effect of the additive inhibitors depends on the degree of the interaction with the catalytic surface both. Whereas in CuO/CeO_2 both CO_2 and H_2O act inhibiting by surface blockage, where H_2O has more impact in the catalytic inhibition; CuO/Cryptomelane is not significatively affected by CO_2 presence but strongly inhibited by H_2O. In any case, the co-supply of $CO_2 + H_2O$ leads to the most detrimental activity.

(3) The most important differences between CuO/CeO_2 and CuO/Cryptomelane arise when successive catalytic runs without pretreatments in between are conducted. Meanwhile in CuO/CeO_2, the activity is well maintained along 4 catalytic cycles in all tested conditions, CuO/Cryptomelane suffers from severe deactivation related to structural collapse and partial reduction from cryptomelane phase (MnO_2) to haussmanite (Mn_3O_4), and the extent of such deactivation is dependent on the inlet gas mixture.

(4) $CO_2 + H_2O$ conditions prevent CuO/Cryptomelane decomposition and allow to obtain for this catalyst the best performance at the forth cycle when the CO-PROX inhibiting effect is maximum and CuO/CeO_2 exhibits its worst behavior.

(5) CuO/Cryptomelane is tentatively claimed to be a potential competitor to CuO/CeO_2 and possesses great positive qualities as a promising catalyst towards CO-PROX reaction in real operation conditions.

(6) According to $^{36}O_2$ isotopic pulse experiments, a key element of cryptomelane good oxidation activity is the molecular water bounded in the tunnels, which turn into quick oxygen exchange sites and species, in contrast with CuO/CeO_2, which presents excellent O_2 uptake features by means of intrinsic high oxygen mobility.

(7) The relative participation of lattice oxygen in the mechanism of reaction (Mars van Krevelen contribution) is much more important in CuO/CeO_2 catalyst, evidenced by the larger emission of non-isotopic products after the pulses, whereas in CuO/Cryptomelane, incoming O_2 molecules preferentially interact with the labile H_2O species hosted in the tunnels.

(8) A relevant feature to be considered for the good catalytic activity maintenance of CuO/Cryptomelane is the presence of H_2O, for the restoration of intratunnel stabilizing species, in spite of the contrary negative effect by the inhibition of surface coverage.

(9) Far from inhibiting the catalytic performance, CO_2 inlet enlarges the positive effect of H_2O in CO_2 + H_2O conditions, attributed to an improved H_2O retention capacity by means of the formation of hydrogen carbonate species. These species firstly inhibit by surface blockage but hold a role in the enhanced retention of H_2O intratunnel molecules that result very positive at preventing the catalyst deactivation.

(10) As a final conclusion, Chapter 8 has shed some light in the potential opportunities of CuO/Cryptomelane catalyst towards CO-PROX reaction in real operation conditions. Nevertheless, the excellent catalytic behavior of CuO/CeO_2 has not been reached by CuO/Cryptomelane even in the most convenient comparable conditions (CO_2 + H_2O in the forth catalytic cycle), given the proficient intrinsic performance of CuO/CeO_2 catalyst.

For this reason, the large scalability studies of CO-PROX reaction with high space velocity tests using 3D-printed cordierite monoliths, presented in Chapter 10, CuO/CeO_2 has been selected as the active phase, in order to guarantee a good stability and the possibility to successfully focus on the effect of monolithic shape and the adequation of the mechanism of reaction.

References

[1] A. Davó-Quiñonero, M. Navlani-García, D. Lozano-Castelló, A. Bueno-López, CuO/cryptomelane catalyst for preferential oxidation of CO in the presence of H_2: Deactivation and regeneration, Catal. Sci. Technol. 6 (2016) 5684-5692.

[2] A. Davó-Quiñonero, D. Lozano-Castelló, A. Bueno-López, Unexpected stability of CuO/Cryptomelane catalyst under Preferential Oxidation of CO reaction conditions in the presence of CO_2 and H_2O, Appl. Catal. B Environ. 217 (2017) 459-465.

[3] A. Davó-Quiñonero, M. Navlani-García, D. Lozano-Castelló, A. Bueno-López, J.A. Anderson, Role of Hydroxyl Groups in the Preferential Oxidation of CO over Copper Oxide-Cerium Oxide Catalysts, ACS Catal. 6 (2016) 1723-1731.

[4] R.N. DeGuzman, Y.F. Shen, E.J. Neth, S.L. Suib, C.L. O'Young, S. Levine, J.M. Newsam, Synthesis and characterization of Octahedral Molecular Sieves (OMS-2) having the hollandite structure, Chem. Mater. 6 (1994) 815–821.

[5] T. Gao, M. Glerup, F. Krumeich, R. Nesper, H. Fjellvâg, P. Norby, Microstructures and spectroscopic properties of cryptomelane-type manganese dioxide nanofibers, J. Phys. Chem. C. 112 (2008) 13134-13140.

[6] P. Scherrer, Bestimmung der Größe und der inneren Struktur von Kolloidteilchen mittels Röntgenstrahlen, Nachrichten von Der Gesellschaft Der Wissenschaften Zu Göttingen, Math. Klasse. 1918 (n.d.) 98–100.

[7] A.W. Burton, K. Ong, T. Rea, I.Y. Chan, On the estimation of average crystallite size of zeolites from the Scherrer equation: A critical evaluation of

its application to zeolites with one-dimensional pore systems, Microporous Mesoporous Mater. 117 (2009) 75–90.

[8] M. Jamshidijam, R. V Mangalaraja, A. Akbari-Fakhrabadi, S. Ananthakumar, S.H. Chan, Effect of rare earth dopants on structural characteristics of nanoceria synthesized by combustion method, Powder Technol. 253 (2014) 304–310.

[9] G.K. Williamson, W.H. Hall, X-ray line broadening from filed aluminium and wolfram, Acta Metall. 1 (1953) 22–31.

[10] C. Bueno-Ferrer, S. Parres-Esclapez, D. Lozano-Castelló, A. Bueno-López, Relationship between surface area and crystal size of pure and doped cerium oxides, J. Rare Earths. 28 (2010) 647–653.

[11] J. Vicat, E. Fanchon, P. Strobel, D. Tran Qui, The structure of $K_{1.33}Mn_8O_{16}$ and cation ordering in hollandite-type structures, Acta Crystallogr. Sect. B. 42 (1986).

[12] D. Jarosch, Crystal structure refinement and reflectance measurements of hausmannite, Mn_3O_4, Mineral. Petrol. 37 (1987) 15–23.

[13] J. Giménez-Mañogil, A. Bueno-López, A. García-García, Preparation, characterisation and testing of $CuO/Ce_{0.8}Zr_{0.2}O_2$ catalysts for NO oxidation to NO_2 and mild temperature diesel soot combustion, Appl. Catal. B Environ. 152–153 (2014) 99–107.

Universitat d'Alacant
Universidad de Alicante

CHAPTER 9

3D-printing technology for the fabrication of improved asymmetrical honeycomb monolith catalyst

Chapter 9 presents the study on the scalability of powdered copper-based active phases in medium-sized monolithic catalysts with unconventional designs prepared by means of 3D-printing technology. An improved honeycomb-like monolith with asymmetrical channels, where the channels section decrease along the monolith, was fabricated using a template prepared by 3D printing. A reference honeycomb monolith was also prepared in the same way but with conventional straight channels. Cu/Ceria active phase was loaded on these supports, and SEM-EDX, Raman spectroscopy and XRD showed that the supported active phase is similar on both monoliths. The supported catalysts were tested for CO oxidation in excess oxygen and for preferential CO oxidation in H_2-rich mixtures (CO-PROX), and the catalyst with the improved support achieved higher conversions in both reactions. The supported catalyst with asymmetrical channels has two benefits with regard to the counterpart catalyst with conventional symmetrical channels: improves the reaction rate with regard to the conventional one because fits better to the equation rate, and favors the turbulent regime of gases with regard to the laminar flow that prevails in symmetrical channels.

Davó-Quiñonero et al., *J. Hazard. Mater.* **368** (2019) 638-643

Universidad de Alicante

9.1 Introduction

Three dimensions (3D) printing is doing successful advances in topics like chemistry [1] or medicine [2-4], among others. Heterogeneous catalysts have been also successfully prepared by 3D printing in the last few years. For instance, Thakkar et al. printed zeolite monoliths [5], aminosilica monoliths [6] and metal−organic framework monoliths [7] for CO_2 removal, and Michorczyk et all. [8] used 3D-printed templates to prepare methane oxidation catalysts. Li et al. [9] prepared monoliths of MFI and FAU zeolites by 3D printing for catalytic cracking of n-hexane and Tubío et al. [10] printed Cu/Al_2O_3 monoliths for liquid-phase catalytic applications.

All these examples demonstrate that preparation of monolith catalysts is feasible by 3D printing, but it would be desirable to go a step further and use this technology to prepare catalysts that cannot be easily prepared by conventional procedures.

Conventional ceramic honeycomb monoliths are prepared by extrusion of a proper paste, obtaining a bundle of symmetric and parallel channels. After thermal stabilization of the monolith, the catalyst active phase is loaded on the channels surface, and all these preparation steps are already well optimized for commercial applications [11-15].

Manufacture of honeycomb supports by extrusion only permits fabrication of monoliths with parallel channels, but not monoliths with more complex designs. 3D printing opens new options for fabrication of substrates with higher freedom in the design [16], and in this line, Li et. al. [17] have recently reported the preparation of monolith catalysts with different channel networks using 3D-printing. Monoliths with straight and parallel cylindrical channels were prepared, which can be also prepared by extrusion, but also monoliths with tetrahedron and tetrakaidecahedron periodic structures. A Ni active phase was loaded on all these monoliths, concluding that he best catalytic results for syngas methanation are obtained in this case with monoliths with straight and parallel cylinders.

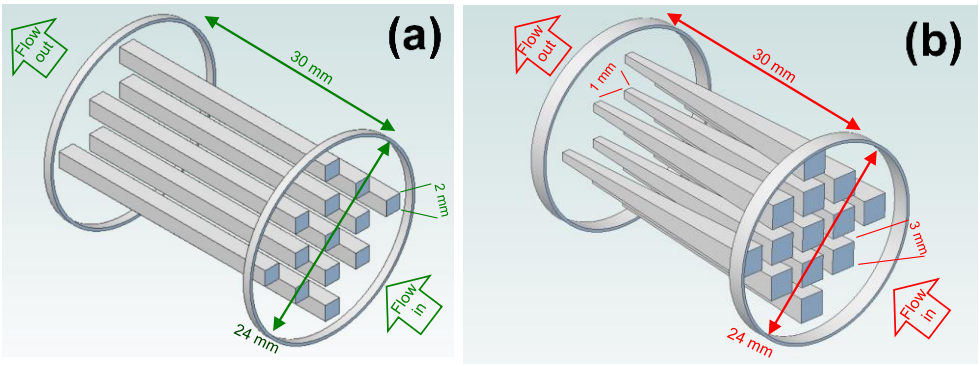

Figure 9.1. Scheme of channels for the (a) symmetrical and (b) asymmetrical monoliths designed and fabricated in this study.

In this Chapter, an improved honeycomb-like monolith has been prepared using 3D printing. This improved support consists of a honeycomb-like structure with asymmetrical channels (see Figure 9.1). Conventional and improved monoliths were prepared using 3D printing and were coated with the same active phase (5 wt. % Cu/Ceria). The catalysts were characterized and tested in two chemical reactions with practical relevance: CO oxidation in excess oxygen, which is relevant for gas pollution control, and preferential oxidation of CO in the presence of H_2 (CO-PROX), which is a topic of ongoing research for H_2 purification in fuel cells.

9.2 Experimental Section

9.2.1. Catalysts preparation

Two monolithic supports have been prepared, and their main design parameters are shown in Figure 1. The designs have been done with Cubify Invent software. Both monoliths consist of cylinders (length of 30 mm; diameter 24 mm) and 14 parallel channels. Channels of the symmetrical monolith have 2x2 mm square section and channels of the asymmetrical monolith have square section of 3x3 mm and 1x1 mm at the reactants inlet and outlet sides respectively. Note that, with these sections, the total area of the channels of both monoliths is equal (240 mm^2 per channel).

Polymeric templates with the designs shown in Figure 1 have been printed with a Project 1200 (3DSYSTEMS) 3D printer using ultraviolet curable polymer (Visijet FTX green). Both templates were filled with commercial cordierite paste (COR-MIK-MP) kindly provided by VICAR S.A. After drying, first at room temperature and at 80ºC overnight afterwards, the templates were removed by combustion in static air at 500ºC for 2 hours, using a heating rate of 1ºC/min. Cordierite was finally sintered in air at 1250 ºC for 2 hours upon heating at 3ºC/min.

The cordierite porosity was sealed with α-Al_2O_3 (Alfa Aesar) by dip coating [18], in order to avoid migration of the catalyst active phases into the cordierite body and to ensure that active phases are located on the channels surface. Both cordierite monoliths were dipped twice (once each side drying the monoliths in between) in α-Al_2O_3 water suspension (11 wt. %), and after drying, were calcined at 900ºC for 2 hours. The weight increase after calcination was 0.4 %.

The catalyst active phase, consisting of CuO/CeO_2, was loaded afterwards. Ceria powder was prepared by calcination of cerium nitrate (Alfa Aesar) at 500ºC for 4 hours and a water suspension with 10 g/ml was prepared with this powder. Both monoliths were dipped twice into this suspension (once each side drying the monoliths in between), and after

drying, were calcined at 600ºC for 2 hours. The ceria loading achieved after calcination was 2 wt. % in both monoliths.

Finally, CuO was loaded (5% wt. copper on ceria basis) by impregnating the monoliths with a copper nitrate water solution (0.4% wt.). The monoliths were dried rapidly just after impregnation in a muffle furnace pre-heated at 200ºC, to improve copper dispersion, and were calcined afterwards at 400ºC for 2 hours using a heating rate of 2ºC/min.

9.2.2 Catalysts characterization

The prepared catalysts on were characterized by means of SEM-EDS microanalysis for the elucidation of the thickness and dispersion the catalytic layers coating the monolithic substrates along the channels. Further details can be found in Section 2.2.2.8 from Chapter 2.

The crystalline nature of cordierite supports and the active CuO/CeO_2 phase were studied by means of XRD, as described in Section 2.2.2.2. Complementary crystalline characterization was conducted via Raman spectroscopy, as detailed in Section 2.2.2.3.

9.2.3 Catalytic tests

The effect of the monolith geometry in the catalytic conversion when reaction behaves under chemical rate control has been studied using CO oxidation in excess oxygen as model reaction [19-20], and when reaction behaves under external gas diffusion rate control has been studied using the CO-PROX as model reaction [21-22].

The catalytic experiments were carried out in a stainless-steel cylindrical using the experimental set-up presented Section 2.2.3, using GC for product gas separation coupled to TCD. In experiments in oxygen excess, the gas mixtures fed to the reactor was 1% CO + 17% O_2, whereas in CO-PROX experiments it was fixed 1% CO + 1% O_2 + 30% H_2, both with He balance. Mass flow controllers were used to prepare the inlet gas mixtures, and total gas flows were ranged from 400 to 700 ml/min.

In a typical experiment, the reaction gas mixture was fed to the reactor at room temperature for 30 min, and then the temperature was raised at 2ºC/min until 200ºC. Then, the reaction gas mixture was replaced by 5% O_2 in He, keeping this flow while cooling. After 15 minutes at 200ºC the furnace was switched off and the reactor was cooled down without control of the cooling rate. Following this protocol, several consecutive experiments were performed with total reproducibility of the catalytic results in the two catalytic reactions tested, confirming the stability of the catalyst active phase under both reaction conditions. This was expected for CuO/CeO_2 catalysts [23], and this is one of the reasons for the selection of this active phase.

9.3 Results and Discussion

9.2.3 Catalysts characterization

Figures 9.2 and 9.3 show representative SEM images of the monoliths with symmetrical and asymmetrical channels, respectively, and the chemical mapping obtained by EDS for Si, Al and Ce. In both SEM images, the catalyst coating is observed on the top of the images and a cordierite wall is shown at the bottom, as confirmed by EDS chemical mapping.

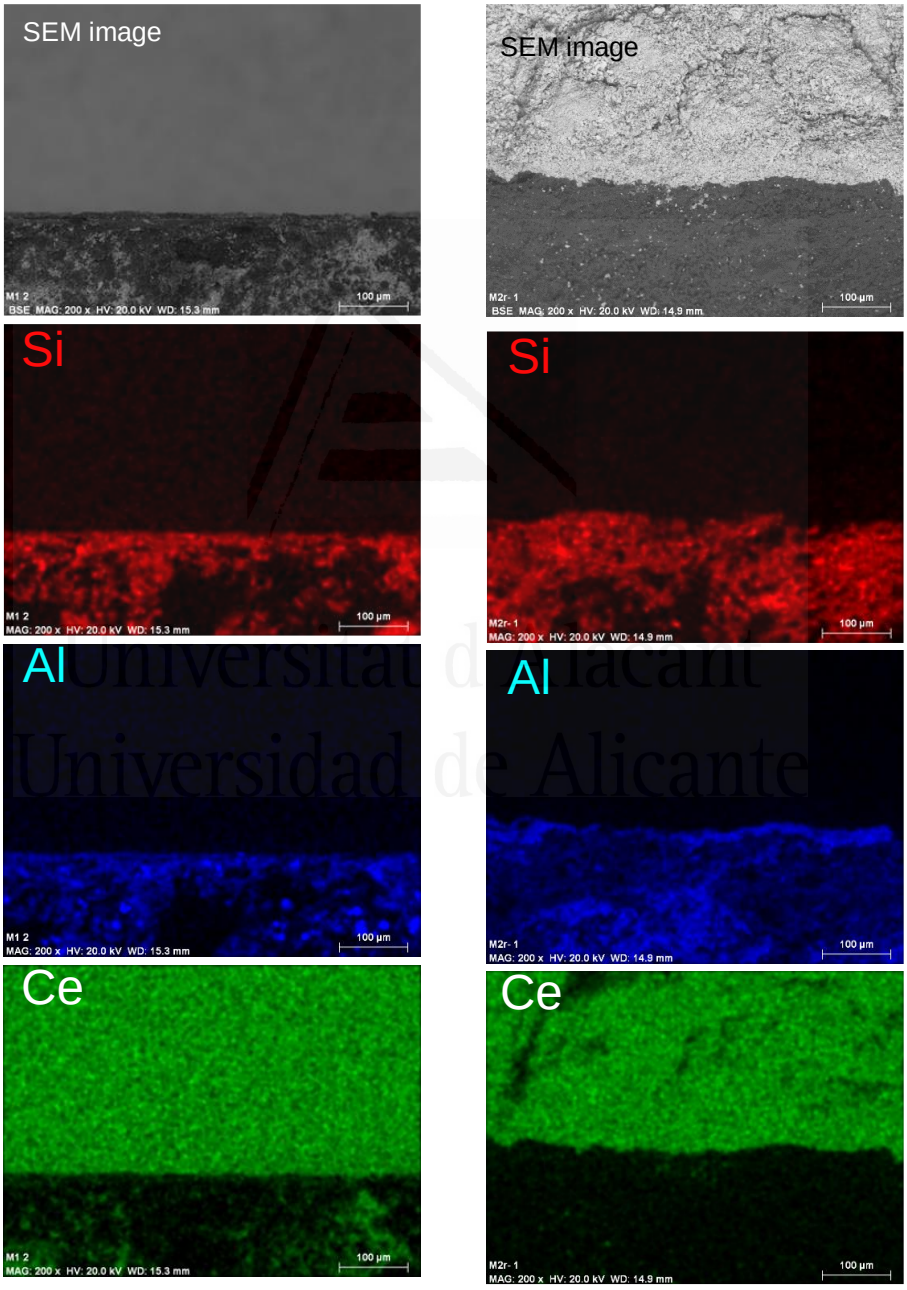

Figure 9.2. SEM-EDS characterization of the monolith catalyst with **(left)** symmetrical channels; **(right)** asymmetrical design.

Ce mapping confirms that the catalyst active phase forms a uniform layer on the cordierite surface and that the diffusion of catalyst active phase into the cordierite walls has been properly prevented. Si belongs to cordierite ($2MgO:5SiO_2:2Al_2O_3$), and Al belongs both to cordierite and to α-Al_2O_3 loaded before the catalyst active phase to seal the cordierite porosity. Al and Si occupy the same area in the images, confirming that the cordierite porosity was properly sealed.

In conclusion, differences in the catalyst active phase coating between the monoliths with symmetrical and asymmetrical channels were not observed by SEM-EDS.

The catalysts were also characterized by XRD, and the diffractograms are included in Figure 9.3. For this characterization, the monoliths were cut and the X-Ray spot was focused on the surface of the active phase layer.

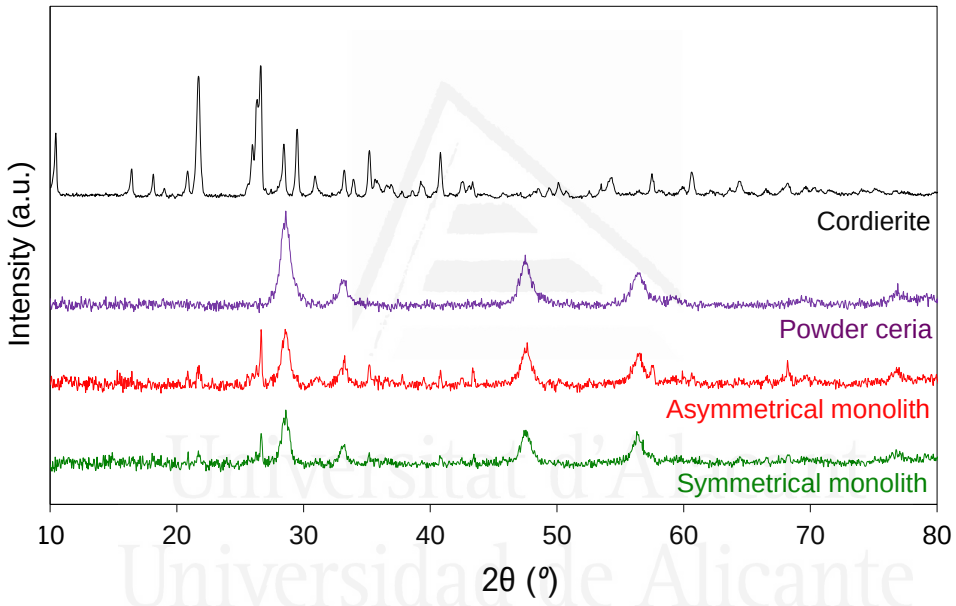

Figure 9.3. XRD characterization of the catalysts.

The X-ray diffractograms of the coated monoliths show the characteristic peaks of the fluorite structure of ceria at 28.5, 33.1, 47.6, and 56.5º, corresponding to the (111), (200), (220), and (311) planes, respectively (JCPDS-340394). Few peaks of cordierite are also shown in both diffractograms, and the CuO peaks that could appear at 35.5º and 38.8º are not observed, indicating that copper oxide is well dispersed on the ceria support forming small crystallites. Proper dispersion of copper oxide is usually obtained on ceria due to the strong interaction between both phases. The crystallite size of ceria was determined with the Scherrer equation, being 12 nm for both supported catalysts, and the lattice parameter is also equal in both samples (0.5401 nm). This lattice parameter value is similar to that reported in the JCPDS-340394 standard. This XRD characterization

suggests that there are not relevant differences in the crystalline phases supported on the monoliths with symmetrical and asymmetrical channels, as expected.

This conclusion was confirmed by Raman spectroscopy characterization. Raman spectra of the active phases, which are included in Figure 9.4, show a single band at 465.5 cm^{-1} that is assigned to the F_{2g} mode of the fluorite structure of ceria. This peak is related to the vibration of the oxide anions around its equilibrium position in the octahedral sites of the cubic cell. The position of the F_{2g} peak is the same for both monoliths, and this confirms that the ceria lattice is equal.

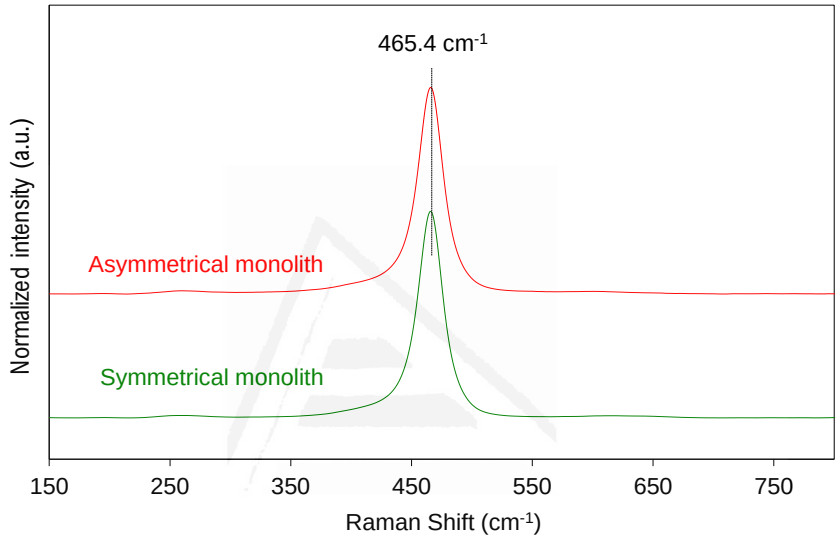

Figure 9.4. Raman characterization of the catalytic active phases.

In conclusion, SEM-EDS, XRD and Raman spectroscopy characterization indicate that the active phases are equal in the monoliths with symmetrical and asymmetrical channels, and therefore, differences in the catalytic behavior can be attributed to differences in the shape of the channels.

9.3.2 CO oxidation in oxygen excess

Figure 9.5 shows CO oxidation rates as a function of temperature obtained with the symmetrical and asymmetrical monoliths in oxidation experiments performed with excess oxygen, where it is demonstrated the benefit of the asymmetrical design with regard to the conventional symmetrical one.

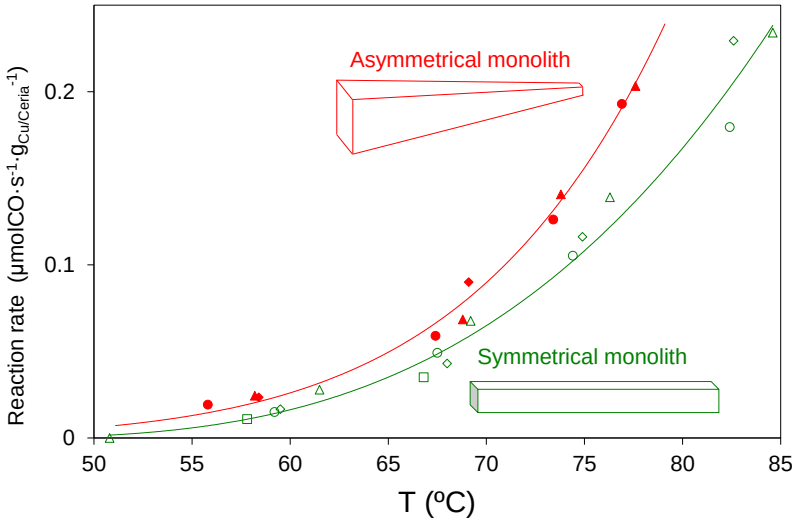

Figure 9.5. Reaction rate as a function of temperature for CO oxidation experiments performed with excess oxygen (1 % CO + 17 % O_2 in He) under different total gas flows (ml/min): ■ 400, ● 500, ▲ 600, ♦ 700. Rates were measured with CO conversions < 10%.

The improvement obtained with the asymmetrical monolith can be explained considering reaction kinetics. The kinetic equation to describe the CO oxidation rate under the experimental conditions of these experiments can be derived assuming that O_2 concentration remains constant during the reaction, since this reactant is feed in a large excess.

Therefore, CO oxidation to CO_2 can be considered generically like a chemical reaction where a gas A is converted to B:

the reaction rate is described by $A \xrightarrow{k} B$ Eq. 9.1

$$\text{Reaction rate} = -dP_A/dt = k \cdot P_A \quad \text{Eq. 9.2}$$

Where first order kinetic has been assumed for A, P_A is the partial pressure of A, k is the reaction rate constant and t is the reaction time.

Integration of equation 9.2 with the boundary conditions

$P_A = P_{A,initial}$ for $t = 0$ $P_A = P_{A,final}$ for $t = \tau$

yields equation 9.3

$$P_{A,final} = P_{A,initial} \cdot e^{-k \cdot \tau} \quad \text{Eq. 9.3}$$

which allows calculating the partial pressure of A ($P_{A,final}$) after a certain time under reaction conditions (τ) for a particular initial partial pressure of A ($P_{A,initial}$). The reaction rate can be calculated as a function of reaction time by substituting equation 9.3 in equation 9.2.

$$\text{Reaction rate} = k \cdot P_{A,initial} \cdot e^{-k \cdot \tau} \quad \text{Eq. 9.4}$$

This calculation predicts that the reaction rate decreases with time under reaction conditions, because the rate depends on the concentration of reactant A, and this reactant is consumed during the course of the reaction.

Considering a heterogeneous catalysis reaction taking place on a fluid that flows through a conventional honeycomb monolith, the reaction rate will be fastest when the fluid enters into the monolith and it will decrease along the channels, because the reactants are progressively depleted. In this system, the reaction time is the residence time of A inside the monolith, and for a constant gas flow, is proportional to the monolith length. The relationship between residence time (τ) and the average distance that a reactant molecule covers inside the channel (d) is described by equation 9.5

$$\text{Residence time } (\tau) = S \cdot d/F \qquad \text{Eq. 9.5}$$

where S is the channel section area and F is the gas flow. Substituting equation 5 in equation 3 yields

$$P_{A,final} = P_{A,initial} \cdot e^{-k \cdot S \cdot d/F} \qquad \text{Eq. 9.6}$$

Equation 9.6 predicts the decrease of the reactant A partial pressure along the monolith length as a function of the channels section, kinetic rate constant and gas flow. For conventional monoliths with symmetrical channels, section S remains constant along the channel. Nevertheless, for asymmetrical monoliths with different inlet and outlet sections, S changes along the channel.

As an example, equation 9.6 has been used to simulate the decrease of A partial pressure along channels of total length = 30 mm, comparing a conventional monolith with square section S with an asymmetrical monolith with channels of 2.25·S and 0.25·S inlet and outlet square sections, respectively. Note that these section areas are consistent with those in the monoliths prepared in this study using 3D printing, and with these section areas the total areas of the symmetrical and asymmetrical channels are equal. The A partial pressure profiles obtained with this simulation have been plotted on Figure 9.6 for the symmetrical and asymmetrical monoliths.

Universidad de Alicante

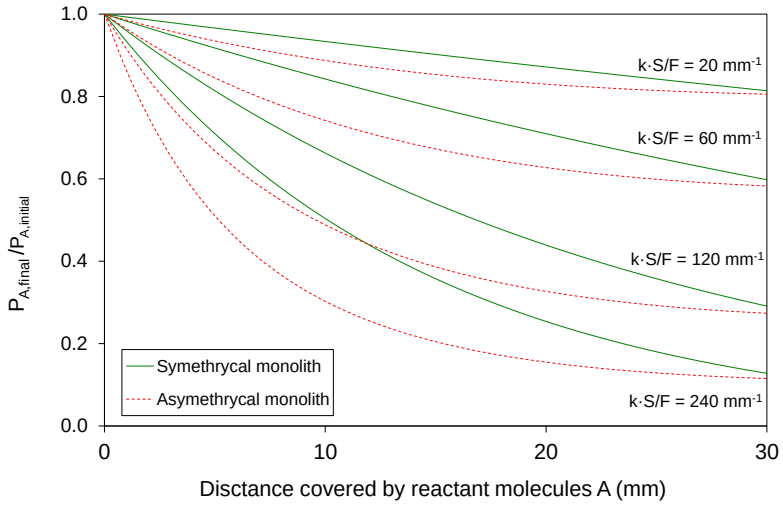

Figure 9.6. Qualitative simulation predicted by equation 6 of the reactant A partial pressure along channels of monolith reactors with symmetrical (conventional) and asymmetrical geometry. Settings for the simulation: symmetrical channels with square section S; asymmetrical channels with 2.25·S and 0.25·S inlet and outlet square sections, respectively. Monoliths length = 30 mm.

This simulation predicts that the asymmetrical monolith is more efficient than the symmetrical one, in agreement with the experimental results plotted in Figure 9.6, and for the same monolith length, the reactant conversion achieved with the asymmetrical monolith is predicted to be higher. As mentioned, honeycomb monoliths with asymmetrical channels cannot be prepared by convention extrusion procedures, but it is possible to use 3D printing for this purpose.

9.3.3 CO oxidation in CO-PROX conditions

The channels geometry also affects the fluid dynamics into the monoliths, and CO-PROX experiments were performed to analyze this effect. Figure 9.7 shows the CO conversions in CO-PROX experiments, where it is observed that the asymmetrical monolith achieves higher CO conversion than the symmetrical counterpart. Differences between both monoliths are observed above 130 ºC, once high CO conversions are achieved and external gas diffusion is expected to play a key role in the reaction rate.

Universitat d'Alacant
Universidad de Alicante

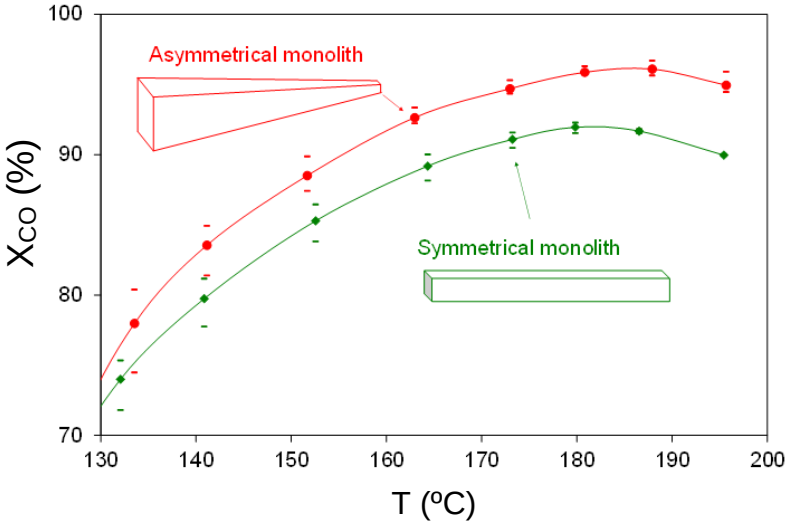

Figure 9.7. CO conversion as a function of temperature in CO-PROX experiments. (1% CO + 1% O_2 + 30% H_2; total gas flow: 700 ml/min).

This improvement of the asymmetrical monolith can be explained considering the fluid regime into the channels. A fluid flowing through the channels of a monolith can follow a laminar or turbulent regime, depending on the total fluid flow and geometry of the channels. Laminar flow occurs when viscous forces are dominant, and is characterized by smooth fluid motion, while inertial forces dominate the turbulent flow, which tend to produce chaotic movement of the molecules into the fluid. Radial diffusion of molecules is significantly improved under turbulent regime with regard to laminar flow, and this radial diffusion plays a role in the conversion whether a heterogeneous catalysis reaction behaves under diffusional control of the rate. The Reynolds number is a dimensionless parameter that predicts if the flow regime is laminar or turbulent depending on the space velocity, density and viscosity of a fluid and geometry of the pipe (channel in the case of a monolith) where the fluid flows through.

It has been proposed that the flow regime is laminar for Reynolds numbers below ~1800 and turbulent above ~ 4000 [27], with a transition regime in between where neither the viscous nor the inertial forces prevail. The Reynolds number for the symmetrical monolith and the CO-PROX mixture used in this study is lower than 100, indicating that the laminar flow clearly prevails. In the laminar regime, the reactant molecules flowing in the center of the channel have less chance to reach the catalyst active phase layer coating the channel surface than those flowing near the walls, and that is why gas diffusion limits the reaction rate for high conversions. At high conversion, the molecules near the walls have already reacted, and the last reactant molecules left are those in the channels center, which are affected by radial diffusion restrictions in the laminar regime.

Nevertheless, the asymmetrical channels break the laminar flow as the channel diameter becomes progressively narrow, and for this reason, the conversions achieved with the asymmetrical channels are higher than those obtained with the symmetrical ones, as observed in Fig. 9.7 for high conversions.

In summary, the theoretical calculations predict that an asymmetrical monolith improves both the reaction rate and the radial diffusion of the molecules in comparison with a symmetrical monolith, and the experimental results confirm these theoretical predictions.

9.4 Conclusions

3D printing has been used to prepare a honeycomb-like cordierite monolith with asymmetrical channels that improves the performance of conventional honeycomb catalyst supports. 3D-printing technology overcomes the limitations of conventional manufacture procedures based on extrusion and gives higher freedom in the design of monolith supports with complex shapes.

Channels section of the improved asymmetrical monolith are larger at the reactants entrance side than in the exit side, improving with regard to conventional monoliths both the reaction rate, when reaction behaves under kinetic rate control, and the radial diffusion of reactants, when reaction behaves under external gas diffusion rate control. As proof of concept, a Cu/Ceria active phase loaded on conventional and improved honeycomb monoliths has been used to accelerate CO oxidation in excess oxygen and preferential CO oxidation in H_2-rich mixtures.

Universidad de Alicante

References

[1] M.D. Symes, P.J. Kitson, J. Yan, C.J. Richmond, G.J.T. Cooper, R.W. Bowman, T. Vilbrandt, L. Cronin, Integrated 3D-printed reactionware for chemical synthesis and analysis, Nat. Chem. 4 (2014) 349-354.

[2] S.V. Murphy, A. Atala, 3D bioprinting of tissues and organs, Nat. Biotechnol. 32 (2014) 773-785.

[3] J.S. Miller, K.R. Stevens, M.T. Yang, B.M. Baker, D.T. Nguyen, D.M. Cohen, E. Toro, A.A. Chen, P.A. Galie, X. Yu, R. Chaturvedi, S.N. Bhatia, C.S. Chen, Rapid casting of patterned vascular networks for perfusable engineered three-dimensional tissues, Nat. Mater. 11 (2012) 768-774.

[4] B.C. Gross, J.L. Erkal, S.Y. Lockwood, C.P. Chen, D.M. Spence, Evaluation of 3D Printing and Its Potential Impact on Biotechnology and the Chemical Sciences, Anal. Chem. 86 (2014) 3240-3253.

[5] H. Thakkar, S. Eastman, A. Hajari, A.A. Rownaghi, J.C. Knox, F. Rezaei, 3D-Printed Zeolite Monoliths for CO_2 Removal from Enclosed Environments, ACS Appl. Mater. Interfaces 8 (2016) 27753-27761.

[6] H. Thakkar, S. Eastman, A. Hajari, A.A. Rownaghi, F. Rezaei, Formulation of Aminosilica Adsorbents into 3D-Printed Monoliths and Evaluation of Their CO_2 Capture Performance. ACS Appl. Mater. Interfaces 9 (2017) 7489-7498.

[7] H. Thakkar, S. Eastman, Q. Al-Naddaf, A.A. Rownaghi, F. Rezaei. 3D-Printed Metal−Organic Framework Monoliths for Gas Adsorption Processes. ACS Appl. Mater. Interfaces 9 (2017) 35908-35916.

[8] P. Michorczyk, E. Hedrzak, A. Wegrzyniak. Preparation of monolithic catalysts using 3D printed templates for oxidative coupling of methane. J. Mater. Chem. A 4 (2016) 18753-18756.

[9] X. Li, W. Li, F. Rezaei, A. Rownaghi. Catalytic cracking of n-hexane for producing light olefins on 3D-printed monoliths of MFI and FAU zeolites. Chem. Eng. J. 333 (2018) 545-553.

[10] C.R. Tubío, J. Azuaje, L. Escalante, A. Coelho, F. Guitián, E. Sotelo, A. Gil, 3D printing of a heterogeneous copper-based catalyst. J. Catal. 334 (2016) 110-115.

[11] V. Meille, Review on methods to deposit catalysts on structured surfaces. Appl. Catal. A, 315 (2006) 1-17.

[12] T.A. Nijhuis, A.E.W. Beers, T. Vergunst, I. Hoek, F. Kapteijn, J.A. Moulijn, Preparation of monolithic catalysts, Catal. Rev.: Sci. Eng. 43 (2001) 345-380.

[13] A. Cybulski, J. Moulijn, Monoliths in heterogeneous catalysis, Catal. Rev.: Sci. Eng. 34 (1994) 179-270.

[14] P. Avila, M. Montes, E.E. Miró, Monolithic reactors for environmental applications: A review on preparation technologies, Chem. Eng. J. 109 (2005) 11-36.

[15] T. Boger, A.K. Heibel, C.M. Sorensen, Monolithic Catalysts for the Chemical Industry, Ind. Eng. Chem. Res. 43 (2004) 4602-4611.

[16] Z. Eckel, C. Zhou, J.H. Martin, A.J. Jacobsen, W.B. Carter, T.A. Schaedler, Additive manufacturing of polymer-derived ceramics, Science 351 (2016) 58-62.

[17] Y. Li, S. Chen, X. Cai, J. Hong, X. Wu, Y. Xu, J. Zou, B.H. Chen, Rational design and preparation of hierarchical monoliths through 3D printing for syngas methanation, J. Mater. Chem. A 6 (2018) 5695-5702.

[18] A.F. Pérez-Cadenas, M.M.P. Zieverink, F. Kapteijn, J.A. Moulijn, High performance monolithic catalysts for hydrogenation reactions, Catal. Today 105 (2005) 623-628.

[19] X. Xie, Y. Li, Z.Q. Liu, M. Haruta, W. Shen, Low-temperature oxidation of CO catalyzed by Co_3O_4 nanorods, Nature 458 (2009) 746-749.

[20] S. Royer, D. Duprez, Catalytic Oxidation of Carbon Monoxide over Transition Metal Oxides, ChemCatChem 3 (2011) 24-65.

[21] E.D. Park, D. Lee, H.C. Lee, Recent progress in selective CO removal in a H_2-rich stream. Catal. Today 139 (2009) 280-290.

[22] G. Sedmak, S. Hoevar, J. Levec, Kinetics of selective CO oxidation in excess of H_2 over the nanostructured $Cu_{0.1}Ce_{0.9}O_{2-y}$ catalyst, J. Catal. 213 (2003), 135-150.

[23] A. Davó-Quiñonero, M. Navlani-García, D. Lozano-Castelló, A. Bueno-López, J.A. Anderson, Role of Hydroxyl Groups in the Preferential Oxidation of CO over Copper Oxide-Cerium Oxide Catalysts, ACS Catal. 6 (2016) 1723-1731.

Universitat d'Alacant
Universidad de Alicante

[24] G.L. Morini, M. Lorenzini, S. Salvigni, M. Spiga, Analysis of laminar-to-turbulent transition for isothermal gas flows in microchannels, Microfluid. Nanofluid. 7 (2009) 181-190.

Universitat d'Alacant
Universidad de Alicante

CHAPTER 10

General conclusions

Universitat d'Alacant
Universidad de Alicante

In this PhD Thesis, the Preferential CO Oxidation in presence of H_2 excess, so-called CO-PROX reaction has been studied with active copper-based materials from different chemical nature but analogue synergistic redox properties: namely CuO/CeO_2 and CuO/Cryptomelane. The work related in this Project Thesis comprises the preparation, full characterization, activity testing and CO-PROX mechanistic approach over both formulations, in order to unravel the key catalytic features for the sake of a deep understanding of the process and the critical evaluation of their real opportunities.

All along this PhD Thesis, specific conclusions have been presented on each research part as distributed in the different Chapters. As an outline compendium, these main research outcomes and most relevant achievements can be drawn in the following general conclusions:

1. From mechanistic studies over CuO/CeO_2 catalysts in CO-PROX reaction, it can be concluded that the CO oxidation rate accelerated by copper oxide-cerium oxide catalysts in CO-PROX conditions correlates to the formation of the Cu^+-CO carbonyl above a critical temperature, being copper carbonyl formation the rate limiting step. However, desorption of carbon products formed in the ceria surface is the slowest step below this threshold temperature. The hydroxyl groups on the catalyst surface play a key role in determining the nature of the carbon-based intermediates formed upon CO chemisorption and oxidation, whose abundance depends on the redox features of the CuO/CeO_2-based catalysts. Essentially, hydroxyls favor the formation of bicarbonates with respect to carbonates, and catalysts forming more bicarbonates reach faster CO oxidation rates than those which favor carbonates. All tested CuO/CeO_2-based catalysts exhibited good catalytic activity in CO-PROX reaction, although the presence of dopants (20% at.) on the ceria lattice produced in general detrimental effect on the optimum performance of pure CuO/CeO_2.

2. The fundamental study presented herein on CuO/CeO_2 catalyst with the use of cutting-edge experimental techniques and DFT modelling has disentangled the participation of CeO_2 support in lattice oxygen restitution during CO-PROX reaction progress. Namely, O_2 restoration takes place in CuO species when these are mostly oxidized, in the low temperature range. Then, CO-PROX reaction progress reduces Cu_XO particles in a gradual surface to "bulk" process by the lattice oxygen abstraction and CO_2 release. The accelerated CO oxidation by the increasing temperature leads to a critical reduced state over Cu_XO particles that activate the undesired competitive H_2 oxidation reaction, henceforward boosting at the same time, Cu_xO reduction to a much faster and larger extent. At such point of reducing state over Cu_xO particles, direct O_2 uptake is not efficient and preferentially occurs on CeO_2 support, which aids to O-restoration in the labile Cu – O – Ce redox joints. *Operando* CO-PROX NAP-XPS experiments revealed a

highly superficial reduction on CeO_2 and the nature of event has been associated with lattice oxygen transfer to Cu_xO particles during O-restitution via CeO_2.

3. The active enrolment of CeO_2 support in the catalyst reoxidation mechanism involves several implications that result in the improved performance of CuO/CeO_2 with regards to any other CuO-supported catalyst, allowing absolute reversibility upon reduction – oxidation cycles in the ongoing CO-PROX reaction.

4. Cryptomelane mineral is an abundant, non-toxic material with a scalable easy and reproducible laboratory synthetic preparation that presents promising opportunities as an active catalyst for CO oxidation and CO-PROX reaction. The physico-chemical properties of Cryptomelane in terms of high oxygen mobility and facile redox cycling among the different Mn oxidation states remind of CeO_2, with a well-known oxygen storage capacity (OSC) upon the quick electronic exchange between Ce^{3+}/Ce^{4+} pairs, so it is postulated as a promising potential substitute of CeO_2-based catalytic systems.

5. In the same line, when Cryptomelane is loaded with copper oxide, conforming CuO/Cryptomelane formulations, the catalytic activity in CO-PROX reaction is largely improved because of the enhancement of its redox features relying on the formation of active Cu – O – Mn entities, that lead to the promotion of labile oxygen species with good interaction with reactant CO molecules.

6. The improved activity of CuO/Cryptomelane with regards to Cryptomelane, is though, counteracted by a major stability loss and significative deactivation after CO-PROX reaction catalytic cycles. The study over CuO/Cryptomelane deactivation mechanisms suggested that Cryptomelane's basic micro-structure consisting of well-defined tunnelled arrangements (α-MnO_2) partially collapses into the inactive phases Mn_3O_4 and crystalline $CuMn_2O_4$, which involve an average reduction of manganese and copper species from initial CuO/Cryptomelane state. Thus, the redox promotion of Cu loading in CuO/Cryptomelane results positively in an activity gain for the MVK ongoing mechanism in CO-PROX reaction, but at the same time, its enhanced reducibility makes too easy lattice oxygen abstraction and CuO/Cryptomelane is eventually reduced and deactivated.

7. Potential regeneration strategies for CuO/Cryptomelane catalysts have been discussed, such as reoxidation pre-treatments in O_2 atmospheres at different temperatures, namely 200ºC and 400ºC. On the one hand, the treatment in O_2 at 200ºC was not efficient enough to restore significatively the activity over deactivated CuO/Cryptomelane, attributed to the large

stability of the inactive resulting Mn_3O_4 and $CuMnO_4$ phases. Hence, it was necessary to increase the pre-treatment temperature up to 400ºC to achieve sufficient reactivation, but at the same time, the catalyst suffered from CuO sintering and crystalline reorganization.

8. Surprisingly, and as a rare feature of CuO/Cryptomelane, the operation in CO-PROX real conditions, comprising CO_2+H_2O introduction in the reactant mixture led to an improved stability with regards to the more simple CO + O_2 + H_2 conditions. Therefore, with these settings including CO_2+H_2O, inhibitors considered universally detrimental for the catalytic activity in CO-PROX reaction, CuO/Cryptomelane exhibits, contrarily, an improved stability and catalytic activity once reached stationary performance after several catalytic cycles, which is a unique feature of this material and results very interesting from a practical point of view.

9. The improved performance of CuO/Cryptomelane catalyst in the CO-PROX mixture containing CO_2+H_2O elements was studied by means of different techniques that revealed that co-addition of these species largely increased chemisorption of both CO_2 and H_2O. Specifically, improving H_2O retention is relevant for the case of hydrophobic CuO/Cryptomelane material, since water molecules may be hosted in the intrachannel structure providing structure reinforecement while balancing forward oxidized states of manganese in the mixed potassium – (α-MnO_2) crystals.

10. Mechanistic studies on CuO/Cryptomelane catalyst based on non-conventional techniques have presented relevant conclusions with important similarities with those well-reported for CuO/CeO_2 catalyst, such as: (1) the participation of lattice oxygen in the CO-PROX reaction following MVK-type mechanism; (2) the identification of the CO oxidation reaction site in the partially reduced Cu species in the labile Cu – O – Mn bridges, as in Cu – O – Ce for CuO/CeO_2; (3) the role of the support in the assistance on the regeneration of lattice oxygen.

11. The excellent activity and stability of CuO/CeO_2 catalysts is not found for CuO/Cryptomelane, since Cryptomelane support is not so active at facilitating oxygen to Cu_xO particles, as demonstrated by a poorer oxygen exchange capacity by isotopic pulse experiments. Hence, reduction – reoxidation processes in CO-PROX reaction course remain imbalance and eventually lead to an average reduction with irreversible consequences on the activity of CuO/Cryptomelane.

12. Finally, as a proof of concept, 3D printing has been used to prepare a honeycomb-like cordierite monolith with asymmetrical channels that improves the performance of conventional honeycomb catalyst supports. 3D-printing technology overcomes the limitations of conventional manufacture

procedures based on extrusion and gives higher freedom in the design of monolith supports with complex shapes. Provided that the study was focused on the effect of monolith support design with complex shapes on the catalytic activity in CO-PROX reaction, CuO/CeO_2 catalyst was chosen as active phase in order to skip the complicated stability considerations inherent to CuO/Cryptomelane catalyst. Channels section of the improved asymmetrical monolith are larger at the reactants entrance side than in the exit side, improving with regard to conventional monoliths both the reaction rate, when reaction behaves under kinetic rate control, and the radial diffusion of reactants, when reaction behaves under external gas diffusion rate control.

Universitat d'Alacant
Universidad de Alicante

Universitat d'Alacant
Universidad de Alicante

Resumen en castellano

Estudio sobre catalizadores de óxido de cobre soportados para la reacción CO-PROX

Universitat d'Alacant
Universidad de Alicante

Introducción general

Actual problemática medioambiental

Actualmente vivimos en un mundo dinámico en pleno desarrollo industrial y tecnológico en el que las grandes potencias establecidas y los países emergentes consumen cada año más energía, principalmente obtenida a partir de combustibles fósiles (petróleo, carbón, gas natural), a pesar de que su uso lleva asociados una multitud de problemas. En primer lugar, la quema de estos recursos produce cantidades incontroladas de CO_2, gas involucrado en el calentamiento global a través del *efecto invernadero.* Pese a los compromisos internacionales y una mayor concienciación política, la emisión de CO_2 no deja de aumentar año tras año, lo que es origen de una severa preocupación medioambiental[1, 2]. En segundo lugar, la producción de contaminantes atmosféricos como NO_x, VOCs o SO_2, suma una importante problemática adicional asociada al uso de estos recursos, por los perjuicios que ocasionan en el medioambiente y en la salud de las personas.

Además de ello, debido a la irregular distribución de las reservas mundiales de combustibles fósiles se ha gestado una sólida dependencia energética hacia las potencias sustentadoras de estos recursos condicionando el panorama de desarrollo económico internacional. Y si se considera el hecho de que estas reservas se irán agotando, esta situación de dependencia puede desencadenar una grave crisis energética si no se perfeccionan soluciones alternativas a tiempo.

Hidrógeno como vector energético

Así pues, ante unos pronósticos que vaticinan un importante incremento de la demanda energética a nivel mundial en las próximas décadas, la búsqueda de formas de obtención de energía sostenible se convierte en un objetivo de prioridad máxima. En este contexto de exploración, el hidrógeno ha sido señalado por parte de la comunidad científica como la alternativa capaz de sustituir a los combustibles fósiles y generar la mayor parte de la energía del futuro, ya sea mediante combustión, o como alimentación a dispositivos electroquímicos especiales, como las pilas de combustible de membrana de intercambio protónico (*Proton Exchange Membrane fuel cell*, PEMFC).

Los argumentos que refuerzan esta tesis se basan en su alta exotermicidad de combustión, que lo convierte en el combustible de mayor capacidad de almacenamiento por unidad de masa. Idealmente, se podrían satisfacer las demandas energéticas de forma inextinguible, eficiente, libre de emisiones contaminantes y con un coste razonable, si se lograra superar las limitaciones actuales en la producción, almacenamiento y distribución de H_2[3]. Pero, aun siendo el elemento más abundante del universo, en nuestro planeta el H se encuentra siempre combinado con otros átomos como C, O ó N, y no en forma de gas diatómico, por lo que se precisa irremediablemente de un método por el cual se obtenga a partir de otras fuentes. Es por ello por lo que no se considera al H_2 como una fuente de energía, sino como un *vector energético.*

Rutas de producción y purificación de hidrógeno

De las opciones que se conocen para sintetizar hidrógeno, la electrólisis del agua es la ruta más limpia y la que produce un H_2 de más alta pureza, pero requiere del suministro de una gran cantidad de energía eléctrica, y el proceso no es ventajoso todavía sin el apropiado desarrollo de las energías renovables[4]. De ser posible su implantación extendida, se obtendría H_2 muy puro mediante un proceso completamente respetuoso con el medio ambiente. Sin embargo, hasta la fecha prácticamente la totalidad del H_2 producido procede de combustibles fósiles, y su uso lleva asociado una co-producción de CO_2 importante[5,6]. Aun así, se puede actuar capturando esas emisiones localizadas de forma eficiente para su almacenamiento y posterior transformación, con el fin de garantizar un proceso neto medioambientalmente muy sostenible[7,8]. A día de hoy, el método de producción de H_2 más empleado es el reformado de hidrocarburos con vapor de agua, por ser el más barato, a pesar de ser el método que más impacto medioambiental supone[1,3,9].

En la búsqueda de soluciones a corto-medio plazo en relación a los aspectos de su producción, hasta la rentabilidad de la electrólisis del agua, se pretende optimizar la eficiencia y reducir el impacto medioambiental de los métodos actuales para producir H_2, que emplean hidrocarburos como precursor. De entre ellos, el más extendido es el reformado con vapor (*Steam Reforming*, SR), reacción (1)[3,10-13]:

$$C_nH_m + n\,H_2O \rightarrow n\,CO + (n + 0.5m)H_2 \qquad \Delta H^0_{298ºK} >> 0 \qquad (1)$$

Como se expresa en la reacción (1), la producción de H_2 viene acompañada de un 10-15% de CO, mezcla conocida como *gas de síntesis*, intermediario en la generación de productos de gran importancia industrial, entre otros usos destacados. Sin embargo, cuando se tiene interés en la obtención de H_2 puro, este subproducto debe ser eliminado, por ejemplo, en la síntesis del amoníaco o en las PEMFC, cuyo electrocatalizador (Pt/C) se envenena con la presencia de CO. En estos casos, se requiere de etapas subsiguientes a la de reformado para la eliminación del CO hasta un nivel de tolerancia establecido[10-14].

En este sentido, a la reacción de reformado le sigue otra etapa catalítica conocida como reacción de desplazamiento de agua (*Water Gas Shift reaction*, WGS), reacción (2).

$$CO + H_2O \rightarrow CO_2 + H_2 \qquad \Delta H^0_{298ºK} = -41.2\ \mathrm{kJ/mol} \qquad (2)$$

Con ella, se reduce el CO en dos etapas, a alta temperatura (HTWGS) y a más baja temperatura (LTWGS) hasta un pequeño porcentaje en volumen de mezcla, y se incrementa la concentración de combustible. A la salida del reactor de WGS, la composición típica en volumen del caudal de salida es cercana al 0.5-1% de CO, pero aún así, ese pequeño porcentaje de CO afecta negativamente al funcionamiento de la PEMFC debido a la quimisorción preferente de CO sobre el Pt electródico[15]. Es por ello que el procedimiento requiere de una etapa adicional de purificación en la que se reduzca hasta la cantidad permitida de 10 ppm de CO la alimentación a la pila[14].

Para este propósito, existen 2 vías: (i) separación física del H_2, mediante procedimientos como la separación criogénica, adsorción a presión oscilante (*Pressure Swing Adsorption*, PSA), o la difusión selectiva, y (ii) transformación catalítica de CO, a CH_4 (*Selective Methanation*, SMET) o a CO_2 (*Preferential Oxidation*, PROX CO). De ellos, la ruta catalítica es la más conveniente para aplicaciones portátiles o a pequeña escala[10,11,13,14]. Ambos procedimientos, SMET y PROX CO han demostrado eliminar satisfactoriamente el CO residual del flujo de salida del reactor WGS. No obstante, de entre ellos, la oxidación preferente de CO es el más destacado, debido a un menor consumo no deseado de H_2 (menor pérdida eficiencia para la pila) aun siendo más difícil de ejecutar, dada la mayor exotermicidad de la reacción de oxidación y la necesidad de inyección controlada de un caudal supletorio de oxidante[6,16].

Reacción de Oxidación Preferente de CO (CO-PROX)

La reacción de PROX CO ha sido ampliamente estudiada debido a su gran interés. El aspecto más significativo es la reacción selectiva de un componente minoritario de la mezcla gaseosa (CO) frente a altas concentraciones de H_2, siendo ambos susceptibles de oxidarse, por lo que el desarrollo de un catalizador apropiado que se ajuste a las exigencias del proceso es indispensable. Así, las reacciones implicadas vienen descritas según las reacciones 3 y 4:

$$CO + \frac{1}{2}O_2 \leftrightarrow CO_2 \qquad \Delta H^0_{298ºK} = -283\ kJ/mol \qquad (3)$$

$$H_2 + \frac{1}{2}O_2 \leftrightarrow H_2O \qquad \Delta H^0_{298ºK} = -242\ kJ/mol \qquad (4)$$

Ambas reacciones son competitivas por el oxígeno suministrado, siendo la reacción (3) la única que interesa que suceda idealmente, puesto que la reacción (4) supone un consumo de H_2 (combustible de la pila). Adicionalmente, también pueden ocurrir en las condiciones de operatividad otras reacciones paralelas que pueden repercutir en la eficiencia neta del proceso, como la reacción WGS (2); reacción inversa WGS (RWGS), (5); metanación del CO, (6); o de CO_2[3,11]:

$$CO_2 + H_2 \rightarrow CO + H_2O \qquad \Delta H^0_{298ºK} = -206\ kJ/mol \qquad (5)$$

$$CO + 3H_2 \rightarrow CH_4 + H_2O \qquad \Delta H^0_{298ºK} = -165\ kJ/mol \qquad (6)$$

En este escenario, los catalizadores adecuados para su uso en la reacción de PROX CO deben cumplir una serie de requisitos:

1. Alta actividad en la oxidación de CO.
2. Alta selectividad frente a la reacción de oxidación de H_2.
3. Operatividad en el rango de temperaturas conveniente (típicamente 80-200ºC), limitado por los procesos de WGS y el funcionamiento de la pila PEMFC.
4. Resistencia a la desactivación por H_2O y CO_2.

Catalizadores para la reacción CO-PROX: estado del arte

El extenso trabajo realizado en este campo, ha concluido hasta ahora con grandes avances, desarrollando catalizadores de diversa índole con un buen

Universidad de Alicante

funcionamiento. En términos generales, se trata de catalizadores metálicos soportados con características particulares, que varían en base al tipo de metal, naturaleza del soporte, contenido metálico, y las condiciones de preparación. De la amplia gama que se puede encontrar en la bibliografía científica, se pueden agrupar fundamentalmente en 3 categorías, según el metal.

Catalizadores basados en metales nobles[17,18]. Siendo los más estudiados Pt[19,20], Pd[21,22], Ru[23,24] y Rh[25], soportados en Al_2O_3, SiO_2 y otros soportes tales como zeolitas u óxidos metálicos, así como también algunas combinaciones bimetálicas[26-28]. Con carácter general, estos sistemas reducen el CO hasta los límites demandados, y operan bien bajo la presencia de H_2O y CO_2. Como inconvenientes, destacan su moderada selectividad y su alto precio, lo que frena su uso generalizado.

Catalizadores basados en oro[29-31]. Habiéndose empleado distintos soportes como TiO_2[32], Fe_2O_3[33,34], CeO_2[35], ó MnO_2[36], entre otros muchos, los resultados son dispares y altamente dependientes del procedimiento experimental de preparación. A grandes rasgos se puede afirmar que estos catalizadores presentan una alta actividad catalítica, por lo que trabajan a temperaturas más bajas que los anteriores, pero como limitación importante, se desactivan fácilmente en presencia de la mezcla de H_2O y CO_2.

Catalizadores basados en metales de transición[37]. Liderando este grupo se encuentra indudablemente el sistema formado por óxido de cobre y óxido de cerio ($CuO\text{-}CeO_2$) en sus diversas configuraciones[38-45]. Este conjunto presenta unas propiedades catalíticas excelentes debido a la fuerte interacción sinérgica metal-soporte sin suponer un excesivo coste, por lo que actualmente centra múltiples campos áreas de investigación en catálisis.

Universitat d'Alacant
Universidad de Alicante

Propiedades del sistema CuO/CeO_2

En el caso de la ceria, la semirreacción del par redox $Ce^{3+} \leftrightarrow Ce^{4+}$ ocurre con mucha facilidad en su estructura típica de fluorita, lo que contribuye a una gran movilidad de oxígeno en la red cristalina, y la capacidad de adsorber reversiblemente oxígeno para suministrarlo de forma modulada a sustrato reactivo, que se conoce de forma genérica como *capacidad de almacenamiento de oxígeno*. Este óxido parcialmente reducible mejora sus propiedades catalíticas en gran medida cuando se le incorporan pequeños porcentajes de Cu, debido a procesos redox que ocurren entre el soporte y la fase dispersa, que se maximizan con el mayor contacto interfacial[43-45]. Así, debido al gran interés que despierta este tipo de catalizadores, se han publicado múltiples estudios relativos a su caracterización detallada en base al método de preparación, contenido metálico o el dopaje con otros iones, y el efecto que ejercen dichos factores en su actividad catalítica para diversas reacciones[37, 44, 46, 47].Para la reacción de PROX CO y en particular para el tándem óxido de cobre-óxido de cerio, se han obtenido excelentes resultados en trabajos anteriores, y se ha realizado un análisis mecanístico muy completo como el de Martínez-Arias et al. [39] o Polster et al. [45]. En ellos, se ha concluido que el mecanismo transcurre a través de reacciones redox que afectan tanto al Cu (mayoritariamente presente como CuO) como al

soporte, en un sistema en el que la reducibilidad de cada uno de ellos está favorecida por la presencia del otro componente[48]. Dicha reducibilidad es beneficiosa para la reacción tanto en términos de selectividad como de conversión, formando grupos Cu^+ superficiales en la interfase metal-soporte, que se han descrito como los sitios activos para la adsorción de CO, preferente sobre la adsorción disociativa de H_2.

Criticalidad de los sistemas dependientes de Ce y motivación del proyecto

No obstante, pese a los prometedores resultados que se han alcanzado para estos catalizadores, existe un problema fundamental de carácter estratégico que se ha de considerar antes de implantar a gran escala estos sistemas: la dificultad de la extracción y producción en masa de las tierras raras, como el Ce. Aunque las menas de este grupo de elementos es bien dispersa en la Tierra, actualmente China es el principal productor, con el 95% de mercado. Debido a la escasa concentración relativa de estos recursos en la mayor parte del mundo, no resulta rentable asumir las altas inversiones para su extracción, por lo que la comunidad internacional ha optado por importarlo del principal proveedor, concediendo a China una posición muy favorecedora de la que el país está siendo beneficiado por el auge del uso de estos elementos. Así pues, dispuestos a abandonar una dependencia energética de los países con reservas de petróleo o gas natural, pasar a la economía del hidrógeno empleando estos catalizadores supondría someterse a otro yugo, del que las políticas actuales son conscientes y pretenden evitar a toda costa. Es por ello que cada vez se mira más hacia un horizonte libre de tierras raras, en el que otros materiales igualen (o superen) sus magníficas prestaciones en el ámbito tecnológico y catalítico.

La motivación de este trabajo es encontrar un sustituto apropiado de la ceria como soporte para catalizar la reacción de PROX CO, a partir de una aproximación a su química especial utilizando óxidos parcialmente reducibles como los MnO_x, quienes, debido a sus múltiples estados de oxidación y posibilidad de formación de óxidos mixtos, su abundancia natural y su reducido coste, son unos candidatos muy prometedores[49, 50]. Estos materiales se han probado como catalizadores y soportes de catalizadores para reacciones de oxidación de diversa índole en publicaciones precedentes[51-54], así como en la reacción de PROX CO[55-57], mostrando unos resultados muy positivos, pero lejos de superar a los óxidos de cerio.

En este punto, cabe destacar que la mezcla natural de óxidos Cu-Mn denominada popularmente *hopcalita*, ha venido empleándose ampliamente desde hace décadas para la oxidación de CO en sistemas de protección respiratorios en minería, campo militar y dispositivos espaciales[58,59], lo que ha inspirado estas investigaciones y conducido al estudio en profundidad de estos catalizadores. Así, además de ello, los MnO_x despiertan un gran interés gracias a la versatilidad de estos óxidos para formar distintas estructuras cristalinas organizadas, lo que permite sintetizar arquitecturas tridimensionales especiales, que ayuden a mejorar sus propiedades catalíticas[60,61].

En este contexto, el material en el que se ha centrado la atención de este trabajo es el óxido mineral de manganeso *criptomelano*, cuyo nombre deriva de las palabras en griego “negro” y “oculto”, con el que se le bautizó debido a su tardía identificación dentro de la mezcla de minerales conocida como *psilomelano*[62]. Se trata de una especie natural con fórmula no estequiométrica $K_xMn_8O_{16}$ y estructura definida en túneles formados por la unión de 2x2 octaedros de MnO_6 ocupados parcialmente por cationes potasio, pero existen procedimientos para sintetizar en laboratorio óxidos con la misma estructura y composición denominados de forma genérica por sus siglas en inglés K-OMS-2, o simplemente, OMS-2 (*Octahedral Molecular Sieves*, 2x2)[63-65].

Como características de este material, cabe destacar su desarrollada microporosidad con distribuciones relativamente estrechas de tamaño de poro alrededor de 0.46 x 0.46 nm[66], y un estado de oxidación mixto, en promedio estimado en 3.8 consecuencia de la presencia mayoritaria en la red de cationes Mn^{4+}, junto con Mn^{3+} y en menor proporción Mn^{2+}. Esta variabilidad en el estado de oxidación, junto con su estructura ordenada le otorga una capacidad de intercambio iónico y una alta movilidad de oxígeno lábil en la red cristalina, lo que recuerda en cierto sentido a las propiedades de la ceria[67].

Así, los óxidos tipo criptomelano se han estudiado en profundidad durante las dos últimas décadas, por su gran versatilidad en catálisis para reacciones importantes en el ámbito medioambiental y en el energético, como la oxidación de compuestos orgánicos, y la oxidación de CO, entre otras[64, 68-75]. La principal ventaja de este material es que puede ser diseñado incluyendo modificaciones en el procedimiento de síntesis para adoptar una forma concreta, superficie específica, porosidad, o composición requeridos[68, 76]. De forma general, la incorporación a esta estructura de metales activos conduce a mejoras importantes en todas sus aplicaciones, siendo los procedimientos más reportados aquéllos que introducen Ag^{+}[68, 77, 78] o Cu^{2+}[79-85], por ser los que han aportado resultados más prometedores. Dichas modificaciones dependen del método en el que se haya incorporado el agente dopante, pudiendo ser sólo depositado sobre la superficie del criptomelano, sustituyendo a las especies de potasio dentro de los túneles o reemplazando a iones de Mn constituyentes de los octaedros, multiplicando las posibilidades y las características de los materiales preparados[81].

Objetivos generales del trabajo

Teniendo en cuenta la contextualización general expuesta, este Proyecto de Tesis surge tiene como principal objetivo la exploración de catalizadores activos con formulaciones sostenibles para la reacción de Oxidación Preferencial de CO (CO-PROX), que es un paso crítico hacia la purificación exhaustiva de H_2 procesado con las actuales tecnologías de producción.

Con el objetivo de evitar la costosa utilización de metales nobles y la limitada estabilidad característica de los catalizadores de oro, este Proyecto de Tesis aborda el estudio de catalizadores basados en óxido de cobre como una opción rentable y eficiente para llevar acelerar la reacción CO-PROX. Como primer

enfoque, se han estudiado los sistemas de CuO/CeO_2 convencionales para establecer un conocimiento fundamental de base utilizando un catalizador con una reconocida excelente actividad. A partir de ello, los resultados de la investigación fundamental con el catalizador de CuO/CeO_2 se establecen como punto de referencia en la consideración de su posible sustitución por catalizadores de óxido de cobre y óxido de manganeso alternativos, medioambientalmente mucho más compatibles, a saber, las formulaciones de CuO/Criptomelano.

Por lo tanto, los principales objetivos establecidos en este Proyecto de Tesis se pueden sintetizar en los siguientes cinco puntos generales:

1- *El estudio fundamental sobre los sistemas de CuO/CeO_2 para la evaluación de las características y propiedades físico-químicas que resultan en su sobresaliente actividad como catalizadores CO-PROX.*

De acuerdo a la estructura en la que se ha estructurado esta Tesis, el Objetivo n. 1 se trata en los Capítulos 3 y 4, que comprenden estudios mecanísticos de CO-PROX sobre catalizadores de CuO/CeO_2 puros y dopados, respectivamente.

2- *La preparación, caracterización y evaluación de la actividad de catalizadores CO-PROX soportados en óxidos metálicos alternativos al óxido de cerio, siendo en concreto enfocado el estudio sobre el sistema particular CuO/Criptomelano.*

En este sentido, el objetivo n. 2 se aborda principalmente a lo largo de los Capítulos 5 y 6, con el estudio sistemático de la estabilidad de CuO/Cryptomalene y los problemas de regeneración en condiciones de operación CO-PROX, incluida la simulación de en condiciones reales de operación.

3- *La propuesta de un estudio mecanístico consistente sobre la reacción de CO-PROX con el catalizador alternativo CuO/Criptomelano, en analogía con los fundamentos establecidos a partir de los sistemas de CuO/CeO_2.*

Con el objetivo de abordar el objetivo n. 3, el Capítulo 7 comprende el uso de métodos sofisticados no convencionales para el estudio de problemas mecanísticos de CO-PROX en catalizadores de CuO/Criptomelano, dadas las las limitaciones intrínsecas de las técnicas convencionalmente extendidas para este fin en su aplicación a este particular material.

4- *La comparación crítica entre los catalizadores de CuO/CeO_2 y CuO/Criptomelano en la aplicación de CO-PROX, en términos de actividad y estabilidad en diversas condiciones de reacción, incluida la presencia de inhibidores de CO_2 y H_2O.*

Respecto al objetivo n. 4, el Capítulo 8 recopila resultados más relevantes de los catalizadores de CuO/CeO_2 y CuO/Criptomelano para su evaluación comparativa directa.

5- *La escalabilidad de las fases activas en polvo en base de óxido de cobre a catalizadores monolíticos de tamaño mediano con actividad mejorada preparados por medio de la tecnología de impresión 3D.*

En última instancia, el objetivo n. 5 comprende un salto tecnológico que se traslada el proceso catalítico desde la pequeña escala de los catalizadores en polvo hasta el soporte de monolito, que además se realiza bajo un enfoque muy novedoso mediante impresión 3D, como se presenta en el Capítulo 9.

Resultados y conclusiones más relevantes

(1) A partir de estudios mecanísticos sobre catalizadores de CuO/CeO_2 en la reacción CO-PROX, se puede concluir que la velocidad de oxidación del CO con catalizadores de óxido de cobre-óxido de cerio se correlaciona con la formación del carbonilo Cu^+ -CO. Sin embargo, la desorción de los productos de carbono formados en la superficie de la ceria es el paso más lento por debajo de cierto umbral de temperatura, con lo que la química superficial juega un papel fundamental. Particularmente, los grupos hidroxilo desempeñan un papel clave en la determinación de la naturaleza de los intermedios basados en carbono formados por la quimisorción y oxidación de CO, cuya abundancia depende de las características redox de los catalizadores basados en CuO/CeO_2. Esencialmente, los hidroxilos favorecen la formación de bicarbonatos con respecto a los carbonatos, y los catalizadores que forman más bicarbonatos alcanzan velocidades de oxidación de CO más rápidas que los que favorecen a los carbonatos. Todos los catalizadores basados en CuO/CeO_2 probados mostraron una buena actividad catalítica en la reacción CO-PROX, aunque la presencia de dopantes (20% at.) en la red de ceria produjo en general un efecto perjudicial sobre la óptima actividad de CuO/CeO_2 puro.

(2) El mineral Criptomelano es un material abundante, no tóxico, con una preparación sintética de laboratorio escalable, fácil y reproducible que presenta oportunidades prometedoras como catalizador activo para la oxidación de CO y la reacción de CO-PROX. Las propiedades fisicoquímicas del soporte Criptomelano, con su alta movilidad de oxígeno y lábil ciclo redox entre los diferentes estados de oxidación de Mn, recuerdan ligeramente a las de la CeO_2, con una capacidad de almacenamiento de oxígeno (OSC) bien conocida en el intercambio electrónico rápido entre los pares Ce^{3+} /Ce^{4+}, por lo que se postula como un candidato prometedor para sustituir algunos de los sistemas catalíticos basados en CeO_2.

(3) En la misma línea, cuando el Criptomelano se dopa con óxido de cobre, conforme a las formulaciones de CuO/Criptomelano, la actividad catalítica en la reacción CO-PROX se mejora en gran medida debido a la promoción de sus propiedades redox, a partir de la formación de entidades Cu–O– Mn, dando lugar a grupos de oxígeno lábiles con buena interacción con moléculas de CO reactivas.

(4) Sin embargo, la actividad mejorada de CuO/Criptomelano con respecto a Criptomelano es contrarrestada con una pérdida importante de estabilidad y una desactivación significativa al cabo de los ciclos catalíticos de reacción de CO-PROX. El estudio sobre los mecanismos de desactivación de CuO/Criptomelano ha concluido que la microestructura básica de Criptomelano, configurada a partir

de nano-túneles bien definidos (α-MnO_2), colapsa parcialmente dando lugar a las fases inactivas Mn_3O_4 y $CuMn_2O_4$ cristalino, lo que implica una reducción en promedio de manganeso y cobre con respecto al estado inicial del catalizador. Por lo tanto, la promoción redox con el depósito de Cu en CuO/Criptomelano resulta positiva para la actividad catalítica en la reacción CO-PROX, gobernada por un mecanismo tipo MVK, pero al mismo tiempo, su mayor labilidad hacia la reducción hace que la abstracción de oxígeno de red sea demasiado fácil, haciendo que el catalizador CuO/Criptomelano quede finalmente reducido y desactivado.

(5) En base a las estrategias de regeneración que se pueden establecer en este sentido, se han estudiado tratamientos previos de reoxidación en atmósferas de O_2 a diferentes temperaturas: 200ºC y 400ºC. Se ha constatado que, por un lado, el tratamiento en O_2 a 200ºC no resulta suficientemente eficaz como para restablecer significativamente la actividad sobre CuO/Criptomelano desactivado, debido a la gran estabilidad de las fases inactivas resultantes de Mn_3O_4 y $CuMn_2O_4$. Por lo tanto, fue necesario aumentar la temperatura del pretratamiento hasta 400ºC para lograr una reactivación suficiente, pero al mismo tiempo, el catalizador sufrió de la sinterización de CuO y reorganización cristalina.

(6) Sorprendentemente, y como una característica genuina del catalizador CuO/Criptomelano, el uso condiciones de reacción reales CO-PROX, que incluye la introducción de CO_2 + H_2O en la mezcla de reactivos, supone una estabilidad mejorada con respecto a las condiciones más simples de CO + O_2 + H_2 comúnmente utilizadas. Asimismo, en estas condiciones con adición de los inhibidores CO_2 + H_2O, considerados universalmente perjudiciales para la actividad catalítica en la reacción CO-PROX, CuO / Criptomelano exhibe, por el contrario, una estabilidad y una actividad catalítica mejoradas una vez se alcanza actividad en un estado estacionario después de varios ciclos catalíticos. Ello es, una característica única para este material con implicaciones prácticas altamente interesantes.

Universitat d'Alacant
Universidad de Alicante

(7) La actividad mejorada del catalizador de CuO/Criptomelano en la mezcla de CO-PROX compuesta con CO_2+H_2O se estudió mediante diferentes técnicas, que han revelado que la adición conjunta de estas especies incrementa en gran medida la quimisorción de CO_2 y H_2O. Específicamente, el incremento en la retención de H_2O es un hecho relevante para el caso del catalizador hidrofóbico CuO/Criptomelano, ya que las moléculas de agua se pueden incorporar dentro de los microtúneles proporcionando reforzando la estructura y se equilibrando los estados oxidados de manganeso.

(8) Los estudios mecanísticos sobre el catalizador de CuO/Criptomelano basados en técnicas no convencionales han aportado conclusiones relevantes con importantes similitudes con las bien estudiadas para el caso del catalizador de CuO/CeO_2. Por ejemplo, como: (1) la participación de oxígeno de red en la reacción de CO-PROX, siguiendo el mecanismo de tipo MVK; (2) el sitio de reacción identificado para la oxidación de CO, siendo las especies de Cu parcialmente reducidas en los enlaces lábiles interfaciales de Cu - O - Mn, como

en Cu - O - Ce para CuO/CeO_2; (3) el rol del soporte en la asistencia en la regeneración de oxígeno activo de la red de las partículas de Cu_xO.

(9) El estudio fundamental presentado en este documento sobre el catalizador de CuO/CeO_2 con el uso de técnicas experimentales altamente sofisticadas y el modelado computacional por DFT ha dilucidado la participación del soporte de CeO^2 en la restitución de oxígeno de la red durante el progreso de la reacción CO-PROX. Según los resultados obtenidos, la restauración de O_2 se lleva a cabo directamente en las especies de CuO cuando están principalmente oxidadas, a bajas temperaturas. A medida que la reacción va teniendo lugar, las partículas se van reduciendo parcialmente Cu_xO en proceso gradual iniciado localmente en superficie que va propagando la extensión de la reducción hacia el bulk. La aceleración de la oxidación de CO por el aumento de la temperatura conduce a un estado crítico reducido sobre las partículas de Cu_xO activan la reacción competitiva de oxidación de H_2 que a su vez incrementará importantemente la reducción de Cu_xO. Sobrepasado cierto punto de reducción, la captación directa de O_2 no es eficaz y se produce preferentemente en el soporte de CeO_2, que ayuda a la reposición de O en las interfases con actividad de intercambio redox entre Cu - O - Ce. Los experimentos de NAP-XPS en condiciones CO-PROX *operando* evidenciaron una reducción muy superficial en CeO_2 y la naturaleza de dicho evento se ha asociado con la transferencia de oxígeno de la red de la ceria a las partículas de Cu_xO en el proceso de la restitución de O a través de CeO_2.

(10) La participación activa del soporte de CeO_2 en el mecanismo de reoxidación del catalizador implica, por lo tanto, varias consideraciones que resultan la actividad mejorada del catalizador CuO/CeO_2 con respecto a cualquier otro catalizador basado en CuO, principalmente debido a una gran reversibilidad en los ciclos de reducción - ciclos de oxidación. En contraposición para el catalizador CuO/Criptomelano, el soporte de Criptomelano no es tan activo para facilitar el oxígeno a las partículas de Cu_xO, como se ha demostrado en la más limitada capacidad de intercambio de oxígeno mediante los experimentos de pulsos isotópicos. Por ello, los procesos de reducción - reoxidación necesarios para el curso de la reacción CO-PROX están desequilibrados pasado cierto umbral de reducción de Cu_xO y finalmente conducen a una reducción promedio con consecuencias irreversibles en la actividad de CuO/Criptomelano.

(11) Finalmente, como prueba de concepto, la impresión 3D se ha utilizado para preparar monolitos de cordierita con geometría de canales asimétricos que han mejorado la actividad catalítica con respecto de análogos soportes monolíticos convencionales, sobre los que se depositó la fase activa estudiada en polvo CuO/CeO_2. En este sentido, la tecnología de impresión 3D supera las limitaciones de los procedimientos de fabricación convencionales basados en la extrusión y aporta gran libertad en el diseño de soportes monolíticos con formas complejas. Así pues, en los monolitos con diseños mejorados, la sección de los canales es mayor en el lado de entrada de los reactivos que en el lado de salida, mejorando con respecto a los monolitos convencionales tanto la velocidad de reacción,

cuando la reacción se comporta bajo control cinético, como la difusión radial de los reactivos, cuando la reacción se comporta bajo difusional.

Referencias

[1] Acar, C.; Dincer, I., International Journal of Hydrogen Energy, (2014) 39, 1.

[2] IEA, World Energy Outlook In (2014).

[3] Armor, J. N., Applied Catalysis A: General, (1999) 176, 159.

[4] Cetinkaya, E.; Dincer, I.; Naterer, G. F., International Journal of Hydrogen Energy, (2012) 37, 2071.

[5] Dincer, I., International Journal of Hydrogen Energy, (2012) 37, 1954.

[6] Ashraf, M. A.; Ercolino, G.; Specchia, S.; Specchia, V., International Journal of Hydrogen Energy, (2014) 39, 18109.

[7] Yang, H.; Xu, Z.; Fan, M.; Gupta, R.; Slimane, R. B.; Bland, A. E.; Wright, I., Journal of Environmental Sciences, (2008) 20, 14.

[8] Figueroa, J. D.; Fout, T.; Plasynski, S.; McIlvried, H.; Srivastava, R. D., International Journal of Greenhouse Gas Control, (2008) 2, 9.

[9] Ozbilen, A.; Dincer, I.; Rosen, M. A., Environmental Impact Assessment Review, (2013) 42, 1.

[10] Choudhary, T. V.; Goodman, D. W., Catalysis Today, (2002) 77, 65.

[11] Park, E. D.; Lee, D.; Lee, H. C., Catalysis Today, (2009) 139, 280.

[12] Bion, N.; Epron, F.; Moreno, M.; Mariño, F.; Duprez, D., Topics in Catalysis, (2008) 51, 76.

[13] Ghenciu, A. F., Curr. Opin. Solid State Mater. Sci., (2002) 6, 389.

[14] Farrauto, R., Annu. Rev. Mater. Res. , (2003) 33, 1.

[15] Reshetenko, T. V.; Bethune, K.; Rubio, M. A.; Rocheleau, R., Journal of Power Sources, (2014) 269, 344.

[16] Ercolino, G.; Ashraf, M. A.; Specchia, V.; Specchia, S., Applied Energy, (2015) 143, 138.

[17] Oh, S. H.; Sinkevitch, R. M., Journal of Catalysis, (1993) 142, 254.

[18] Mariño, F.; Descorme, C.; Duprez, D., Applied Catalysis B: Environmental, (2004) 54, 59.

[19] Kahlich, M. J.; Gasteiger, H. A.; Behm, R. J., Journal of Catalysis, (1997) 171, 93.

[20] Wootsch, A.; Descorme, C.; Duprez, D., Journal of Catalysis, (2004) 225, 259.

[21] Miguel-García, I.; Berenguer-Murcia, Á.; Cazorla-Amorós, D., Applied Catalysis B: Environmental, (2010) 98, 161.

[22] Rosso, I.; Galletti, C.; Saracco, G.; Garrone, E.; Specchia, V., Applied Catalysis B: Environmental, (2004) 48, 195.

[23] Han, Y. F.; Kahlich, M. J.; Kinne, M.; Behm, R. J., Physical Chemistry Chemical Physics, (2002) 4, 389.

Universitat d'Alacant
Universidad de Alicante

[24] Chin, S. Y.; Alexeev, O. S.; Amiridis, M. D., Applied Catalysis A: General, (2005) 286, 157.

[25] Galletti, C.; Fiorot, S.; Specchia, S.; Saracco, G.; Specchia, V., Topics in Catalysis, (2007) 45, 15.

[26] Chin, S. Y.; Alexeev, O. S.; Amiridis, M. D., Journal of Catalysis, (2006) 243, 329.

[27] Schubert, M. M.; Kahlich, M. J.; Feldmeyer, G.; Huttner, M.; Hackenberg, S.; Gasteiger, H. A.; Behm, R. J., Physical Chemistry Chemical Physics, (2001) 3, 1123.

[28] Parinyaswan, A.; Pongstabodee, S.; Luengnaruemitchai, A., International Journal of Hydrogen Energy, (2006) 31, 1942.

[29] Landon, P.; Ferguson, J.; Solsona, B. E.; Garcia, T.; Carley, A. F.; Herzing, A. A.; Kiely, C. J.; Golunski, S. E.; Hutchings, G. J., Chemical Communications, (2005), 3385.

[30] Grisel, R. J. H.; Nieuwenhuys, B. E., Journal of Catalysis, (2001) 199, 48.

[31] Schubert, M. M.; Hackenberg, S.; van Veen, A. C.; Muhler, M.; Plzak, V.; Behm, R. J., Journal of Catalysis, (2001) 197, 113.

[32] Schumacher, B.; Denkwitz, Y.; Plzak, V.; Kinne, M.; Behm, R. J., Journal of Catalysis, (2004) 224, 449.

[33] Shodiya, T.; Schmidt, O.; Peng, W.; Hotz, N., Journal of Catalysis, (2013) 300, 63.

[34] Kahlich, M. J.; Gasteiger, H. A.; Behm, R. J., Journal of Catalysis, (1999) 182, 430.

[35] Luengnaruemitchai, A.; Osuwan, S.; Gulari, E., International Journal of Hydrogen Energy, (2004) 29, 429.

[36] Torres Sanchez, R. M.; Ueda, A.; Tanaka, K.; Haruta, M., Journal of Catalysis, (1997) 168, 125.

[37] Mariño, F.; Descorme, C.; Duprez, D., Applied Catalysis B: Environmental, (2005) 58, 175.

[38] Hornés, A.; Hungría, A. B.; Bera, P.; López Cámara, A.; Fernández-García, M.; Martínez-Arias, A.; Barrio, L.; Estrella, M.; Zhou, G.; Fonseca, J. J.; Hanson, J. C.; Rodriguez, J. A., Journal of the American Chemical Society, (2010) 132, 34.

[39] Martínez-Arias, A.; Gamarra, D.; Hungría, A. B.; Fernández-García, M.; Munuera, G.; Hornés, A.; Bera, P.; Conesa, J. C.; Cámara, A. L., Catalysts, (2013) 3, 378.

[40] Gamarra, D.; Martínez-Arias, A., Journal of Catalysis, (2009) 263, 189.

[41] Lee, H. C.; Kim, D. H., Catalysis Today, (2008) 132, 109.

[42] Gamarra, D.; Belver, C.; Fernández-García, M.; Martínez-Arias, A., Journal of the American Chemical Society, (2007) 129, 12064.

[43] Caputo, T.; Lisi, L.; Pirone, R.; Russo, G., Applied Catalysis A: General, (2008) 348, 42.

[44] Zou, H.; Dong, X.; Lin, W., Applied Surface Science, (2006) 253, 2893.

[45] Polster, C. S.; Nair, H.; Baertsch, C. D., Journal of Catalysis, (2009) 266, 308.

Universitat d'Alacant
Universidad de Alicante

[46] Giménez-Mañogil, J.; Bueno-López, A.; García-García, A., Applied Catalysis B: Environmental, (2014) 152-153, 99.

[47] Beckers, J.; Rothenberg, G., Green Chemistry, (2010) 12, 939.

[48] Shan, W.; Shen, W.; Li, C., Chemistry of Materials, (2003) 15, 4761.

[49] Ramesh, K.; Chen, L.; Chen, F.; Liu, Y.; Wang, Z.; Han, Y. F., Catalysis Today, (2008) 131, 477.

[50] Craciun, R.; Nentwick, B.; Hadjiivanov, K.; Knözinger, H., Applied Catalysis A: General, (2003) 243, 67.

[51] Krämer, M.; Schmidt, T.; Stöwe, K.; Maier, W. F., Applied Catalysis A: General, (2006) 302, 257.

[52] Crăciun, R.; Dulămiţă, N., Industrial and Engineering Chemistry Research, (1999) 38, 1357.

[53] Qian, K.; Qian, Z.; Hua, Q.; Jiang, Z.; Huang, W., Applied Surface Science, (2013) 273, 357.

[54] Piumetti, M.; Fino, D.; Russo, N., Applied Catalysis B: Environmental, (2015) 163, 277.

[55] Hasegawa, Y.; Fukumoto, K.; Ishima, T.; Yamamoto, H.; Sano, M.; Miyake, T., Applied Catalysis B: Environmental, (2009) 89, 420.

[56] Hasegawa, Y.-I.; Maki, R.-U.; Sano, M.; Miyake, T., Applied Catalysis A: General, (2009) 371, 67.

[57] Njagi, E. C.; Genuino, H. C.; King'Ondu, C. K.; Chen, C. H.; Horvath, D.; Suib, S. L., International Journal of Hydrogen Energy, (2011) 36, 6768.

[58] Trimble, E. J., Toxicology, (1996) 115, 41.

[59] Mele, A.; Mele, I., American Journal of Applied Sciences, (2012) 9, 265.

[60] Feng, Q.; Kanoh, H.; Ooi, K., Journal of Materials Chemistry, (1999) 9, 319.

[61] Brock, S. L.; Duan, N.; Tian, Z. R.; Giraldo, O.; Zhou, H.; Suib, S. L., Chemistry of Materials, (1998) 10, 2619.

[62] Fleischer, M.; Richmond, W. E., Economic Geology, (1943) 38, 269.

[63] Suib, S. L., Curr. Opin. Solid State Mater. Sci., (1998) 3, 63.

[64] Chen, C. H.; Suib, S. L., Journal of the Chinese Chemical Society, (2012) 59, 465.

[65] Genuino, H. C.; Meng, Y.; Horvath, D. T.; Kuo, C. H.; Seraji, M. S.; Morey, A. M.; Joesten, R. L.; Suib, S. L., ChemCatChem, (2013) 5, 2306.

[66] DeGuzman, R. N.; Shen, Y. F.; Neth, E. J.; Suib, S. L.; O'Young, C. L.; Levine, S.; Newsam, J. M., Chemistry of Materials, (1994) 6, 815.

[67] Sun, M.; Yu, L.; Ye, F.; Diao, G.; Yu, Q.; Hao, Z.; Zheng, Y.; Yuan, L., Chemical Engineering Journal, (2013) 220, 320.

[68] Chen, J.; Li, J.; Li, H.; Huang, X.; Shen, W., Microporous and Mesoporous Materials, (2008) 116, 586.

[69] Ho, P. H.; Lee, S. C.; Kim, J.; Lee, D.; Woo, H. C., Fuel Processing Technology, (2015) 131, 238.

[70] Tian, H.; He, J.; Zhang, X.; Zhou, L.; Wang, D., Microporous and Mesoporous Materials, (2011) 138, 118.

Universitat d'Alacant
Universidad de Alicante

[71] Shen, Y. F.; Zerger, R. P.; DeGuzman, R. N.; Suib, S. L.; McCurdy, L.; Potter, D. I.; O'Young, C. L., Science, (1993) 260, 511.

[72] Genuino, H. C.; Dharmarathna, S.; Njagi, E. C.; Mei, M. C.; Suib, S. L., Journal of Physical Chemistry C, (2012) 116, 12066.

[73] Atribak, I.; Bueno-López, A.; García-García, A.; Navarro, P.; Frías, D.; Montes, M., Applied Catalysis B: Environmental, (2010) 93, 267.

[74] Luo, J.; Zhang, Q.; Huang, A.; Suib, S. L., Microporous and Mesoporous Materials, (2000) 35-36, 209.

[75] Santos, V. P.; Pereira, M. F. R.; Órfao, J. J. M.; Figueiredo, J. L., Topics in Catalysis, (2009) 52, 470.

[76] Deng, Y. Q.; Zhang, T.; Au, C. T.; Yin, S. F., Catalysis Communications, (2014) 43, 126.

[77] Özacar, M.; Poyraz, A. S.; Genuino, H. C.; Kuo, C. H.; Meng, Y.; Suib, S. L., Applied Catalysis A: General, (2013) 462-463, 64.

[78] Fort, A.; Addabbo, T.; Vignoli, V.; Bertocci, F.; Mugnaini, M.; Atrei, A.; Gregorkiewitz, M., Sensors and Actuators, B: Chemical, (2014) 194, 427.

[79] Liu, X. S.; Jin, Z. N.; Lu, J. Q.; Wang, X. X.; Luo, M. F., Chemical Engineering Journal, (2010) 162, 151.

[80] Jothiramalingam, R.; Viswanathan, B.; Varadarajan, T. K., Materials Chemistry and Physics, (2006) 100, 257.

[81] Yang, Y.; Huang, J.; Zhang, S.; Wang, S.; Deng, S.; Wang, B.; Yu, G., Applied Catalysis B: Environmental, (2014) 150–151, 167.

Universitat d'Alacant
Universidad de Alicante

Universitat d'Alacant
Universidad de Alicante

Curriculum Vitae

Universitat d'Alacant
Universidad de Alicante

Curriculum Vitae

Arantxa Davó Quiñonero was born on the 5th July of 1991 in Alicante, Spain. She earned her Bachelor of Science degree in Chemistry from the University of Alicante in 2014, achieving a Graduation with Honorific Mention. After that, she enrolled in her Master Science studies in Materials Science, which was rewarded with an Extraordinary Distinction Prize in 2015. That year, she was awarded with a FPU grant from the Spanish Ministry of Education and started her PhD studies in the Inorganic Chemistry Department of the University of Alicante. This Doctoral Thesis describes the most important findings of the research she conducted in the study of the catalytic CO clean-up in the purification of H_2 by means of the Preferential Oxidation of CO (CO-PROX reaction).

List of Publications

1. **Role of hydroxyl groups in the preferential oxidation of CO over copper oxide-cerium oxide catalysts.**
   A. Davó-Quiñonero, M. Navlani-García, D. Lozano-Castelló, A. Bueno-López, J. Anderson.
   ACS Catalysis, **6(3)** (2016) 1723-1731.

2. **CuO/Cryptomelane catalyst for preferential oxidation of CO in the presence of H_2: deactivation and regeneration.**
   A. Davó-Quiñonero, M. Navlani-García, D. Lozano-Castelló, A. Bueno-López.
   Catalysis Science & Technology, **6(14)** (2016) 5684-5691.

3. **Rapid-scan operando infrared spectroscopy.**
   A. Davó-Quiñonero, A. Bueno-López, D. Lozano-Castelló, A.J. McCue, J. Anderson. *ChemCatChem* **8(11)** (2016) 1905-1908.

4. **Unexpected stability of CuO/Cryptomelane under Preferential Oxidation of CO reaction conditions in the presence of CO_2 and H_2O.**
   A. Davó-Quiñonero, D. Lozano-Castelló, A. Bueno-López.
   Applied Catalysis B: Environmental **217** (2017) 459-465.

5. **Improved CO Oxidation Activity of 3DOM Pr-Doped Ceria Catalysts: Something Other Than an Ordered Macroporous Structure.**
   A. Davó-Quiñonero, J. González-Mira, I. Such-Basáñez, J. Juan-Juan, D. Lozano-Castelló, A. Bueno-López. *Catalysts* **7(2)** (2017) 67-79

Universitat d'Alacant
Universidad de Alicante

6. **Templated Synthesis of Pr-Doped Ceria with Improved Micro and Mesoporosity Porosity, Redox Properties and Catalytic Activity.**
   A. Davó-Quiñonero, J. González-Mira, I. Such-Basáñez, D. Lozano-Castelló, A. Bueno-López. *Catalysis Letters* **148(1)** (2018) 258-266.

7. **Macroporous carrier-free Sr-Ti Catalyst for NO_x Storage and Reduction.**
   V. Alcalde-Santiago, A. Davó-Quiñonero, I. Such-Basáñez, D. Lozano-Castelló, A. Bueno-López. *Applied Catalysis B: Environmenta*l **220** (2018) 524-532.

8. **On the soot combustion mechanism using 3DOM ceria catalysts.**
   V. Alcalde-Santiago, A. Davó-Quiñonero, I. Such-Basáñez, D. Lozano-Castelló, A. Bueno-López. *Applied Catalysis B: Environmental* **234** (2018) 187-197.

9. **Three-dimensionally ordered macroporous PrOx: an improved alternative to ceria catalysts for soot combustion.**
   V. Alcalde-Santiago, E. Bailón-García, A. Davó-Quiñonero, D. Lozano-Castelló, A. Bueno-López. *Applied Catalysis B: Environmental* (2018) DOI: 10.1016/j.apcatb.2018.10.049

10. **Improved asymmetrical honeycomb monolith catalyst prepared using a 3D printed template.**
    A. Davó-Quiñonero, D. Sorolla-Rosario, E. Bailón-García, D. Lozano-Castelló, A. Bueno-López. *Journal of Hazardous Materials* **368** (2019) 638-643

11. **PrOx catalysts for the combustion of soot generated in diesel engines. Effect of CuO and 3DOM structure.**
    V. Alcalde-Santiago, E. Bailón-García, A. Davó-Quiñonero, D. Lozano-Castelló, A. Bueno-López. *Catalysis Science & Technology* (2019). DOI: 10.1039/C9CY00130A.

12. **Effect of metal loading on the CO_2 methanation: A comparison between alumina supported Ni and Ru catalysts.**
    A. Quindimil, U. De-la-Torre, B. Pereda-Ayo, A. Davó-Quiñonero, E. Bailón-García, D. Lozano-Castelló, J. A. González-Marcos, A. Bueno-López, J. R. González-Velasco. Catalysis Today (2019). DOI: 10.1016/j.cattod.2019.06.027

Universitat d'Alacant
Universidad de Alicante

Contributions to conferences

❖ ORAL COMMUNICATIONS

1. **Mechanisms in the catalytic soot combustion with 3-Dimensionally Ordered Macroporous (3DOM) ceria catalysts.**
   Alcalde-Santiago, V., Davó-Quiñonero, A., Lozano-Castelló, D., Bueno-López, A.
   XXVI Spanish American Catalysis Conference (CICat 2018). INTERNATIONAL.
   Celebrated in Coimbra (Portugal) from 09/09/2018 to 14/09/2018.

2. **Surface development of CeO_2 as a redox support in Ru/CeO_2 catalysts towards CO_2 methanation.**
   Quindimil, A., De-la-Torre, U., Pereda-Ayo, B., González-Marcos, J.A., Alcalde-Santiago, V., Davó-Quiñonero, A., Lozano-Castelló, D., Bueno-López, A. González-Velasco, J. R.
   XXVI Spanish American Catalysis Conference (CICat 2018). INTERNATIONAL.
   Celebrated in Coimbra (Portugal) from 09/09/2018 to 14/09/2018.

3. **Ni/LnOx catalysts (Ln = La, Ce or Pr) for CO_2 methanation.**
   Alcalde-Santiago, V., Davó-Quiñonero, A., Lozano-Castelló, D., Quindimil, A., De-la-Torre, U., Pereda-Ayo, B., González-Marcos, J.A., González-Velasco, J. R., Bueno-López, A.
   3rd Fundamentals and applications of cerium dioxide in catalysis. INTERNATIONAL.
   Celebrated in Barcelona (Spain) from 25/06/2018 to 27/06/2018.

4. **Carrier-Free Sr-Ti Catalysts For NOx Storage and Reduction.**
   Alcalde-Santiago, V., Davó-Quiñonero, A., Such-Basáñez, I., Lozano-Castelló, D., Bueno-López, A.
   13th European Congress on Catalysis (Europacat XIII). INTERNATIONAL.
   Celebrated in Florence (Italy) from 27/08/2017 to 31/08/2017.

5. **Improved redox properties and catalytic performance of 3DOM ceria-based catalysts.**
   Davó-Quiñonero, A., González-Mira, J., Such-Basáñez, I., J. Juan-Juan, J., Lozano-Castelló, D., Bueno López, A.
   13th European Congress on Catalysis (Europacat XIII). INTERNATIONAL.
   Celebrated in Florence (Italy) from 27/08/2017 to 31/08/2017.

6. **Macroporous Sr-Ti unsupported catalysts highly efficient towards NOx storage and reduction.**
   Alcalde-Santiago, V., Davó-Quiñonero, A., Such-Basáñez, I., Lozano-Castelló, D., Bueno-López, A.
   Spanish Catalyst Society Conference (SECAT'17). NATIONAL.
   Celebrated in Oviedo (Spain) from 26/06/2017 to 28/06/2017.

Universitat d'Alacant
Universidad de Alicante

7. **DFT study of CO-PROX reaction with copper-based catalysts.**
   Davó-Quiñonero, A., Such-Basáñez, I., Juan-Juan, J., Lozano-Castelló, D., Bueno-López, A.
   Spanish Catalyst Society Conference (SECAT'17). NATIONAL.
   Celebrated in Oviedo (Spain) from 26/06/2017 to 28/06/2017.

8. **CuO/Cryptomelane catalysts as an alternative to CuO/Ceria for CO-PROX reaction.**
   Davó-Quiñonero, A., Lozano-Castelló, D., Bueno-López, A.
   II Young Researchers meeting from Spanish Society of Catalysis. NATIONAL
   Celebrated in Ciudad Real (Spain) from 27/06/2016 to 29/06/2016.

9. **Catalytic soot combustion with strontium titanates prepared through PMMA crystals infiltration.**
   Alcalde-Santiago, V., Davó-Quiñonero, A., Lozano-Castelló, D., Bueno-López, A.
   II Young Researchers meeting from Spanish Society of Catalysis. NATIONAL.
   Celebrated in Ciudad Real (Spain) from 27/06/2016 to 29/06/2016.

❖ POSTER COMMUNICATIONS

1. **On the soot combustion mechanisms using 3DOM ceria catalysts.**
   Alcalde-Santiago, V., Davó-Quiñonero, A., Lozano-Castelló, D., Bueno-López, A.
   3rd Fundamentals and applications of cerium dioxide in catalysis. INTERNATIONAL.
   Celebrated in Barcelona (Spain) from 25/06/2018 to 27/06/2018.

2. **Positive effect of CO_2 and H_2O with CuO/Cryptomelane catalysts at CO-PROX reaction.**
   Davó-Quiñonero, A., Lozano-Castelló, D., Bueno-López, A.
   Spanish Catalyst Society Conference (SECAT'17). NATIONAL.
   Celebrated in Oviedo (Spain) from 26/06/2017 to 28/06/2017.

3. **Improved redox properties and catalytic activity in ceria-based catalysts with 3-dimensionally-ordered macroporous structure.**
   Davó-Quiñonero, A., González-Mira, J., Such-Basáñez, I., Juan-Juan, J., Lozano-Castelló, D., Bueno-López, A.
   Spanish Catalyst Society Conference (SECAT'17). NATIONAL
   Celebrated in Oviedo (Spain) from 26/06/2017 to 28/06/2017.

4. **Influence of ad-atom nature on the chemisorption of CO on a Cu (111) surface.**
   Davó-Quiñonero, A., Such-Basáñez, I., Juan-Juan, J., Lozano-Castelló, D., Bueno-López, A.
   Abinit hands-on 2017. INTERNATIONAL.
   Celebrated in Bruyeres-le-Chatel, Paris (France) from 30/01/2017 to 03/02/2017.

5. **RhO_x supported on three dimensionally ordered macroporous ceria for catalytic decomposition of N_2O.**
   Davó-Quiñonero, A., Fraile-Jiménez, M. I., Lozano-Castelló, D., Bueno-López, A.
   International Thematic Workshop on N_2O Abatement. INTERNATIONAL.
   Celebrated in Krakow (Poland) from 04/05/2016 to 06/08/2016.

6. **Copper oxide supported in mixed manganese oxides as catalysts for the selective oxidation of CO.**
   Davó-Quiñonero, A., Navlani-García, M., Lozano-Castelló, D., Bueno-López, A.
   Spanish Catalyst Society Conference (SECAT'15). NATIONAL.
   Celebrated in Barcelona (Spain) from 13/07/2015 to 15/07/2015.

7. **DRIFTS-MS study in CO-PROX operando conditions using $CuO/Ce_{0,8}X_{0,2}O_2$ (X = Ce, Zr, La, Pr, Nd o Ba) catalysts.**
   Davó-Quiñonero, A., Navlani-García, M., Lozano-Castelló, D., Bueno-López, A., Anderson, J. A.
   Spanish Catalyst Society Conference (SECAT'15). NATIONAL.
   Celebrated in Barcelona (Spain) from 13/07/2015 to 15/07/2015.

Universitat d'Alacant
Universidad de Alicante